Universidade do Minho
Escola de Engenharia

Hadi Mazaheripour

Structural behavior of hybrid GFRP and steel reinforced FRC prestressed beams

Tese de Doutoramento
Engenharia Civil

Trabalho efetuado sob a orientação de
Professor Doutor Joaquim António Oliveira de Barros
Professor Doutor José Manuel de Sena Cruz

December 2015

STATEMENT OF INTEGRITY

I hereby declare having conducted my thesis with integrity. I confirm that I have not used plagiarism or any form of falsification of results in the process of the thesis elaboration.

I further declare that I have fully acknowledged the Code of Ethical Conduct of the University of Minho.

University of Minho, 2015

Full name: Hadi Mazaheripour

Signature: _____

Acknowledgement

The present work was developed at the University of Minho under the supervision of professor Joaquim António Oliveira de Barros and co-supervision of professor José Manuel de Sena Cruz. I would like to express my deepest appreciation to all institutions and individuals who made this work possible, namely:

- The financial support provided by the Portuguese Foundation for the Science and Technology (FCT), with grant number SFRH/BD/77409/2011, and the research project DURCOST with the reference number PTDC/ECM/105700/2008;
- University of Minho, through the laboratory of Structural (LEST), the Institute for Sustainability and Innovation in Structural Engineering (ISISE), and the Department of Civil Engineering (DEC), for providing the facilities and resources to develop this project;
- Professor Joaquim António Oliveira de Barros for his all support provided to this work and for making me grow as a researcher;
- Professor José Manuel de Sena Cruz for all the advice and discussion given to the present work;
- Mrs. Soltanzadeh for her collaboration in the experimental part of the present work;
- Technicians, Mr. Matos and Mr. Marco, from the LEST laboratory for their all contributions in the experimental part of the present work;
- To all my colleagues and friends that contributed to the development of this work.

Finally, I would like to thank my family to whom I owe a great deal. To my late father thank you for encouraging me to learn and study, and for all support providing me.

Abstract

The present thesis intended to contribute for the development of a new generation of high durable and sustainable reinforced concrete (RC) beam structures submitted to flexural loading, by combining the benefits that Glass Fiber Reinforced Polymers (GFRP) and steel bars can provide: the former due to their corrosion immunity, and the latter derived from their high ductility. Furthermore, High Performance Fiber Reinforced Concrete (HPFRC) was developed to improve the ductility of such innovative structures. To avoid corrosion, steel bar was placed with a HPFRC cover thickness, higher than 100 mm, while GFRP bars were applied in the near tensile surface of the HPFRC beams. In addition, the GFRP and steel bars were applied with a certain pre-stress level. The prestressing optimized their reinforcing capabilities, and increased the service load carrying capacity of the beam. On the other hand, conventional shear reinforcements were not used, and they were totally replaced by HPFRC material. Due to the quite high post-cracking tensile strength and energy absorption capacity that HPFRC attained, the composite system showed adequate shear resisting, and also enhancement in the structural performance at both Serviceability and Ultimate Limit States (SLS and ULS). The work started with the assessment to bond behavior between GFRP and HPFRC through experimental tests and analytical investigation. The structural performance of this hybrid prestressed GFRP-steel reinforced HPFRC was investigated by performing four-point bending tests on beams with I-shaped cross section under both monotonic and fatigue loading conditions. Moreover, an extensive analytical formulation was developed in order to theoretically address to the main structural aspect of the tested beams. The obtained experimental results were captured well using the respective results from the analytical study. Finally, finite element (FE) simulations were carried out using two well-known modelling approaches available in the literature for concrete elements in form of both 2D and 3D models. The results obtained from these models were promising, and it can be used for further analyses and developments in the field of present study.

Keywords: GFRP, strand, HPFRC, FE modelling, Analytical modelling, ductility

Resumo

A presente tese pretende contribuir para o desenvolvimento de uma nova geração de estruturas de betão armado, submetidas a esforços de flexão de elevada durabilidade e sustentabilidade, combinando os benefícios do uso de varões de polímeros reforçados com fibras de vidro (GFRP - Glass Fiber Reinforced Polymers) com os de varões de aço convencional: os primeiros devidos à sua imunidade à corrosão, enquanto que os segundos devido à sua ductilidade. Para além disso, foi desenvolvido um betão reforçado com fibras (HPFRC - High Performance Fiber Reinforced Concrete) de alto desempenho de modo a melhorar a ductilidade destas estruturas inovadoras. Para evitar a corrosão, o varão de aço foi colocado com um recobrimento superior a 100 mm, enquanto que os varões de GFRP foram aplicados junto à superfície mais tracionada das vigas de HPFRC. Adicionalmente, os varões de aço e de GFRP e foram aplicados com um determinado nível de pré-esforço. O pré-esforço potenciou os reforços usados para o comportamento em serviço da viga. Por outro lado, haverá que referir que não foram usadas armaduras convencionais de reforço aos esforços transversos (estribos), tendo sido totalmente substituídos pelo HPFRC. Devido à elevada resistência à tração e à elevada capacidade de absorção energia na fase de pós-pico que o HPFRC apresenta, o sistema estrutural mostrou adequada resistência aos esforços transversos, e também melhoria no desempenho estrutural, tanto para os Estados Limite de Serviço, bem como Últimos. O trabalho iniciou-se com o estudo da aderência entre o GFRP e o HPFRC através de ensaios experimentais e investigação analítica. O desempenho estrutural deste sistema híbrido foi investigado através da realização de ensaios experimentais em vigas com secção transversal em forma de I, sob quatro pontos de carga, em condições de carga monotónicas e de fadiga. Além disso, foi desenvolvida uma formulação analítica extensa com o objetivo de contemplar do posto de vista teórico, os principais aspetos estruturais das vigas ensaiadas. Os resultados experimentais obtidos foram simulados com rigor suficiente por intermédio destes estudos analíticos. Finalmente, foram realizadas simulações numéricas com recurso ao método dos elementos finitos utilizando, para tal, duas conhecidas abordagens disponíveis na literatura na simulação do HPFRC, recorrendo a modelos 2D e 3D. Os resultados obtidos a partir destes modelos numéricos foram promissores, podendo ser usados em futuras análises e desenvolvidos no âmbito do estudo desta área.

Content

List of figures

List of tables

Chapter 1

1. INTRODUCTION

1.1 Motivation and objectives

Steel reinforcing bars in aggressive environmental conditions are generally affected by corrosion, which is often responsible for deterioration and damage processes developing in reinforced concrete (RC) members. This corrosion phenomenon can occur after carbonation (Steffens *et al.* 2002) of concrete cortical layers in members exposed to water, humidity or other severe environmental conditions (Ryu *et al.* 20001). Then, the possible oxidation of steel reinforcements causes the reduction of their cross-section area, concrete spalling and possibly the loss of their bond to the surrounding damaged concrete, which can compromise the functionality of RC structures, or even their structural stability. Since the rehabilitation of corroded RC structures is generally an expensive solution, demolition of such structures is a relatively frequent option, though resulting in several unfavorable impacts in terms of economic, social and environmental aspects.

Durability issues related to the possible oxidation of steel reinforcement in concrete structures have brought up the attention of civil engineers towards alternative materials for reinforcing systems (Saadatmanesh and Ehsani 1991). Fiber Reinforced Polymers (FRPs), which were initially developed and employed in the aerospace, aeronautics, naval and automotive industries, generally exhibit high mechanical and durability performance. Thus, the research activities in this field are supporting the publication of design guidelines on the

use of FRP as internal reinforcement of cement-based composite members and, then, FRP bars are becoming more common in the construction sector. FRP bars using Aramid, Carbon or Glass fibers, namely by AFRP, CFRP and GFRP, respectively, are the most widely reinforcing elements that are being used in construction industry.

The most destroyer disadvantage of FRP bars comparing to steel bars is their cost in almost all cases. It is hard to compare the cost of FRP bars with those steel bars due to the many factors that may depend on. For instance, the delivery of FRP bars strongly depends on where they are ordered and from where they are supplied, and how much. But based on a rough analysis, it is expected to be paid almost 3 times as much for GFRP bars and almost 10 times as much for AFRP and CFRP (Burgoyne 2009). Additionally, this cost difference may increase where the high-strength FRP pre-stressing tendons is purposed. To this end, almost all FRP Reinforced Concrete (FRP-RC) applications are uneconomic. But, the answer to this issue is considering a "whole-life" cost of structures and not a "first-cost" basis. The benefits of using FRP bars is to overcome the problem comes from the use of steel reinforcements. Thus, few amount of the cost spent for FRP-RCs refunds within the typical structure lifetime and many for much longer.

In addition to the cost issue, FRP bars have lower Young's modulus and normally lower bond performance (especially in case of GFRP and AFRP bars) when they are compared to conventional steel bars. Moreover, the lack of yielding phase in stress-strain response introduces extra challenges in the behavior of concrete members reinforced with FRP bars mainly in terms of accomplishing the requirements for Serviceability Limit States (SLS) such as controlling crack width, crack spacing and total deformation (Almusallam 1997, Masmoudi *et al.* 1998, Pecce *et al.* 2000, Abdalla 2002, Taheri *et al.* 2012). Finally, the change in the material properties of FRP bars in case of exposure to high temperature affects the overall structure performance (Kashwani and Al-Tamimi 2014).

To overcome such problems, using a hybrid flexural reinforcing system by combining FRP and steel bars seems to be a promising solution. In this hybrid system, steel reinforcement ratio is designed to assure safety and integrity requirements in case of

exposure to high temperatures (e.g. fire), and to enhance the structural performance in terms of crack width, deformability and ductility. To improve the durability, steel bars are placed with relatively larger concrete cover for being better protected against corrosion. Due to the corrosion immunity of FRP bars, a minimum concrete cover is used in order to increase their structural capabilities. Some attempts have been carried out by combining FRP and steel bars (Aiello and Ombres 2002, Qu *et al.* 2009, Taheri *et al.* 2011), where it is reported an improvement in the flexural performance comparing with FRP-RCs. Furthermore, FRP and steel bars can be used with a certain pre-stress level for the optimization of their reinforcing capabilities and to overcome the concerns raise due to the lower elasticity modulus of FRP bars.

On the other hand, shear steel reinforcements also need to be protected against corrosive agents, as they are more susceptible to corrosion due to the smaller concrete cover. For eliminating steel stirrups, a High-Performance Fiber Reinforced Concrete (HPFRC) might be a solution, as long as this material provides similar shear reinforcement effectiveness to the conventional steel reinforcement (Soltanzadeh *et al.* 2015). Due to the quite high post-cracking tensile strength and energy absorption capacity that HPFRC can attain, this composite material can be used not only to assure the required shear capacity of RC elements, but also to enhance the structural performance at Serviceability and Ultimate Limit States (SLS and ULS).

The main objective of the present work is to develop high effective new reinforcing systems for the pre-fabrication industry of concrete beams of longer life span. The beams are designed to support severe environmental agents (e.g. in the coastline), in order to constitute a competitive alternative to the existing conventional structural solutions. The objective is achieved by developing a new generation of pre-fabricated Fiber Reinforced Concrete (FRC) beam with pre-stressed hybrid GFRP/steel reinforcing bars.

1.2 Research steps

In order to achieve the purpose of the study, the following steps were followed in the

present research:

i. Firstly, the study focused on evaluating bond behavior between GFRP bars and FRC. It was also purposed to locate GFRP bars as near as possible to the tensile surface of FRC beam element. In fact, the minimum thickness of FRC cover required for GFRP bar was assessed by performing bending pullout tests of different FRC cover thicknesses. In addition to the experimental pullout tests, extensive analytical was carried out for the development of a model to simulate the bond behavior of reinforcing bars and FRC. This research us detailed in Chapter 3;

ii. As the next step, detailed in Chapter 4, a theoretical study on the interaction between FRC, GFRP and steel bars have been carried out by taking the bond models proposed in the previous step of the work. To this end, FRC member reinforced with GFRP and steel bars (hybrid reinforcement) is subjected to uniaxial tension, and its cracking and tension stiffening behavior is theoretically studied. The predictive performance of this model was validated using some recent experimental results available in the literature.

iii. At third step, the study investigates the structural behavior of beams of high performance fiber reinforced concrete (HPFRC), with I-shaped cross-section, reinforced in flexural with hybrid prestressed steel strand and GFRP bars. For this purpose, the beams were tested in flexure under monotonic and fatigue loading conditions, where the reinforcement ratio and pre-stress level of reinforcing bars were the main experimental parameters. Then, the main structural parameters such as deformation, crack spacing, crack width and ductility under both ultimate and serviceability conditions are examined. This work is detailed in Chapter 5;

iv. Finally, Chapter 6 details the 2D and 3D finite element analysis (FEM) were carried out to simulate the results obtained from the experimental tests with good accuracy. The models are based on the two well-known modeling approaches that are being used to simulate RC structures.

Chapter 2

2. LITERATURE REVIEW

2.1 Introduction

A state of the art with respect to the flexural behavior of concrete (or FRC) beams reinforced by FRP bars, mostly GFRP type, is presented in this chapter. Several studies were analyzed hereafter and their main outcomes are described and summarized.

This literature review is divided into four different parts including:

i. Bond mechanism of GFRP bars as internal reinforcements for concrete members;
ii. Concrete beams reinforced by longitudinal GFRP bars (GFRP-RC beams);
iii. Fiber Reinforced Concrete beams reinforced by longitudinal FRP bars (FRP-FRC beams);
iv. Concrete beams reinforced by hybrid reinforcing system including FRP and steel bars (hybrid FRP/steel RC beams).

2.2 Bond mechanism of GFRP bars

Bond behavior between the reinforcing bars and concrete is an important key issue to study the behavior of Reinforced Concrete (RC) members. For this reason, investigation of bond behavior of GFRP bars to concrete became a main mechanical property for civil engineers as soon as their introduction to construction industry for alternative reinforcing system.

The bond behavior between GFRP bars and concrete has been extensively studied during the last two decades. In contrast with conventional steel bars, GFRP bar has no standardization for surface treatments. Many researcher reported that the surface characteristics (e.g. sand-coated, indented, ribbed, helical or wrapping) of GFRP bar strongly affect the bond shear stress between GFRP and concrete (Rossetti *et al.* 1995, Pecce *et al.* 2001, Achillides and Pilakoutas 2004, Aiello *et al.* 2007, Hao *et al.* 2007, Lee *et al.* 2008, Baena *et al.* 2009). Figure 2-1 shows GFRP bars with different surface configurations. Further, Table 2-1 includes the typical nomination of surface treatments of GFRP bars, which has been presented in Figure 2-1.

Table 2-1 Typical nomination of surface treatments for the GFRP bars shown in Figure 2-1

GFRP types*	**Surface treatments**	**Abbreviation**
Type 1	Ribbed Surface by grooves	RS
Type 2	Single fiber strand winding (Helically Wrapped surface)	HW**
Type 3	Double fiber strand winding (Helically Wrapped surface)	DHW
Type 4	Helically Wrapped surface with Sand Coating	HWSC
Type 5	Sand Coating	SC
Type 6	Ribbed surface with Rope Winding	RRW

* See Figure 2-1 for GFRP types;
** This surface technique in some references it was named as spirally wound technique. But they are categorized as helically wrapped surface in this chapter.

In addition to the surface type, GFRP modulus of elasticity, shear and tensile stiffness of GFRP bar, compressive strength of concrete, concrete cover thickness, bar diameter and embedment length have been reported as the other effective parameters on the bond behavior. Moreover, the bond between GFRP bars and surrounding concrete is controlled by several factors, including chemical bond, friction due to surface roughness of GFRP rods, mechanical interlock between GFRP bars and concrete, confinement applied to the GFRP bars due to concrete shrinkage. The chemical bond (adhesion) is the main resisting mechanism during initial pullout. Afterwards, the friction and mechanical interlock become the main reinforcing mechanisms. In terms of their relevance for the bond transferred force, frictional and mechanical interlock showed an effect that is much higher than the chemical bond between GFRP and concrete (Cosenza *et al.* 1997).

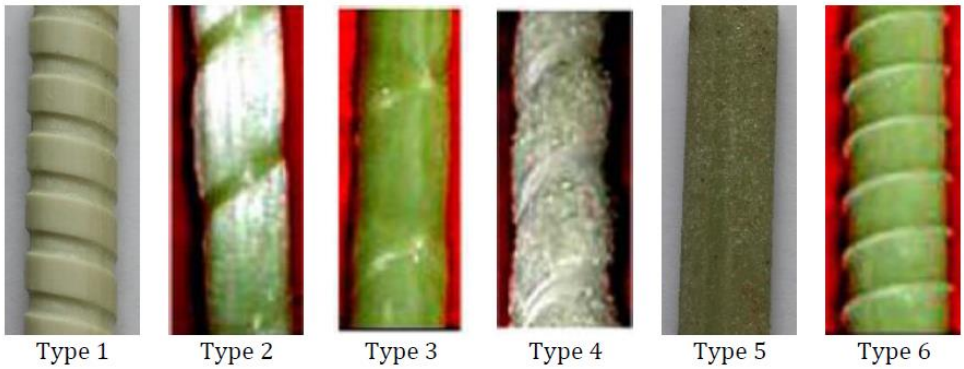

Figure 2-1: Different surface configuration of GFRP bars

2.2.1 Bond evaluation test setup

The bond test setups most widely used to evaluate the bond behavior are: (i) the direct pullout test (with centric or eccentric position of bar), (ii) the beam test, (iii) the splice test and (iv) the ring pullout test; being the direct pullout test the most frequent one. Figure 2-2 shows a schematic representation of these test setups. Despite the direct pullout test has been used to compare the effectiveness of the relevant bond parameters, such is the case of bar diameter, bar surface treatment, and concrete strength, the obtained results are affected by the confinement applied to the surrounding concrete during the pullout process (Aiello *et al.* 2007). This type of confinement can be also effective in the ring pullout test (Figure 2-2b), due to a similar compression action on the surrounding concrete at the loaded end applied by the specimen's supporting system. These setups, therefore, do not replicate the bond conditions of a reinforcing system in a real concrete element. Hence, to avoid the influence of concrete confinement, beam test (or splice test) might be a better pullout test for evaluation of bond behavior.

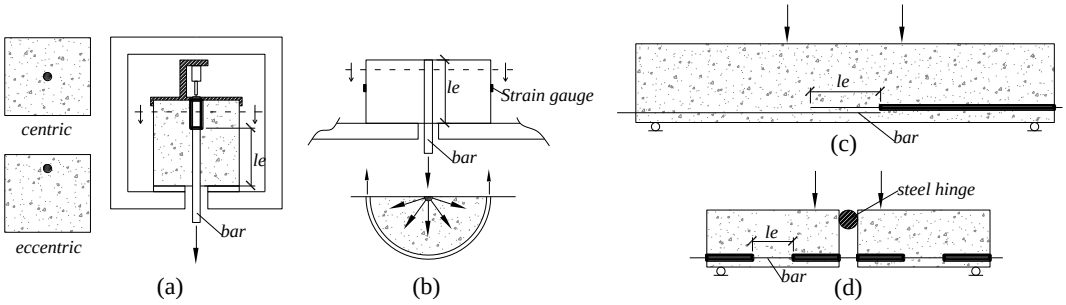

Figure 2-2: Schematic illustration of bond test setups: (a) Direct pullout, (b) Ring, (c) Splice, and (d) Beam test

In the pullout tests, typically, bond behavior of an embedded bar is evaluated by recording the applied pullout force against the relative slip between the bar and concrete (*i.e.* δ) at "*loaded-end*" (the cross-section of the bar at the beginning of the embedded length where the pullout load is applied) and "*free loaded-end*" (the cross-section of the bar at the extremity of the embedded length). Then, the bond behavior of the embedded bar is typically presented as $\tau - \delta$ curve where τ is the bond shear stress. This value can be defined as an average bond shear stress over the embedded length, which is calculated by

$$\tau_m = \frac{F}{l_e P_r} \tag{2-1}$$

where F , l_e and P_r are, respectively, the pullout force, the embedded length and the perimeter of reinforcing bar.

2.2.2 Pullout test results

In this section, a brief review on the experimental results of GFRP pullout tests is given by considering $F - \delta$ curve obtained from test data. The aim is to review the influence of some main parameters on the variation of the bond shear strength (*i.e.* τ_m) and its corresponding slip at loaded end (*i.e.* δ_m). Then, these values are compared with those obtained for conventional steel bars.

2.2.2.1 Bond shear strength of GFRP bars

A summary of the pullout test results in literature for different types of GFRP bars of 8~10 mm, 12~15 mm and >15 mm of diameter are written, respectively, in Table 2-2, Table 2-3, and Table 2-4 in terms of τ_m and δ_m . Further, Table 2-5 reports the same results but for conventional steel bars. The tests were carried out with different concrete types, thus the mechanical properties of concrete were different. In order to take into account the effect of the diversity of concrete type on the bond behavior, τ_m is modified by multiplying the following coefficient (Aiello *et al.* 2007):

$$\left(\frac{f_c'}{f_{cREF}'} \right)^{0.5} \tag{2-2}$$

where f_c' is the concrete compressive strength at 28th day of concrete curing reported in the literature and f_{cREF}' is the reference compressive strength that is assumed to be 30 MPa as a moderate value in analysis.

Table 2-2 Summary of the pullout results for different types GFRP bars (ϕ_b =6-10 mm)

Surface Type *	ϕ_b (mm)	τ_m ** (MPa)	δ_m (mm)	l_e/ϕ_b (-)	f_c' (MPa)	**Reference**
Rough surface	8.5	9.2	1.10	6	41	Achillides and Pilakoutas 2004
	8.5	11.7	1.00	8		
	8.5	12.5	1.31	10		
Medium Rough surface with surface deformation (24 roving)	10.5	4.0	0.23	6		
	10.5	3.9	0.45	8		
	10.5	4.1	0.46	10		
Medium Rough surface with surface deformation (36 roving)	10.5	4.0	0.26	6		
	10.5	4.7	0.49	8		
	10.5	5.5	0.51	10		
Sand coating, Helical wrapping	6	12.3	1.35	5	40	Okelo and Yuan 2005
	10	16.5	1.2	5		
	10	13.3	1.2	7		
	10	10.8	1.1	9		
Ribbed surface	10	15.5	0.98	5		
	10	15.0	1.34	7		
	10	12.7	1.17	9		
Sand coating	10	15.5	0.22	5		
Surface texture	8	11.2	0.76	5		
Fine sand coating and spiral wound	8.5	15.9		5	53	Aiello *et al.* 2007
	8.5	8.7		7		
Fine sand coating	8	3.0	0.45	5		
Coarse sand coating	8	3.0	0.49	5		
Ribbed surface	10	12.5	2.83	4	27	Hao *et al.* 2007
Double strand fiber winding	10	11.0	3.08	4		
Single strand fiber winding	8	17.2	4.48	4		
Single strand fiber winding and sand coating	6.5	22.2	2.34	4		
	9.5	19.3	0.60	4		
Ribbed surface with rope winding	10	9.8	3.00	4		
Helically wrapped and sand coating	9.5	13.5	0.30	5	63	Davalos *et al.* 2008
Sand coating	9.5	14.5	0.40	5	59	
Sand coating	10.2	12.3	1.95	5	53	Baena *et al.* 2009
Sand coating and helically wrapped	9.3	16.6	2.48	5	52	
Ribbed surface (grooves)	8.5	13.2	1.73	5	50	
	8.5	12.5	1.34	5	29	
Helically wrapped	8	22.4	6.38	5	47	
	8	17.1	5.06	5	30	
Ribbed surface (grooves)	8	13.1	1.76	4	29	Hao *et al.* 2009
	10	12.4	2.83	4	29	

* The surface description of GFRP bars is based on what was named by the respective authors;

** τ_m is the average bond shear strength of pullout specimens, which was modified by coefficient presented by Eq. (2-2)

Table 2-3: Summary of the pullout results for different types GFRP bars (ϕ_b=12-15 mm)

Surface Type *	ϕ_b (mm)	τ_m ** (MPa)	δ_m (mm)	l_e/ϕ_b (-)	f_c' (MPa)	**Reference**
Spirally wound and sand coated	12.7	11.1	0.46	6	31	Tighiouart *et al.* 1998
Spirally wound and sand coated	12.7	10.4	0.33	10		
Spirally wound and sand coated	12.7	9.84	0.50	16		
Ribbed surface with Rope Winding	12.7	12.1	0.30	10		
Sand Coating, and Helical wrapping	12.7	13.0		5	34	Katz 1999
Helical wrapping	12.7	11.5		5		
Sand Coating, Helical wrapping (deep dents)	12.7	3.8		5		
Deformed by resin	12.7	13.7		5		
Smooth bar (no surface treatment)	12	0.9		5		
Deformed by resin	12.7	12.3	0.68	5	39	Pecce *et al.* 2001
	12.7	11.7	1.14	10	39	
	12.7	5.5	1.28	20	54	
Rough surface	13.5	8.4	0.62	4	45	Achillides and Pilakoutas 2004
	13.5	7.4	0.85	6		
	13.5	5.9	0.82	8		
	13.5	6.1	0.92	10		
Ribbed surface	12.7	10.8	0.59	5	53	Aiello *et al.* 2007
Single fiber strand winding	12	10.6	3.03	4	27	Hao *et al.* 2007
Single strand fiber winding and sand coating	12.7	12.1	3.32	4	26	
Helically wrapped and sand coating	12.7	14.8	0.70	5	63	Davalos *et al.* 2008
Sand coating	12.7	21.6	0.39	4	25	Lee *et al.* 2008
		19.9	0.49		35	
		18.4	0.42		40	
		15.8	0.34		55	
		15.4	0.11		75	
		14.4	0.12		90	
Helically wrapped	12.7	20.7	4.34	4	25	
		18.3	5.23		35	
		18.6	4.84		40	
		14.7	5.02		55	
		15.0	3.97		75	
		15.1	0.41		90	
Sand coating	14.13	11.9	1.91	5	53	Baena *et al.* 2009
		11.2	1.99		28	
Helically wrapped and sand coating	13.73	12.9	2.31		52	
		9.84	6.54		30	
Ribbed surface	12	11.3	1.42		54	
		8.79	1.42		30	
Helically wrapped	12	20.7	8.92		47	
		16.64	7.07		30	
Ribbed surface	12	10.6	3.03	4	29	Hao *et al.* 2009

* The surface description of GFRP bars is based on what was called by the respective authors;

** τ_m is the average bond shear strength of pullout specimens, which was modified by coefficient presented by Eq. (2-2)

Table 2-4: Summary of the pullout results for different types GFRP bars (ϕ_b >15 mm)

Surface Type *	ϕ_b (mm)	τ_m ** (MPa)	δ_m (mm)	l_e/ϕ_b (-)	f_c' (MPa)	**Reference**
Spirally wound, Sand coated	15.9	10.4	0.34	6	31	Tighiouart *et al.* 1998
	19.1	7.0	0.18	6		
	25.4	6.9	0.20	6		
	15.9	7.2	0.54	10		
	19.1	6.5	0.39	10		
	25.4	6.3	0.39	10		
	19.1	6.2	0.60	16		
	25.4	5.8	0.49	16		
Ribbed surface with Rope Winding	15.9	10.6	0.42	10		
	25.4	7.3	0.35	10		
Smooth bar	16	1.5	0.65	5	45	Achillides and Pilakoutas 2004
Sand coating, Helical wrapping	16	15.5	4.90	5	40	Okelo and Yuan 2005
	16	15.7	4.32	7		
	16	12.8	1.95	9		
	19	13.5	3.32	5		
	19	12.1	2.90	7		
	19	8.1	2.31	9		
Ribbed surface	19	14.5	0.98	5		
	19	10.7	0.81	7		
	19	5.5	0.53	9		
Sand coating	16.4	14.6	1.87	5	53	Baena *et al.* 2009
	19.5	11.5	1.53	5	53	
Sand coating and helically wrapped	16.1	12.3	5.86	5	52	
	19.1	11.1	4.99	5	52	
Ribbed surface (grooves)	16	11.0	1.25	5	29	
Helically wrapped	16	16.5	7.97	5	47	
	19	13.2	5.46	5	47	

* The surface description of GFRP bars is based on what was called by the respective authors;

** τ_m is the average bond shear strength of pullout specimens, which was modified by coefficient presented by Eq. (2-2)

Table 2-5 Summary of the pullout results for different type conventional steel bars

Surface Type	ϕ_b (mm)	τ_m * (MPa)	δ_m (mm)	l_e/ϕ_b (-)	f_c' (MPa)	**Reference**
Ribbed surface	12.7	22.7		6	31	Tighiouart *et al.* 1998
	15.9	21.5		6		
	19.1	15.7		6		
	25.4	13.3		6		
Ribbed surface	12	11.4		5	34	Katz 1999
Ribbed surface	12	17.4	0.29	5	56	Pecce *et al.* 2001
Ribbed surface	10	20.4	0.15	5	40	Okelo and Yuan 2005
Ribbed surface	12	17.5	1.00	5	53	Aiello *et al.* 2007
Ribbed surface	10	22.2	1.08	4	27	Hao *et al.* 2007
	12	21.7	1.24	4		
Ribbed surface	12.7	23.6	0.97	4	25	Lee *et al.* 2008
Ribbed surface	10	22.8	1.30	5	49	Baena *et al.* 2009
	12	18.3	1.70	5		
	16	17.9	1.62	5		
	20	14.5	0.52	5		

* τ_m is the average bond shear strength of pullout specimens, which was modified by coefficient presented by Eq. (2-2)

Figure 2-3 is plotted based on the results of pullout tests reported in the literature where the embedded length of the bars were 4~6 times of the bar diameter. In this figure, the bond shear strength of different GFRP bar's surfaces, which has been written in Table 2-1, are compared with the typical ribbed surface steel bars. The results are categorized by three groups of bar's diameters as mentioned above. According to this analysis, the most widely used GFRP bar's surface was helically wrapped surface with sand coating technique (HWSC). However, GFRP bars with only helically wrapped surface technique (*i.e.* HW) show an average bond shear strength higher than HWSC. This is, the combination of sand coating and helically wrapped techniques may not lead to a significant improvement in terms of the value of τ_m. Ribbed surface (RS) and fine sand coating (SC) are the other common type external surface for GFRP bars. Although, the reliability of the results for RS seems to be better than SC, both showed almost the same average bond shear strength.

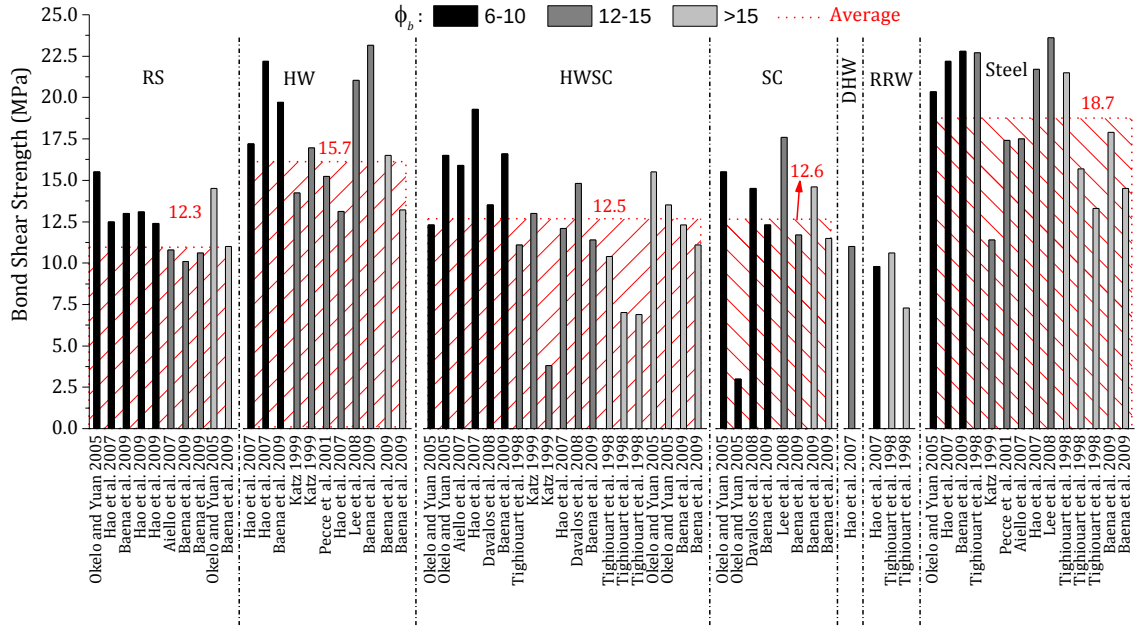

Figure 2-3: Comparison between different GFRP bar's surfaces and steel bars in terms of the average bond shear strength based on the pullout test results

Double fiber strand winding (DHW) and Ribbed surface with Rope Winding (RRW) are two surface's treatment techniques that were rarely used, hence, a few number of pullout test was available for them. In addition, the average bond shear strength for DHW and RRW were lower than those from the other surface's treatments. In addition to the results of GFRP

bars, the average bond shear strength of ribbed surface steel bar also shown in Figure 2-3. As shown, the average bond shear strength of ribbed conventional steel bar was generally higher than all GFRP bar's surfaces for three bar's diameter categories. The bond shear strength of steel bars can be estimated about 1.2 to 1.5 times of magnitude higher than the average bond shear strength of GFRP bar, being dependent on GPFR bar's surface. It is worth noticing that all the values reported in Figure 2-3 are corrected by using coefficient presented in Eq. (2-2) in order to minimize the effect of concrete compressive strength on the value of τ_m .

2.2.2.2 Slip at the peak bond shear strength

Figure 2-4 shows the results of pullout test in terms of τ_m *versus* δ_m for different GFRP bar's surfaces and conventional ribbed steel bar. In contrast with the results of steel bars, the dispersion of data for GFRP bars even for the same surface configuration is high. Thus, it is quite difficult to derive specific conclusion for the relationship between τ_m and δ_m . The variety of modulus of elasticity of GFRP bars (ranged 35-65 GPa), using different resin types in the diverse producing processes, diversity of test setup configurations, the error in measuring slip during the pullout test among other aspects that can affect the results, can be named as the reasons of this fact. As an example, in almost all pullout tests, it is difficult to measure the loaded end slip of internal reinforcing bar exactly at the beginning of the embedded length due to the distance of this point from the concrete surface. For this reason, the slip measuring device (e.g. LVDT: Linear Variable Differential Transformer) is normally installed with a prescribed distance from the loaded end section. Thus, the total recorded slip needs to be corrected by subtracting the elastic elongation of the bar along this distance, which can be a significant value for GFRP bars whose the young's modulus are lower than steel. In the pullout tests that carried out by Okelo and Yuan 2005, the slip was measured according to this procedure. However, the other authors did not correct the value of slip, or at least they did not mention in their work.

In addition to the scatter data in Figure 2-4, two lines have been plotted. The sold line is

based on the minimum ratio τ_m / δ_m that covers all the results of steel bars, and the dashed-line is with the same concept but for GFRP bars. The ratio of the slope of these two lines closely represents the ratio between the Young's modulus of steel and GFRP bars. This modular ratio may represent the ratio between the bond stiffness of GFRP bar and steel bar for the same level of bond shear strength.

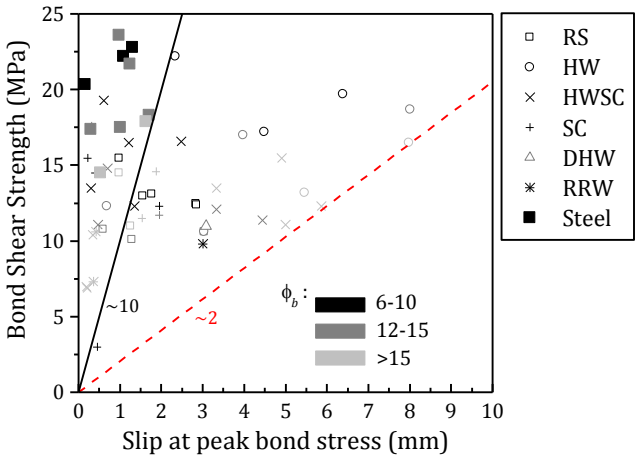

Figure 2-4 Bond shear strength *versus* the corresponding slip for all GFRP bar's surface type and conventional ribbed steel bars based on the data from the literature

2.2.2.3 Effect of concrete compressive strength

Based on the results of pullout test in the studies carried out by Lee *et al.* (2008) and by Baena *et al.* (2009), the bond strength of GFRP bars increased when the concrete compressive strength (*i.e.* f_c') increased. This is the same as found for conventional steel bars. In Figure 2-5, the experimental results of pullout test in terms of bond shear strength *versus* the concrete strength is plotted.

The following equation is recommended by ACI 440.1R-06 for estimation of bond strength of FRP bars, which is function of $\sqrt{f_c'}$:

$$\tau_m = \left(0.332 + 0.025\frac{C}{\phi_b} + 8.3\frac{\phi_b}{l_e} \right)\sqrt{f_c'} \qquad (2\text{-}3)$$

where C is the concrete cover thickness. A comparison between the pullout test results and the predictions given by ACI is also depicted in Figure 2-5 for the embedded length of $5\phi_b$ and concrete cover thickness of $3\phi_b$. As shown in Figure 2-5, the design equation by ACI

estimates reasonably the bond shear strength results in the tests for different GFRP bar type in terms of surface treatment and bar diameter. For having more precise result, a care should be taken to include the effect of FPR bar's external surface in this equation.

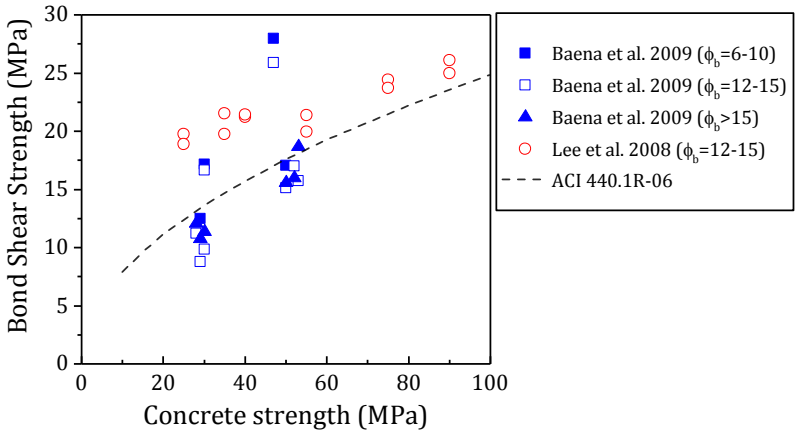

Figure 2-5: Effect of concrete compressive strength on bond shear strength of GFRP bars

2.2.2.4 Effect of embedded length

A small embedment length of 4 to 6 time of bar diameter was usually considered in most of the pullout test carried out and found in the literature (data can be found in Table 2-2, Table 2-3, and Table 2-4). When the bond shear strength is calculated by Eq. (2-1), the value decreases by increasing in the embedded length, which is regardless of the type of reinforcement and concrete compressive strength. This effect is shown in Figure 2-6 for some results of the pullout in the literature whose values are included in the mentioned tables. More discussion will be given in regards to this effect in the next chapter, where the bond behavior of GFRP bars utilized in the present study is extensively investigated.

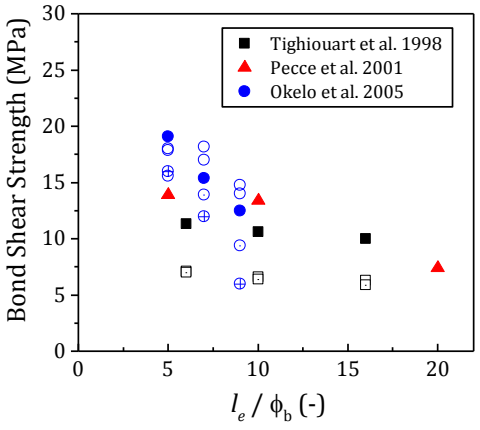

Figure 2-6: Effect of embedded length of FRP bars on the bond shear strength

2.3 GFRP-RC beams

During the last two decades, many attempts have been done to evaluate the structural performance of FRP reinforced concrete structures (Benmokrane *et al.* 1996, Almusallam 1997, Theriault and Benmokrane 1998, Aiello and Ombres 2000, Alsayed *et al.* 2000, Pecce *et al.* 2000, Toutanji and Saafi 2000, Abdalla 2002, Toutanji and Deng 2003, Rasheed *et al.* 2004, Tavares *et al.* 2008, Barris *et al.* 2009). Since the present work will purpose the use GFRP bars as internal reinforcing bars for beam members, a brief review is given in this section on structural performance of GFRP-RC beams. Due to the lower modulus of elasticity and inferior bond strength of GFRP bars comparing with steel bars, it is expected that the requirements in terms of serviceability limit states (such as service deflection and crack width at service loads) becomes the design criterion for GFRP-RC beams. Additionally, due to the lack of yielding phase for GFRP reinforcing bars, their failure mode becomes an important issue in terms of ductility.

Benmokrane *et al.* (1996) carried out two series of experimental tests on the evaluation of the flexural performance of GFRP-RC beams as well as conventional steel RC beams. The beams were 3300 mm long with the same reinforcement ratio for both GFRP and steel bars, but different rectangular cross-sections of 200×300 mm^2 for series S1, and 200×550 mm^2 for series S2. The GFRP-RC beams were over-reinforced for the series S1 of tests and under-reinforced for the S2, while steel RC beams were under-reinforced for both series. The details regarding to the specimens and test setup are written in Table 2-6. Figure 2-7 shows the load-deflection history of the tested beams. Typical respond of GFRP-RC beams against steel-RC beams can be observed from this figure. For the same level of load carrying capacity, much higher deformation was obtained for GFRP-RC beams. As shown, ACI formulations were used to predict the force-deflection response of steel RC beams, overestimates the force-deflection response of GFRP-RCs due the nature of GFRP bars that exhibited larger deformation than steel bars. Moreover, based on the cracking pattern of the tested beams, they reported that the average cracking space for GFRP-RCs at low loading level (25% of ultimate) was similar to the steel-RC beams for both series of the

tests. But for higher level of applied load, the lower average cracking space and wider crack were observed for the GFRP-RCs rather than the steel RC beams.

Table 2-6: Details of specimens and the measured ductility index for the tested GFRP RC beams in literature

Beam ID		Section size	Span (shear span)	f_c'	Longitudinal reinforcement				
					Quantity	type	Tensile strength (yielding)	Modulus of elasticity	ρ *
		(mm×mm)	(mm)	(MPa)			(MPa)	(GPa)	(%)
Benmokrane *et al*. 1996									
Series S1	ISO1	300x200	3300 (1000)	43	2Ø20	GFRP	640 (-)	40	1.10
	ISO2					GFRP			
	ST1					Steel	600 (480)	200	
	ST2					Steel			
Series S2	ISO3	550x200				GFRP	640 (-)	40	0.56
	ISO4					GFRP			
	ST3					Steel	600 (480)	200	
	ST4					Steel			
Alsayed 1998									
	Series A	210x200	2700 (100)	31	3Ø14	Steel	- (553)	200	0.68
	Series B	210x200			4Ø19	GFRP	700	50	1.34
	Series C	260x200			4Ø12.7	GFRP	886	50	0.64
	Series D	250x200		41	4Ø19	GFRP	700	50	0.90
Masmousdi *et al.* 1998									
S1	CB2B-1	300x200	3000 (500)	52	2Ø14	GFRP	773 (-)	38	0.56
	CB2B-2			52					0.56
	ST2B			46		Steel	600 (480)	200	0.42
S2	CB3B-1			52	3Ø14	GFRP			0.91
	CBSB-2			52					0.91
S3	CB4B-1			45	4Ø14	GFRP	773 (-)	38	1.38
	CB4B-2			45					1.38
S4	CB6B-1			45	6Ø14	GFRP			2.15
	CB6B-2			45					2.15
	ST6B			46		Steel	600 (480)	200	2.00
Toutanji *et al.* 2003									
1	GB1-1	300x180	2800 (400)	35	2Ø12.7	GFRP	695 (-)	40	0.52
	GB1-2								0.52
2	GB2-1				3Ø12.7				0.79
	GB2-2								0.79
3	GB3-1				4Ø12.7				1.1
	GB3-2								1.1
Barris *et al.* 2009									
C-212-D1		190x140	1800 (600)	59.8	2Ø12	GFRP	1353 (-)	63	0.99
C-216-D1				56.3	2Ø16		995 (-)	64	1.78
C-316-D1				55.2	3Ø16		995 (-)	64	2.67
C-212-D2		190x160		39.6	2Ø12		1353 (-)	63	0.99
C-216-D2				61.7	2Ø16		995 (-)	64	1.78
C-316-D2				60.1	3Ø16		995 (-)	64	2.67

* Reinforcement ratio

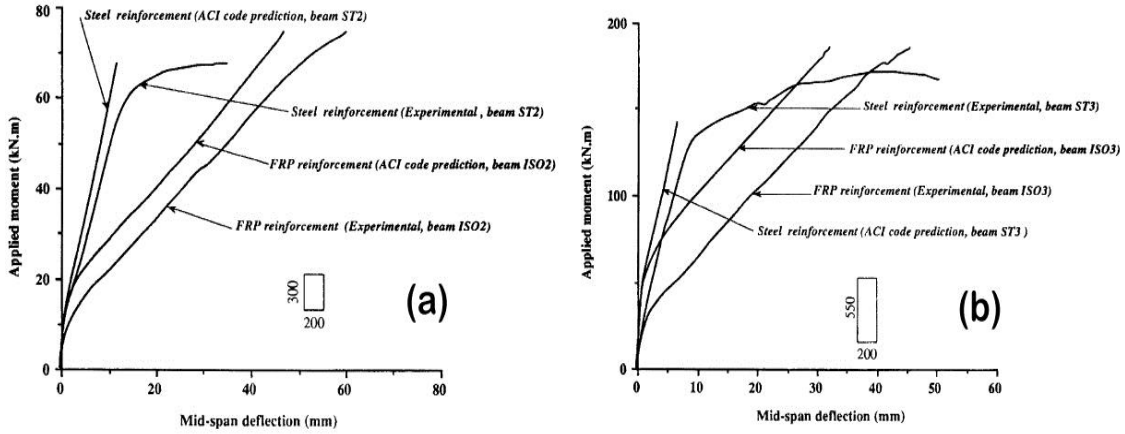

Figure 2-7: Typical load-deflection history of tested beams carried out by Benmokrane *et al.* (1996): (a) series S1 and (b) series S2

Alsayed (1998) carried out a total of 12 beams divided in four main groups, being each group composed of three identical beam specimens. The specimen details of these series of beam tests are included in Table 2-6. The force-deflection response of the tested beams are shown in Figure 2-8 for the four series of the beams. Alsayed (1998) concluded that for GFRP-RC beams that were designed to be failed by crushing of concrete in compression zone (*i.e.* over-reinforced beams), the deflection at service load may be the design criterion. Based on the obtained results, the authors also reported that for the same ultimate flexural capacity of GFRP-RC and steel-RC beams, the average measured deflection of the GFRP-RC beams is about 2 times higher than the one obtained in the beams reinforced by steel bars.

Masmoudi *et al.* (1998) carried out a series of 3000 mm long span beams reinforced by GFRP bars and steel bars. The tested GFRP-RC beams were all over-reinforced in order to have failure mode in concrete compression zone. The corresponding details about the specimens are found in Table 2-6. Their study was focused more on cracking and deflection behavior of the tested beams. The typical cracking pattern of GFRP-RC and steel-RC obtained from their study for the same reinforcement ratio is shown in Figure 2-9. As they concluded, average crack spacing for GFRP-RC beams was similar to the corresponding beams reinforced with steel bars at low level of loading (about 25% of ultimate loading capacity). However, at moderate and high loading, as shown in Figure 2-9, the average crack spacing was less for the GFRP-RC beams than the steel-RC beams. This result was in

agreement with the work carried out by the previous authors (Benmokrane *et al*. 1996 and Alsayed 1998). The authors also reported that the effect of the reinforcement ratio on the crack spacing is negligible. The results in terms of moment *versus* crack width are plotted in Figure 2-10. The maximum observed crack width in the GFRP-RC beams were three to five times higher than the observed values in the steel-RC beams. Further, the maximum crack width deceased by increasing FRP reinforcement ratio for the same level of applied moment. The authors suggested that the crack width limitation recommended by ACI committee 318 and Canadian code for conventional reinforced concrete should be modified since the corrosion does not exist for GFRP bars. They also stated that the crack width can be controlled for reason of undesirable appearance.

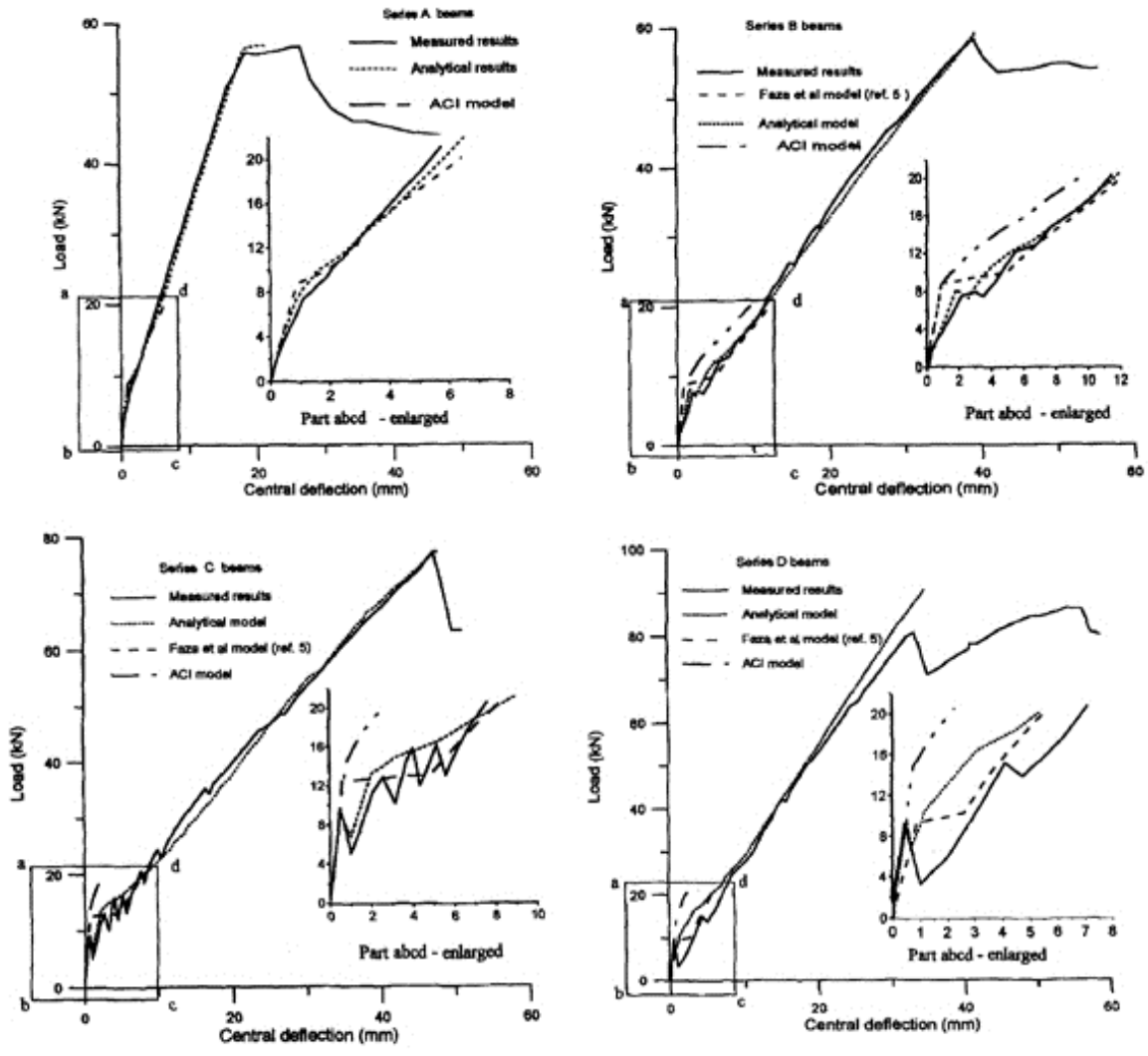

Figure 2-8: Force-deflection response of the tested beams by Alsayed (1998)

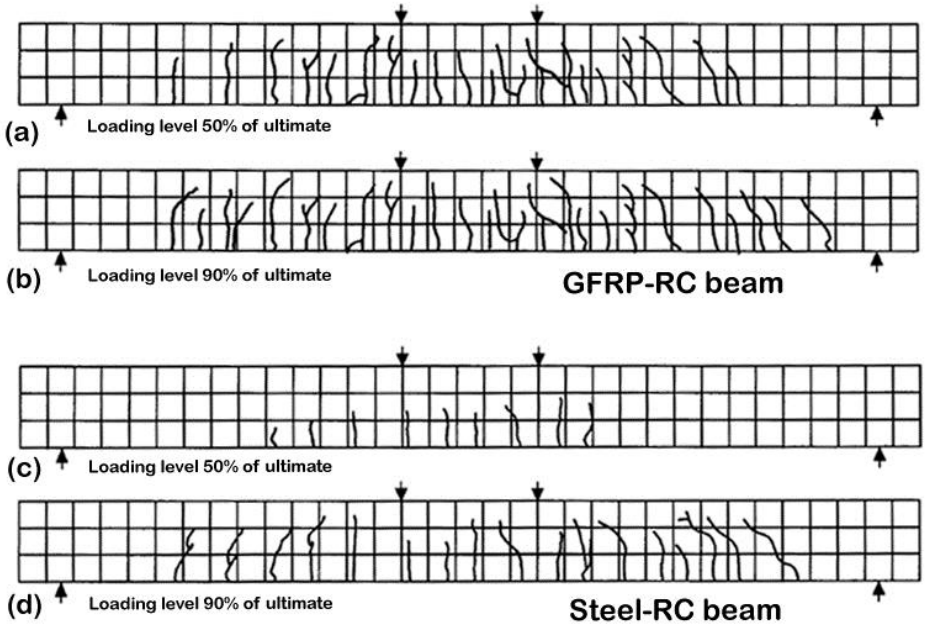

Figure 2-9: Typical cracking pattern of reinforced beams at (a)(c) moderate 50% and (b)(d) high 90% level of loading (Masmoudi *et al.* 1998)

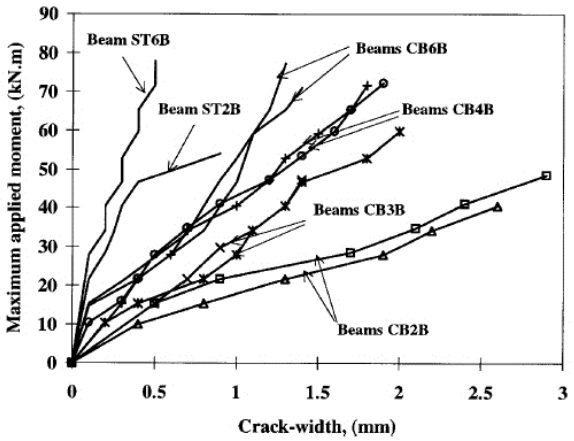

Figure 2-10: Moment *versus* crack width for the tested beams by Masmoudi *et al.* (1998)

An extensive number of concrete beam specimens were tested by Theriault and Benmokrane (1998) to evaluate the flexural behavior of GFRP bars as internal reinforcement. They obtained similar results to ones obtained by the previous authors. They have also showed that the existing formulations in the available codes for steel reinforced concrete beams in terms of both serviceability limit state (SLS) and ultimate limit state (ULS) had to be modified in order to be applied for GFRP-RC beams.

In 2000, several GFRP-RC beams were tested by Alsayed *et al.* and Houssam *et al.* Their main purpose was to recommend some modifications to the currently used ACI 318 model

for computing flexural strength, service load defection, and the minimum reinforcement required to be used for case of GFRP-RCs. Alsayed *et al.* (2000) suggested a model to estimate the minimum required reinforcement ratio for GFRP-RC beams in order to avoid the possibility of a catastrophic failure of GFRP bars. This minimum reinforcement ratio was calculated based on a safety factor of 1.5 for GFRP bar, meaning that the ultimate tensile strain of GFRP was set to 67% of the corresponding nominal value.

In 2001, the first version of ACI code by committee 440 as title of "*Guide for the design and construction of concrete reinforced with FRP bars*" was published. So far, it has been updated twice, once in 2006 and another recently in 2012. Afterward, many other countries have published the codes and guidelines for FRP reinforced concrete members, namely: The International Federation for Structural Concrete (CEB-FIB), Canadian Standard Association (CSA), and Japan Society of Civil Engineers (JSCE). After 2001, the purpose of most of the research studies was to verify the effectiveness of different parameters on the reliability of the equations and design formulations that have been recommended by the aforementioned codes and guidelines. As example, Toutanji and Deng (2003) carried out a series of six GFRP-RC beams in order to verify the effectiveness of high reinforcement ratio on the load-deflection and crack width prediction provided by ACI 440. Their main focus was to evaluate the effects when the reinforcements are arranged in two layers in the section. Figure 2-11 compares the experimental trends of moment *versus* crack width and moment *versus* deflection at mid span with those values predicted by ACI 440. In this figure, the three sets of GFRP-RC beams named GB1, GB2 and GB3 with reinforcement ratios of 0.52, 0.79 and 1.2%, respectively, are depicted (the specimens and test setup details can be found in Table 2-6). Note that for GB3, GFRP bars were installed in two layers. According to the conclusions derived by their study, for GFRP bars placed in one layer, ACI 440 equations accurately estimate the crack width, however, this code underestimated for the third series of beams (*i.e.* GB3), where the GFRP bars were arranged in two layers.

Barris *et al.* (2009) carried out a set of GFRP-RC beams with ribbed GFRP bar that have a relatively high modulus of elasticity (about 64 GPa) comparing to other GFRP types. The

main aim of their study was to evaluate the short-term flexural behavior, and to compare with the predictions recommended by different design codes. Based on the results obtained from the tested beams, they concluded that the code formulations and some available models predicted well the behavior up to service load (see Figure 2-12). However, at the ultimate limit state, load capacity was underestimated. Note that the reinforcement ratio and depth-to-height ratio of the tested beams were the main variables (specimen details are given in Table 2-6).

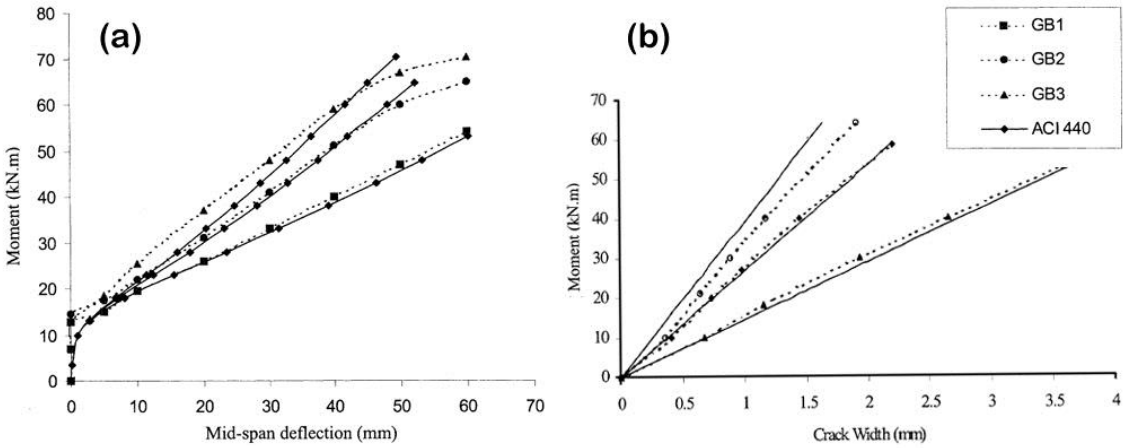

Figure 2-11: Comparison between the experimental trends and those predicted by ACI 440: moment *versus* (a) mid span deflection and (b) crack width (Toutanji and Deng 2003);

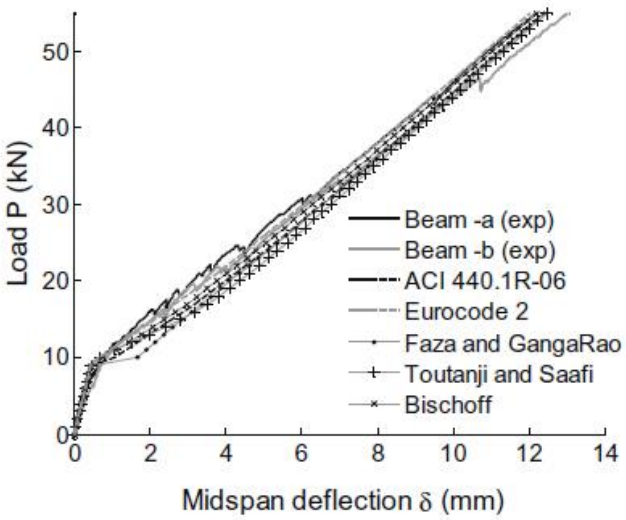

Figure 2-12: Load *versus* mid span deflection up to service load for the GFRP-RC beams tested by Barris *et al.* (2009), and the comparison with the theoretical trends

2.4 FRP-FRC beams

Many studies have been allocated to the evaluation of the structural performance of FRP-

RC structures (mostly flexural members) during the last two decades. Furthermore, there are several codes and guidelines that have been already published in regards to concrete member reinforced by FRP bars, which shows the success of this type of application in construction industry. USA, Canada, Switzerland and Germany are the countries that they are widely using FRP bars in bridge decks and roads owing to the seasonal use of de-icing salts which causes the corrosion of traditional steel reinforcement when is used. Meanwhile, some concrete structures require non-metallic material as the constituent, such as the Magnetic Resonance Imaging (MRI) rooms in hospitals or research laboratories, as well as the roads and bridge decks near electronic toll plazas. In all these applications, FRP bars are good substitutions for the conventional steel bars in RC structures (Lau and Pam 2010). But, unfortunately, FRP bars are brittle materials, a weakness that decreases the ductility of FRP concrete member comparing to conventional steel RCs. This weakness may limit the use of FRP bars in many other civil works. For this reason, some trials have been already done in the literature in order to improve the ductility of FRP-RCs. These trials can be categorized as follow:

i. ***Using hybrid FRP reinforcing bars***: the first idea of improving the ductility of FRP concrete members was to use hybrid FRP rebars. This ductile bars are fabricated by combining two or more FRP bars in order to have similar elasto-plastic behavior of steel bars (See Figure 2-13 for schematic view of this composition). Harris *et al.* (1998) carried out a group of concrete beam specimens reinforced with this type of hybrid FRP bars. The hybrid FRP bar showed some success in their study, however, complicated and costly manufacturing process resulted in limited practical applications;

ii. ***Improving concrete properties***: FRP reinforced structure are usually over-reinforced to be failed in crushing of concrete. Therefore, the ductility of FRP-RCs depends on concrete properties. Hence, improving the concrete properties may lead to ductility improvement. One way to improve concrete properties is to add discrete fibers into concrete mix, *i.e.* using Fiber Reinforced Concrete (FRC)

instead of plain concrete. A quick review on some already carried out studies in this topic is presented in the present section;

iii. ***Using hybrid FRP and Steel bars*:** one of the other trials in literature to improve the ductility and structural performance of FRP-RCs is the use of hybrid FRP and steel bars in concrete sections. A quick review on literature in this technique is described in the next section.

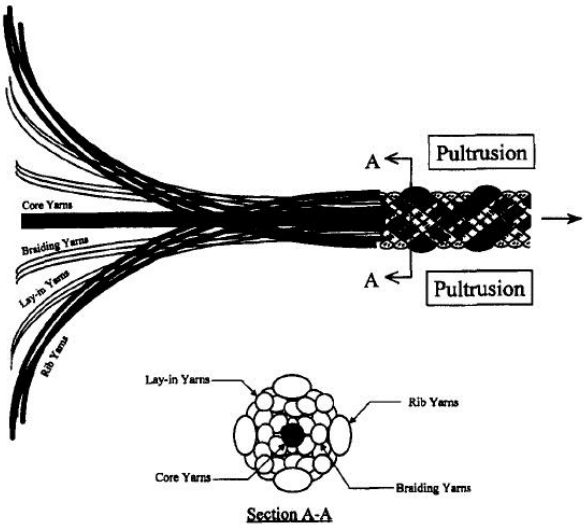

Figure 2-13: Schematic composition of ductile hybrid FRP rebar (Harris *et al.* 1998)

Ductility of conventional reinforced structures by steel bars is defined by the ratio of post-yield deformation to yield deformation according to yielding phase of steel bars. However, this definition cannot be directly extended to FRP-RCs due to the lake of yielding phase in the behavior of FRP materials. Energy-based approach and deformation-based approach are two widely used methods that are defined in literature to measure the ductility index of FRP-RCs (Alsayed and Alhozaimy 1999, Wang and Belarbi 2011). According to the Energy-based approach, the ductility is defined as ratio between the total absorbed energy (E_{total}) to the elastic energy ($E_{elastic}$). The total energy is simply estimated by measuring the area under the load-deflection response of the FRP-RCs. Figure 2-14 shows measurement of the elastic energy based on the method presented by Naaman and Jeong 1995. As shown, the definition of elastic energy depends on the definition of the points of $P_{failure}$, P1, and P2 (as defined in Figure 2-14). Naaman and Jeong 1995 proposed the following equation for the ductility index:

$$\mu = \frac{1}{2}\left(\frac{E_{total}}{E_{elastic}} + 1\right) \tag{2-4}$$

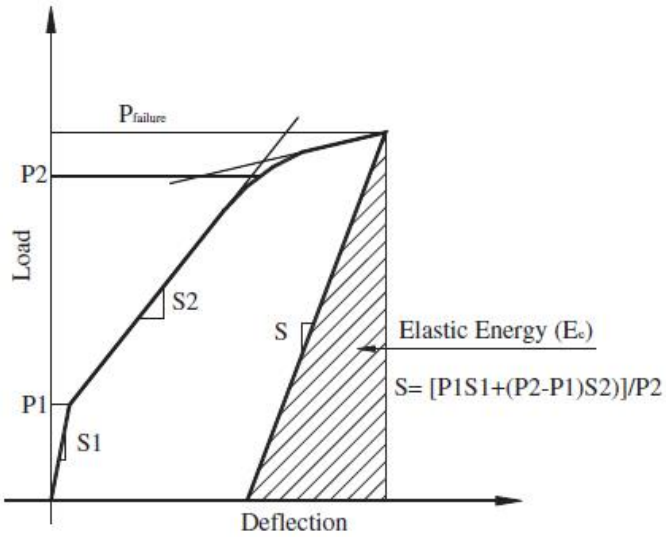

Figure 2-14: Definition of the elastic energy to calculate the ductility index based on the energy-based approach (Wang and Belarbi 2011)

For the deformation-based approach, which was firstly proposed by Jaejer *et al.* (1997), the ductility index is presented by measuring deformability margin between the ultimate stage and the service stage taking into account the strength effect (C_s) as well as the deflection effect (C_d). Note that the deflection can be replaced by curvature for flexural members. Jaejer *et al.* (1997) proposed the service stage being correspond to the compressive strain value of 0.001 for concrete in FRP-RCs, which defines the beginning of inelastic deformation in concrete in compression. Ultimate stage is also defined as the failing point of the member. Therefore, the ductility index based on the deformation-based approach is calculated by

$$\mu = C_s \times C_d \tag{2-5}$$

being C_s and C_d calculated by

$$C_s = \frac{M_u}{M_{SLS}}, C_d = \frac{\Delta_u}{\Delta_{SLS}} \tag{2-6}$$

where M_u and Δ_u are, respectively, the moment and deflection at ultimate. Further, the parameters M_{SLS} and Δ_{SLS} are, respectively, the moment and deflection corresponding to serviceability limit state.

Alsayed and Alhozaimy (1999) presented the results of nine FRC concrete beams reinforced by GFRP bars to assess the ductility improvements of the beams due to the addition of discrete fibers. The beams were 2500 mm long with cross-section of 200×210 mm^2, which were subjected to 4-point test setup configuration. They added two types of hooked and crimped steel fibers to their concrete mix. In addition to that, three reference beams with no fibers were tested. Further, the beams were all over reinforced in order to be failed by concrete crushing as it is often suggested for FRP-RCs. Table 2-7 includes the details of these tested beam specimens. The obtained results in terms of the applied load *versus* deflection at mid span are plotted in Figure 2-15. Moreover, the calculated ductility index in accordance with the energy-based approach is included in the last column of Table 2-7. Note that the failure point was assumed as the point where the applied load drops 80% of its ultimate capacity. Also, the elastic energy was calculated assuming 75% of total area under the load-deflection curve up to the point of maximum load. The results indicate that the ductility index is directly related to the volume fraction of steel fibers. The ductility of Group D beams was about 2 times of the reference beams of the first series (Group B) and for Group F with hooked steel fibers was about 3 times of Group E. Based on these results, they concluded that adding steel fibers to concrete is one of the possible methods to improve the ductility of GFRP-RC beams.

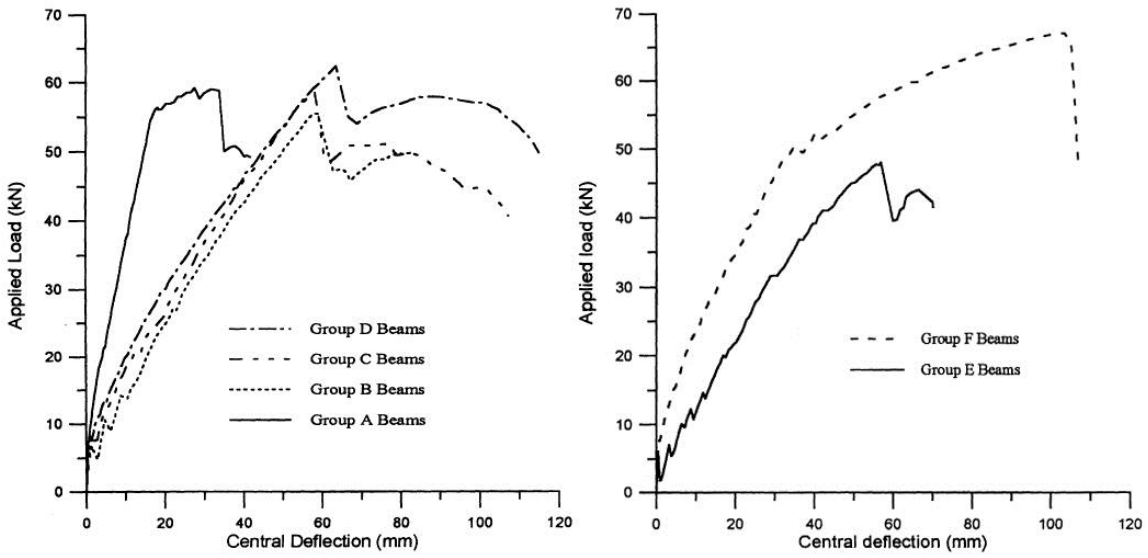

Figure 2-15: Load *versus* deflection for the tested beams by Alsayed and Alhozaimy (1999)

Table 2-7: Details of the specimens and the measured ductility index for FRP-FRC RC beams in literature

Beam ID	$h \times b$ (mm×mm)	**Span *** (mm)	f_c' (MPa)	**Longitudinal reinforcement**		**Fiber****		**Ductility index** μ
				Quantity	**Type**	V_f (%)	**Type**	
Alsayed and Alhozaimy 1999								
A	200×210	2700 (200)	41.42	3Ø14	Steel	0.0	-	5.37
B			41.42	3Ø16	GFRP	0.0	-	2.19
C			42.16	3Ø16	GFRP	0.5	ST-C	2.90
D			43.24	3Ø16	GFRP	1.0	ST-C	4.50
E			35.90	3Ø19	GFRP	0.0	-	2.37
F			36.66	3Ø19	GFRP	1.0	ST-H	6.96
Wang and Belarbi 2011								
P4G	178×229	1829 (-)	48	5Ø13	GFRP	0.0	-	6.05
P8G			48	2Ø25	GFRP	0.0	-	7.04
P4C			48	2Ø13	CFRP	0.0	-	5.50
F4G			30	5Ø13	GFRP	0.5	PP	8.94
F8G			30	2Ø25	GFRP	0.5	PP	7.56
F4C			30	2Ø13	CFRP	0.5	PP	8.35
Issa *et al.* 2011								
NO	150×150	1500 (450)	22.93	3Ø12	GFRP	0.0	-	3.6
HO			52.98			0.0	-	5.9
NP			31.58			0.5	PP	6.0
HP			51.42			0.5	PP	8.7
NG			24.88			0.5	GF	7.7
HG			43.62			0.5	GF	11.3
NS			18.38			0.5	ST-H	13.6
Yang *et al.* 2012								
CC	230×250	1900 (300)	75.9	4Ø9	CFRP	0.0	-	1.84
CC-SN			89.3	4Ø9	CFRP	2.0	SN	1.64
CC-ST			104.4	4Ø9	CFRP	1.0	ST	1.84
GG			75.9	6Ø13	GFRP	0.0	-	1.92
GG-SN			89.3	6Ø13	GFRP	2.0	SN	3.24
GG-ST			104.4	6Ø13	GFRP	1.0	ST-H	3.43

* The value inside the parenthesis is the distance of the loading points; ** V_f is volume friction of fibers in the concrete mix; ST-C: Crimped steel fibers; ST-H: Hooked steel fibers; GF: Glass fibers; SN: synthetic fibers; PP: Polypropylene fibers.

Wang and Belarbi (2011) carried out two groups of tests on RC beams specimens. In the first group, they used plain concrete beam reinforced by FRP bars including GFRP and CFRP. For the second group, the plain concrete was replaced by FRC where the polypropylene fibers of 57 mm length were added to the concrete mix. The identification of the specimens are included in Table 2-7. The applied load *versus* mid span deflection of their

tested beams are shown in Figure 2-16 for the beams reinforced by GFRP bars only. They concluded that the various aspects of structural behavior of GFRP reinforced concrete beams can be improved by using FRC instead of plain concrete. Based on the obtained results, the crack widths of FRC beams were smaller than plain concrete beam, especially at service loads. The amount of decrease in the measured values of crack width for the specimens in this study are included in Table 2-8. Furthermore, the ultimate concrete strains measured in the FRC beams were larger than the plain concrete beams. Therefore, for design purpose, they recommended to increase the design value of the ultimate concrete strain to take advantage of using discrete fibers in the concrete mix. Based on the deformation-based approach, they showed that the ductility index increased by more than 30% by adding polypropylene fibers to concrete mix.

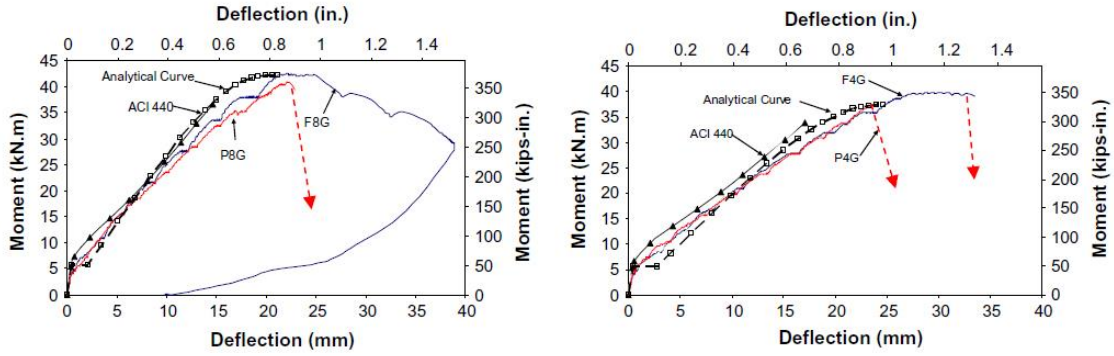

Figure 2-16: Load *versus* deflection for the tested beams by Wang and Belarbi (2011)

Table 2-8: Comparison of crack width between FRC and plain concrete FRP reinforced beams at service loads (Wang and Belarbi 2011)

Specimens ID	**P4C**	**P4G**	**P8G**	**F4C**	**F4G**	**F8G**
Crack width (mm)	0.60	0.49	0.45	0.54	0.41	0.36
% decrease relative to respective plain concrete	-	-	-	10%	16%	20%

Note: the values are average of two beams

Issa *et al.* (2011) carried out a research study with the purpose of evaluating the flexural behavior and ductility of concrete beams reinforced by GFRP bar as longitudinal reinforcement and different types of discrete fibers in concrete mixes. They tested four groups of beams in which the first one was the reference beams with no fibers and the rests included concrete mix that was reinforced by polypropylene fibers, glass fibers and hooked

steel fibers. The details of the tested specimens are summarized in Table 2-7. Figure 2-17 shows the load *versus* mid span deflection curves of the tested beams. Based on the ductility index calculated and reported by Issa *et al.* (2011) (see the last column Table 2-7), a high ductility improvement was obtained for the FRC beams comparing with those plain concrete RC beams. According to the results from this study, the FRC beams with hooked steel fibers attained the highest ductility increment of about 277.8%. Note that the ductility index was computed based on the energy-based approach, in which the ductility index was defined as the ratio between the energy absorption at the ultimate load (area under load–deflection curve up to ultimate load) and the energy absorption at the service load taking the deflection limit value of beam span dividing by 180 (Issa *et al.* 2011). Similar to what was obtained from the previous researches, they also reported significant structural improvement in terms of value of crack width at service loads and the higher concrete compressive strain at ultimate strength, which was reflected in the ductility improvement.

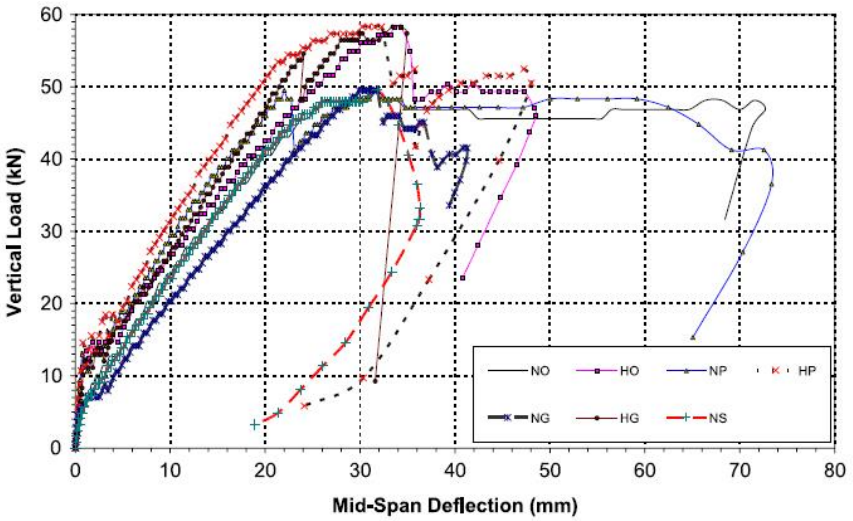

Figure 2-17: Load *versus* deflection for the tested beams by Issa *et al.* (2011)

Finally, an experimental test program of six high-strength concrete beams were recently carried out by Yang *et al.* (2012) where three of them reinforced by GFRP bars and the other three by CFPR bars. For each series, one beam was considered as reference beam with no fiber in concrete mix, the second reinforced by discrete polypropylene fibers, and the third by hooked steel fibers. Details of these specimens are given in Table 2-7. Experimental load-deflection curves of mid span section for all tested beam are plotted in Figure 2-18. As the

obtained results, the following conclusion were derived:

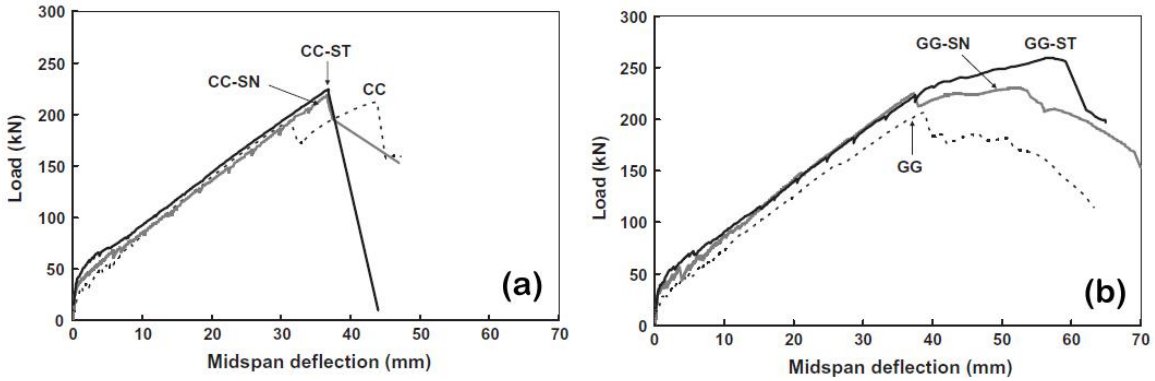

Figure 2-18: Load *versus* deflection for the tested beams by Yang *et al.* (2012)

i. The addition of discrete fibers in concrete mix delayed the crack initiation and also decreased the crack widths at service loads. This can be observed by comparing the results in terms of the applied load *versus* maximum crack, which is shown in Figure 2-19;

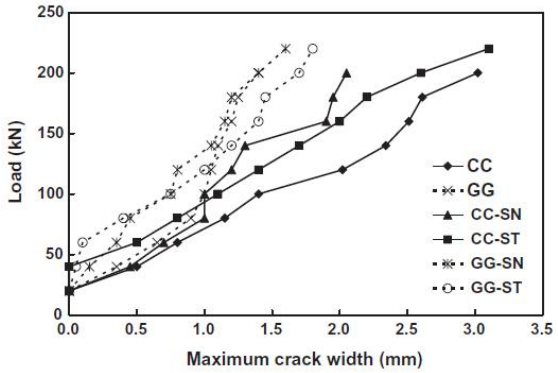

Figure 2-19: Load *versus* maximum crack width for the tested beams by Yang *et al.* (2012)

ii. Although the tested FRC beams reinforced by CFRP bars were over-reinforced to be failed by concrete crushing, the beams were failed by CFRP bar rupturing due to the increased concrete compressive strain at ultimate load. Also, the increased ultimate compressive strain of FRC in the GFRP-RC beams increased the ultimate flexural strength of these beams. This can be observed from the results plotted in Figure 2-18;

iii. The ductility indexes of GFRP beams, which were calculated in accordance with Eq. (2-4), with steel and synthetic fibers were, respectively, about 70% and 80%

higher than the ductility index of GFRP beam with no fibers. The values of the ductility indexes are also included in Table 2-7.

2.5 Hybrid FRP-steel RC beams

Combining FRP and steel bars as internal reinforcing bars for concrete is one of the way to improve the structural performance of FRP-RCs. Since the first idea of using FRP materials was to increase the durability of RCs, a question might be raised that why again using steel bars?

In hybrid FRP-steel reinforcing system introduced in literature (e.g. Aiello and Ombres 2002), steel bars are contributed to only improve the structural performance such as deformability and ductility of FRP-RCs mainly up to the service loading stage. Therefore, in this hybrid system, the steel bars will be placed in the inner layers of concrete section to avoid the development of corrosion of such reinforcement, and FRP bars will be placed to the near concrete tensile surface. Hence, FRP bars are responsible to take up the strength and the steel bars are designed only to increase the minimum serviceability requirements of FRP-RCs as well as improving the ductility. In this section, a brief review of literature on concrete beams that have been reinforced in flexural by this hybrid system are described. Before that, a brief description is given about the definition of the balanced reinforcement ratio in hybrid system (*i.e.* ρ_{hb}).

For steel-RC beam, the balanced steel reinforcement ratio (*i.e.* ρ_{sb}) is defined as a condition that the beam fails by crushing of concrete in compression and yielding of steel in tension simultaneously. For FRP-RC beam, the balanced FRP reinforcement ratio (ρ_{fb}) is a condition that the beam fails by the crushing of concrete in compression and the tensile rupture of FRP bar simultaneously. When FRP and steel bars are combined in a concrete section, the balanced reinforcement ratio for a hybrid FRP-steel RC beam, ρ_{hb} , can be defined as a failure condition that crushing of concrete, yielding of steel and tensile rupture of FRP occur simultaneously. But, this failing scenario is almost impractical due to the large difference between tensile strain of FRP at rupturing and tensile strain of steel at yielding.

That means, steel bars would have been yielded long before the FRP bars break (Lau and Pam 2010). Hence, in the structural behavior of hybrid GFRP and steel reinforced FRC prestressed beams in literature, the balanced reinforcement ratio defined for hybrid FRP-steel reinforced beams is a condition that concrete crushing in compression and tensile rupturing of FRP bars occur at the same time while the steel bars have already yielded. From this standpoint, the proposed balanced reinforcement ratio by ACI 440.1R-06 for case of FRP-RC beams can be also adopted for hybrid FRP-steel RC beam (Lau and Pam 2010):

$$\rho_{hb} = \rho_{fb} = 0.85\beta_1 \frac{f_c'}{f_{fu}} \frac{E_f \varepsilon_c'}{E_f \varepsilon_c' + f_{fu}} \tag{2-7}$$

where β_1 is ratio between the depth of equivalent rectangular concrete stress block and the neutral axis depth, $\varepsilon_c' = 0.003$ extreme fiber concrete compressive strain in conjunction with f_c'. The parameters E_f and f_{fu} are, respectively, Young's modulus and ultimate tensile stress of FRP bars. In order to consider the effect by the presence of steel reinforcements, the effective reinforcement ratio of hybrid FRP-steel RC beam is defined as follow:

$$\rho_{f,eq} = \rho_f + m\rho_s \tag{2-8}$$

where ρ_f and ρ_s are, respectively, FRP reinforcement ratio and steel reinforcement ratio. The parameter m is defined by (Lau and Pam 2010)

$$m = \frac{f_y}{f_{fu}} \tag{2-9}$$

where f_y is yielding stress of steel bar.

Aiello and Ombres (2002) carried out an experimental program comprising three groups of concrete beams in order to evaluate the flexural behavior of the hybrid system. The first group (Group A) included hybrid AFRP/steel RC beams, the second group (Group B) included two reference beams where one reinforced only by steel bars and another by AFRP (Aramid FRP) bars. The last group of beams (Group C) was a hybrid FRP/steel RC beam where the steel and AFRP bars were placed at the same level in the concrete section. The last group was only carried out in order to analyze the influence of the cover thickness on the structural performances of the beams (Aiello and Ombres 2002). The details of these

three groups of beams are summarized in Table 2-9. Based on the obtained results from their study, the two following conclusion can be derived:

i. Based on the load-deflection and moment-curvature responses of the tested beams (shown in Figure 2-20), the hybrid reinforcing system including AFRP and steel bars showed a significant improvements in terms of beams' deformability under service load conditions. However, since the FRP-RC beams were over-reinforced, the contribution of steel bars to increase the flexural capacity was less than 15% (see specimens A1 and B2 in Figure 2-20);

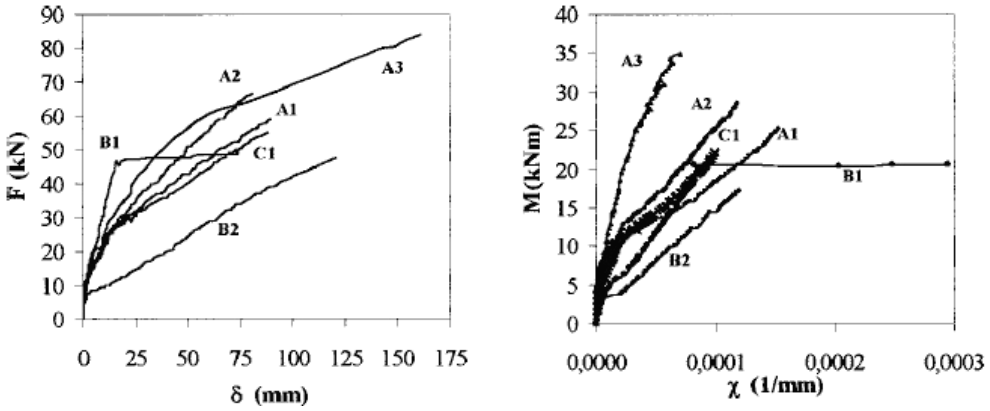

Figure 2-20: Load *versus* deflection and moment *versus* curvature relationships of tested beams by Aiello and Ombres (2002)

ii. Decrease in the measured value of crack width for the hybrid reinforced beams comparing to the FRP-RC beam. In Figure 2-21, the comparison among the result of tested beams in terms of applied force *versus* maximum crack width and crack spacing is given.

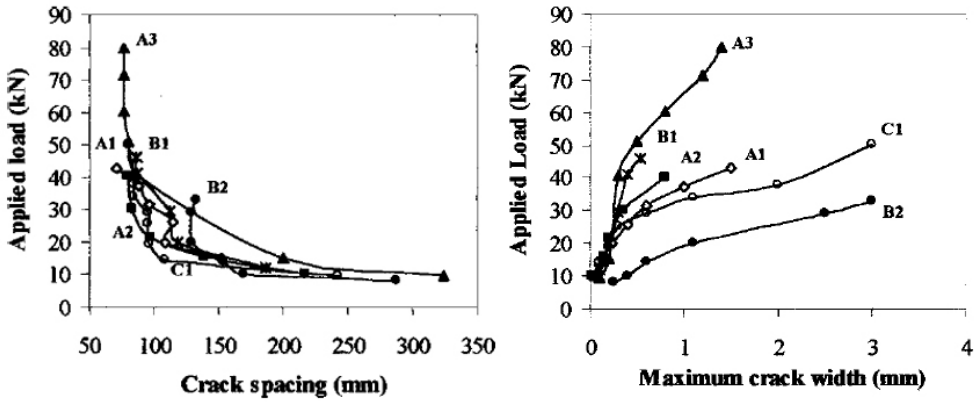

Figure 2-21: Load *versus* maximum crack width and load *versus* crack spacing relationship of tested beams by Aiello and Ombres (2002)

Leung and Balendran (2003) carried out an experimental program of seven beam specimens. The tests were conducted in form of two main groups (L and H). For the first group, a design value of 30 MPa for concrete strength and for the second group, value of 50 MPa was considered. In each group of tests, one GFRP-RC beam (indicated by L1 and H1) and two hybrid GFRP/steel RC beams (indicated by L2, L5, H2 and H5) were tested. In addition to that, one steel RC beam was tested as reference beam of the first group (named L0). More details of the tested beams are reported in Table 2-9. The load-deflection response of all tested beams by Leung and Balendran (2003) are shown in Figure 2-22. By comparing the beams L1 and L2, as well as H1 and H2, the significant increasing in load carrying capacity for hybrid system at service stage (*i.e.* L2 and H2) was obtained. As it was observed, the failing point of beams L2 and L5 were in the same level of mid-span deflection of L1. However, for series H where the higher concrete strength was used, the failing point of beam H2 and H5 occurred at the greater value of mid span deflection rather than H1. This means that the ductility improvement of the hybrid beams in group H was much greater than those from group L. Based on the results of group L, the initial stiffness of the hybrid reinforced beams were similar to the beam L0 (with no FRP bars). Leung and Balendran (2003) did not measure the improvement in terms of crack width. Additionally, they reported that the ductility improvement of hybrid GFRP/steel RC beams were much pronounced when high concrete strength level was used. This may attributed to the fact that the bond behavior of GFRP bars are also improved when higher strength concrete is utilized.

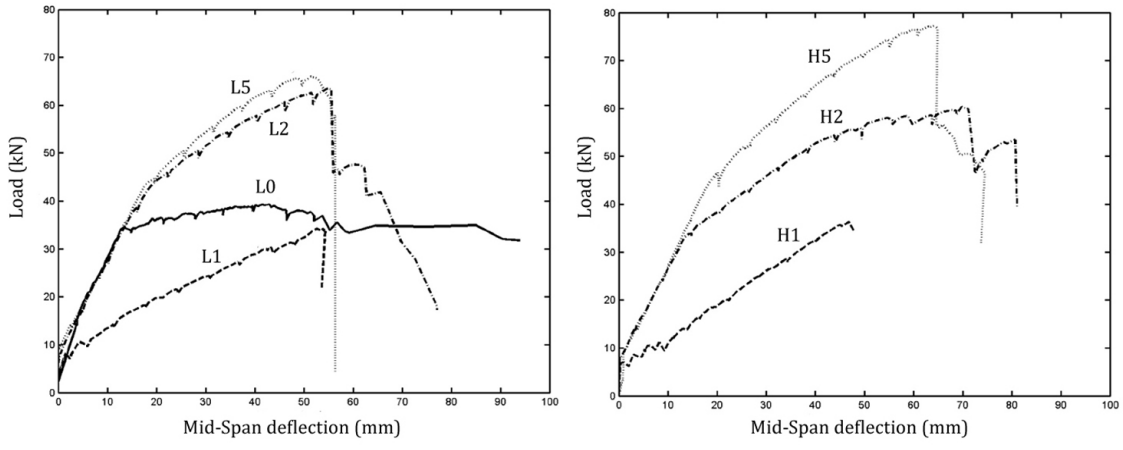

Figure 2-22: Load *versus* deflection for the tested beams by Leung and Balendran (2003)

Qu *et al.* (2009) carried out eight concrete beams including two control beams reinforced with only steel or only GFRP bars (named B1 and B2), and six beams reinforced by hybrid GFRP-steel bars (named B3 to B8). The reinforcement ratio and the ratio of GFRP to steel were the main parameters that the authors investigated (Qu *et al.* 2009). Table 2-9 includes the details of the tested beams by these researchers. The experimental load-deflection curve of all tested beams are plotted in Figure 2-23. Based on the obtained results, the following conclusions were derived:

i. The axial stiffness ratio between GFRP and steel bars had little influence on ultimate flexural capacity. The balanced effective reinforcement ratio, which were reported in Table 2-9, could be used as a criterion to predict the failure mode for hybrid FRP-steel RC beams. All the hybrid beams were failed in concrete crushing as it was designed, since the effective reinforcement ratio for all of them was greater than the calculated balanced reinforcement ratio;
ii. The steel bars increased the ductility of hybrid GFRP-steel RC beams. Also, an increase in the reinforcement ratio of steel bars increased the initial stiffness of the load-deflection respond of the hybrid beams;
iii. The values of crack width measured for the hybrid beams showed significant decrease comparing to the GFRP-RC beam.

Finally, Lau and Pam (2010) carried out a total of 12 concrete beam specimens reinforced by steel bars, GFRP bars, hybrid GFRP-steel bars and with no reinforcements (plain concrete). They had three main investigation purposes including:

- Flexural strength and ductility improvement of hybrid system;
- Minimum content of flexural FRP bar;
- Effects of 90°and135°hook angle in stirrups.

For their purpose, they divided the beams in four main groups (A, B, C and D) where the tested beams in Group A and B were designed for investigating the flexural and ductility improvements of the hybrid GFRP-steel RC beams. Hence, the results of these two groups are only discussed. The main difference of these two groups was in the reinforcement ratio

in which the Group A included balanced-reinforced GFRP-RC beams, and Group B included over-reinforced GFRP-RC beams. The details of the tested beams in Group A and B are included in Table 2-9. Additionally, the measured force-deflection curve at mid-span of the tested beam of group A and B are shown in Figure 2-24. As it is observed from this figure and also similar to what resulted by the previous authors, adding steel bars to GFRP-RC beams enhances the initial stiffness of the load-deflection curves as well as the ductility of GFRP-RC beams.

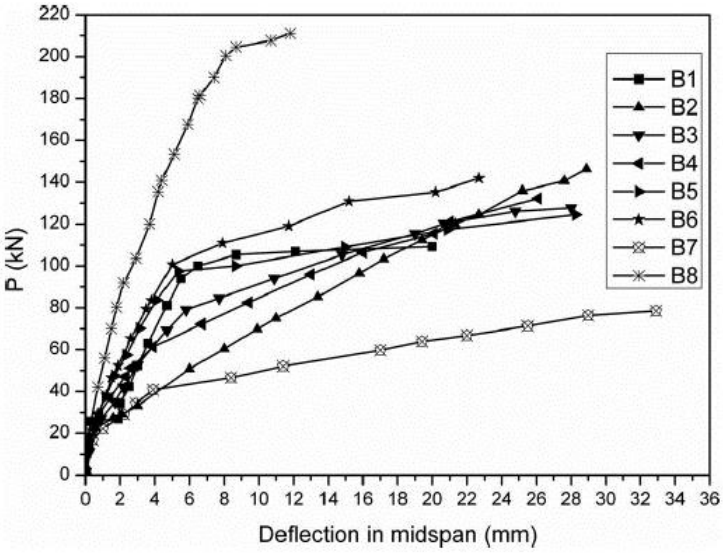

Figure 2-23: Load *versus* mid span deflection for tested beams by Qu *et al.* (2009)

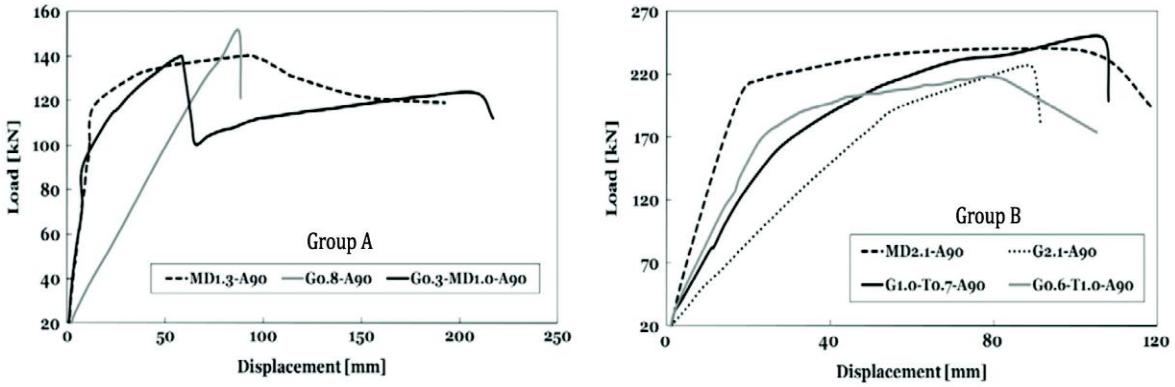

Figure 2-24: Load *versus* mid span deflection of the tested beams by Lau and Pam (2010)

Table 2-9: Details of the specimens and the measured ductility index for the hybrid FRP and steel reinforced concrete beams in the literature

Beam ID	$h \times b$ **(mm²)**	**Span (mm)**	f_c' **(MPa)**	**Longitudinal reinforcements**						ρ_b * **(%)**	$\rho_{f,eq}$ ** **(%)**	μ **(-)**
				FRP	ρ_f **(%)**	d_f **(mm)**	**Steel**	ρ_s **(%)**	d_s **(mm)**			
Aiello and Ombres 2002												
A1	200×150	2700 (1000)	45.70	2Ø7.5	0.34	175	2Ø8	0.45	150	0.14	0.47	10.39
A2				2Ø10	0.60	175	2Ø8	0.45	150	0.21	0.75	7.53
A3				3Ø10	0.90	175	2Ø12	1.00	150	0.21	1.24	3.95
B1				-	-	-	2Ø12	0.86	175	3.56	0.86	-
B2				2Ø7.5	0.34	175	-	-	-	0.14	0.34	16.21
C1				2Ø7.5	0.34	175	2Ø8	0.39	175	0.14	0.45	6.99
Leung and Balendran 2003												
L0	200×150	2200 (800)	28.50	-	-	-	2Ø10	0.81	130	2.84	0.81	-
L1				2Ø9.5	0.59	160	-	-	-	0.45	0.59	-
L2				2Ø9.5	0.59	160	2Ø10	0.81	130	0.45	0.99	-
L5				3Ø9.5	0.89	160	2Ø10	0.81	130	0.45	1.29	-
H1				2Ø9.5	0.59	160	-	-	-	0.63	0.59	-
H2			48.50	2Ø9.5	0.59	160	2Ø10	0.81	130	0.63	0.99	-
H5				3Ø9.5	0.89	160	2Ø10	0.81	130	0.63	1.29	-
Qu *et al.* 2009												
B1	250×180	1800 (600)	31.00	-	-	-	4Ø12	1.14	220	3.23	1.14	-
B2				4Ø12.7	1.28	220	-	-	-	0.40	1.28	-
B3				2Ø12.7	0.64	220	2Ø12	0.57	220	0.40	0.90	-
B4				2Ø15.9	1.00	220	1Ø16	0.51	220	0.39	1.27	-
B5				2Ø9.5	0.36	220	2Ø16	1.02	220	0.34	0.80	-
B6				2Ø12.7	0.64	220	2Ø16	1.02	220	0.40	1.08	-
B7				2Ø9.5	0.36	220	1Ø12	0.28	220	0.34	0.49	-
B8				2Ø15.9	1.00	220	6Ø16	3.35	200	0.39	2.49	-
Lau and Pam 2010												
Group A												
MD1.3-A90	380×280	4200 (0)	-	-	-	-	4Ø20	1.31	345	4.71	1.31	-
G0.8-A90			36.6	4Ø16	0.83	350	-	-	-	0.75	0.83	-
G0.3-MD1.0-A90			41.3	1Ø19	0.30	345	2Ø25	1.03	345	0.85	0.89	-
Group B												
MD2.1-A90	380×280	4200 (0)	-	-	-	-	4Ø25	2.07	345	5.27	2.07	-
G2.1-A90			41.3	4Ø25	2.07	345	-	-	-	0.84	2.07	-
G1.0-T0.7-A90			39.8	2Ø25	1.03	345	2Ø20	0.66	345	0.81	1.71	-
G0.6-T1.0-A90			44.6	2Ø19	0.59	350	2Ø25	1.03	345	0.92	1.56	-

* The balanced reinforcement ratio is calculated by Eq. (2-7) for FRP-RC and hybrid FRP-Steel RC beams. For Steel RC beams, the proposed equation by ACI 318M-02 has been used.
** Calculated by Eq. (2-8).

Notations

b	width of RC beam cross section	M_u	moment carried by RC beam at failure
C	concrete cover of reinforcing bar	P_r	perimeter of reinforcing bars
C_s	strength effect	V_f	volume fraction of fibers in concrete mix
C_d	deformation effect	β_1	factor relating depth of equivalent rectangular compressive stress block to neutral axis depth
d_f	distance from extreme compression fiber to centroid of FRP bars in RC beam section	δ_m	slip corresponding to peak bond shear stress
d_s	distance from extreme compression fiber to centroid of steel bars in RC beam section	Δ_{SLS}	deflection of RC beam corresponding to serviceability limit state
$E_{elastic}$	energy absorbed by RC in elastic domain	Δ_u	deflection of RC beam corresponding to M_u
E_{total}	total absorbed energy by RC beam	ε_c'	concrete compressive strain corresponding to f_c'
f_c'	concrete compressive strength	μ	ductility index of RC beam
f_{cREF}'	reference compressive strength	ρ	reinforcement ratio
f_{fu}	ultimate FRP tensile stress	ρ_{fb}	FRP balanced reinforcement ratio
f_y	steel yield tensile stress	$\rho_{f,eq}$	equivalent FRP reinforcement ratio in hybrid reinforced concrete cross section
F	pullout force of reinforcing bar	ρ_{hb}	balanced reinforcement ratio in hybrid reinforced concrete cross section
h	height of RC beam cross section	ρ_{sb}	steel balanced reinforcement ratio
l_e	embedment length	τ_m	bond shear strength
m	ratio between steel yielding stress to FRP ultimate tensile stress	ϕ_b	reinforcing bar's diameter
M_{SLS}	moment carried by RC beam corresponding to serviceability limit state		

Chapter 3

3 BOND PERFORMANCE OF GFRP BARS IN FRC

3.1 Introduction

An experimental program was conducted to evaluate bond behavior between GFRP bars and steel fiber reinforced self-compacting concrete (SFRSCC) by carrying out pullout bending tests. The effect of GFRP bar diameter, surface characteristics of the GFRP bars, bond length, and the thickness of SFRSCC cover on the bond behavior was assessed. In addition, a bond analytical formulation was presented by adopting a multi-linear bond-slip relationship ($\tau - \delta$) for the types of GFRP bars used in the pullout bending tests. The results of the experimental program were used to calibrate $\tau - \delta$ diagram and to appraise the analytical formulation. Moreover, a parametric study was carried out with aid of the analytical formulation in order to evaluate the influence of involved bond-slip law's parameters on the maximum theoretical force transferred by the bond behavior between GFRP bar and SFRSCC. Finally, the minimum theoretical bond length (*i.e.* the development bond length) required to achieve the tensile strength of the GFRP bars was determined, and the obtained values are compared with the recommendations proposed by design codes.

3.2 Experimental program

In the present experimental program, a total of 36 pullout bending tests were carried out to evaluate the bond behavior of two types of GFRP bars supplied by European companies. The tests were conducted at the laboratory of the Structural Division of the Civil Engineering

Department of University of Minho (LEST), Portugal.

3.2.1 Material properties

3.2.1.1 GFRP bars

Two types of GFRP bar in terms of surface treatment were used in this study, and the designation of type A and type B was assumed for deformed and smooth bars, respectively. The ribs of the deformed surface of type A bar have a constant height of 6% of bar diameter and a spacing of about 8.5 mm. Spherical natural quartz-crystal sand with triangular structure was used for sand-coating in type B bar. The mechanical properties of bars based on the information provided by the manufacturers are included in Table 3-1. A tensile strength higher than 1000 MPa was indicated for both types of bar, while values of 60 and 40 GPa were suggested for the modulus of elasticity of type A and type B bar, respectively. Direct tensile tests were carried out to obtain the modulus of elasticity, whose values are indicated in Table 3-1. Two diameters, 8 and 12 mm, were adopted for type A bar, while only one diameter (12 mm) was considered for type B bar (see Figure 3-1). The obtained values for the modulus of elasticity of both types were higher than those provided by the company; exceptionally, when the diameter measured in the bar was considered for Ø12 type A (13.08 mm instead of 12 mm), the value of the modulus of elasticity (56 GPa) was lower than 60 GPa reported by the supplier.

Table 3-1: The mechanical properties of GFRP bars

Type	Surface treatment	Bar diameter		Density	Content of glass	Tensile strength	Modulus of elasticity
		Nominal	Measured[1]				
		(mm)	(mm)	(gr/cm^3)	(%)	(MPa)	(GPa)
A	Ribbed	8	8.64	2.23	~ 75	1500	60 (71 [2]) [65 [3]]
		12	13.08	2.23	~ 75	1350	60 (67 [2]) [56 [3]]
B	Sand-coated	12	12.36	1.9	~ 70	~ 1000	40 (53 [2]) [49 [3]]

[1] The values are measured by immersing a prescribed length of the bar in water to determine its buoyant weight;
[2] Results obtained from the performed experimental tests by adopting the nominal bar diameter indicated by the supplier (average of 5 specimens);
[3] Results obtained from the performed experimental tests by adopting the measured bar diameter (average of 5 specimens).

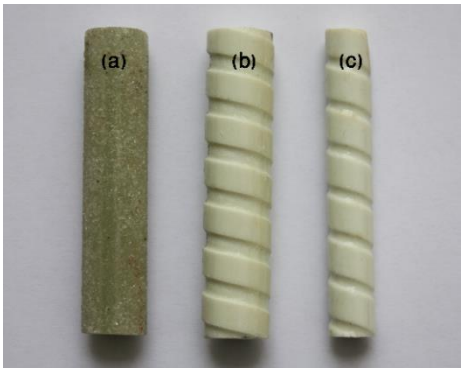

Figure 3-1: GFRP bars: (a) Sand-coated 12 mm diameter (type B), (b) Ribbed 12 mm diameter (type A), and (c) Ribbed 8 mm diameter (type A)

3.2.1.2 SFRSCC

A self-compacting concrete reinforced with 60 kg/m3 of hooked end steel fibers was used to build the pullout bending specimens. The mix of this concrete is included in Table 3-2. Ordinary Portland cement produced according to the standard EN 197-1:2000 and labeled as CEM I 42.5 R, fine and coarse river sand and crushed granite gravel aggregate with maximum size of 12 mm were used, and the water/cement ratio was 0.39. Optimized amount of 1.9% superplasticizer was adopted to contribute for the attainment of self-compacting requisites for the mix. Hooked end steel fibers of 33 mm length (l_{fr}), 0.55 mm diameter (ϕ_{fr}), aspect ratio (*i.e.* l_{fr}/ϕ_{fr}) of 60, and a tensile strength of about 1100 MPa were used. The concrete mixture showed good homogeneity and cohesion, and the total spread measured in the slump-flow tests ranged between 680 and 720 mm, with no visual sign of segregation.

Table 3-2: Composition of the SFRSCC

Components	**Quantity (kg/m^3)**
Cement	412
Limestone filler	353
Fine river sand (0-2.38 mm)	179
Coarse river sand (0-4.76 mm)	655
Crushed granite (4.76-12.70 mm)	588
Water	160
Superplastizier	7.83
Hooked end steel fibers	60

The SFRSCC compressive strength was determined according to ASTM C39 with cylinder samples taken from all batches (three cylinders with 150 mm diameter and 300 mm

height for each batch). Prior to those tests, the three cylinders were used to determine the Young's modulus of SFRSCC according to ASTM C469. A total number of five beams with dimensions of 600×150×150 mm^3 were also cast to determine the flexural tensile strength and the flexural residual strength parameters of SFRSCC according to the recommendations of RILEM. The average value of the Young's modulus and flexural tensile strength of SFRSCC were 30.36 GPa with a coefficient of variation (CoV) of 15.48%, and 6.28 MPa (CoV=17.48%), respectively (see Table 3-3).

Table 3-3: Properties of the SFRSCC batches

Batch designation	**Compressive strength** (MPa)	**Flexural tensile strength** (MPa)	**Modulus of elasticity** (GPa)	**Bond modified factor[1]**
M1	58.58 (3.15%)			1.00
M2	61.45 (4.71%)			0.98
M3	67.58 (4.86%)	6.28 (17.48%)[2]	30.36 (15.48%)[2]	0.93
M4	64.58 (1.25%)			0.95
M5	66.38 (4.28%)			0.94

[1] From Eq. (3-1);
[2] The values between parentheses are the corresponding coefficients of variation.

The average compressive strength for the five SFRSCC batches was varied from 58.58 to 67.58 MPa (Table 3-3). Since to produce all the specimens for the pullout bending program it was necessary to execute five batches, the mechanical properties of SFRSCC from the mix batches were slightly different (less than 10% from the average value). Assuming that bond stress (and concrete tensile strength) can be related to the square root of compressive strength, the differences were taken into account by correcting the bond values by applying the following bond modified factor γ_i :

$$\gamma_i = \sqrt{\frac{f_{cmr}}{f_{cmi}}}, \quad (i = 1, 2, ..., 5) \tag{3-1}$$

where f_{cmi} is the average compressive strength of the i^{th} concrete batch, and f_{cmr} is the reference value. Assuming for f_{cmr} the average compressive strength of SFRSCC of the batch used to produce the first series of pullout specimens (M1), the values of the bond modified factor are those included in Table 3-3.

3.2.2 Test procedure

3.2.2.1 Specimens

A beam test similar to the one recommended by RILEM TC9-RC was adopted in this study for assessing the behavior between the GFRP bars and SFRSCC. A schematic representation of the specimen is shown in Figure 3-2a. The specimen is composed of two prismatic SFRSCC blocks, A and B, which are connected by a GFRP bar as a flexural reinforcement at bottom part, and a steel hinge at top zone. Type of GFRP bar's surface, SFRSCC cover thickness, embedment length (L_e) and bar diameter varied in those specimens in order to assess their influence in the GFRP-SFRSCC bond behavior. In the front part of each block, in a length of 50 mm (75 mm from the symmetry axis) the bar is unbonded to avoid premature fracture of SFRSCC in these zones. The embedded length of GFRP bars was only changed in the block A (where debonding failure is supposed to develop), while in the block B a constant embedment length of 335 mm was considered for all specimens. In order to create an unbonded length at the edge, the GFRP bars were covered by 50 mm long plastic tubes with low elastic modulus.

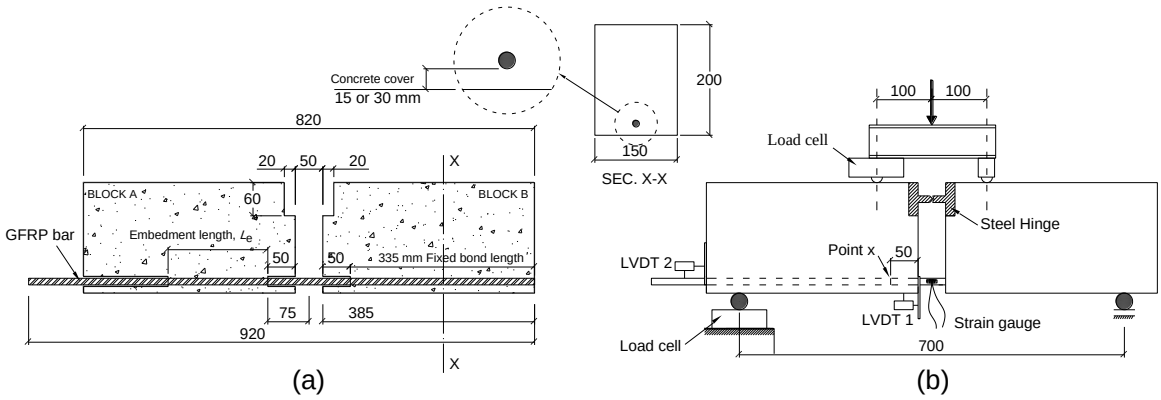

Figure 3-2: (a) Details of the specimen, and (b) test setup (dimensions in mm)

The specimens are identified by assuming the following labels: the first letter, A or B, indicates the type of bar surface; the second set of symbols refers the bar diameter (Ø8 or Ø12); the third one, denoted as LXØ, symbolizes the embedment length, being X the multiple of the bar diameter (X=5, 10 and 20); the fourth label represents the concrete cover thickness, 15 mm (C15) or 30 mm (C30); and the last set is a regular counting of the specimens. For

example, the label A-Ø8-L10Ø-C30-07 corresponds to the specimen number 7 reinforced with a ribbed surface type A bar of 8 mm diameter (Ø8), with an embedment length of 80 mm (10Ø=10×8 mm), and with a concrete cover of 30 mm (C30).

3.2.2.2 Test setup and measuring devices

Figure 3-2b shows the test setup configuration used to study the bond behavior of the GFRP bars. To measure the slip at loaded and free ends of GFRP bar, two linear variable differential transducers, LVDT 1 and LVDT 2, respectively, were used. LVDT 1 was supported on the bar close to loaded end section, and measured the relative displacement between this section and the concrete front surface of the block A (see Figure 3-2b), while LVDT 2 was fixed to the free extremity of the bar and measured the relative displacement between the free end part of the bar and the concrete rear surface. As shown in Figure 3-2b, a strain gauge was installed in the cross section of the bar coinciding with specimen symmetry axis to record the strains in the bar during the test. Three load cells with a maximum load carrying capacity of 200 kN were utilized to determine the applied load in each contact point of the specimen with the exterior. Two of these load cells were disposed according to the scheme represented in Figure 3-2b, while the third was coupled to the actuator. The pullout force (*i.e.* F) was calculated by multiplying the evaluated average Young's modulus (E_f) of the bar by the strain recorded in the strain gauge (ε_f) and considering the measured cross sectional area of the bar (A_f), $F = E_f A_f \varepsilon_f$ (see Table 3-1). The force installed in the bar was calculated by equilibrium between the applied loads and the corresponding reactions to the specimen. The change of the internal arm (distance between hinge connection point and the center of the bar) at mid-span was measured by two vertical LVDT's installed in the first 12 specimens (for all 5Ø bond length specimens). The force values derived from both methods showed negligible differences, therefore, the one based on measuring the strains in the GFRP bars was adopted for all the tested specimens. Due to the elastic elongation of GFRP bar between the loaded end section (coinciding with the Point x indicated in Figure 3-2b) and the measuring section of LVDT 1 (front face of

the concrete block A), the slip at loaded end (s_{lp}, in mm) was obtained by deducing from the displacement measured by the LVDT 1 (s_{LVDT1}, in mm) the elastic deformation in this segment of the bar ($50\varepsilon_f$, in mm):

$$s_{lp} = s_{LVDT1} - 50\varepsilon_f \tag{3-2}$$

where ε_f is the strain in the GFRP bars measured by the strain gauge.

The tests were carried out by using a closed-loop hydraulic system with a servo actuator of 200 kN capacity. Two loading phases of different slip rate were adopted by using LVDT 1 for test control: 3 μm/s up to 5 mm slip, and 5 μm/s up to the end of the test.

3.3 Test results and discussion

The results of GFRP bars type A and B, obtained from the pullout bending tests, are, respectively, summarized in Table 3-4 and Table 3-5. These tables include the maximum pullout force, $F_{\max}$, the corresponding slip at loaded (*i.e.* s_{lp}) and free ends (*i.e.* s_{fp}), the maximum average bond stress (*i.e.* $\bar{\tau}_{\max}$) assuming that bond stresses are constant along the embedment length (*i.e.* L_e), modified bond stress normalized by using γ_i coefficient (to account the type of concrete) and the failure mode.

The relationships between the pullout force and the slip at loaded end ($F - s_{lp}$) and free end ($F - s_{fp}$) are plotted in Figure 3-3, Figure 3-4, and Figure 3-5. In general, the pullout force *versus* slip responses were characterized by a short linear branch, in which damage in the debonding process was not sufficiently intense to produce irreversible slip (somehow representing chemical and micro mechanical bonds between bar and SFRSCC), followed by a nonlinear response up to peak load due to the increase of the damage. The post peak phase was characterized by a descending branch of the pullout force with the increase of slip. The tests ended with a relatively high residual pullout force due to the friction resistance between the GFRP and SFRSCC. As expected, these graphs show that the peak pullout force and its corresponding slip increased with the embedment length. Furthermore, at peak load, the free end slip was non null in all specimens, confirming that the embedment length was not enough

to mobilize the tensile capacity of the utilized GFRP bars.

Table 3-4: Bond test results of GFRP bar (type A)

Specimen designation	Concrete			F_{max}	s_{lp}	s_{fp}	$\bar{\tau}_{max}$	Modified bond stress	Failure Mode[1]
	Mix	f_c'	γ_i						
		(MPa)	(-)	(kN)	(mm)	(mm)	(MPa)	(MPa)	
A-Ø8-L5Ø -C15-01	M1	58.58	1.00	20.02	0.27	0.23	19.92	19.92	P
A-Ø8-L5Ø-C15-02	M1			20.73	0.39	0.24	20.63	20.63	P
A-Ø8-L5Ø-C30-03	M1			20.77	0.31	0.27	20.67	20.67	P
A-Ø8-L5Ø-C30-04	M1			19.14	0.37	0.27	19.05	19.05	P
A-Ø8-L10Ø-C15-05	M5	66.38	0.94	32.18	0.88	0.23	16.01	15.05	P
A-Ø8-L10Ø-C15-06	M5			29.58	0.89	0.07	14.72	13.84	P
A-Ø8-L10Ø-C30-07	M4	64.58	0.95	35.34	0.85	0.34	17.59	16.71	P
A-Ø8-L10Ø-C30-08	M4			35.30	0.65	0.31	17.57	16.69	P
A-Ø8-L20Ø-C15-09	M4	64.58	0.95	56.11	1.67	0.12	13.96	13.26	P
A-Ø8-L20Ø-C15-10	M4			58.18	1.46	0.11	14.47	13.74	P
A-Ø8-L20Ø-C30-11	M4			64.66	2.22	0.29	16.10	15.28	P
A-Ø8-L20Ø-C30-12	M4			68.88	-	-	17.13	16.28	R
A-Ø12-L5Ø-C15-13	M2	61.45	0.98	48.30	0.36	0.31	21.36	20.93	P
A-Ø12-L5Ø-C15-14	M2			41.22	0.30	0.19	18.23	17.87	P
A-Ø12-L5Ø-C30-15	M2			57.86	0.26	0.17	25.59	25.08	P
A-Ø12-L5Ø-C30-16	M2			57.13	0.32	0.29	25.27	24.76	P
A-Ø12-L10Ø-C15-17	M3	67.85	0.93	-	-	-	-	-	S
A-Ø12-L10Ø-C15-18	M3			70.62	0.84	0.16	15.62	14.53	PS
A-Ø12-L10Ø-C30-19	M3			82.50	1.30	0.31	18.24	16.97	P
A-Ø12-L10Ø-C30-20	M3			96.57	1.38	0.24	21.35	19.86	P
A-Ø12-L20Ø-C15-21	M3	67.85	0.93	127.57	2.67	0.10	14.10	13.11	PS
A-Ø12-L20Ø-C15-22	M3			116.05	2.45	0.12	12.83	11.93	PS
A-Ø12-L20Ø-C30-23	M3			146.23	3.00	0.16	16.17	15.04	P
A-Ø12-L20Ø-C30-24	M3			-	-	-	-	-	S

[1] Failure modes: P - Pullout; PS - Pullout and Splitting crack; R - bar rupture; S - SFRSCC shear failure.

Table 3-5: Bond test results of GFRP bar (type B)

Specimen designation	Concrete			F_{max}	s_{lp}	s_{fp}	$\bar{\tau}_{max}$	Modified bond stress	Failure mode [1]
	Mix	f_c'	γ_i						
		(MPa)	(-)	(kN)	(mm)	(mm)	(MPa)	(MPa)	
B-Ø12-L5Ø-C15-25	M1	58.58	1.00	40.79	0.46	0.09	18.04	18.04	P
B-Ø12-L5Ø-C15-26	M2			43.33	0.49	0.10	19.17	18.71	P
B-Ø12-L5Ø-C30-27	M2	61.45	0.98	53.63	0.48	0.10	23.72	23.15	P
B-Ø12-L5Ø-C30-28	M2			48.00	0.50	0.07	21.23	20.72	P
B-Ø12-L10Ø-C15-29	M3	67.85	0.93	-	-	-	-	-	S
B-Ø12-L10Ø-C15-30	M3			62.92	0.81	0.09	13.91	12.94	P
B-Ø12-L10Ø-C30-31	M3			-	-	-	-	-	S
B-Ø12-L10Ø-C30-32	M3			76.64	1.50	0.08	16.95	15.76	P
B-Ø12-L20Ø-C15-33	M5	66.38	0.95	97.70	1.77	0.08	10.80	10.15	P
B-Ø12-L20Ø-C15-34	M5			99.78	2.31	0.08	11.03	10.36	P
B-Ø12-L20Ø-C30-35	M5			107.53	2.01	0.10	11.89	11.17	P
B-Ø12-L20Ø-C30-36	M5			104.94	2.71	0.09	11.60	10.90	P

[1] Failure modes: P - Pullout; PS - Pullout and Splitting crack; R - bar rupture; S - SFRSCC shear failure.

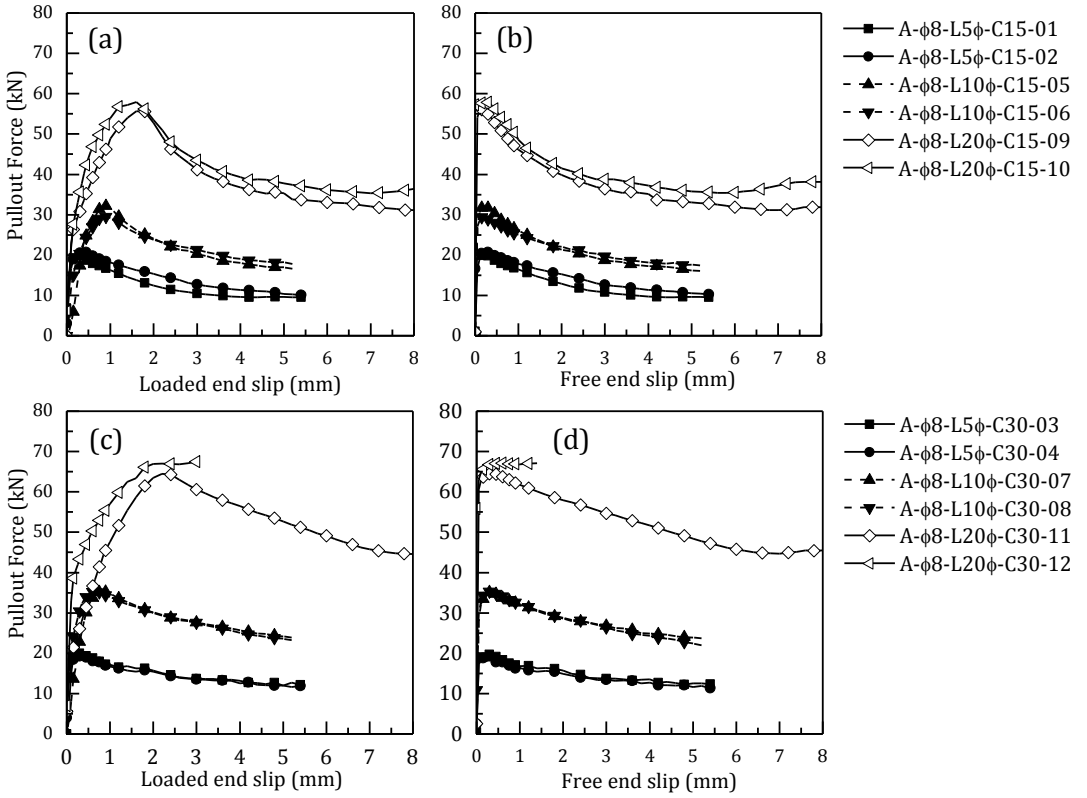

Figure 3-3: Pullout force *versus* loaded and free end slip for type A of Ø8 with 5Ø, 10Ø and 20Ø bond lengths: (a)-(b) 15 mm concrete cover, (c)-(d) 30 mm concrete cover

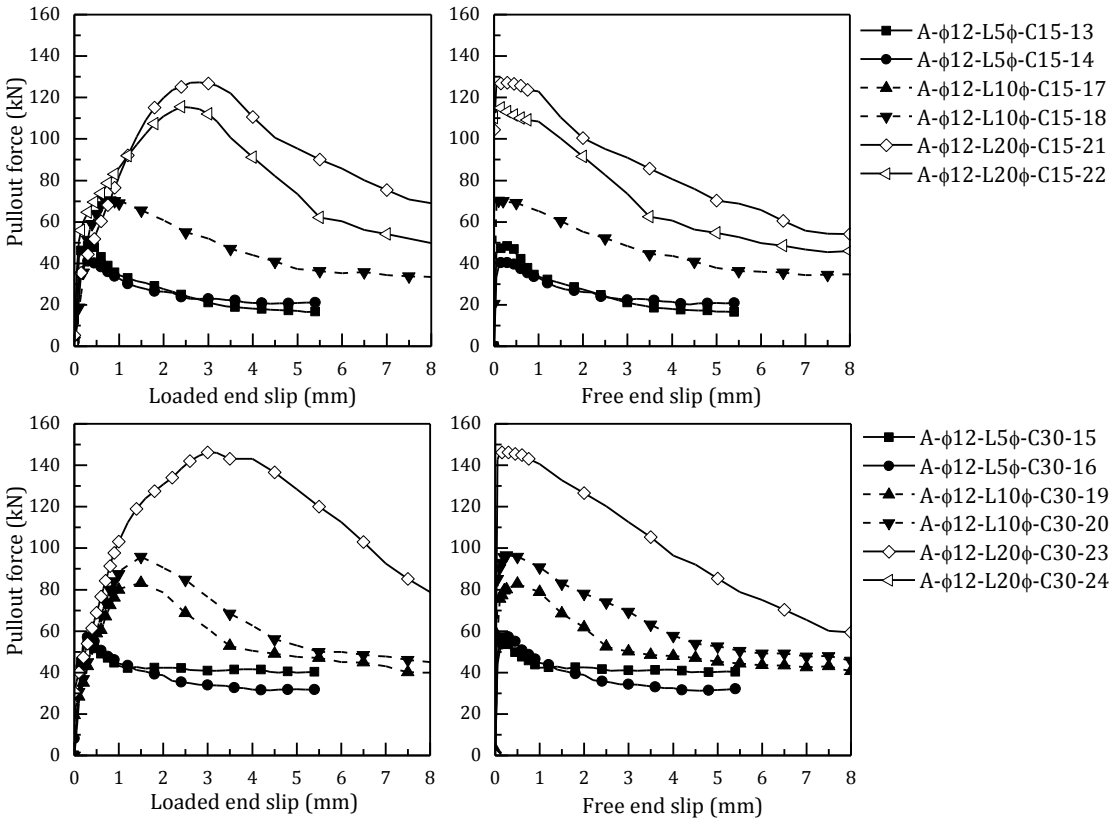

Figure 3-4: Pullout force *versus* loaded and free end slip for type A of Ø12 with 5Ø, 10Ø and 20Ø bond lengths: (a)-(b) 15 mm concrete cover, (c)-(d) 30 mm concrete cover

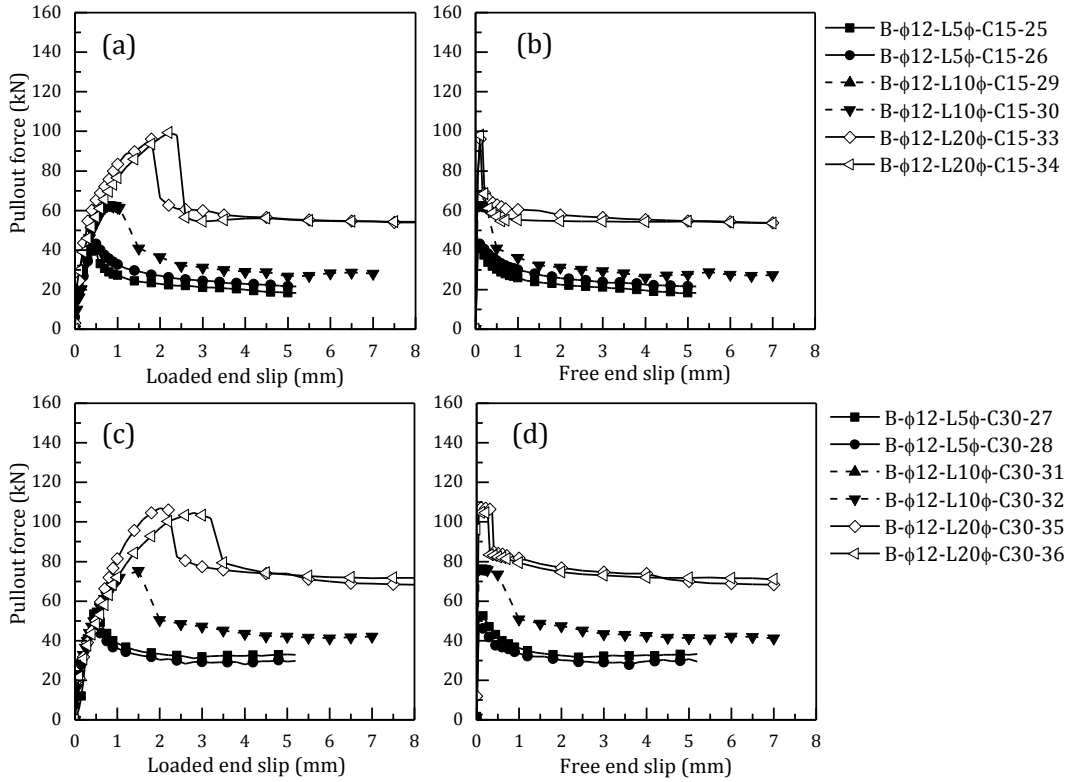

Figure 3-5: Pullout force *versus* loaded and free end slip for type B of Ø12 with 5Ø, 10Ø and 20Ø bond lengths: (a)-(b) 15 mm concrete cover, (c)-(d) 30 mm concrete cover

3.3.1 Failure modes

Due to the relative high pullout force supported by specimens reinforced with the larger bar diameter and embedment length, the specimens number 17, 24, 29 and 31 failed due to insufficient shear resistance of SFRSCC. To avoid this type of failure mode, carbon fiber reinforced polymer (CFRP) laminates were applied in the lateral faces of the specimens, according to the near surface mounted technique (Sena Cruz 2004), in locations that do not affect the GFRP-SFRSCC bond behavior. Hence, except specimen number 12 (A-Ø8-L20Ø-C30-12), the remaining ones failed by debonding. In case of ribbed bars (type A) with concrete cover of 15 mm (specimens number 18, 21 and 22) a single crack appeared along the embedment length. This crack had naturally a detrimental effect on the bond performance of these specimens, since the concrete confinement decreased with the increase of the opening of this crack. However, splitting failure mode never occurred due to the contribution of fibers bridging this crack that had maintained the crack width at very small value. According to the bond study carried out by Achillides and Pilakoutas (2004), for concrete of compressive strength higher than 30 MPa, bond failure partly occurs on the surface of the

bar and partly in the concrete by peeling the cortical layer of the bar. Since a relatively high concrete compressive strength was used in this study (>50 MPa), the bond failure mode significantly depended on the surface treatment of FRP bars. The block A of each specimen was cut after testing in order to have a deeper inspection of the failure mode. Figure 3-6a shows the damages on surface of GFRP bars after testing. The resin over the surface of GFRP bar was chopped and crushed in case of type B, and the ribs were scratched in the type A bars. However, in the type A bar of specimens, where a single splitting crack was formed, signs of concrete damage was observed at the bottom of the bar's surface due to the lower confinement provided by the cracked concrete cover. This means that the bond failure for these specimens was controlled by both type of failure modes at the top and bottom of the GFRP-SFRSCC interface (see Figure 3-6b).

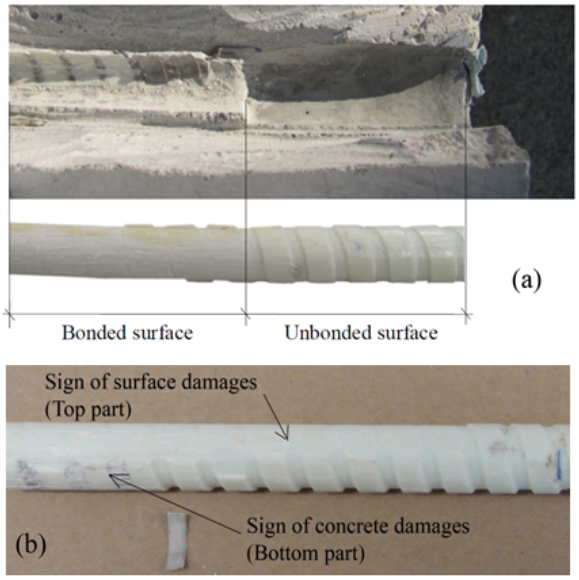

Figure 3-6: Type A bar: (a) appearance after specimen has been tested, and (b) mix damage in specimens with a splitting crack

This mixed damage configuration was more prone in the bars of higher flexural stiffness surrounded by smaller SFRSCC cover thickness, since the curvature of the GFRP bar along the embedment length increased with the reduction of the SFRSCC cover thickness (more deformable medium). This favors the increase of the radial stresses applied by the SFRSCC to the top surface of the bar, and due to the Mohr-Coulomb effect the shear stresses increase, leading to the scratch of the ribs of the bar in these zones. Furthermore, due to the intrinsic

nature of SFRSCC casting conditions, at the bottom part of the bar a higher percentage of porous and flaws exist. Therefore, the combination of the smaller strength of this material with the local radial stresses due to the curvature of the bar justifies the presence of this cement paste material in between the GFRP ribs at the bottom part of the bar.

3.3.2 Effect of bar diameter

The bond performance of 8 mm and 12 mm GFRP bars type A in terms of $\bar{\tau}_{max}$ is compared in Figure 3-7. For the specimens with 15 mm of SFRSCC cover, the maximum bond stress achieved in the case of 12 mm bar diameter was almost equal or even smaller than the corresponding $\bar{\tau}_{max}$ obtained for 8 mm bar. However, in the specimens with 30 mm of SFRSCC cover, the maximum bond stress ($\bar{\tau}_{max}$) for a bar diameter of 12 mm was higher than for the 8 mm with exception of 20 embedment length. It is worth noting that, this trend decreased with the increase of L_e . By increasing the bar diameter and the bond length, the maximum pullout force was conditioned by the splitting strength capacity of SFRSCC cover.

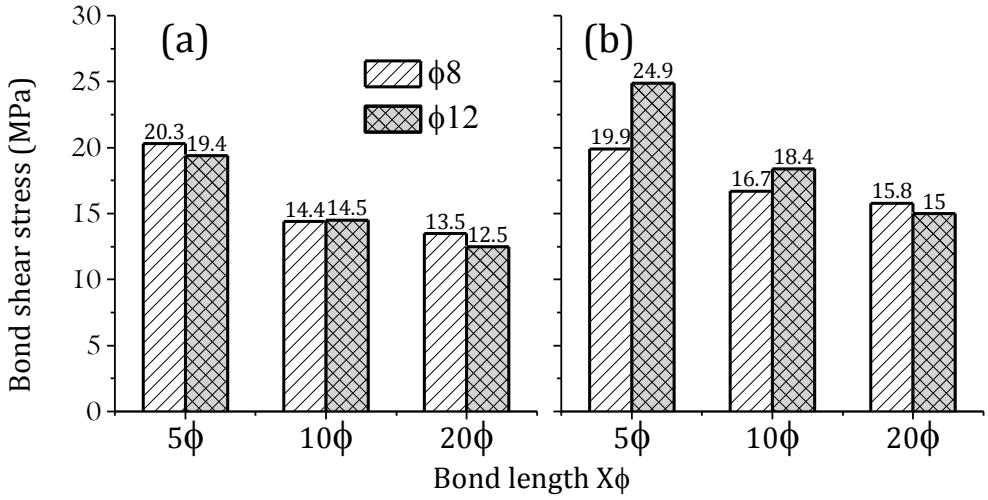

Figure 3-7: Influence of bar diameter of type A bar on the maximum average bond stress: (a) SFRSCC cover 15mm, and (b) SFRSCC cover 30mm

3.3.3 SFRSCC cover thickness

The increase in $\bar{\tau}_{max}$ the for the specimens with 30 mm SFRSCC cover thickness with respect to the corresponding values obtained for 15 mm SFRSCC cover is presented in Figure 3-8. This analysis was carried out for the three types of bars and for the different

values of L_e. The results show higher maximum average bond shear stress, $\bar{\tau}_{max}$, when 30 mm SFRSCC cover thickness was used, with the exception of the 8 mm bar diameter with 5Ø embedment length, since in this case the relatively low pullout force is not influenced by the splitting strength of the SFRSCC cover. The values of $\bar{\tau}_{max}$ were also higher in case of ribbed bars (type A) than in sand-coated bars (type B), which reveals the influence of the surface treatment and bar stiffness (the type A bar has higher elasticity modulus and measured diameter, see Table 3-1). Since the type B bar has a lower elasticity modulus and, consequently, lower stiffness, apart the effects pointed out in the last paragraph of Section 3.3.1, the higher contraction of the bar in the plane of its cross section due to the Poisson's effect is expected to have contributed for the smaller performance of the type B bar. The better performance of the specimens with 30 mm SFRSCC cover can be explained by the higher volume of concrete surrounding the bar that promotes the superior confinement, and smaller damage in the concrete cover.

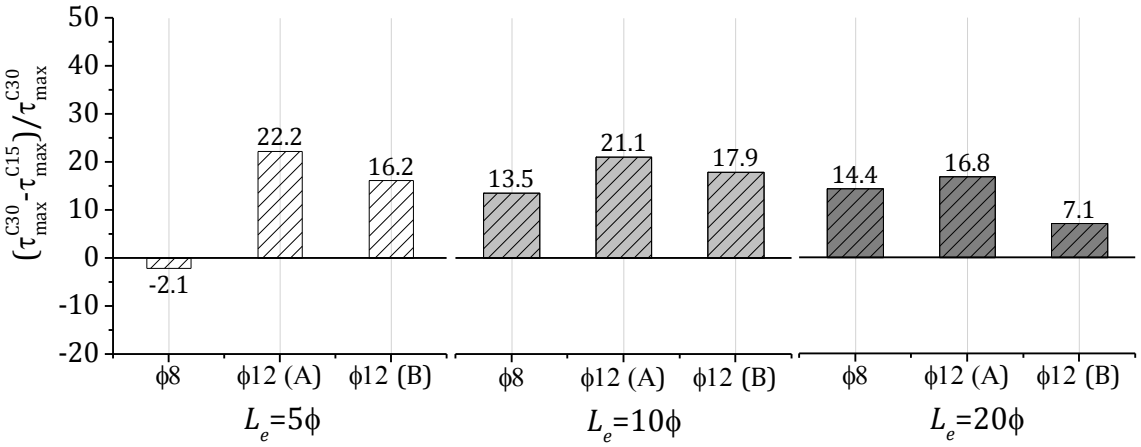

Figure 3-8: The comparison between the maximum average bond stress in case of 15 (C15) and 30 (C30) concrete cover

The average residual bond stress, $\bar{\tau}_{res}$, is another important parameter characterizing the pseudo-ductility of the bond behavior. This value was calculated for a pullout force corresponding to a relatively high value of loaded end slip (8 mm), when the debonding process is in the post-peak branch of the curve pullout force *versus* slip for all the specimens. The ratio between $\bar{\tau}_{res}$ and $\bar{\tau}_{max}$ is compared in Figure 3-9 for the type of bars, bar diameter, and SFRSCC cover, where it is visible that the $\bar{\tau}_{res}/\bar{\tau}_{max}$ ratio increases with concrete cover.

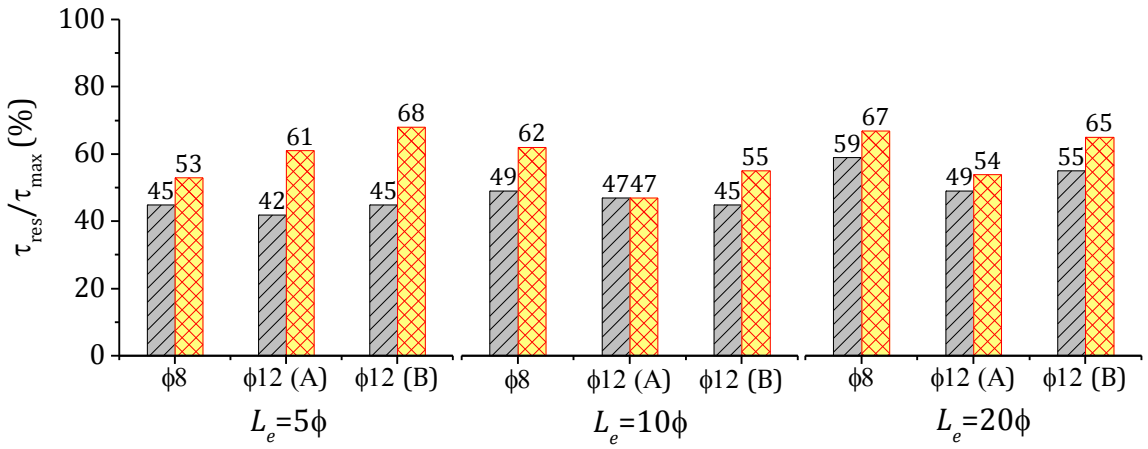

Figure 3-9: Variation between the residual bond shear stress and the average maximum bond shear stress

3.3.4 Embedment length

The evolution of the maximum average bond stress, $\bar{\tau}_{max}$, with the embedment length (*i.e.* L_e) is plotted in Figure 3-10a. As expected, the value of $\bar{\tau}_{max}$ decreased with the increase of L_e, which was a consequence of the nonlinear distribution of the bond stress along L_e (Tighiouart *et al.* 1998). As shown in Figure 3-10b, the loaded end slip at peak pullout force (s_{lp}) increased with L_e and bar diameter. The increase of s_{lp} with L_e is a natural consequence of the increase of the maximum pullout force with the increase of L_e, and the similar stiffness of the $F-s_l$ pre-peak phase for the different L_e test series (Figure 3-3, Figure 3-4, and Figure 3-5). The increase of s_{lp} with L_e was more pronounced in bars of ribbed surface (type A) than in bars of sand coated surface (type B). In fact, s_{lp} was higher in type B bar for the smallest L_e, almost equal in both types of bars for the intermediate L_e, and smaller in type B bar for the largest L_e. On the other hand, no significant variation was observed in terms of free end slip at peak pullout force (s_{fp}) by increasing L_e (see Figure 3-10b). However, the free end slip in type B bar was considerably smaller than in type A (0.09 mm against 0.24 mm, respectively), which was a consequence of the larger damage introduced by the stiffer type bar A along the embedment length, as already discussed in previous sections.

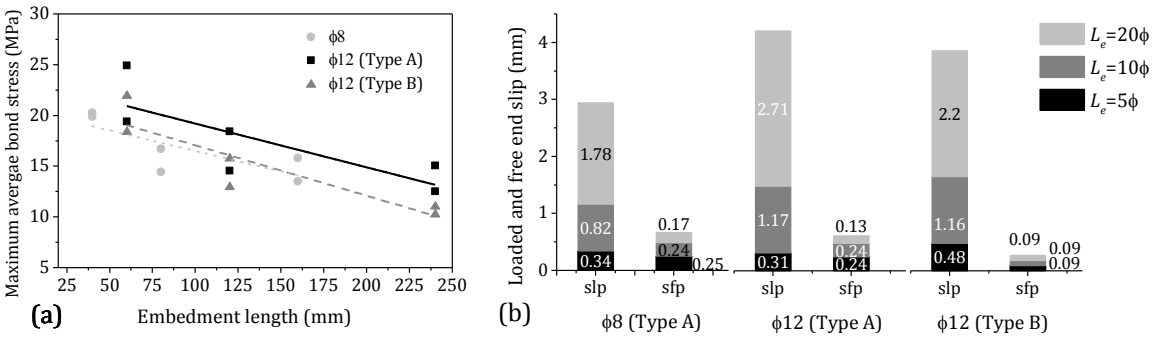

Figure 3-10: (a) Maximum average bond stress *versus* embedment length (b) corresponding slip at loaded end for different bar type and embedment length

3.3.5 Surface treatment

Figure 3-11a shows that $\bar{\tau}_{max}$ was larger in the ribbed GFRP bars (type A) than in the sand-coated GFRP bars (type B), regardless of the bar embedment length and SFRSCC cover. Figure 3-11b represents a comparison between the pullout force *versus* loaded end slip up to $s_{lp} = 2\text{mm}$, for type A and type B bar, in case of 15 and 30 mm SFRSCC cover thickness. Figure 3-11b clearly shows that type A bar had a higher bond stiffness and peak pullout force than type B bar, which was not only a consequence of the surface characteristics of these bars, but also the larger stiffness of the type A bar (larger determined elasticity modulus and measured diameter, Table 3-1), as already indicated. The higher pullout force in the post-peak phase evidenced by the type A bar (Figure 3-11b) can also be a consequence of the higher frictional resistance provided by the ribbed surface characteristics of this type of bar.

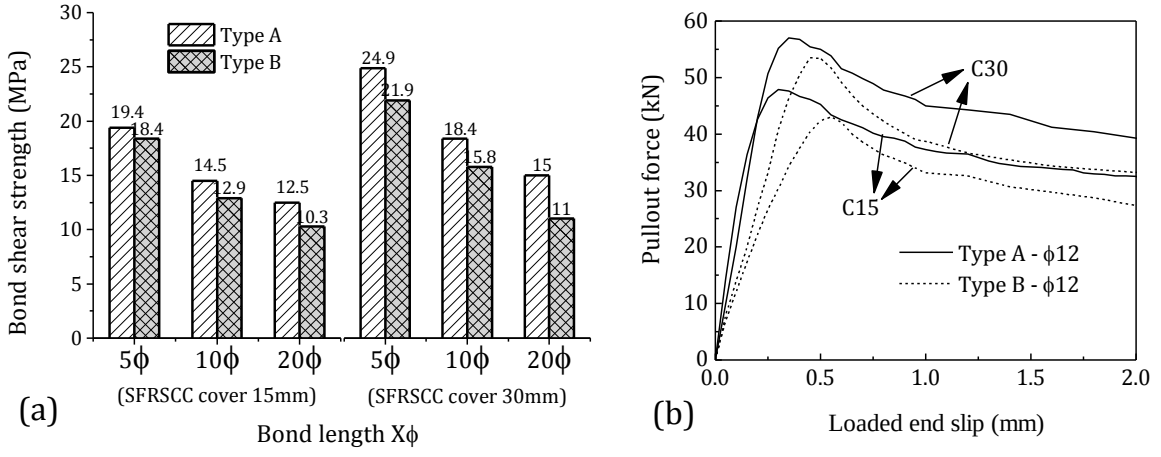

Figure 3-11: Comparison between two types of GFRP bars: (a) maximum average bond stress; (b) Pullout force *versus* loaded end slip for specimens with 5Ø bond length

The relationship between the average strain in the bar at the load end and the slip at this loaded end section ($\varepsilon_f - s_{lp}$) up to peak pullout force for type bar A and B is compared in Figure 3-12. For this purpose, the bars of 12 mm diameter with $L_e = 5\phi$ were selected, but the obtained trends are representative of the behavior registered in the other analyzed cases. This figure shows that for any average strain in the loaded end section, the type bar B always presented a higher loaded end slip, regardless of the SFRSCC cover thickness. This discrepancy between both types of bars increased during the loading process and was higher in the specimens of smaller SFRSCC cover thickness.

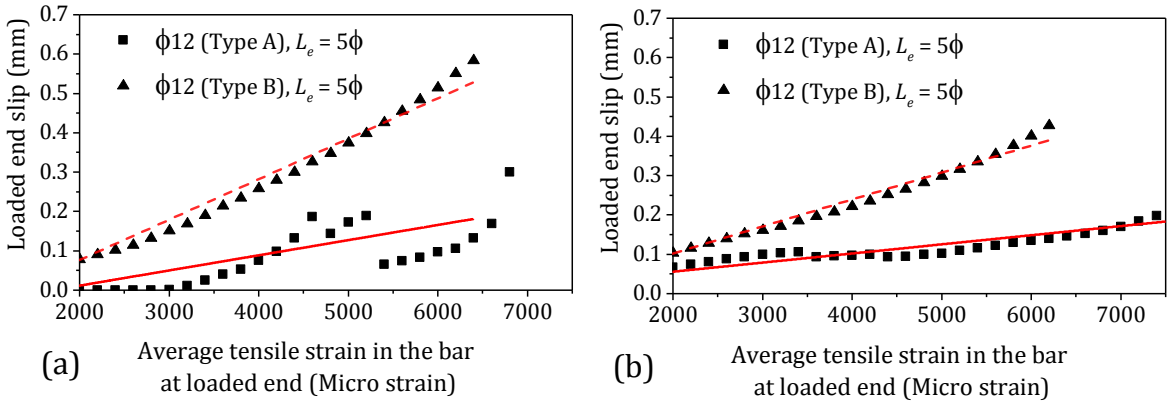

Figure 3-12: Average strain in the bar *versus* loaded end slip: (a) 15 mm concrete cover, and (b) 30 mm concrete cover

3.4 Analytical study

A bond analytical formulation was presented by adopting a multi-linear bond-slip relationship ($\tau - \delta$) for the types of GFRP bar's surface (ribbed and sand-coated) embedded in SFRSCC tested. The developed model was calibrated by taking the experimental results of pullout force *versus* slip that was obtained from the tests discussed earlier in the previous sections. Additionally, a parametric study was carried out using the analytical formulation in order to evaluate the influence of involved bond-slip law's parameters on the maximum theoretical force that can be transferred to the surrounding SFRSCC through the bond length. Finally, the minimum theoretical bond length required to achieve the tensile strength of the GFRP bars was determined, and the obtained values were compared with those recommended by some published codes.

3.4.1 Bond model

3.4.1.1 Governing equations

Neglecting the deformability of surrounding concrete, and assuming a linear and elastic behavior for an embedded bar to concrete, the second-order differential equation that governs the bond behavior along the bond length can be stated as follow (Russo *et al.* 1990):

$$\frac{d^2\delta(x)}{dx^2} - J\,\tau(\delta(x)) = 0 \tag{3-3}$$

where J is the ratio between the perimeter (πd_f) and axial stiffness ($E_f A_f$) of the bar, being d_f, E_f and A_f, respectively, the diameter, the longitudinal modulus of elasticity and the cross-sectional area of the bar. In Eq. (3-3), $\delta(x)$ represents the slip between GFRP and surrounding concrete at a section x from the free end. Based on Hook's law, the following equation can also be deduced:

$$\sigma_f(x) = E_f \frac{d\,\delta(x)}{dx} \tag{3-4}$$

where σ_f is the axial tensile stress of the bar. Further, the distribution of bond shear stress along the bond length (*i.e.* $\tau(x)$) is given by Eq. (3-5) based on Eq. (3-3):

$$\tau(x) = \frac{1}{J}\frac{d^2\delta(x)}{dx^2} \tag{3-5}$$

3.4.1.2 Local bond-slip relationship

A multi-linear diagram presented in Figure 3-13 is proposed as local bond shear stress-slip ($\tau - \delta$) relationship for embedded GFRP bar to SFRSCC in this study. This relationship is stated by the following equation:

$$\tau(\delta) = \begin{cases} \tau_0 + \dfrac{\tau_m - \tau_0}{\delta_1}\cdot\delta & 0 \le \delta \le \delta_1 \quad (\textit{elastic phase}) \\ \tau_m & \delta_1 < \delta \le \delta_2 \quad (\textit{plastic phase}) \\ \tau_m - \dfrac{\tau_m - \tau_R}{\delta_3 - \delta_2}\cdot(\delta - \delta_2) & \delta_2 < \delta \le \delta_3 \quad (\textit{softening phase}) \\ \tau_R & \delta > \delta_3 \quad (\textit{frictional phase}) \end{cases} \tag{3-6}$$

The rigid branch ($0 - \tau_0$) represents the overall initial shear strength and it is attributable to the micro-mechanical and chemical properties of the involved materials and interfaces.

The ascending branch represents the bond behavior between the initial bond shear stress (*i.e.* τ_0) and the bond strength (τ_m) ends at a slip δ_1. Between δ_1 and δ_2, constant bond strength, τ_m, simulates the initiation of the damage in the bar-concrete interface. With the advance of this damage, the bond stress starts decreasing with the increase of slip, and this slip-softening phase, which is governed by friction and micromechanical interlocking along the bond length, is simulated by the third branch that ends at a slip δ_3, when a residual bond shear stress, τ_R, is attained. For $\delta > \delta_3$, due to friction mechanism between bar and surrounding concrete, this residual bond stress is assumed constant, in agreement with previous research (Hao *et al.* 2008; Baena *et al.* 2009) and results obtained in the experimental tests.

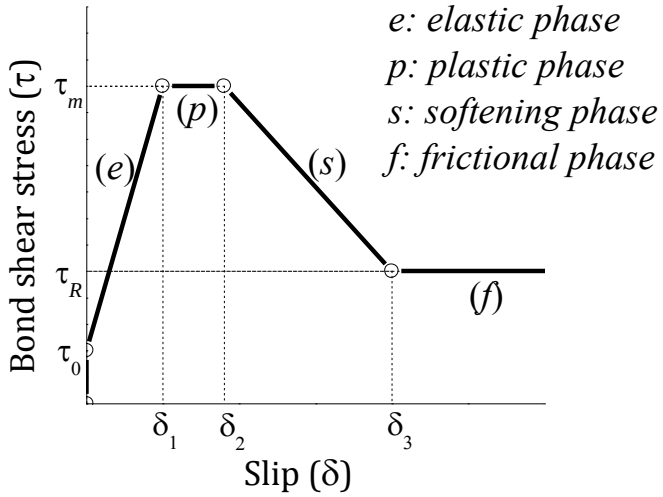

Figure 3-13: The adopted bond-slip relationship in the bond model

3.4.1.3 Theoretical pullout force in case of Infinite Bond Length (IBL)

Debonding process for infinite bond length of GFRP bar is described hereafter by introducing the proposed $\tau - \delta$ relationship in Eq. (3-6) into Eq. (3-3). For each phase, slip distribution along the bar, $\delta(x)$, required bond transfer length, $L_{tr}(\delta_L)$, and corresponding pullout force at each section of the bar, $F(x)$, are determined for whatever value of loaded end slip (imposed slip, δ_L). These concepts, as well as the definition of the local reference systems in elastic (x_e), plastic (x_p), softening (x_s) and frictional (x_f) bond phases, are illustrated in Figure 3-14. The study is based on the works carried out by Bianco *et al.* (2009)

and Sena-Cruz and Barros (2004) in the case of NSM-CFRP laminate.

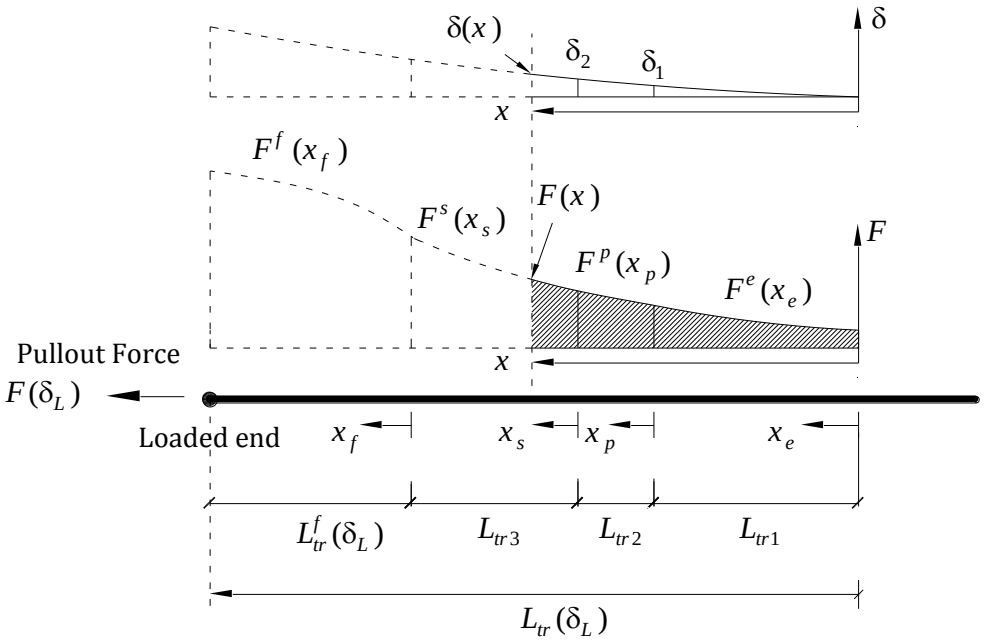

Figure 3-14: Debonding process in case of infinite bond length: pullout force, slip distribution, the required transfer bond length, and definition of local reference systems

Elastic Phase: When the imposed slip is $\delta_L \le \delta_1$, Eq. (3-3) is solved in the local reference system of x_e, and the solution becomes (Bianco *et al.* 2009):

$$\delta^e(x_e) = C_1^e e^{\lambda x_e} + C_2^e e^{-\lambda x_e} - C_3^e \tag{3-7}$$

with

$$\frac{1}{\lambda^2} = \frac{\delta_1}{(\tau_m - \tau_0)\cdot J} \tag{3-8}$$

and the particular solution is

$$C_3^e = \frac{\tau_0 J}{\lambda^2} \tag{3-9}$$

By imposing the following boundary conditions into Eq. (3-7):

$$\begin{cases} \delta^e = 0 \ \text{ at } \ x_e = 0 \\ \delta^e = \delta_L \ \text{ at } \ x_e = L_{tr}^e(\delta_L) \end{cases} \tag{3-10}$$

where $L_{tr}^e(\delta_L)$ is the bond transfer length corresponding to the first phase ($\delta_L \le \delta_1$), the integration constants are obtained as follows:

$$C_1^e = \left[\delta_L + C_3^e \cdot \left(1 - e^{-\lambda \cdot L_{tr}^e(\delta_L)}\right)\right] \cdot \frac{1}{e^{\lambda \cdot L_{tr}^e(\delta_L)} - e^{-\lambda \cdot L_{tr}^e(\delta_L)}} \tag{3-11}$$

$$C_2^e = C_3^e - C_1^e \tag{3-12}$$

By imposing the following equilibrium equation along the bond length:

$$F(x = L_{tr}(\delta_L)) = \pi d_f \cdot \int_0^{L_{tr}(\delta_L)} \tau(x_e) dx_e \tag{3-13}$$

$L_{tr}^e(\delta_L)$ becomes

$$L_{tr}^e(\delta_L) = \frac{1}{\lambda} \cdot \operatorname{arcosh}\left(\frac{\delta_L + C_3^e}{C_3^e}\right) \tag{3-14}$$

The pullout force at the value of imposed slip can be determined by using Eq. (3-4)

$$F(x = L_{tr}(\delta_L)) = F^e(x = L_{tr}^e(\delta_L)) = \pi d_f \int_0^{L_{tr}^e(\delta_L)} \tau(x_e) dx_e = E_f A_f \left(\frac{d\delta^e}{dx^e}\right)\Big|_0^{L_{tr}^e(\delta_L)} \tag{3-15}$$

and the maximum pullout force and maximum bond transfer length undergoing the elastic phase (F_1^e and L_{tr1} respectively) are obtained by imposing a loaded end slip equals δ_1

$$L_{tr1} = L_{tr}^e(\delta_L = \delta_1) \tag{3-16}$$

$$F_1^e = F^e(x_e = L_{tr1}) \tag{3-17}$$

Plastic Phase: the plastic phase corresponds to the loaded end slip in the interval of $\delta_1 < \delta_L \le \delta_2$ and the corresponding bond shear stress remains constant ($\tau(\delta) = \tau_m$). The solution for Eq. (3-3) is a polynomial function in the local reference system of x_p as follow

$$\delta^p(x_p) = C_1^p (x_p)^2 + C_2^p x_p + C_3^p \tag{3-18}$$

with

$$C_1^p = \frac{\tau_m J}{2} \tag{3-19}$$

The boundary conditions are

$$\begin{cases} \delta^p = \delta_1 \ \text{ at } \ x_p = 0 \\ \delta^p = \delta_L \ \text{ at } \ x_p = L_{tr}^p(\delta_L) \end{cases} \tag{3-20}$$

where $L_{tr}^p(\delta_L)$ is the bond transfer length in the plastic phase ($\delta_1 < \delta_L \le \delta_2$), and the integration constants become

$$C_2^p = \frac{(\delta_L - \delta_1) - C_1^p \left(L_{tr}^p(\delta_L)\right)^2}{L_{tr}^p(\delta_L)} \tag{3-21}$$

$$C_3^p = \delta_1 \tag{3-22}$$

By imposing the equilibrium equation along the bond length (*i.e.* $F(x = L_{tr}(\delta_L)) = \pi d_b \cdot \int_0^{L_{tr}^p(\delta_L)} \tau(x_p) dx_p + F_1^e$), $L_{tr}^p(\delta_L)$ is obtained as the following closed-form equation:

$$L_{tr}^p(\delta_L) = \frac{-F_1^e + \sqrt{F_1^e + 4C_1^p(\delta_L - \delta_1)}}{2C_1^p} \tag{3-23}$$

and the overall bond transfer length is

$$L_{tr}(\delta_L) = L_{tr1} + L_{tr}^p(\delta_L) \tag{3-24}$$

The pullout force for whatever value of the imposed slip in this phase is

$$F^p(x_p = L_{tr}^p(\delta_L)) = \pi d_b \cdot \int_0^{L_{tr}^p(\delta_L)} \tau_m dx_p = \pi d_b \cdot L_{tr}^p(\delta_L) \cdot \tau_m \tag{3-25}$$

and the total pullout force becomes

$$F(x = L_{tr}(\delta_L)) = F_1^e + F^p(x_p = L_{tr}^p(\delta_L)) \tag{3-26}$$

The maximum bond transfer length and maximum pullout force undergoing this phase can be also calculated by substituting δ_L by δ_2 in Eqs. (3-23) and (3-25) respectively:

$$L_{tr2} = L_{tr}^p(\delta_L = \delta_2) \tag{3-27}$$

$$F_2^p = F^p(x_p = L_{tr2}) \tag{3-28}$$

and the total force at the end of this phase becomes

$$F_2 = F\left(x = L_{tr}(\delta_L = \delta_2)\right) = F_1^e + F_2^p \tag{3-29}$$

Softening Phase: for $\delta_2 < \delta_L \leq \delta_3$, the corresponding bond shear stress, $\tau(\delta_L)$, decreases up to attain the residual bond shear stress, τ_R, at $\delta_L = \delta_3$ (Figure 3-14). Introducing into Eq. (3-3) the corresponding function in the adopted bond-slip law yields a function in the local coordinate system of x_s as follow (Bianco *et al.* 2009):

$$\delta^s(x_s) = C_1^s \cdot \sin(\beta \cdot x_s) + C_2^s \cdot \cos(\beta \cdot x_s) + C_3^s \tag{3-30}$$

with

$$\frac{1}{\beta^2} = \frac{(\delta_3 - \delta_2)}{(\tau_m - \tau_R) J} \tag{3-31}$$

and particular solution becomes

$$C_3^s = \frac{\tau_m J}{\beta^2} + \delta_2 \tag{3-32}$$

By considering the relevant boundary conditions of the softening phase

$$\begin{cases} \delta^s = \delta_2 \quad \text{at} \quad x^s = 0 \\ \delta^s = \delta_L \quad \text{at} \quad x^s = L_{tr}^s(\delta_L) \end{cases} \tag{3-33}$$

where $L_{tr}^s(\delta_L)$ is the bond transfer length in the softening phase ($\delta_2 < \delta_L \leq \delta_3$), the integration constants are obtained from

$$C_1^s = \frac{1}{\sin\left(\beta \cdot L_{tr}^s(\delta_L)\right)} \cdot \left\{ \delta_L - \delta_2 + \frac{\tau_m \cdot J}{\beta^2} \cdot \left[\cos\left(\beta \cdot L_{tr}^s(\delta_L)\right) - 1 \right] \right\} \tag{3-34}$$

$$C_2^s = \delta_2 - C_3^s \tag{3-35}$$

The equilibrium condition along the bond length (*i.e.* $F(x = L_{tr}(\delta_L)) = \pi d_b \cdot \int_0^{L_{tr}^s(\delta_L)} \tau(x^s) dx^s + F_2^p + F_1^e$) is used to derive the bond transfer length as function of δ_L. So, $L_{tr}^s(\delta_L)$ can be expressed by (Bianco *et al.* 2009)

$$L_{tr}^s(\delta_L) = \frac{1}{\beta} \cdot \left[\phi + \arcsin \frac{C_s}{\sqrt{(A_s)^2 + (B_s)^2}} \right] \tag{3-36}$$

with

$$A_s = F_1^e + F_2^p = F_2 \tag{3-37}$$

$$B_s = \pi d_b \cdot \frac{\tau_m}{\beta} \tag{3-38}$$

$$C_s = \frac{\pi d_b \cdot \beta}{J} \cdot \left(\delta_L - C_3^s \right) \tag{3-39}$$

and

$$\phi = \operatorname{asin}\left(\frac{B_s}{\sqrt{A_s{}^2 + B_s{}^2}} \right) \tag{3-40}$$

and the overall bond transfer length at the end of the softening phase is

$$L_{tr}(\delta_L) = L_{tr1} + L_{tr2} + L_{tr}^s(\delta_L) \tag{3-41}$$

The pullout force for whatever value of imposed slip in this phase is calculated by means of the following equation:

$$F^s(x^s = L_{tr}^s(\delta_L)) = \pi d_b \int_0^{L_{tr}^s(\delta_L)} \tau(x^s) dx^s = E_f A_f \left(\frac{d\delta^s}{dx^s}\right)\Big|_0^{L_{tr}^s(\delta_L)} \quad (3\text{-}42)$$

and the total pullout force becomes

$$F(x = L_{tr}(\delta_L)) = F_1^e + F_2^p + F^s(x^s = L_{tr}^s(\delta_L)) \quad (3\text{-}43)$$

The maximum bond transfer length and the corresponding pullout force in this phase are calculated for a value of imposed slip equals to δ_3:

$$L_{tr3} = L_{tr}^s(\delta_L = \delta_3) \quad (3\text{-}44)$$

$$F_3^s = F(x^s = L_{tr3}) \quad (3\text{-}45)$$

and the total force at the end of the softening phase becomes

$$F_3 = F(x = L_{tr}(\delta_L = \delta_3)) = F_1^e + F_2^p + F_3^s \quad (3\text{-}46)$$

Frictional Phase: when $\delta_L > \delta_3$, $\tau(\delta_L)$ equals to a constant value of bond shear stress (*i.e.* τ_R) due to a stable amount of interfacial friction is established between GFRP and surrounding SFRSCC. Therefore, the solution for Eq. (3-3) is a polynomial function similar to the plastic phase:

$$\delta^f(x_f) = C_1^f (x_f)^2 + C_2^f x_f + C_3^f \quad (3\text{-}47)$$

with

$$C_1^f = \frac{\tau_R J}{2} \quad (3\text{-}48)$$

and the relevant boundary conditions are

$$\begin{cases} \delta^f = \delta_3 \text{ at } x_f = 0 \\ \delta^f = \delta_L \text{ at } x_f = L_{tr}^f(\delta_L) \end{cases} \quad (3\text{-}49)$$

where $L_{tr}^f(\delta_L)$ is the bond transfer length for $\delta_L > \delta_3$. By imposing these boundary conditions into Eq. (3-47), the integration constants become

$$C_2^f = \frac{(\delta_L - \delta_3) - C_1^f \left(L_{tr}^f(\delta_L)\right)^2}{L_{tr}^f(\delta_L)} \quad (3\text{-}50)$$

$$C_3^f = \delta_3 \quad (3\text{-}51)$$

and using equilibrium equation (*i.e.* $F(x = L_{tr}(\delta_L)) = \pi d_b \cdot \int_0^{L_{tr}^f(\delta_L)} \tau(x_f) dx_f + F_3^s + F_2^p + F_1^e$), $L_{tr}^f(\delta_L)$ is calculated by:

$$L_{tr}^f(\delta_L) = \frac{F_3 - \sqrt{F_3 + 4C_1^f(\delta_L - \delta_3)}}{2C_1^f} \tag{3-52}$$

The pullout force for whatever value of $\delta_L > \delta_3$ is obtained by using

$$F^f(x_f = L_{tr}^f(\delta_L)) = \pi d_b \int_0^{L_{tr}^f(\delta_L)} \tau_R dx_f = \pi d_b \cdot L_{tr}^f(\delta_L) \cdot \tau_R \tag{3-53}$$

and the total pullout force is calculated by

$$F(x = L_{tr}(\delta_L)) = F_1^e + F_2^p + F_3^s + F^f(x^f = L_{tr}^f(\delta_L)) \tag{3-54}$$

3.4.1.4 Theoretical pullout force for Finite Bond Length (FBL)

In case of finite bond length, the debonding process for embedded GFRP bars (or other types of bars) into concrete can be analyzed by solving Eq. (3-3) imposing appropriate boundary conditions for slip at the extremity of the bond transfer length (L_{tr}), which cannot be exceed of an available finite bond length (L_f). While slip at free end (δ_f) is null, *i.e.* $L_f \geq L_{tr}$, the pullout force for whatever value of δ_L is obtained by considering the equations for infinite bond length condition (IBL), this is, Eqs. (3-15), (3-26) , (3-43) and (3-54). However, when $\delta_F > 0$, *i.e.* $L_f < L_{tr}$, and two or more bond-slip phases are acting over L_f, deriving closed-form equations for pullout force is not straightforward due to the complexity of the equations. To overcome this complexity, Bianco *et al.* (2009) presented a bond model for NSM-CFRP strips taking a three-linear bond-slip relationship (one ascending and two descending branches) by assuming that the slip distribution (*i.e.* $\delta(x)$) for the IBL condition could also be applied to FBL condition. This is, the closed-form equations developed for case of infinite bond length were directly used for finite length by considering the possible configurations between L_f and L_{tr} (Bianco *et al.* 2009). In the present study, an analytical-numerical method is presented to determine the pullout force (F) as well as δ_F for whatever value of δ_L in case of the finite bond length condition ($L_f < L_{tr}$) by taking the relevant boundary conditions at free and loaded ends (*i.e.* $\delta = \delta_L$ at $x = L_f$ and $\delta = \delta_F$ at $x = 0$).

Therefore, for each bond phases, new values are derived for those integration constants in Eqs. (3-7), (3-18), (3-30) and (3-47). Calculation of the pullout force, as well as the slip at free end for whatever value of the imposed slip in case of FBL condition is described hereafter by considering different configurations of the proposed bond phases over L_f .

When one bond phase acting:

Fully elastic: when $\delta_L \le \delta_1$ and $0 < \delta_F \le \delta_1$, the bond length, L_f , is thoroughly covered by the linear elastic phase (see Figure 3-15a). Eqs. (3-11) and (3-12) become

$$C_1^e = \left[(\delta_L - \delta_F) + C_3^e \cdot \left(1 - e^{-\lambda \cdot L_f}\right) \right] \cdot \frac{1}{e^{\lambda \cdot L_f} - e^{-\lambda \cdot L_f}} \tag{3-55}$$

$$C_2^e = (\delta_F + C_3^e) - C_1^e \tag{3-56}$$

and using equilibrium condition, leads to express δ_F as function of δ_L :

$$\delta_F = \frac{(\delta_L + C_3^e)}{\cosh(\lambda L_f)} - C_3^e \tag{3-57}$$

The pullout force is calculated by adopting Eqs. (3-55) and (3-56)

$$F^e(x_e = L_f) = A_f \sigma_f(x_e = L_f) = E_f A_f \cdot (C_1^e(\delta_L) \cdot \lambda e^{\lambda L_f} - C_2^e(\delta_L) \cdot \lambda e^{\lambda L_f}) \tag{3-58}$$

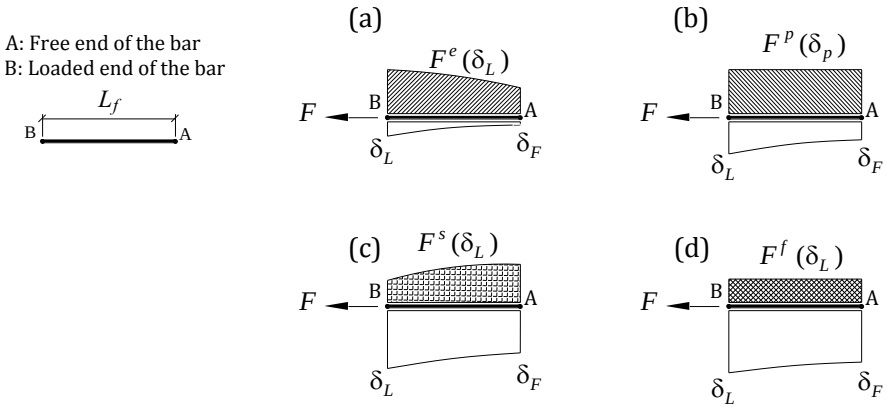

Figure 3-15: The configurations for slip and pullout force distribution over the finite length when one bond phase is acting: (a) Fully Elastic, (b) Fully Plastic, (c) Fully Softening, and (d) Fully Frictional

Fully plastic: if $\delta_F \ge \delta_1$ and $\delta_1 < \delta_L \le \delta_2$, L_f undergoes only the plastic phase (see Figure 3-15b). The integration of constants in Eqs. (3-21) and (3-22) become

$$C_2^p = \frac{(\delta_L - \delta_F) - C_1^p (L_f)^2}{L_f} \tag{3-59}$$

$$C_3^p = \delta_F \tag{3-60}$$

where δ_F is also determined by considering equilibrium condition

$$\delta_F = \delta_L - C_1^p (L_f)^2 \tag{3-61}$$

and F is simply obtained by using

$$F^p(x_p = L_f) = L_f \pi d_f \tau_m \tag{3-62}$$

Fully softening: for the case shown in Figure 3-15c, L_f fully undergoes softening. Hence, the integration of constants in Eqs. (3-34) and (3-35) become

$$C_1^s = \frac{1}{\sin(\beta \cdot L_f)} \cdot \left\{ \delta_L - \delta_F + \frac{\tau_m \cdot J}{\beta^2} \cdot [\cos(\beta \cdot L_f) - 1] \right\} \tag{3-63}$$

$$C_2^s = \delta_F - C_3^s \tag{3-64}$$

and δ_F can be expressed as function of δ_L by using the equilibrium condition

$$\delta_F = \delta_L - \frac{\tau_m J}{\beta^2} \cos(\beta \cdot L_f) + (C_3^s - \delta_2) \tag{3-65}$$

Therefore, F is obtained by Eq. (3-65) adopting Eqs. (3-63) and (3-64)

$$F^s(x_s = L_f) = \pi d_f \int_0^{L_f} \tau(x_s) dx_s = E_f A_f \left(\frac{d\delta^s}{dx_s}\right)\Big|_0^{L_f} \tag{3-66}$$

Fully frictional: if $\delta_2 \le \delta_F < \delta_3$ and $\delta_L > \delta_3$, the frictional bond phase is acting over L_f (see Figure 3-15d). Similar to the fully plastic condition, the integration of the constants in Eqs. (3-50) and (3-51) become

$$C_2^f = \frac{(\delta_L - \delta_F) - C_1^f (L_f)^2}{L_f} \tag{3-67}$$

$$C_3^f = \delta_F \tag{3-68}$$

and δ_f is derived as follow

$$\delta_F = \delta_L - C_1^f (L_f)^2 \tag{3-69}$$

The total pullout force, F, is simply obtained by using

$$F^f(x_f = L_f) = L_f \pi d_f \tau_R \tag{3-70}$$

When two bond phases acting:

When two or more bond phases are acting over L_f, a numerical strategy is adopted in the present study to obtain the slip and force (or bond stress) distributions. By considering a small increment for the imposed slip at i^{th} step of the calculations, *i.e.* $\delta_L^i = \delta_L^{i-1} + \Delta\delta_L$, and initially using the value of the pullout force at the last step of the calculation, $(i\text{-}1)^{\text{th}}$, for each bond phase (*i.e.* $(F^e)^{i-1}$, $(F^p)^{i-1}$, $(F^s)^{i-1}$ and $(F^f)^{i-1}$), a new value of the pullout force is calculated:

Elastic-Plastic **(Figure 3-16*a*)**: by imposing δ_L^i, $(L_{tr}^p)^i$ is calculated by Eq. (3-23) where F_1^e is replaced by $(F_1^e)^i$. Being obtained $(L_{tr}^p)^i$, $(L_{tr}^e)^i$ is simply derived by $L_f - (L_{tr}^p)^i$. Therefore, $(\delta_F)^i$ and $(F^e)^i$ are calculated by Eqs. (3-57) and (3-58) respectively at $x_e = (L_{tr}^e)^i$. The value of $(F^p)^i$ is calculated from Eq. (3-62) at $x_p = (L_{tr}^p)^i$. The total force becomes

$$F^i = (F^e)^i + (F^p)^i \tag{3-71}$$

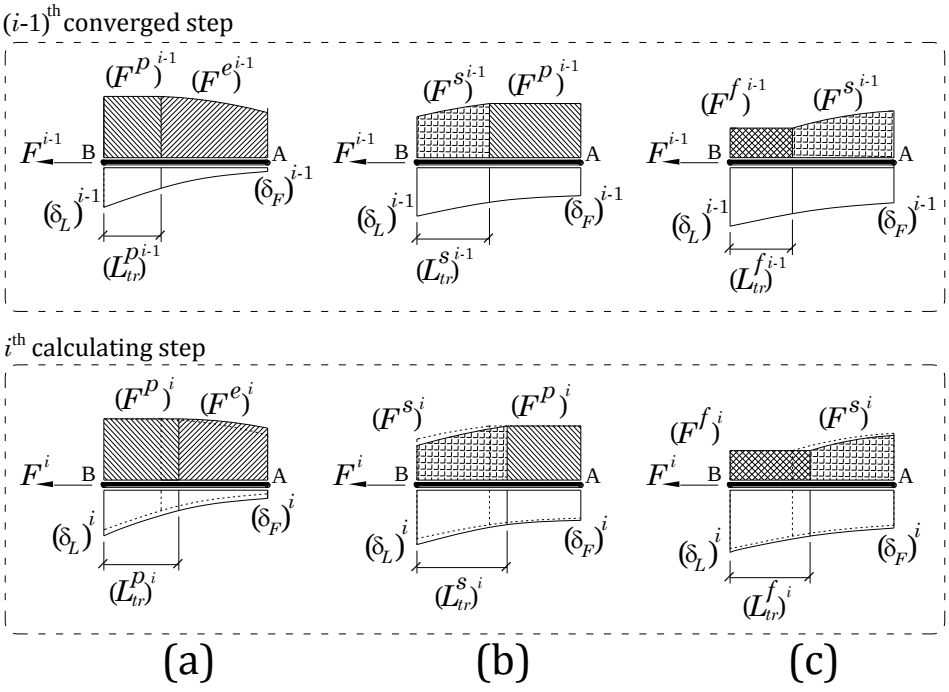

Figure 3-16: The configurations for slip and pullout force over the bond length when two bond phases are acting: (a) Elastic-Plastic, (b) Plastic-Softening, and (c) Softening-Frictional

Plastic-Softening **(Figure 3-16*b*)**: for δ_L^i, $(L_{tr}^s)^i$ is calculated by means of Eq. (3-36) where

F_1^e is null and F_2^p is substituted by $(F^p)^{i-1}$. Being obtained $(L_{tr}^s)^i$, $(L_{tr}^p)^i$ is simply obtained by $L_f - (L_{tr}^s)^i$. Therefore, $(F^p)^i$ and $(\delta_F)^i$ are calculated by Eqs. (3-61) and (3-62) respectively at $x_p = (L_{tr}^p)^i$. The value of $(F^s)^i$ is calculated from Eq. (3-66) at $x_s = (L_{tr}^s)^i$, and the total pullout force becomes

$$F^i = (F^p)^i + (F^s)^i \tag{3-72}$$

***Softening-Frictional* (Figure 3-16*c*)**: here by imposing an increment for the imposed slip, $(L_{tr}^f)^i$ is calculated by Eq. (3-52) where F_1^e and F_1^p are null, and F_3^s is substituted by $(F^s)^{i-1}$. Being obtained $(L_{tr}^f)^i$, $(L_{tr}^s)^i$ is simply calculated by $L_f - (L_{tr}^f)^i$. Hence, $(F^s)^i$ and $(\delta_F)^i$ are determined by Eqs. (3-65) and (3-66) respectively at $x_s = (L_{tr}^s)^i$. The value of $(F^f)^i$ is also determined by Eq. (3-70) at $x_f = (L_{tr}^f)^i$. The total pullout force becomes

$$F^i = (F^s)^i + (F^f)^i \tag{3-73}$$

When three or more bond phases acting:

***Elastic-Plastic-Softening* (Figure 3-17*a*):** for small increment of imposed slip, $(L_{tr}^s)^i$ is calculated by Eq. (3-36) where F_1^e and F_2^p are substituted by $(F^e)^{i-1}$ and $(F^p)^{i-1}$ respectively. Additionally, $(L_{tr}^p)^i$ is determined by Eq. (3-23) where F_1^e is also replaced by $(F^e)^{i-1}$. Therefore, $(L_{tr}^s)^i$ is given by

$$(L_{tr}^e)^i = L_f - (L_{tr}^p)^i - (L_{tr}^s)^i \tag{3-74}$$

Since the free loaded end undergoes elastic bond phase, $(\delta_F)^i$ is calculated by Eq. (3-57) at $x_e = (L_{tr}^e)^i$. Then, $(F^e)^i$ is calculated by Eq. (3-58) at $x_e = (L_{tr}^e)^i$, $(F^p)^i$ by Eq. (3-62) at $x_p = (L_{tr}^p)^i$, and $(F^s)^i$ by Eq. (3-66) at $x_s = (L_{tr}^s)^i$. The total pullout force becomes

$$F^i = (F^e)^i + (F^p)^i + (F^s)^i \tag{3-75}$$

***Plastic-Softening-Frictional* (Figure 3-17*b*):** similar to the previous configuration, $(L_{tr}^f)^i$ is

calculated by Eq. (3-52) where F_1^e is null, while F_2^p and F_3^s are substituted by $(F^p)^{i-1}$ and $(F^s)^{i-1}$ respectively. Besides, $(L_{tr}^s)^i$ is determined by Eq. (3-36) where F_1^e is null, and F_2^p is replaced by $(F^p)^{i-1}$. Finally, $(L_{tr}^p)^i$ is given by

$$(L_{tr}^p)^i = L_f - (L_{tr}^s)^i - (L_{tr}^f)^i \tag{3-76}$$

Since free end undergoes plastic phase, $(\delta_F)^i$ is derived by Eq. (3-61) at $x_p = (L_{tr}^p)^i$. Then, $(F^p)^i$, $(F^s)^i$ and $(F^f)^i$ are obtained by Eqs. (3-62) at $x_p = (L_{tr}^p)^i$, (3-66) at $x_s = (L_{tr}^s)^i$ and (3-70) at $x_f = (L_{tr}^f)^i$ respectively. The total pullout force becomes

$$F^i = (F^p)^i + (F^s)^i + (F^f)^i \tag{3-77}$$

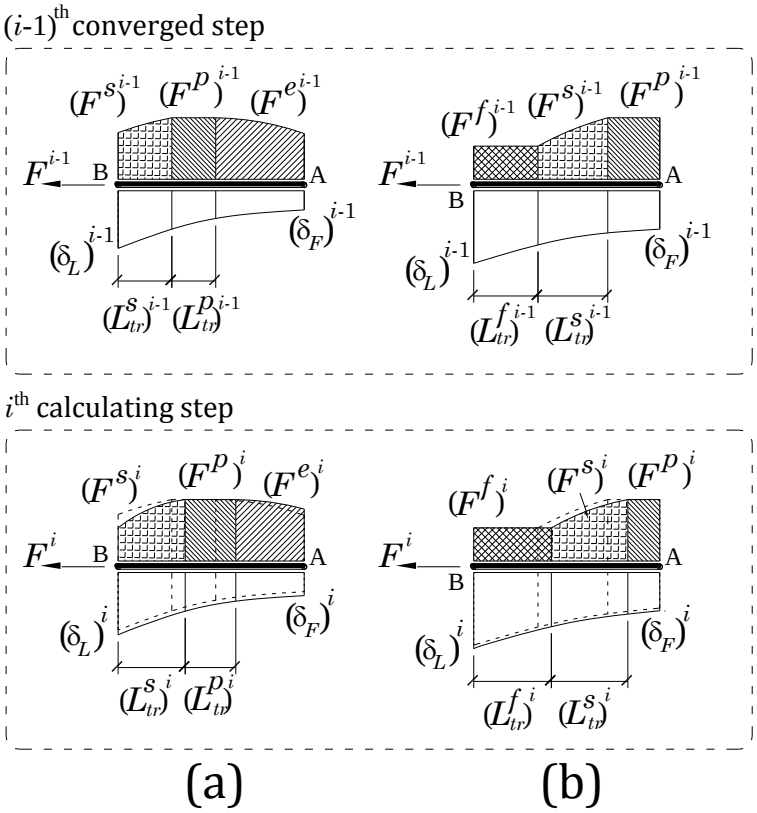

Figure 3-17: The configurations for slip and pullout force over the bond length when three bond phases are acting: (a) Elastic-Plastic-Softening and (b) Plastic-Softening-Frictional

Elastic-Plastic-Softening-Frictional **(Figure 3-18):** when $\delta_L > \delta_3$ and $L_{tr}(\delta_L) < L_f$, L_f undergoes simultaneously the four proposed bond phases. By imposing a small increment for δ_L, the same strategy can be also applied in this case to determine $(L_{tr}^p)^i$, $(L_{tr}^s)^i$ and $(L_{tr}^f)^i$

by initially taking F_1^e, F_2^p and F_3^s equal to $(F^e)^{i-1}$, $(F^p)^{i-1}$ and $(F^p)^{i-1}$ respectively. Then, $(L_{tr}^e)^i$ is given by

$$(L_{tr}^e)^i = L_f - (L_{tr}^p)^i - (L_{tr}^s)^i - (L_{tr}^f)^i \tag{3-78}$$

and the following equation gives the total pullout force:

$$F^i = (F^e)^i + (F^p)^i + (F^s)^i + (F^f)^i \tag{3-79}$$

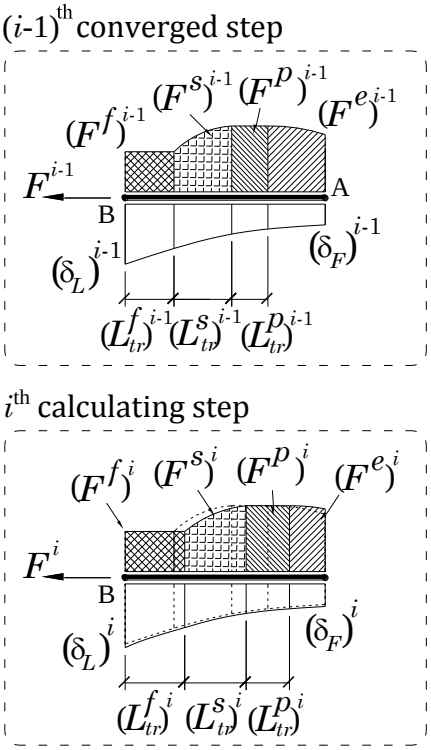

Figure 3-18: The configurations for slip and pullout force over the bond length when four bond phases are acting: Elastic-Plastic-Softening-Frictional

The flowchart of the proposed analytical-numerical algorithm is presented in Figure 3-19. In all above cases, once $(L_{tr})^i$ is obtained for the all active bond phase (e.g. *Elastic*, *Plastic* and *Softening* are the active bond phase in case of Figure 3-17a), the values of $(F^e)^{i-1}$, $(F^p)^{i-1}$, $(F^s)^{i-1}$ and $(F^f)^{i-1}$ are substituted respectively by the new calculated values of $(F^e)^i$, $(F^p)^i$, $(F^s)^i$ and $(F^f)^i$. Then, $(L_{tr})^i$ is recalculated until achieving a value of error less than a tolerance adopted for ΔL_{tr}. This calculation loop is also illustrated in the flowchart.

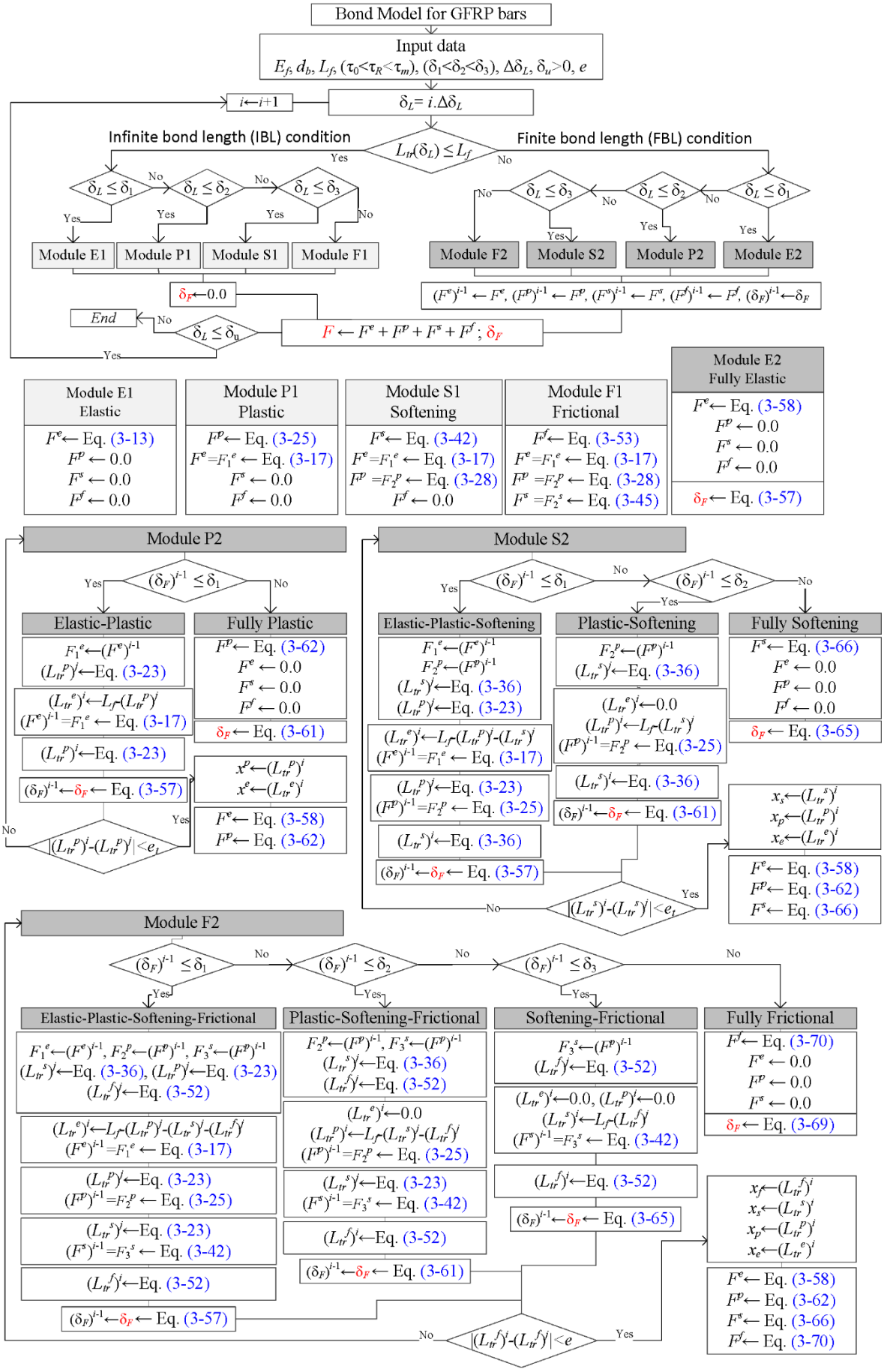

Figure 3-19: Flowchart of the proposed bond model

3.4.2 Predictive performance of the proposed bond model

To assess the predictive performance of the proposed bond model, the obtained $F-\delta$ from the model is compared with the results registered in the previously described bond tests. The values of the parameters to define the $\tau-\delta$ relationship in the model were calibrated using inverse analysis by minimizing the absolute value of error, e, which is defined as $\left|A_{F-\delta}^{\text{model}}-A_{F-\delta}^{\text{exp}}\right| / A_{F-\delta}^{\text{exp}} \times 100$, where $A_{F-\delta}^{\text{exp}}$ is the area under the average $F-\delta$ of the experimental curves, and $A_{F-\delta}^{\text{model}}$ is the area of the $F-\delta$ obtained theoretically. Table 3-6 presents the results of the inverse analysis as well as the error (*e*), in percentage. In this table, the following experimental results are also reported: the maximum pullout force ($F_{\max}$); its corresponding loaded end slip (δ_m) and the residual pullout force at the end of the tests (*i.e.* F_{res}) which was calculated for a pullout force corresponding to the relatively high value of slip (8 mm), when for all the specimens the debonding process was in the post-peak pullout force.

Table 3-6: Relevant experimental results and values of the parameters of the bond model obtained from the inverse analysis

		Experimental results			The results from the bond model							
L_f		$F_{\max}$	δ_m	F_{res}	τ_0	τ_m	τ_R	δ_1	δ_2	δ_3	τ_R/τ_m	e
		(kN)	(mm)	(kN)	(MPa)	(MPa)	(MPa)	(mm)	(mm)	(mm)	(-)	(%)
Deformed GFRP bar, 12 mm diameter												
$5d_f$	C15:	44.76	0.33	17.64	1.0	18.1	7.6	0.09	0.15	2.30	41.5	0.87
	C30:	57.49	0.29	19.75	1.0	23.2	14.8	0.07	0.19	1.50	64.4	0.57
$10d_f$	C15:	70.62	0.84	31.59	1.0	14.3	6.8	0.09	0.50	5.0	46.6	0.63
	C30:	89.54	1.34	40.99	1.0	18.3	8.7	0.15	0.70	5.2	47.4	0.01
$20d_f$	C15:	121.81	2.56	50.22	1.0	12.5	5.1	0.12	1.80	7.0	39.0	0.48
	C30:	146.23	3.00	61.63	1.0	14.9	5.9	0.11	1.20	8.6	33.9	2.63
Smooth GFRP bar, 12 mm diameter												
$5d_f$	C15:	42.06	0.47	18.63	1.0	18.0	8.3	0.10	0.16	1.1	47.2	0.80
	C30:	50.815	0.44	38.73	1.0	21.9	13.1	0.09	0.15	1.1	60.5	0.97
$10d_f$	C15:	62.92	0.81	28.08	1.0	14.0	6.0	0.10	0.35	1.9	42.7	1.09
	C30:	76.64	1.50	42.06	1.0	16.5	9.0	0.10	0.55	2.0	50.5	2.60
$20d_f$	C15:	98.74	2.04	54.47	1.0	12.2	5.8	0.10	0.5	2.0	44.7	1.23
	C30:	106.24	2.36	70.06	1.0	13.2	7.6	0.10	0.7	2.0	50.7	1.20

3.4.2.1 Loaded end slip

The $F-\delta_L$ relationship registered experimentally and determined by the proposed bond

model are compared in Figure 3-20a and Figure 3-21a, respectively, for the deformed GFRP bars with 15 mm and 30 mm SFRSCC cover thickness. In addition, the same comparison is given for the smooth GFRP bar in Figure 3-22a and Figure 3-23a, respectively, with 15 mm and 30 mm SFRSCC cover thickness. The results for the 8 mm bar diameter were not considered in the present study. This comparison evidences that the proposed method is capable of simulating with good accuracy the pullout force *versus* loaded end slip for the two types of GFRP bars.

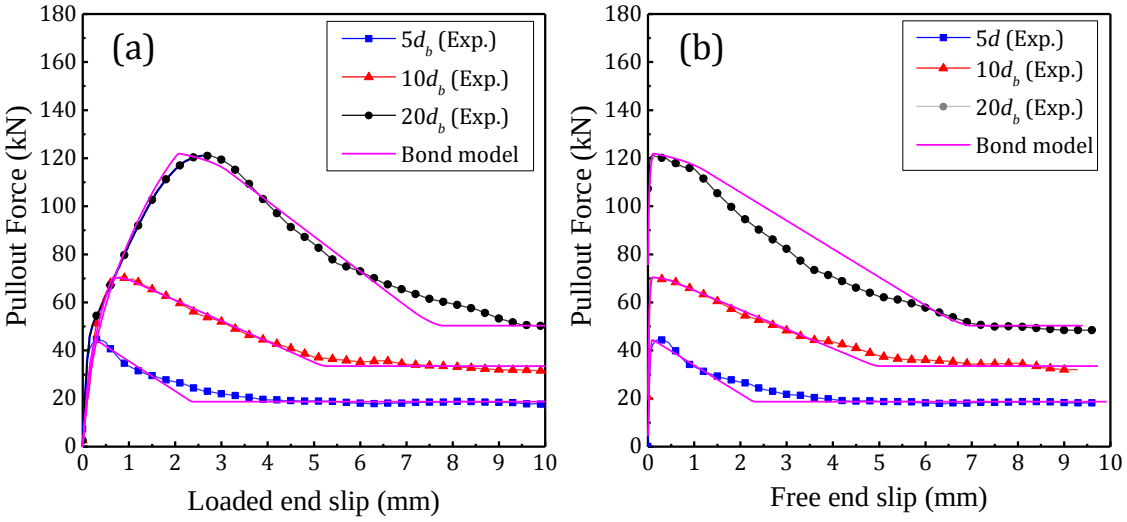

Figure 3-20: The comparison between theoretical and experimental pullout force *versus* (a) loaded end slip and (b) free end slip for deformed GFRP bar with 15 mm SFRSCC cover

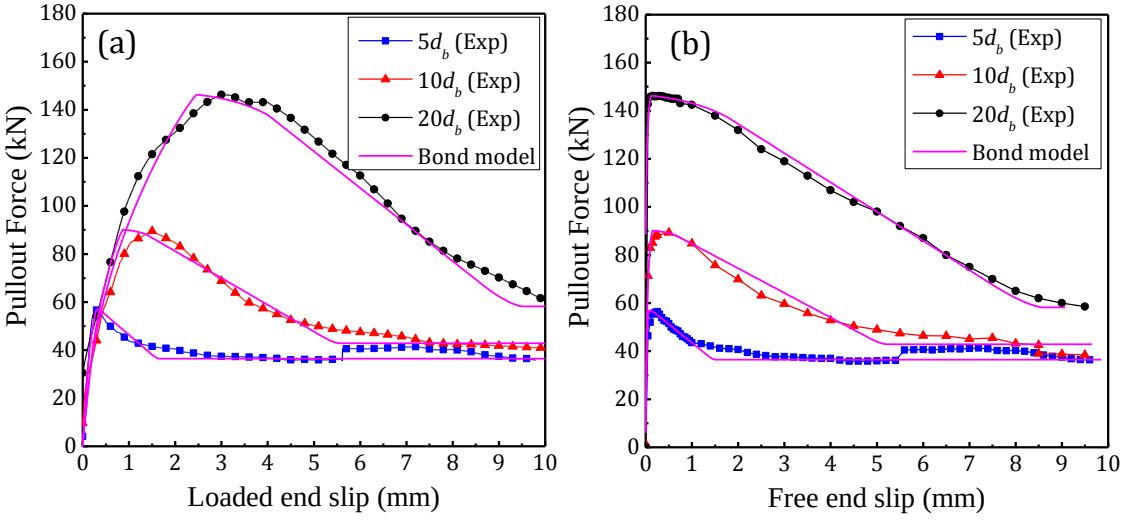

Figure 3-21: The comparison between theoretical and experimental pullout force *versus* (a) loaded end slip and (b) free end slip for deformed GFRP bar with 30 mm SFRSCC cover

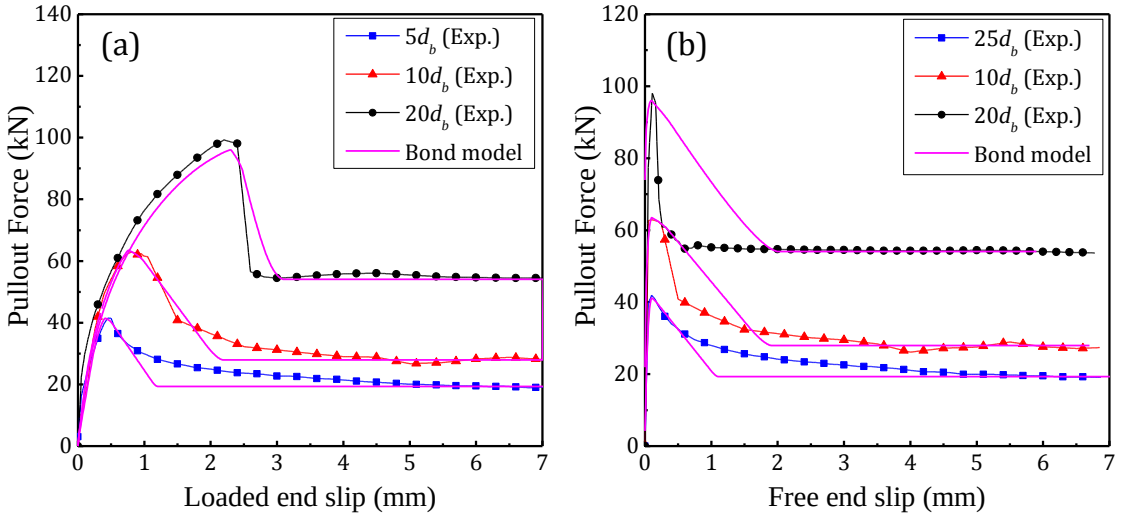

Figure 3-22: The comparison between theoretical and experimental pullout force *versus* (a) loaded end slip and (b) free end slip for smooth GFRP bar with 15 mm SFRSCC cover

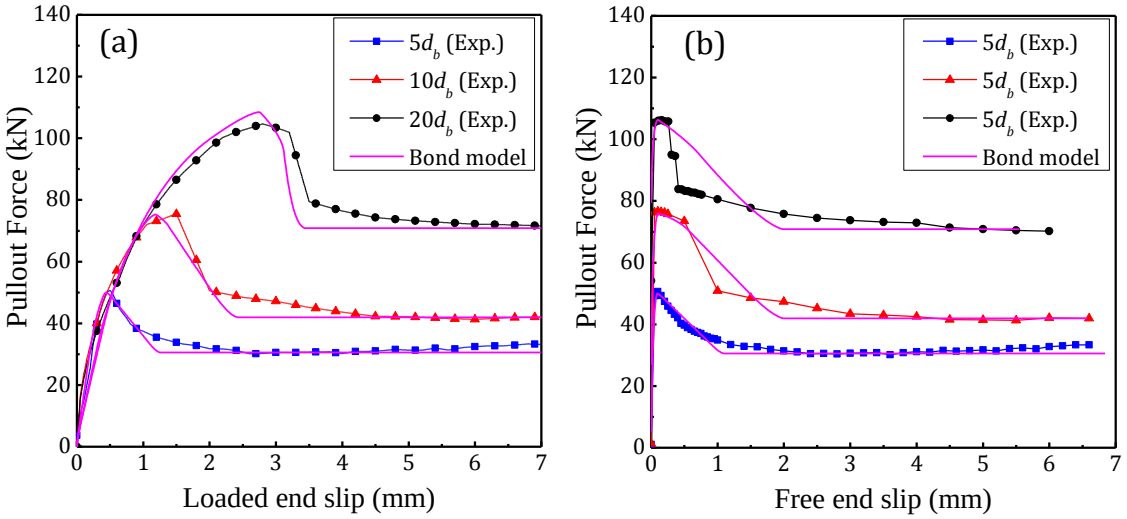

Figure 3-23: The comparison between theoretical and experimental pullout force *versus* (a) loaded end slip and (b) free end slip for smooth GFRP bar with 30 mm SFRSCC cover

3.4.2.2 Free end slip

The experimental and theoretical $F-\delta_F$ curves were compared in Figure 3-20b and Figure 3-21b for the deformed GFRP bars, respectively, with 15 an 30 mm SFRSCC cover thickness. The same comparison is also given for the smooth GFRP bar in Figure 3-22b and Figure 3-23b, respectively, with 15 and 30 mm SFRSCC cover thickness. As shown, the proposed bond model predicts with acceptable accuracy the slip at free loaded end. To evaluate better this predictive performance, Figure 3-24 represents the relationship between

δ_L and δ_F obtained experimentally and theoretically for the specimens with $L_f = 20d_b$. As shown, the $\delta_L - \delta_F$ curve obtained by the proposed bond model is in agreement with the experimental $\delta_L - \delta_F$ curve for both GFRP bars. This confirms the accurate prediction of the obtained $\delta(x)$ by the proposed bond model.

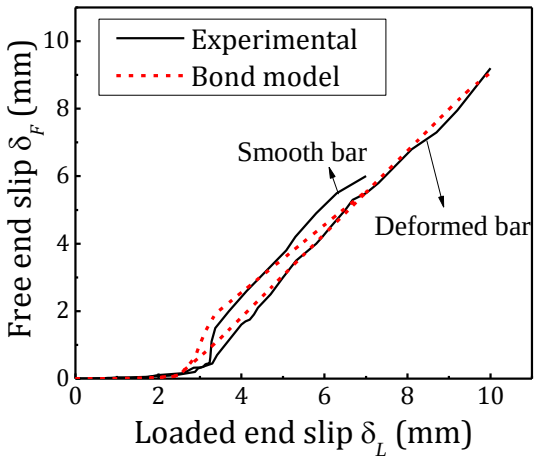

Figure 3-24: The relationship between loaded and free end slip for specimen with highest bond length

3.4.2.3 Observations

"Material" versus "structural" bond-slip property: the slip between bar and surrounding concrete is typically measured at the free and loaded ends by using displacement transducers. The slip, therefore, is the relative deformation between the concrete zones where the transducer is supported, and the section of the FRP bar where the other extremity of the sensor is connected. This means that the value recorded by this sensor is always affected by the deformation of the concrete zone supporting the transducer, which is a quantity difficult to obtain with accuracy. Additionally, bonding strain gauges to the FRP bar along the embedment length is another common alternative to measure indirectly the slip. In this case, the slip variation along the embedment length can only be representative if a reasonable number of strain gauges are applied, which has, however, a detrimental effect on the bond conditions between the bar and the surrounding concrete. Furthermore, the strategy of converting strain values from these strain gauges into a slip concept between bar and

surrounding materials is quite arguable, and only admissible if negligible deformation is assumed for the surrounding concrete. Considering all these aspects, a local bond-slip relationship only exists, and therefore considered as a material property, when the deformation and damage in the surrounding concrete is much smaller than the deformation in the FRP bar. This means that a local bond-slip relationship is a material property only if assessed from experimental data corresponding to FRP-concrete bond length short enough to avoid significant deformation and damage in the surrounding concrete. For the other cases the bond-slip relationship is a structural property, since the sensors are affected by the relevant deformation and damage formed in the surrounding concrete. Furthermore, due to the crack arrestment provided by the fibers bridging the micro-cracks, the damage due to crack formation in the surrounding concrete became limited. Therefore, for modeling the bond behavior between the GFRP bars and the SFRSCC considered in the present work, the bond-slip relationship derived from the tests with the lowest embedment length is recommended.

Theoretical bond strength and its corresponding slip: taking the results from Table 3-6, which were obtained from inverse analysis, the influence of the bond length (L_f) on the value of the bond strength (τ_m) is represented in Figure 3-25a. The parameter τ_m shows tendency to decrease with the increase in L_f for a fixed SFRSCC cover thickness and type of GFRP bar. Additionally, the value of τ_m in case of 30 mm concrete cover was higher than that of 15 mm. It was also higher in deformed bar rather than in smooth bar's surface. However, in case of 15 mm concrete cover thickness, τ_m was similar for both types of GFRP bars, because the relatively low confinement provided by this SFRSCC cover thickness is not enough to mobilize the advantages of deformed bar surface characteristics. Hence, cover thickness higher than about 15 mm (>1.25Ø) is recommended for deformed GFRP bars in order to attain higher magnitude of bond strength (τ_m).

The influence of increasing L_f on the slip at the end of the plastic phase, δ_2, is also shown

in Figure 3-25b. By increasing L_f , δ_2 increased for both types of GFRP bar. This means that δ_2 is another parameter of the bond-slip constitutive law that increased with increase in L_f for the same type of bar, SFRSCC and SFRSCC cover thickness.

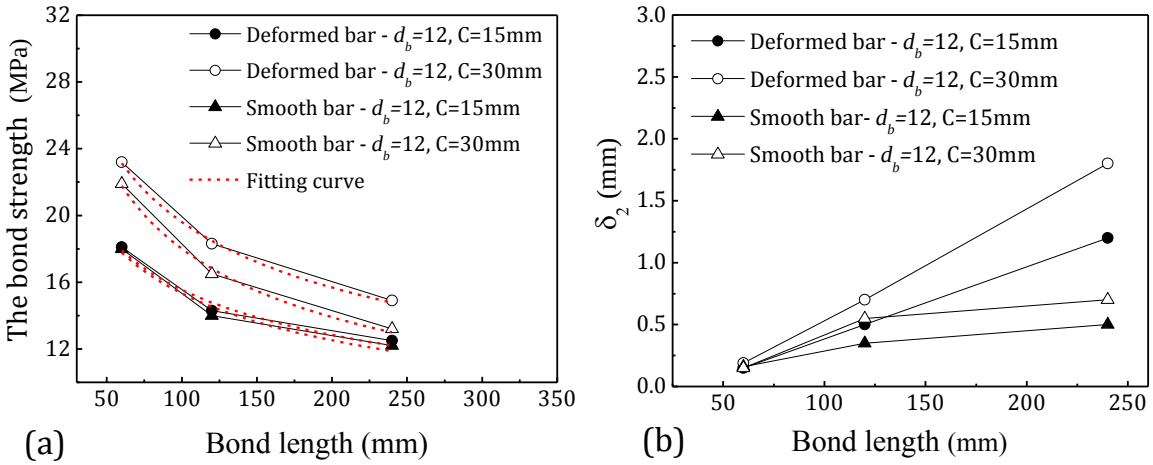

Figure 3-25: (a) The analytical bond strength and (b) the corresponding slip at the end of the plastic phase *versus* the variation of bond length

3.4.3 Parametric study

Hereafter, a parametric study was carried out to evaluate the influence of some involved parameters on the maximum pullout force ($F_{\max}$), namely: the bond shear strength (τ_m) and its corresponding slips (δ_1 and δ_2), bond length (L_f), longitudinal Young's modulus of the bar (E_f), and the slip corresponds to the end of softening phase (δ_3) of bond-slip constitutive law (see Figure 3-13). The study comprised six stages and for each stage, the influence of one parameter on $F_{\max}$ was appraised by considering three different values for L_f (5, 10 and 20d_b bond length) while a constant value was given to the rest of the parameters. The range of given values to the parameter at each stage are written in Table 3-7. The initial bond stress (τ_0) and bar diameter (d_f) considered as 1.0 MPa and 12 mm in all cases, respectively. The results of the parametric study are plotted in Figure 3-26(a) to (f). As shown, the maximum pullout force, $F_{\max}$, is significantly influenced by L_f and τ_m (see Figure 3-26a and b). The influence of δ_1 and δ_3 depends on the value given to δ_2. When the

difference values of δ_2 and δ_1 (or δ_2 and δ_3) are small, their influence on $F_{\max}$ is more visible (see Figure 3-26c and e). In general, the impact of all these slip values and also the magnitude of E_f on $F_{\max}$ are not significant when the $L_f < 20d_b$.

Table 3-7: Values of parameters adopted for parametric study

Study	d_b	τ_0	τ_m	τ_R	δ_1	δ_2	δ_3	E_f	L_f
	(mm)	(MPa)	(MPa)	(MPa)	(mm)	(mm)	(mm)	(GPa)	(mm)
1	12	1	**5-25**	$0.5\,\tau_m$	0.1	0.2	3.0	60	**(5-30)** d_b
2	12	1	**14-18**	$0.5\,\tau_m$	0.1	0.2	3.0	60	**(5-30)** d_b
3	12	1	18	$0.5\,\tau_m$	**0.01-0.5**	**(1.0-3.0)** δ_1	3.0	60	**5,10, 20** d_b
4	12	1	18	$0.5\,\tau_m$	0.1	**0.1-2**	3.0	60	**5,10, 20** d_b
5	12	1	18	$0.5\,\tau_m$	0.1	**(0.1-0.5)** δ_3	**1.0-5.0**	60	**5,10, 20** d_b
6	12	1	18	$0.5\,\tau_m$	0.1	0.2	3.0	**30-65**	**5,10, 20** d_b

3.4.4 Theoretical development length

The minimum transferred bond length required to reach the ultimate tensile stress (σ_{fu}) in the bar can be predicted by means of the proposed bond model. Based on the results of the bond test, the minimum development length of the GFRP bars will be higher than $20d_b$ since no tensile rupture was reported for the GFRP bars in the pullout bending tests (with an exception of one specimen). On the other hand, according to the paramedic study presented in the previous section, among the set of local bond-slip law's parameters, only L_f and τ_m showed significant influence on the maximum pullout force. Therefore, τ_m was defined as function of the bond length (L_f) in the proposed bond model. Accepting exponential fit for the $\tau_m - L_f$, τ_m can be estimated with the following expression:

$$\tau_m(L_f) = b_1(L_f)^{b_2} \tag{3-80}$$

where b_1 and b_2 are the constant values fit the equation with the test results of different bond length (see Figure 3-25a). By imposing Eq. (3-80) into the model instead of τ_m, the maximum pullout force is obtained for whatever value of L_f. The other parameters adopted

in the bond model are summarized in Table 3-8.

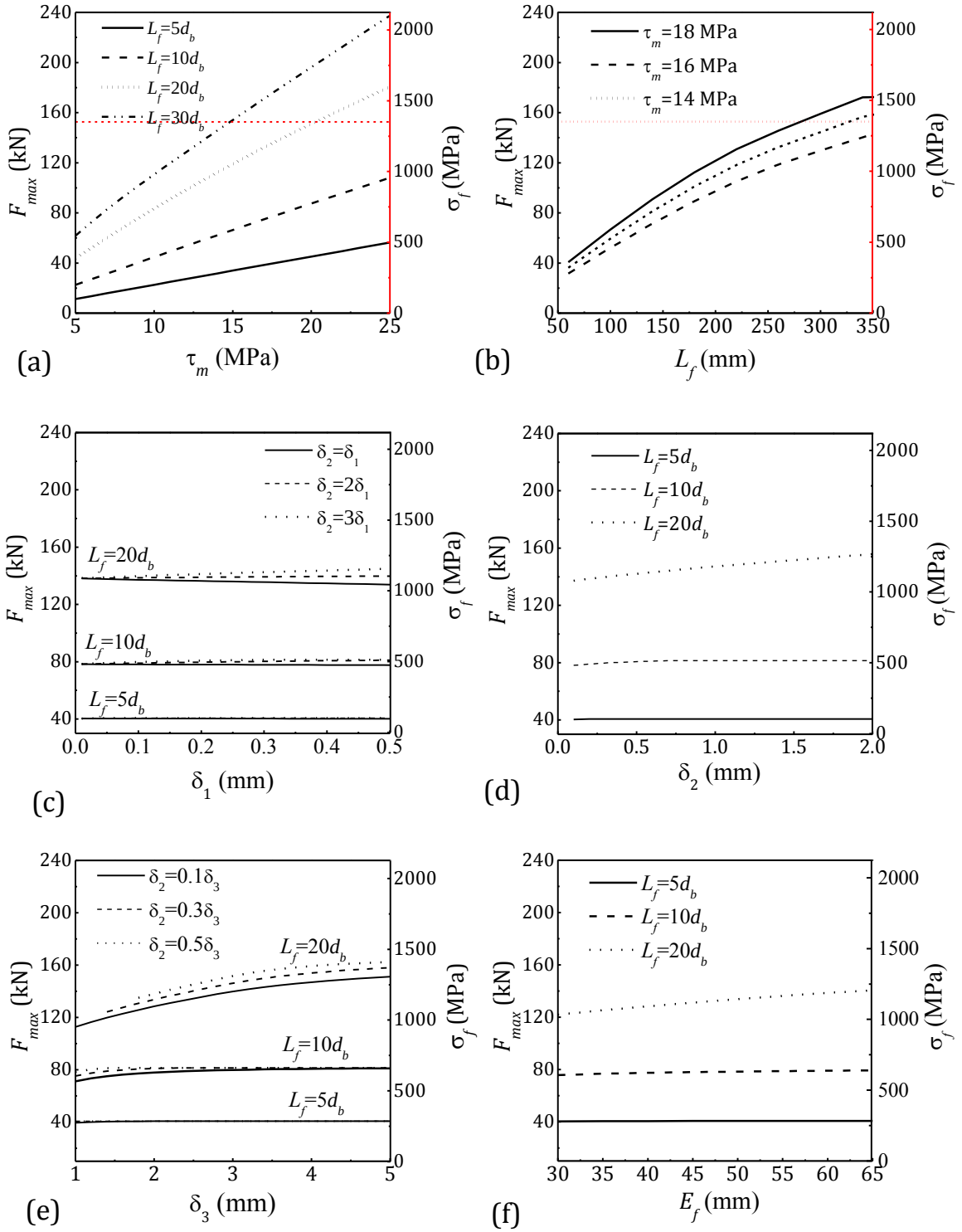

Figure 3-26: Appraisal of influence of (a) the maximum bond stress, (b) bond length, (c) slip at the end of elastic phase (δ1), (d) slip at the end of plastic phase, (e) slip at the end of softening phase, and (f) Young's modulus of the bar on the maximum force transferred

Table 3-8: The parameters adopted in the model to obtain the maximum tensile stress for whatever value of the bond length

Type of GFRP		d_b	E_f	δ_1	δ_2	δ_3	τ_0	τ_m *		τ_R
								b_1	b_2	
		(mm)	(GPa)	(mm)	(mm)	(mm)	(MPa)	(-)	(-)	(MPa)
Deformed bar	C15:	13.08	56.0	0.10	0.50	3.0	1.0	55.41	-0.276	0.5 τ_m
								(R^2=0.96)**		
	C30:	13.08	56.0	0.10	0.50	3.0	1.0	86.70	-0.323	0.5 τ_m
								(R^2=0.99)		
Smooth bar	C15:	12.36	49.0	0.10	0.50	2.0	1.0	58.61	-0.291	0.5 τ_m
								(R^2=0.95)		
	C30:	12.36	49.0	0.10	0.50	2.0	1.0	100.09	-0.373	0.5 τ_m
								(R^2=0.99)		

* Obtained from Eq. (3-80); ** Coefficient of determination;

The achievable theoretical tensile stress (σ_f) for whatever value of (L_f/d_b) obtained from the bond model is plotted in Figure 3-27. These results were also compared with those values calculated from the existing formulations of several codes by means of the following equations for given L_f/d_b and C/d_b:

$$\sigma_f = \frac{0.083\sqrt{f_c'}}{\alpha}\left(13.6\frac{L_f}{d_b}+\frac{C}{d_b}\frac{L_f}{d_b}+340\right) \quad \text{(ACI2006)} \tag{3-81}$$

$$\sigma_f = 1.25\sqrt{f_c'}\left(0.318\left(\frac{L_f}{d_b}\right)+0.795\left(\frac{C}{d_b}\right)\left(\frac{L_f}{d_b}\right)+13.3\right) \quad \text{(JSCE1997)} \tag{3-82}$$

$$\sigma_f = 54\left(\frac{f_c'}{25}\right)^{0.25}\left(\frac{25}{d_b}\right)^{0.20}\left(\frac{L_f}{d_b}\right)^{0.55}\left(\frac{C}{d_b}\right)^{0.33}\left(\frac{C_{\max}}{C}\right)^{0.1} \quad \text{(CEB– FIB Model Code 2010)} \tag{3-83}$$

$$\sigma_f = 1.13\sqrt{f_c'}\cdot\frac{1}{k_1k_4}\left(\frac{L_f}{d_b}\right)\left(\frac{C}{d_b}\right) \quad \text{(CSA 2000)} \tag{3-84}$$

where α is modification factor which considered as 1.0 for test specimen's condition. The parameter C indicates the value of concrete cover thickness in millimeters. The compressive strength (f_c') of SFRSCC reported in Table 3-3. The parameter $C_{\max}$ is the maximum horizontal distance from the bar to concrete surface which equals to 69 mm for position of the GFRP bars in the cross-section of the experimental pullout. The parameters k_1 and k_4 in Equation presented by CSA 2000 are bar location and bar surface factors, respectively. The former equals to 1.0 for the installation of the GFRP bars in the test specimens and the

later is the ratio between the bond strength of FRP bars to that steel bars with the same diameter, but not greater than 1.0. Here, the parameter k_4 is also considered as 1.0. The equation given by the CEB-FIB Model Code 2010 is originally used for steel bars; however, this equation is also recommended for FRP bars as internal reinforcement for concrete (*fib* Bulletin 40 2007). Note that the confinement effect provided by the transverse reinforcement was neglected in the above equations since no stirrup was applied to the test specimens, in spite of using SFRSCC. In general, the recommendations included in ACI, JSCE, CEB-FIB and CSA do not predict the experiments, particularly for the case of the lower concrete cover ($C/d_b = 1.25$). From the obtained results, it can be concluded that these formulations might not be straightforwardly considered for the types of GFRP bar and SFRSCC, which were used in this present work.

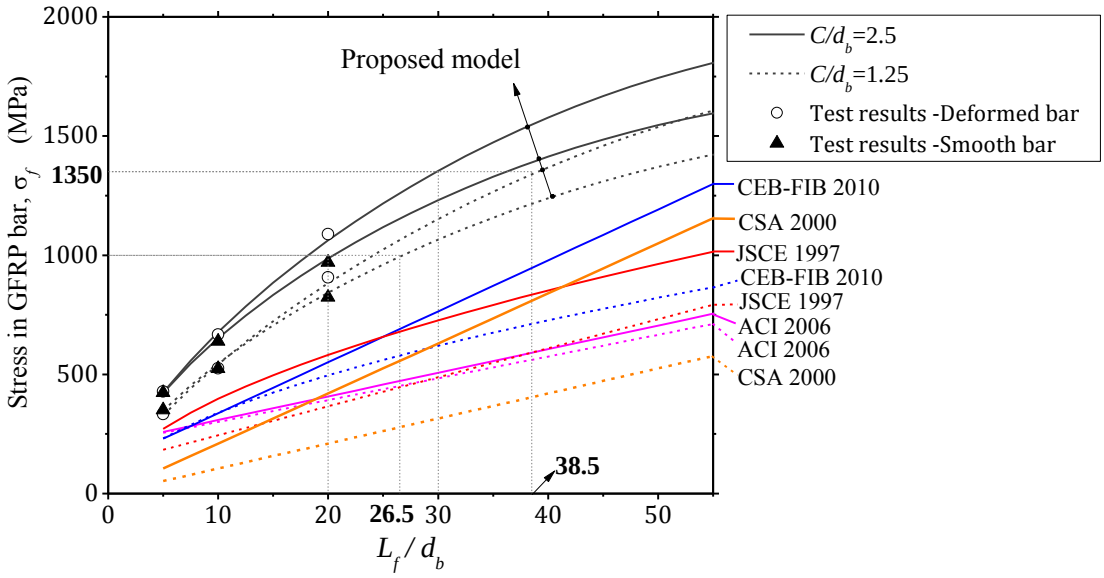

Figure 3-27: The tensile stress of GFRP bars *versus* the variation of ratio between its bond length and bar diameter

Based on the obtained results, for deformed GFRP bar, the minimum bond lengths required to reach the σ_{fu} (1350 MPa reported by supplier) are around $38.5\,d_b$ and $30\,d_b$ for $C/d_b = 1.25$ and $C/d_b = 2.5$, respectively. These values for smooth GFRP bar (with σ_{fu} of around 1000 MPa specified by the supplier) are $26.5\,d_b$ and $20\,d_b$. Note that the maximum

tensile stress obtained in the test for smooth bar were close to 1000 MPa in case of $20d_b$ bond length and 30 mm SFRSCC cover; however, no rupture was reported in the bar. That means σ_{fu} would be greater than the value reported by the manufacturer.

3.5 Summary and conclusions

The bond performance between two types of GFRP bars and steel fiber reinforced self-compacting concrete (SFRSCC) was investigated by performing thirty-six pullout bending tests. The influence of bar diameter (8 mm and 12 mm) and surface configuration (ribbed *versus* sand-coated), concrete cover thickness (15 mm and 30 mm), and bar embedment length (5Ø, 10Ø and 20Ø, where Ø is the bar diameter) on the bond performance was investigated. From the obtained experimental results the following main remarks can be pointed out:

- In general the specimens failed by debonding, indicating that the bond length to attain the ultimate tensile strength of the bars is higher than 20Ø for the two types of GFRP bars when embedded in the adopted SFRSCC;
- For the specimens with a concrete cover of 15mm, mainly in those of higher bar diameter, a single crack was formed in the alignment of the bars, which had a detrimental effect on the bond performance of these specimens. However, splitting failure never occurred because fiber reinforcement mechanisms avoided the degeneration of micro into macro-cracks;
- By observing the surface of the bars after the experimental tests it was concluded that the bond failure was, in general controlled by the shear resistance of GFRP surface layers. However, in the type A bar of specimens where a single splitting crack was formed, a mixed damage configuration in the bar was observed, with scratched ribs on the top surface of the bar and inclusions of cement paste in between the GFRP ribs at the bottom part of the bar. This type of failure mode was more prone in the bars of higher flexural stiffness surrounded by smaller concrete cover thickness;

- By increasing the bar diameter and the bond length, the maximum pullout force become limited by the SFRSCC splitting strength, which increased with the concrete cover thickness. The concrete cover had, in fact, an important role on the bond behavior of GFRP-SFRSCC, since the maximum average bond shear stress for both types of GFRP bars (smooth and ribbed surface) increased with the SFRSCC cover;
- By increasing the concrete cover the post-peak pullout force increased, and consequently the average residual bond stress as well, which contributes for a better bond behavior by reducing crack width and crack spacing. The higher pullout force in the post-peak phase evidenced by the type A bar can also be a consequence of the higher frictional resistance provided by the ribbed surface characteristics of this type of bar;
- Type A bar had a higher bond stiffness and peak pullout force than type B bar, which is not only a consequence of the surface characteristics of these bars, but also the larger stiffness of the type A bar.

Additionally, a theoretical bond model was developed to calibrate the parameters which define a multi-linear bond shear stress–slip relationship ($\tau - \delta$) able to estimate the bond behavior between SFRSCC and GFRP. The model involved data from the experimental tests, and using an analytical-numerical algorithm to solve the governing equation on bond phenomenon of the longitudinal bars. The proposed algorithm showed good accuracy comparing with the experimental result of bending pullout tests obtaining the distribution of the bond shear stress and slip over the bond transfer length. Due to the complexity of taking concrete deformation in the second-order differential equations, the relative slip (δ) was assumed to be equal to bar's elongation resulting that the local $\tau - \delta$ is dependent on the bond length. When the bond length is increased, the pullout force and consequently the force transferred to the surrounding concrete increases and lead to increase the amount of concrete damages over the interface which is normally formed as some inclined cracks over the embedded bar to concrete. A "material" *versus* "structural" bond-slip property was

introduced. A local bond-slip law is a material property only when it is derived from pullout tests where the deformation and damage of the concrete surrounding the embedment FRP bar is marginal compared to the deformation of the FRP bar. This law can be used as the slip component of the constitutive law of an interface finite element, and a robust and reliable model should be adopted for modeling the behavior of the surrounding concrete up to its collapse. In the remaining cases the bond-slip relationship is a structural property.

The bond strength, which was theoretically obtained from the proposed model, was utilized to determine the development length of the GFRP bars at the ultimate limit state failed by tensile rupture in the bar. The values obtained by the model for the types of GFRP bars and concrete considered in this study showed a large discrepancy with the values recommended by the guideline of ACI committee 440 (American Concrete Institute ACI 2006), Japan Society of Civil Engineers (JSCE, 1997), CEB-FIB Model Code 2010 and Canadian Standards Association (CSA, 2000). That means, the recommendations by these guidelines may not be straightforwardly used for the reinforcing system adopted in this study.

Notations

A_f	area of the embedded bar cross section	E_f	Young's modulus of embedded bar
$A_{F-\delta}^{\exp}$	area under the experimental curve of $F-\delta$	f_{cmr}	the reference compressive strength
$A_{F-\delta}^{Model}$	area under the theoretical curve of $F-\delta$	f_{cmi}	the average compressive strength of the i^{th} concrete batch
A_s	constant in the expression of the softening phase transfer length	f_c'	the compressive strength of concrete
B_s	constant in the expression of the softening phase transfer length	F	value of pullout force transferred by bond length
b_1	first constant value of fitting equation expressed $\tau_m - L_f$ relationship	F_2	value of pullout force transferred by elastic and plastic bond phases over the bond length
b_2	second constant value of fitting equation expressed $\tau_m - L_f$ relationship	F_3	value of pullout force transferred by elastic and plastic and softening bond phases over the bond length
C	concrete cover thickness from the bottom surface	F_1^e	maximum value of force transferred in the elastic phase in case of infinite bond length
$C_{\max}$	maximum concrete cover thickness from the concrete surface	F^e	value of force transferred in the elastic phase in case of infinite bond length
C_s	constant in the expression of the softening friction transfer length	F^f	value of force transferred in the friction phase in case of infinite bond length
C_1^e	first integration constant for the elastic phase	$F_{\max}$	value of the maximum pullout force transferred by prescribed bond length (L_f)
C_2^e	second integration constant for the elastic phase	F_2^P	maximum value of force transferred in the plastic phase in case of infinite bond length
C_3^e	constant value for the elastic phase	F^P	value of force transferred in the plastic phase in case of infinite bond length
C_1^f	constant value for the friction phase	F_3^s	maximum value of force transferred in the softening phase for the infinite bond length
C_2^f	first integration constant for the friction phase	F^s	value of force transferred in the softening phase in case of infinite bond length
C_3^f	second integration constant for the friction phase	F_{res}	residual pullout force by residual bond shear stress over bond length (L_f)
C_1^p	constant value for the plastic phase	J	constant in the governing differential equation with unknown $\delta(x)$
C_2^p	first integration constant for the plastic phase	k_1	bar location factor in Eq. (3-84)
C_3^p	second integration constant for the plastic phase	k_4	bar surface factor in Eq. (3-84)
C_1^s	first integration constant for the softening phase	l_{fr}	length of steel fibers
C_2^s	second integration constant for the softening phase	L_e	embedment length of reinforcing bar
C_3^s	constant value for the softening phase	L_f	available finite bond length
d_b	diameter of embedded bar	L_{tr1}	maximum invariant value of transfer length that can undergo elastic phase
e	error between experimental and theoretical pullout force-slip curves	L_{tr2}	maximum invariant value of transfer length that can undergo plastic phase

Notations

L_{tr3}	maximum invariant value of transfer length that can undergo softening phase	δ_1	first value of slip corresponding to peak of local bond stress-slip relationship
L_{tr}	transferred bond length corresponding to whatever value of the imposed slip	δ_2	second value of slip corresponding to peak of local bond stress-slip relationship
L_{tr}^{e}	transferred bond length undergoing elastic phase	δ_3	slip corresponding to the start of frictional bond phase in bond stress-slip relationship
L_{tr}^{f}	transferred bond length undergoing friction phase	δ_F	free end slip computed at free loaded end
L_{tr}^{s}	transferred bond length undergoing softening phase	δ_m	slip experimentally recorded at the loaded end corresponding to F_{max}
L_{tr}^{p}	transferred bond length undergoing plastic phase	δ_L	imposed slip at the loaded extremity of the bar
s_{fp}	slip at free loaded end slip corresponding to maximum pullout force	ε_f	tensile strain of reinforcing bar
s_{lp}	slip at loaded end corresponding to maximum pullout force	λ	constant entering the governing differential equation for elastic phase
s_f	Slip at free loaded end	σ_f	tensile stress of embedded bar
s_l	Slip at loaded end slip	$\tau(\delta)$	local bond shear stress-slip relationship
s_{LVDT1}	The values of slip recorded by LVDT1	τ_R	residual bond shear stress at the friction phase of local bond
α	modification factor for recommended equation from ACI	$\bar{\tau}_{\max}$	maximum average bond stress of embedded bar
β	constant entering the governing differential equation for the softening phase	$\tau(x)$	bond shear stress distribution over L_{tr}
γ_i	factor to normalized the experimental value of average maximum bond shear stress	τ_0	chemical initial bond stress of GFRP-SFRSCC
ϕ	indication for embedded bar's diameter in the pullout bending test	τ_m	peak stress of the local bond stress-slip relationship
ϕ_{fr}	diameter of steel fibers	$\bar{\tau}_{res}$	residual average bond stress of embedded bar
δ	relative slip between reinforcing bar and surrounded concrete along the bond length	ψ	angle necessary to determine the softening subject amount of transfer length

Chapter 4

4 TENSION-STIFFENING OF FRC REINFORCED WITH HYBRID FRP/STEEL BARS

4.1 Introduction

From the previous chapter it became clear that the interaction between Fiber Reinforced Concrete (FRC), Fiber Reinforced Polymer (FRP) and steel bars should be accounted for a reliable prediction of the behavior of hybrid FRC members. For this purpose, a FRC member reinforced with FRP and steel bars (hybrid reinforcement) was subjected to uniaxial tension, and its cracking and tension stiffening behavior was theoretically studied by developing a tension-stiffening model for Fiber Reinforced Concrete (FRC) containing both FRP and steel bars. The model was developed through an explicit analytical bond formulation based on the bond model developed in the previous chapter that was also adopted in this chapter for both steel and FRP bars. The adopted multi-linear constitutive law in the tension-stiffening model was similar to the bond-slip previously used in the bond model in Chapter 3. However, a "*hardening*" bond phase was also considered in addition to the elastic phase, prior to reach the plastic phase. In fact, two linear phases were adopted in the bond-slip law (elastic and hardening bond phases) in order to increase the predictive capability of the bond model to simulate efficient range of slipping for reinforcing bars in FRC applications. The proposed tension-stiffening model was capable of simulating both the fiber reinforcement contribution and the yielding stage of steel bar at cracked section.

Additionally, a FE Modeling was carried out using a multi-directional fixed smeared crack approach for modeling cracking process in FRC, and adopting interface finite elements to simulate the bond behavior between reinforcements and FRC, whose constitutive model was defined from the aforementioned bond law.

Finally, an extensive parametric study was performed by using the analytical model, and the influence of the involved parameters on the tension-stiffening and cracking behavior of hybrid FRP/steel FRC tensile member was investigated.

4.2 Tension-stiffening model

A FRC member is considered to be reinforced with a constant reinforcement ratio of FRP and steel bars along its longitudinal axis, which is subjected to uniaxial tension load in order to analyze the tension-stiffening effect and its cracking behavior. To prevent bending effects in the member, symmetric arrangement of the reinforcements is assumed in the FRC cross-section.

4.2.1 Crack formation stage

When the load is applied to the member, it is transmitted to the FRC throughout a part of embedded length of reinforcing bar in which the total bond shear force over this distance is in static balance with the applied load. This part of embedded length can be named as transferred bond length (L_{tr}), which depends on the bond mechanism between the reinforcing bars and surrounding FRC. The part of the member beyond the L_{tr} behaves as a real composite element ("tie region" in Figure 4-1), where the slip (δ) between the bars and surrounding FRC is null and the total applied force is shared between them in accordance with their axial stiffness. Since the total applied load is transferred throughout two different L_{tr} that belong to FRP and steel bars, the higher value is adopted to calculate the tie region.

As long as the FRC tensile stress in the tie region is less than its tensile strength, f_{ct}, the member remains un-cracked. At this stage, the fibers are almost inactive. Once f_{ct} is reached in the tie region, a crack is formed over the weakest section (it is assumed that this section

is L_{cr} from the specimen's extremity, see Figure 4-1). At this cracked section, the tensile stress of concrete matrix tends to drop to zero with the crack opening, while the tensile stresses in the bars and discrete fibers, which are now active, tend to increase. By increasing the tensile stresses in the reinforcements, the reinforcing bars and fibers start slipping out from the surrounding concrete matrix, leading to an increase of the crack width. The total force is redistributed to the concrete, and if once again the tensile strength is reached, a second crack is formed. At this stage, the force transferred by fibers at the first cracked section also contributes to the formation of the second crack. This process, which named "crack formation stage" (CEB-FIB Model Code 2010), continues until all cracks are formed along the member and no tie region exists anymore.

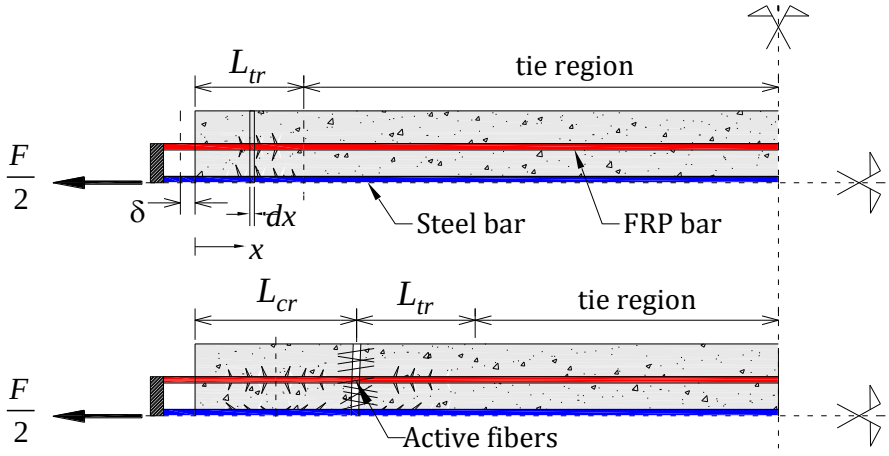

Figure 4-1: The transferred bond length and tie region in the primary crack formation stage of FRC tensile member reinforced by hybrid FRP-steel bars

4.2.2 Bond formulation and bond-slip law of the reinforcing bars

An infinitesimal length *dx* of the tensile member at a distance *x* (see Figure 4-1) is shown in Figure 4-2. The equilibrium of this element can be expressed by

$$\frac{d\sigma_s(x)}{dx} = \frac{P_s}{A_s}\tau_s(x) \tag{4-1}$$

$$\frac{d\sigma_F(x)}{dx} = \frac{P_F}{A_F}\tau_F(x) \tag{4-2}$$

$$\left(\frac{d\sigma_c(x)}{dx} + \frac{d\sigma_{cf}(x)}{dx}\right) = -\left(\frac{P_F}{A_c}\tau_F(x) + \frac{P_s}{A_c}\tau_s(x)\right) \tag{4-3}$$

and also

$$\left(\sigma_c(x)+\sigma_{cf}(x)\right)A_c+\sigma_F(x)A_F+\sigma_s(x)A_s=F \tag{4-4}$$

where σ_{cf} is the local tensile stress of concrete due to the force transferred to the concrete matrix by the steel fibers at cracked section in the member. The parameters σ_c, σ_s and σ_F are the tensile stress of concrete matrix, steel bar and FRP bar, respectively. Hereafter, subscript "*s*" is used to designate parameters for steel bar, while "*F*" is for FRP bar. The perimeter of the steel and FRP bars is designated by P_s and P_F, respectively, while the cross sectional area of these bars is A_s and A_F. The concrete axial stiffness becomes E_cA_c.

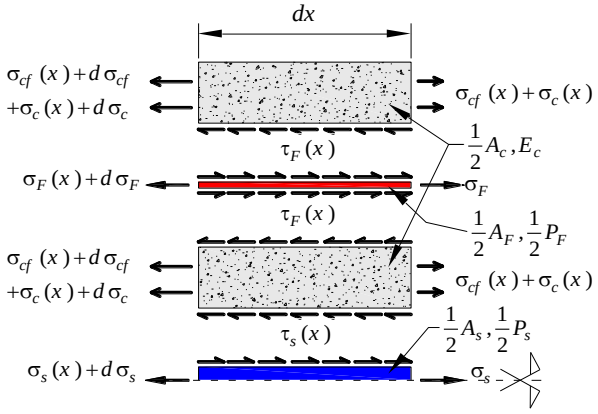

Figure 4-2: Infinitesimal *dx* of the FRC tensile member reinforced by steel and FRP bars (only half part is represented)

The slip (δ) between the reinforcements and FRC is defined by the following equations for steel and FRP bar, respectively.

$$\delta_s(x)=u_s(x)-u_c(x)\Rightarrow\frac{d\delta_s(x)}{dx}=\varepsilon_s(x)-\varepsilon_c(x)\Rightarrow\frac{d^2\delta_s(x)}{dx^2}=\frac{d\varepsilon_s(x)}{dx}-\frac{d\varepsilon_c(x)}{dx} \tag{4-5}$$

$$\delta_F(x)=u_F(x)-u_c(x)\Rightarrow\frac{d\delta_F(x)}{dx}=\varepsilon_F(x)-\varepsilon_c(x)\Rightarrow\frac{d^2\delta_F(x)}{dx^2}=\frac{d\varepsilon_F(x)}{dx}-\frac{d\varepsilon_c(x)}{dx} \tag{4-6}$$

where u and ε represent elongation and strain, respectively. By substituting Eqs. (4-1) and (4-3) into Eq. (4-5), and also Eq. (4-2) and (4-3) into Eq. (4-6) yield the following set of nonlinear differential equations governing the bond problem of the member:

$$\begin{cases}\dfrac{d^2\delta_s(x)}{dx^2}=\dfrac{P_s}{E_sA_s}(1+n_s\rho_s)\tau_s(x)+\dfrac{P_F}{E_cA_c}\tau_F(x)+\dfrac{1}{E_c}\dfrac{d\sigma_{cf}}{dx}\\ \dfrac{d^2\delta_F(x)}{dx^2}=\dfrac{P_F}{E_FA_F}(1+n_F\rho_F)\tau_F(x)+\dfrac{P_s}{E_cA_c}\tau_s(x)+\dfrac{1}{E_c}\dfrac{d\sigma_{cf}}{dx}\end{cases} \tag{4-7}$$

where n is the modular ratio ($n_s=E_s/E_c$, $n_F=E_F/E_c$), and ρ is the reinforcement ratio,

being $\rho_s = A_s / A_c$ and $\rho_F = A_F / A_c$. It should be noticed that the materials are assumed to follow the Hook's constitutive law. Moreover, in the equilibrium conditions expressed in Eqs. (4-1) to (4-3), the resisting tensile stress due to the concrete softening at cracked section is neglected since this value drops asymptotically to zero for a very small slip of the reinforcements.

To simplify the complexity of solving the set of second-order nonlinear differential equations presented in Eqs. (4-7), the elastic deformation of surrounding concrete matrix is neglected against the reinforcement's deformation at the interface ($u_s >> u_c$ and $u_F >> u_c$). By this assumption, Eqs. (4-5) and (4-6) become

$$\frac{d^2\delta_s(x)}{dx^2} = \frac{d\varepsilon_s(x)}{dx}, \qquad \frac{d^2\delta_F(x)}{dx^2} = \frac{d\varepsilon_F(x)}{dx} \tag{4-8}$$

Hence, Eq. (4-7) is derived as

$$\begin{cases} \dfrac{d^2\delta_s(x)}{dx^2} = J_s \tau_s(x) \\ \dfrac{d^2\delta_F(x)}{dx^2} = J_F \tau_F(x) \end{cases} \tag{4-9}$$

where

$$\begin{cases} J_s = \dfrac{P_s}{E_s A_s}(1 + n_s \rho_s) \\ J_F = \dfrac{P_F}{E_F A_F}(1 + n_F \rho_F) \end{cases} \tag{4-10}$$

Depending on the bond-slip relationship between reinforcing bar and concrete, Eqs. (4-9) can be solved explicitly or by using a numerical procedure (Bianco *et al.* 2009). There are several bond-slip constitutive laws in the literature that have been proposed for FRP reinforcing bars, namely Malvar Model (Malvar 1995), mBEP Model, CMR Model (Cosenza *et al.* 1997), the model proposed by CEB-FIB Model Code 2010, and *etc*. In all these models, nonlinear formula has been adopted for the first branch of the constitutive law. Thus, by substituting any of these models in Eq. (4-9), it does not lead to an explicit solution. Then, numerical procedure is required to solve the equation. From this standpoint, a multilinear bond-slip diagram, consisting of two linear ascending branches prior to the peak bond shear stress, is adopted in the present study to solve Eq. (4-9) for both steel and FRP

bars. This multi-linear bond-slip diagram is shown in Figure 4-3a, and is mathematically represented by the following equation:

$$\tau(\delta)=\begin{cases}\tau_0+\dfrac{\tau_1-\tau_0}{\delta_1}\cdot\delta & 0\le\delta\le\delta_1\\ \tau_1+\dfrac{\tau_m-\tau_1}{\delta_2-\delta_1}\cdot(\delta-\delta_1) & \delta_1<\delta\le\delta_2\\ \tau_m & \delta_2<\delta\le\delta_3\\ \tau_m-\dfrac{\tau_m-\tau_R}{\delta_4-\delta_3}\cdot(\delta-\delta_3) & \delta_3<\delta\le\delta_4\\ \tau_R & \delta>\delta_4\end{cases} \tag{4-11}$$

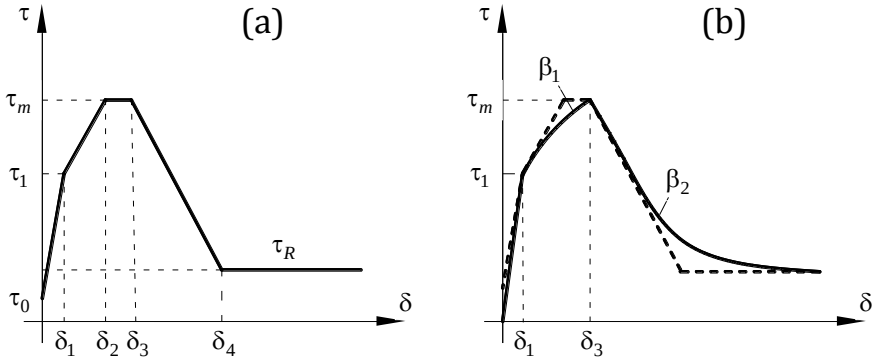

Figure 4-3: Local bond-slip constitutive laws for steel and FRP bars: (a) adopted for the proposed analytical model and (b) used in FE model

4.2.3 Contribution of discrete fibers

Once the crack formed, the fibers start pulling out from the crack plane with increase in crack width. In order to calculate the force transferred by these discrete fibers at the cracked plane, two methods can be used according to the data available for modeling the fiber reinforcement contribution. If the fiber bond-slip behavior is known, the following equations represent the bond problem formulation of each fiber at cracked plane:

$$\begin{cases}\dfrac{d^2\delta_{fr}}{dx_{fr}^{\,2}}=\dfrac{P_{fr}}{E_{fr}A_{fr}}\tau_{fr}(\delta_{fr})\\ \varepsilon_{fr}=\dfrac{d\,\delta_{fr}}{dx_{fr}}\end{cases} \tag{4-12}$$

where the subscript "*fr*" designates the parameters for discrete fibers with the same concepts as defined previously for reinforcing bars. The local reference of x_{fr} origins at the extremity of the effective bond length of a fiber crossed by the cracked plane (see Figure 4-4a).

According to the literature, this fiber effective bond length is statistically considered 0.25 of total length (Wang 1989, Cunha 2010), leading to pulled out of fiber at one side of the cracked plane ($\delta_{fr} = w_{cr}$), therefore, Eq. (4-12) can be solved by the following boundary conditions

$$\begin{cases} \dfrac{d\,\delta_{fr}}{dx}\left(x_{fr}=0\right)=\varepsilon_{fr}\left(x_{fr}=0\right)=0 \\ \delta_{fr}\left(x_{fr}=0.25l_{fr}\right)=w_{cr} \end{cases} \tag{4-13}$$

where l_{fr} is the fiber length and w_{cr} is the crack width. Based on what bond-slip constitutive law is adopted for fiber, Eq. (4-12) can have an explicit solution, or a numerical procedure is required (e.g. Runge-Kutta-Nystrom method (Krayszing 1993). Cunha *et al.* (2010) presented different bond-slip constitutive laws for steel fibers depending on the angle between fibers and crack plane they are crossing, as well as the type of steel fibers. Therefore, by adopting a proper bond-slip law, the pullout force of steel fibers can be calculated using the analytical model proposed by these authors. Lee *et al.* (2011) developed a model named "*Diverse Embedment Model* (*DEM*)" to calculate the tensile behavior of FRC by considering the pullout characteristics of fibers, as well as the effective orientation of fibers in regards to the crack plane. Abrishambaf *et al.* (2013) also compared different post-cracking response of steel fiber Reinforced Self-Compacting Concrete (SFRSCC) by taking into account fiber's orientation towards the crack plane. Once the pullout force of each fiber is calculated, the total force of fibers can be determined by considering an average number of fibers at cracked section in accordance with their volume fraction in concrete mix.

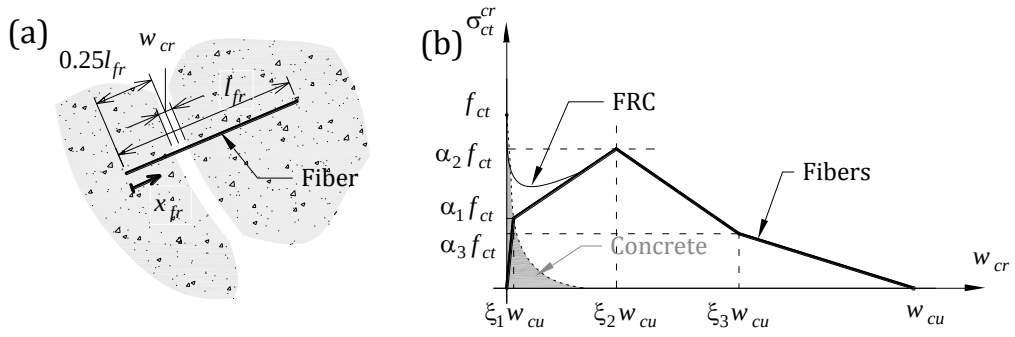

Figure 4-4: Contribution of discrete fibers over a cracked plane: (a) Bond mechanism of each fiber with concrete matrix, and (b) FRC post-cracking response

On the other hand, if the uniaxial behavior of FRC in tension is known, the contribution of fibers may be measured alternatively by subtracting the tension softening diagram of concrete from the post-cracking diagram of FRC. The tension softening diagram of concrete can be estimated according to the CEB-FIB Model Code 2010 or from available experimental data, by considering the effective length equal to distance between two cracks. This concept is shown in Figure 4-4b. In the present study, the contribution of fibers is calculated based on the average post-cracking response of FRC, which can be obtained by performing uniaxial tensile tests or from inverse analysis considering the results recorded in three point notched beam bending tests (Pereira *et al.* 2012, Barros and Sena Cruz 2001). Therefore, the total force transferred to the concrete matrix by fibers is calculated by

$$(V_c)_{fr} = \sigma_{ct}^{cr}(w_{cr}) \cdot A_c \tag{4-14}$$

where σ_{ct}^{cr} is the concrete crack tensile stress as function of crack width, w_{cr} .

4.2.4 Bond boundary conditions and solutions for reinforcing bars

Bond mechanism of a reinforcing bar crossing by two consecutive cracks can be analyzed solving Eq. (4-9) using boundary condition as follow:

$$\begin{cases} x = 0, & \delta_r = 0 \\ x = L_b, & \delta_r = \delta_{cr} \end{cases} \tag{4-15}$$

where x origins from the midway section between two consecutive cracks, L_b is the bond length that is equal to $L_{cr}/2$ being L_{cr} the distance between two cracks, and δ_{cr} is the slip at crack section. Based on Eqs. (4-5) and (4-6), the strain of reinforcing bars at the midway section is equal to the derivation of the slip at this point (*i.e.* $\varepsilon_r^m = d\delta(x=0)/dx$). The total force that is transferred to the concrete matrix by the reinforcing bars is calculated using the difference of the tensile strain of reinforcing bars at cracked section ($\varepsilon_r^{cr} = d\delta(x=L_b)/dx$) and at midway section, multiplying by the reinforcing bar's axial stiffness:

$$(V_c)_r = E_r A_r (\varepsilon_r^{cr} - \varepsilon_r^m) \tag{4-16}$$

where $(V_c)_r$ is the total force transferred to the surrounding concrete matrix due to the bond action of reinforcing bars. Note that the subscript "r" represents parameters for both

reinforcing bars, FRP and steel bars.

During the "*crack formation stage"*, where the tie region exists in the member, bond mechanism at one side of the last formed crack (designated by letter "R" meaning right side) undergoes "*Infinite Bond Length*" (IBL) boundary conditions (see Figure 4-5). IBL represents a bond boundary condition where the L_{tr} increases with the pullout force in which the slip and its derivative at the extremity of L_{tr} are always null (*i.e.* $\delta(x_R = 0) = 0$, $d\delta(x_R = 0)/dx_R = 0$).

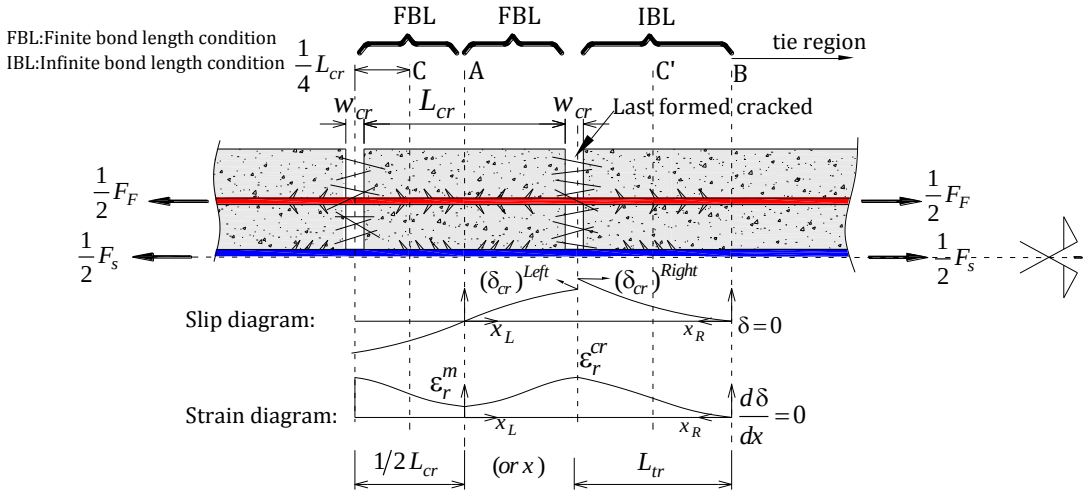

Figure 4-5: Bond mechanism of reinforcing bars in the cracked FRC tensile member

On the other hand, another side of the last formed crack (designated by letter "L" meaning left side) undergoes "*Finite Bond Length*" (FBL) boundary conditions. FBL represents bond boundary condition where the transferred bond length (L_{tr}) equals to a finite bond length (for case of this study $L_b = L_{cr}/2$) and slip at the extremity of this bond length is null, while its derivative is not null (*i.e.* $\delta(x_L = 0) = 0$, $d\delta(x_L = 0)/dx_L \neq 0$). Under this consideration, at the last formed cracked plane two bond conditions govern the bond formulation, where the slips on left and right sides of this crack are not necessarily equal (Figure 4-5), and, therefore, Eqs. (4-9) is solved by using the following boundary conditions:

$$FBL\begin{cases}\delta(x_L = 0) = 0\\ \delta(x_L = L_b) = (\delta_{cr})^{Left}\end{cases} \qquad IBL\begin{cases}\delta(x_R = 0) = 0\\ \delta(x_R = L_{tr}) = (\delta_{cr})^{Right}\end{cases} \tag{4-17}$$

where x_R has its origin at section *B*, and x_L at section A. The slip at left $(\delta_{cr})^{Left}$ and right

side $(\delta_{cr})^{Right}$ of the last formed crack is not necessarily equal, but due to the compatibility of strain at this section, the derivatives of the slip at right and left are equal to the reinforcing bar's strain, ε_r^{cr} by

$$\varepsilon_r^{cr} = (\frac{d\delta}{dx_R})_{Right} = (\frac{d\delta}{dx_L})_{Left} \quad (4\text{-}18)$$

By solving the governing equation using FBL and IBL boundary conditions, for whatever value of δ_{cr}, slip distribution, $\delta(x)$, reinforcing bar's tensile strain, $\varepsilon_r(x)$, and bond shear stress, $\tau(x)$, as well as the force transferred to concrete by the bond action, $(V_c(x))_r$, are calculated throughout crack spacing (L_{cr}), as will be explained in the following sections.

The formulations for IBL conditions and its solving procedures are described in detail in Chapter 3 for the adopted four-linear bond-slip law (Figure 3-13). However, in Annex 4A, the solving formulation derived for the new "*hardening*" phase is briefly explained. The formulation for FBL conditions is summarized hereafter. Note that the FBL condition described in the previous chapter was with different boundary conditions that only explain the free pullout process of a reinforcing bar (allowing free end slip).

According to the adopted bond-slip law, see Figure 4-3a, five different bond phases are considered during debonding progress, namely:

1) *Elastic phase* (*e*): $\delta_{cr} \le \delta_1$;
2) *Hardening phase (h)*: $\delta_1 < \delta_{cr} \le \delta_2$;
3) *Plastic phase* (*p*): $\delta_2 < \delta_{cr} \le \delta_3$;
4) *Softening phase* (*so*): $\delta_3 < \delta_{cr} \le \delta_4$;
5) *Frictional phase* (*f*): $\delta_{cr} > \delta_4$.

Based on these five bond-slip phases, substituting Eq. (4-11) into Eq. (4-9), and taking FBL boundary conditions indicated in Eq. (4-17) the closed-form solution of Eq. (4-9) for each reinforcing bar can be expressed by

$$\delta(x)=\begin{cases}\delta(x_e)=C_1e^{\lambda_1 x_e}+C_2e^{-\lambda_1 x_e}-C_e; & 0\le x_e\le L_{tr}^e\\ \delta(x_h)=C_3e^{\lambda_2 x_h}+C_4e^{-\lambda_2 x_h}-C_h+\delta_2; & 0\le x_h\le L_{tr}^h\\ \delta(x_p)=C_p{x_p}^2+C_5x_p+\mathrm{C}_6; & 0\le x_p\le L_{tr}^p\\ \delta(x_{so})=C_7\sin(\gamma x_{so})+C_8\cos(\gamma x_{so})+C_{so}+\delta_3; & 0\le x_{so}\le L_{tr}^{so}\\ \delta(x_f)=\mathrm{C}_f\,{x_f}^2+\mathrm{C}_9x_f+\mathrm{C}_{10}; & 0\le x_f\le L_{tr}^f\end{cases} \quad (4\text{-}19)$$

where the definition of x_e, x_h, x_p, x_{so}, x_f, L_{tr}^e, L_{tr}^h, L_{tr}^p, L_{tr}^{so}, and L_{tr}^f can be found in Annex 4B, as well as how the slip solutions of C_e, C_h, C_p, C_{so} and C_f are determined. Note that these solutions are obtained for whatever value of δ_{cr} and the transferred bond length of each bond phases (*i.e.* L_{tr}^e, L_{tr}^h, L_{tr}^p, L_{tr}^{so}, and L_{tr}^f).

By considering the compatibility conditions of the strain at the connection point of two consecutive bond phases (found in Annex 4B), as well as the following conditions of the bond length ($L_b=\frac{1}{2}L_{cr}$) with respect to the different stages of δ_{cr}, the values of L_{tr}^e, L_{tr}^h, L_{tr}^p, L_{tr}^{so} and L_{tr}^f are calculated for whatever value of δ_{cr}. Therefore, by imposing δ_{cr}, theses transferred bond lengths and the slip solutions are found.

- Stage 1 ($0<\delta_{cr}\le\delta_1$): the total bond length undergoes only the elastic bond phase, *i.e.* $L_b=L_{tr}^e$;
- Stage 2 ($\delta_1<\delta_{cr}\le\delta_2$): the total bond length undergoes the elastic and hardening bond phases, *i.e.* $L_b=L_{tr}^e+L_{tr}^h$;
- Stage 3 ($\delta_2<\delta_{cr}\le\delta_3$): the total bond length undergoes elastic, hardening and plastic bond phases, *i.e.* $L_b=L_{tr}^e+L_{tr}^h+L_{tr}^p$;
- Stage 4 ($\delta_3<\delta_{cr}\le\delta_4$): the total bond length undergoes elastic, hardening, plastic and softening bond phases, *i.e.* $L_b=L_{tr}^e+L_{tr}^h+L_{tr}^p+L_{tr}^{so}$;
- Stage 5 ($\delta_{cr}>\delta_4$): the total bond length undergoes all the bond phases, *i.e.* $L_b=L_{tr}^e+L_{tr}^h+L_{tr}^p+L_{tr}^{so}+L_{tr}^f$.

If the compatibility conditions of the strain at the connection point of two consecutive bond phases (e.g. elastic-hardening or hardening-plastic) are considered, the values of L_{tr}^e,

L_{tr}^{h} , L_{tr}^{p} , L_{tr}^{so} and L_{tr}^{f} can be calculated for whatever value of δ_{cr} . The compatibility conditions of each solving stage are included in Annex 4B.

By imposing a value of δ_{cr} and using the above compatibility conditions, the transferred bond lengths, as well as the slip solutions (*i.e.* C_1 to C_{10}) are found. Once $\delta(x)$ is found, the distribution of tensile strain in the reinforcing bars and also the bond shear stress are given by

$$\begin{cases} \varepsilon_r(x) = E_r \dfrac{d\,\delta(x)}{dx} \\ \tau(x) = \dfrac{1}{J_r} \dfrac{d^2\delta(x)}{dx^2} \end{cases} \tag{4-20}$$

where J_r is defined in Eq. (4-10) for both FRP and steel bars, and E_r is the elasticity modulus of reinforcing bar. The solving procedure of Eq. (4-9) under FBL boundary conditions, and the respective formulations, as well as the flowchart of the FBL algorithm are given in detail in Annex 4B.

4.2.5 Secondary crack formation stage

Once all the cracks are formed at "*crack formation stage*", by increasing the slips at cracked sections, the tensile strains of reinforcement at crack, ε_r^{cr} , and midway section, ε_r^{m} , increase. Note that, at this stage no "tie region" exists in the member, and only FBL boundary conditions govern the bond formulation. The total value of the force transferred to the concrete matrix by the bond mechanism of the reinforcements (both reinforcing bars and fibers) is estimated by

$$(V_c)_t = (V_c)_r + (V_c)_{fr} \tag{4-21}$$

where $(V_c)_{fr}$ is the total force transferred to the concrete matrix by fibers, which is calculated by Eq. (4-14). In this equation, the value of crack opening, w_{cr}, is estimated as double value of reinforcing bar's slip at cracked section due to the symmetric bond action (Visintin 2012), which means:

$$w_{cr} = 2\delta_{cr} \tag{4-22}$$

If the value of $(V_c)_t$ reaches the concrete cracking force, $V_{cr} = f_{ct} \cdot A_c$, a new crack is

formed in the midway section between two consecutive cracks (e.g. section A in Figure 4-5). The bond length associated to this new crack is $L_{cr}/4$, and the symmetric section between two cracks is now changed from section A to C (see Figure 4-5). This stage can be named as "*secondary crack formation stage"*.

4.2.6 Updating bond-slip constitutive law during the analysis

The proposed local bond-slip constitutive law is valid while the slip is increasing. If the slip at a local point of interface tends to decrease, $\tau = \delta$ follows an "unloading" branch. If the slip at this point once again tends to increase, it follows a "reloading" branch. This unloading/reloading branch can be defined by a single linear branch of stiffness $K_{un/re}$ that depends on the maximum slip reached during the loading phase, which is named as δ_m in this study (see Figure 4-6a). If $0 < \delta_m \le \delta_1$, which means the slip is in the elastic bond phase, it is assumed that $K_{un/re}$ is calculated by $K_{un/re,e} = \tau(\delta_m)/\delta_m$ where $\tau(\delta_m)$ is the corresponding value of the bond shear stress at δ_m (see Figure 4-6a where $0 < \delta_m \le \delta_1$). For the cases where $\delta_m > \delta_1$, which means the slip is in the inelastic bond phase, $K_{un/re} = K_{un/re,in}$ is assumed to be equal to τ_1/δ_1 similar to the idealized unloading/reloading of inelastic materials discussed in the plasticity theory (Jones 2009) (see Figure 4-6a where $\delta_1 < \delta_m$). Therefore, the value of $K_{un/re}$ is given by the following equation:

$$K_{un/re}(\delta_m) = \begin{cases} \dfrac{\tau(\delta_m)}{\delta_m} & \delta_m < \delta_1 \\ \dfrac{\tau_1}{\delta_1} & \delta_m \ge \delta_1 \end{cases} \tag{4-23}$$

In fact, this unloading/reloading branch defines a permanent bond damage at the interface between the reinforcing bar and concrete. This damage is theoretically simulated by an irreversible slip, δ_{ir}, that remains in the interface when the applied load is totally removed (see Figure 4-6a). For RC member under direct tension, this unloading/reloading phase may occur when a new *crack formation stage* starts (e.g. "*secondary crack formation stage"*). Figure 4-6b compares the slip distribution at primary and secondary *crack formation stages*. As shown, by forming a new crack (*section B* in Figure 4-6b), slip at this new crack section

tends to increase, while it tends to decrease at the already existing cracks. In order to consider the effect of increasing/decreasing of the slip in the theoretical formulation, an updated bond-slip constitutive law is used at the beginning of each new *crack formation stage*. This updated bond-slip law can be calculated using an average value of slip (named as δ_m) at $x = L_{cr}/2$ from the previous *cracking stage*, where x has its origin from section C (see Figure 4-6b). Then the value of irreversible slip, δ_{ir}, is calculated by:

$$\begin{cases} \delta_{ir} = 0 & \delta_m \le \delta_1 \\ \delta_{ir} = \delta_m - \dfrac{\tau(\delta_m)}{K_{un/re}} & \delta_m > \delta_1 \end{cases} \tag{4-24}$$

Figure 4-6a shows all possible updated bond-slip law according to the value of δ_m.

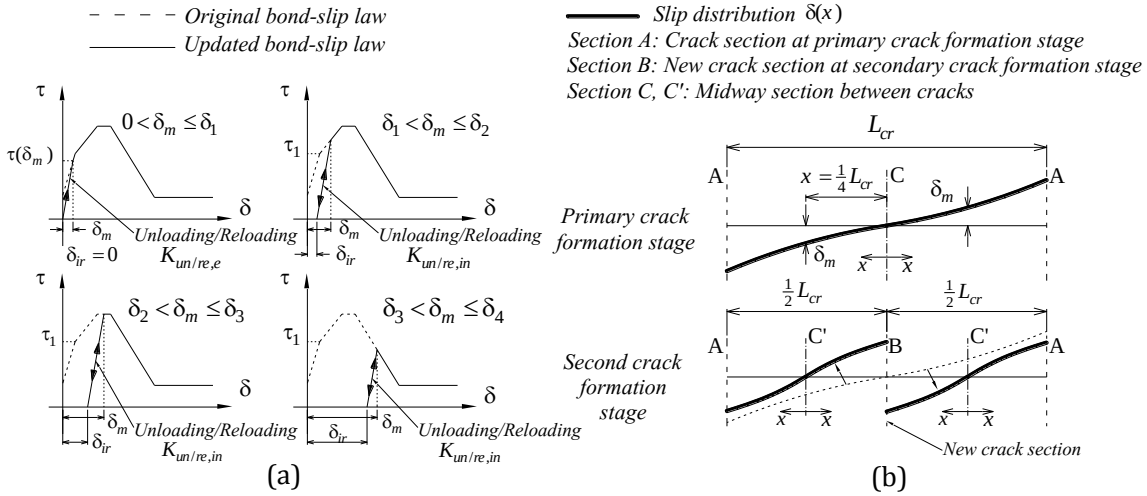

Figure 4-6: (a) Updating bond-slip constitutive law due to the unloading and reloading phase of slip and (b) Comparison between the slip distribution over the crack spacing at primary and secondary cracking stage

4.2.7 Effect of steel yielding strain on its bond behavior

The tensile strain of steel bar at cracked section (ε_s^{cr}) can exceed its yielding strain (ε_{sy}), even if the mean value of tensile strain of the member is still less than the yielding strain (Lee *et al.* 2013). This means that the steel bar is locally yielded at the cracked section. The yielding strain of steel bar affects its bond behavior (Ruiz *et al.* 2007). Hence, this effect should be considered in the formulation. For this purpose, the K_b factor proposed by Ruiz *et al.* (2007) is adopted in this study to modify the bond-slip law of steel bar after yielding:

$$\tau_s^{\mathrm{mod}}(\delta_s) = K_b \cdot \tau_s(\delta_s) \tag{4-25}$$

where

$$K_b = \begin{cases} 1 & \varepsilon_s^{cr} \le \varepsilon_{sy} \\ e^{10(\varepsilon_{sy} - \varepsilon_s^{cr})} & \varepsilon_s^{cr} > \varepsilon_{sy} \end{cases} \tag{4-26}$$

After yielding of steel bar, the force transferred to the concrete by steel, $(V_c)_s$, which was previously calculated by Eq. (4-16), is now given by

$$(V_c)_s = A_s(\sigma_{sy} - E_s \varepsilon_s^m) \qquad \varepsilon_s^{cr} > \varepsilon_{sy} \tag{4-27}$$

where σ_{sy} is the yielding stress of steel bar, and ε_s^m is the steel bar's strain at the midway section (see Figure 4-5), which is computed by FBL model (see Annex 4B) by considering the modified bond shear stress provided by Eq. (4-25).

4.2.8 Effect of pre-stress of reinforcing bars

Applying pre-stress on internal embedded reinforcing bars enhances the structural performance of RC beams at serviceability limit states (Soltanzadeh *et al.* 2014, Rezazadeh *et al.* 2014). The pre-stressing force in RC beams creates an initial compressive strain in the concrete tensile zones and a negative camber to RC beam, which delays concrete to reach its tensile strength (Rezazadeh *et al.* 2014). However, for uniaxial tensile member with a symmetric arrangement of reinforcements, pre-stress theoretically creates only an initial compressive strain that can be estimated from:

$$\varepsilon_c^{pre} = n_s \rho_s \varepsilon_s^{pre} + n_F \rho_F \varepsilon_F^{pre} \tag{4-28}$$

where ε_c^{pre} is the initial concrete compressive strain due to the pre-strain applied to steel (*i.e.* ε_s^{pre}) and FRP bars (*i.e.* ε_F^{pre}). The force due to the pre-stress of reinforcing bars is transferred to the member by the bond mechanism between reinforcing bars and surrounding FRC throughout the bond transferred length. The bond transferred length due to the pre-stress of reinforcing bars (*i.e.* L_{tr}^{pre}) can be calculated using IBL boundary conditions:

$$\begin{cases} \dfrac{d\delta}{dx} = 0 \; at \; x = 0 \\ \dfrac{d\delta}{dx} = \varepsilon_F^{pre} \; (or \; \varepsilon_s^{pre}) \; at \; x = L_{tr}^{pre} \end{cases} \tag{4-29}$$

where x origins from the extremity of the member where the pre-stress force is released. It should be noted that the RC system located beyond L_{tr}^{pre} behaves as a real composite similar to the "tie region", as previously explained. In the next chapter, Eq. (4-29) will be used to derive the bond-slip behavior of reinforcing bars used for hybrid reinforcing system (refer to Section 5.2.6 in Chapter 5).

4.2.9 Analysis procedure

The algorithm of the analysis procedure, which was described in the previous sections, is presented in Figure 4-7. At the beginning, the algorithm calculates the total applied force (*i.e.* F) by using IBL model for both FRP and steel bars until formation of the first crack (Module 1). When first crack is formed, the algorithm calculates the total applied force by taking the strain compatibility condition of reinforcing bars, which was presented in Eq. (4-18), at right (using IBL model) and left sides (using FBL model) of this crack, as well as the contribution of fibers (by using Eq. (4-14), where $w_{cr} = (\delta_{cr})^{Left} + (\delta_{cr})^{Right}$), (Module 2). If the value of F reaches the cracking force of the member (V_{cr}), the next crack is formed. The algorithm repeats the calculation process at the location of this new crack, which is now the last formed crack. This process continues until the bond progress of the reinforcing bars reaches the extremity of the member, by considering that

$$\sum_{i=1}^{n_{cr}} (L_{cr})_i > L_{eff} \tag{4-30}$$

where n_{cr} is the number of cracks and L_{eff} is the total embedded length of reinforcing bars to the surrounding concrete, which is assumed to be equal to member's length in the further analysis. When Eq. (4-30) is satisfied, no "*tie region*" exists in the member, hence, the algorithm moves to Module 3, where the bond length L_b is calculated as half of the average value of crack spacing from Module 2:

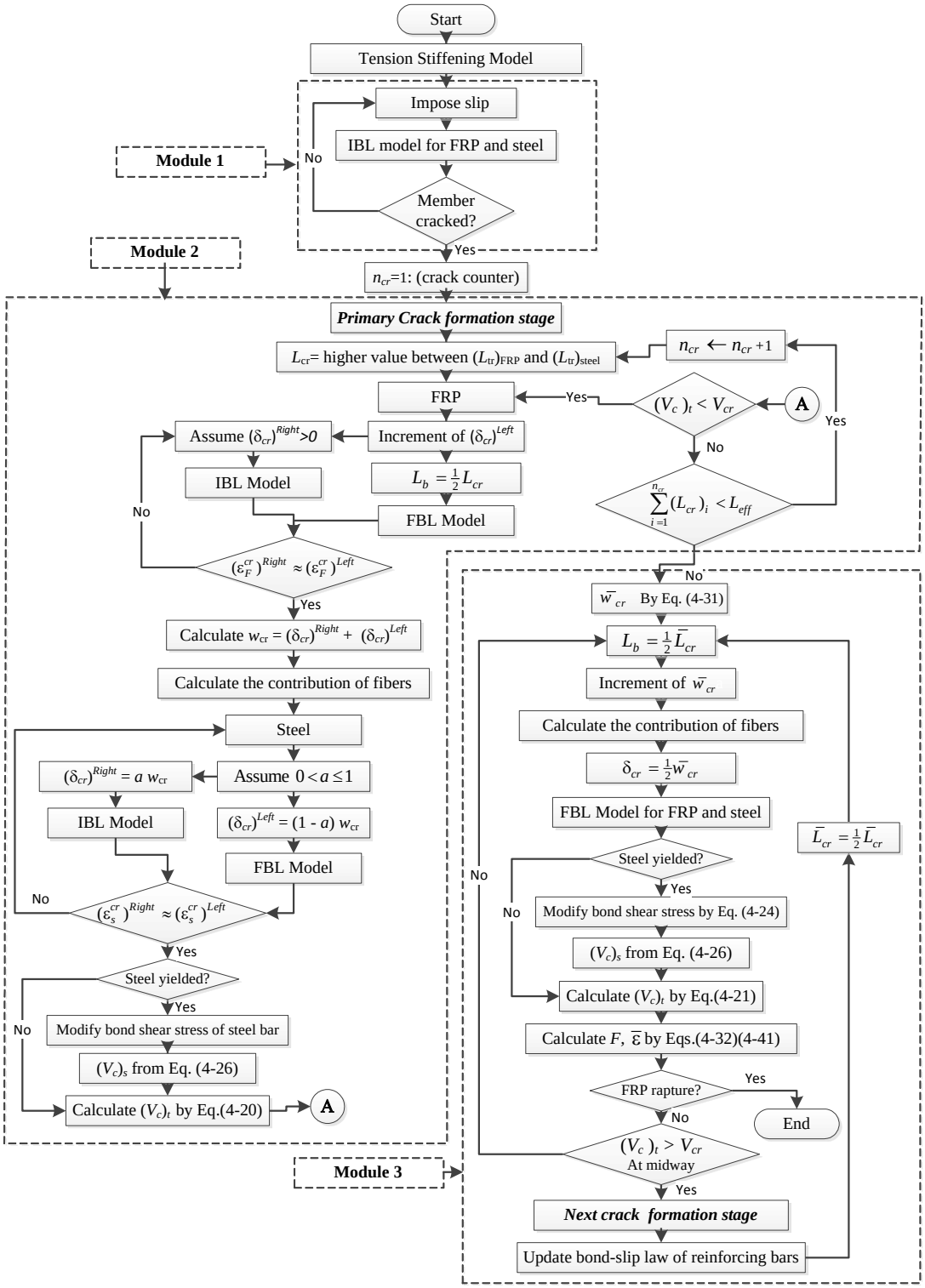

Figure 4-7: The algorithm of crack analysis procedure for hybrid steel/FRP reinforced FRC tensile member

$$2L_b = \frac{1}{n_{cr}}\sum_{i=1}^{n_{cr}}(L_{cr})_i = \bar{L}_{cr} \tag{4-31}$$

consequently, the average value of crack width at the beginning of Module 3 is

$$\bar{w}_{cr} = \frac{1}{n_{cr}} \sum_{i=1}^{n_{cr}} (w_{cr})_i \tag{4-32}$$

Then, for each increment of $\bar{w}_{cr}$, the total applied force is calculated by

$$F = F_r + (V_c)_{fr} \tag{4-33}$$

where F_r is the total tensile force of the reinforcing bars, which is given by

$$F_r = \begin{cases} E_s A_s \varepsilon_s^{cr} + E_F A_F \varepsilon_F^{cr} & \varepsilon_s^{cr} \le \varepsilon_{sy} \\ A_s \sigma_{sy} + E_F A_F \varepsilon_F^{cr} & \varepsilon_s^{cr} > \varepsilon_{sy} \end{cases} \tag{4-34}$$

where ε_s^{cr} and ε_F^{cr} are computed by running the FBL model described in the Annex 4A, and $(V_c)_{fr}$ is determined by Eq. (4-14).

Additionally, the total value of force transferred to the concrete matrix by the reinforcements, $(V_c)_t$, is calculated using Eq. (4-21). If $(V_c)_t$ reaches the cracking force of the member, *i.e.* V_{cr}, the midway section (A in Figure 4-5) cracks, in which the number of cracks becomes double, and the bond length becomes half of its value. The bond-slip law of the reinforcing bars is updated based on the value of δ_m, which was described in Section 4.2.6.

Module 3 is repeated until FRP bar's strain meets its rupturing strain. If steel bar yields before, the bond shear stress of steel bar is modified based on Eq. (4-25). In the model, a bi-linear elasto-plastic stress-strain relationship is considered for steel bar in tension. It is assumed that the ultimate tensile strain of FRP bar's (ε_{Fu}) is always reached before the steel tensile strain at hardening initiation (ε_{sh}) is attained (Figure 4-8b).

4.3 Description of finite element (FE) model

The hybrid FRP/steel FRC tensile member analyzed in the previous section is simulated by using Finite Element (FE) models available in FEMIX, a FEM-based computer program (Sena Cruz *et al.* 2007). In this section some relevant information is given about the numerical model including FEs and constitutive laws adopted for concrete and reinforcements. More description about the modeling approach and the used FEs will be given in Chapter 6. The predictive performance of the proposed analytical and FE models

are appraised by simulating recent experimental tests dedicated to the tension-stiffening phenomenon.

4.3.1 Finite elements

Eight-node Plane Stress FEs are used to simulate concrete, with a Gauss-Legendre (G-L) integration scheme of 2×2, while the reinforcing bars are simulated by using 3-nodes Cable 2D elements with 2 G-L integration points. To simulate bond between the reinforcements and concrete, 6-nodes 2D Interface FEs are employed by using Gauss-Lobatto integration scheme of 3 points.

4.3.2 Constitutive laws for the materials

A multi-directional fixed smeared crack model described in detail elsewhere (Sena Cruz 2004), and available in FEMIX (Sena Cruz *et al.* 2007), is assigned to the Plane Stress FEs to simulate the elasto-cracked behavior of FRC. In this model, a linear and elastic constitutive law is adopted for concrete in compression and also in tension prior to crack initiation. When the tensile strength is attained in a certain integration point, a four-linear constitutive law (the constitutive law shown in Figure 4-8a) is followed in order to simulate the post-cracking response of FRC.

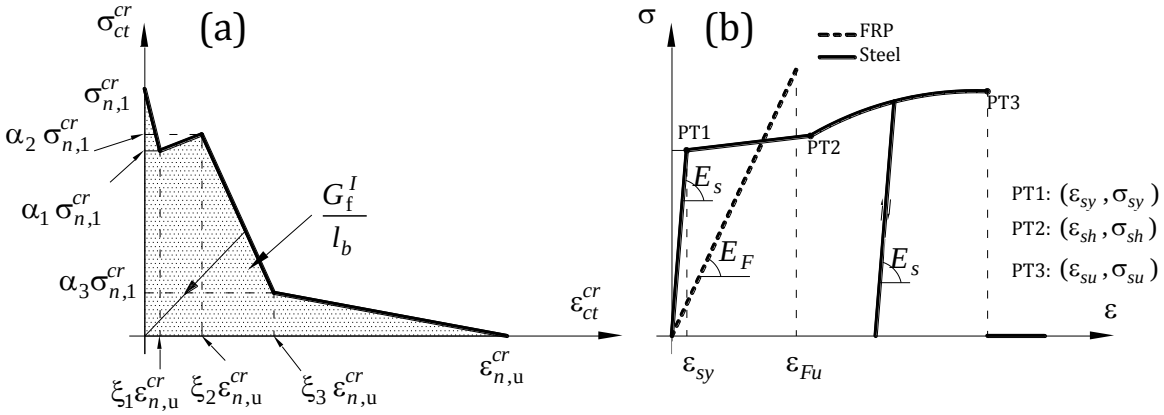

Figure 4-8: Constitutive laws of materials in tension: (a) Four-linear stress-strain diagram to simulate the fracture mode I crack propagation of FRC and (b) steel and FRP bars

In this figure, the parameter G_f is the mode I fracture energy of FRC (Barros and Sena Cruz 2001) and the parameter l_b is the crack band width, which is assumed equal to the square root of the area assigned by each integration point in order to assure that the results

are not dependent of the FE mesh refinement. ε_n^{cr} and σ_n^{cr} are the crack tensile strain and stress components, respectively, normal to the crack plane. The coefficients α_i and ξ_i being $i = 1,2,3$ define the transition points of the branches of the diagram. More detail about the smeared crack modeling approach for concrete material will be given in Chapter 6.

The linear-elastic stress-strain diagram represented in Figure 4-8b is adopted for FRP bars, where ε_{Fu} is the ultimate strain, while an elasto-plastic model (Sena Cruz 2004) is employed to simulate the tensile behavior of steel bars, by using the following equation (Figure 4-8b):

$$\sigma_s(\varepsilon_s) = \begin{cases} E_s \varepsilon_s & \varepsilon_s \le \varepsilon_{sy} \\ E_{sy}(\varepsilon_s - \varepsilon_{sh}) + \sigma_{sh} & \varepsilon_{sy} < \varepsilon_s \le \varepsilon_{sh} \\ \sigma_{su} + (\sigma_{sh} - \sigma_{su})\left(\dfrac{\varepsilon_{su} - \varepsilon_s}{\varepsilon_{su} - \varepsilon_{sh}}\right)^p & \varepsilon_{sh} < \varepsilon_s \le \varepsilon_{su} \\ 0 & \varepsilon_s > \varepsilon_{su} \end{cases} \quad (4\text{-}35)$$

where

$$E_{sy} = (\sigma_{sh} - \sigma_{sy}) / (\varepsilon_{sh} - \varepsilon_{sy}) \quad (4\text{-}36)$$

and ε_{sy}, ε_{sh}, ε_{su}, σ_{sy}, σ_{sh} and σ_{su} are defined in Figure 4-8b. The parameter p normally ranged between 1 and 4.

4.3.3 Interface behavior

The sliding component of the constitutive model for the Interface FEs is defined by the bond-slip relationship represented in Figure 3b, which is characterized by the following three branches (Pepe *et al.* 2013, Sena Cruz 2004):

$$\tau(\delta) = \begin{cases} \tau = \tau_1 \cdot (\delta/\delta_1) & 0 \le \delta \le \delta_1 \\ \tau = \tau_m \cdot (\delta/\delta_2)^{\beta_1} & \delta_1 < \delta \le \delta_2 \\ \tau = \tau_m \cdot (\delta/\delta_2)^{-\beta_2} & \delta > \delta_2 \end{cases} \quad (4\text{-}37)$$

where $\delta_1 = \delta_2 (\tau_1/\tau_m)^{1/\beta_1}$.

4.3.4 Geometry, mesh and boundary conditions

The typical scheme of tension-stiffening specimens used in experiments, as well as the mesh and geometry of FE model proposed in the present study are shown in Figure 4-9.

As shown, the FE model has a line of symmetry through its axis at center of the section. The interface elements are located at this symmetric line, where the axial stiffness of the reinforcing bar sets as half value. The interface elements are assigned only to the bonded area as shown in this figure.

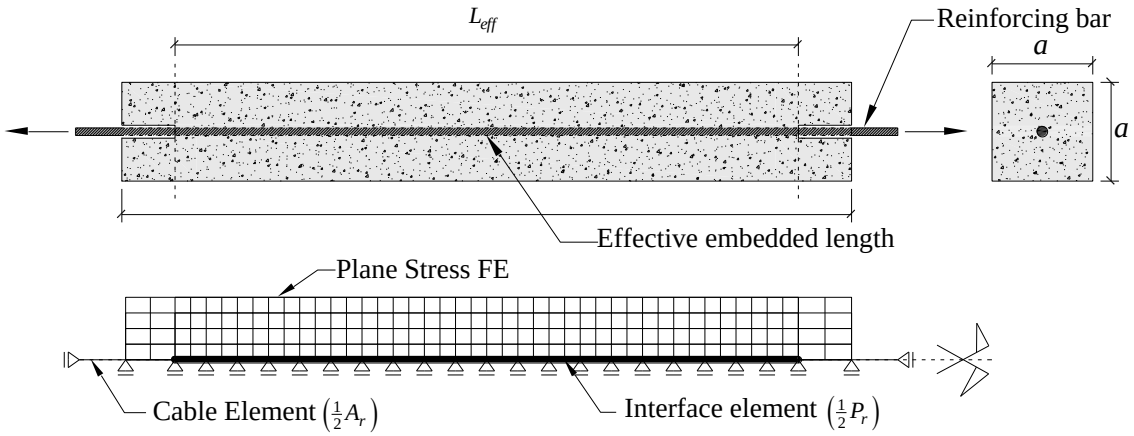

Figure 4-9: Typical scheme for tension stiffening test specimen and FE simulation

4.4 Model validation

Two sets of data of RC in direct tension tests have been selected from the literature. The first is GFRP-RC carried out by Baena *et al.* (2011), and the second belongs to the work recently carried out by Moreno *et al.* (2014) on Hybrid Fiber-Reinforced Concrete (named as "HyFRC") containing conventional steel bar. For the second one, the bond-slip law suggested by CEB-FIB Model Code 2010 for steel bars is adopted. However, for the first one, the local bond-slip law of the used GFRP bar is calibrated by employing the bond model proposed in Chapter 3 by fitting the theoretical pullout force *versus* loaded end slip to the experimental results of the direct pullout tests presented by the same authors in 2009 (Baena *et al.* 2009). It is worth noticing that the bond length in their tests was five times of the GFRP bar's diameter. The values that define the bond-slip law used in the proposed numerical models are included in Table 4-1, Table 4-2 contains the relevant properties of the used concrete and FRC, and reinforcements, which were reported by the studies carried out by (Baena *et al.* 2011 and Moreno *et al.* 2014).

Additionally, the post-cracking behavior of "HyFRC" is simulated by the diagram represented in Figure 4-8a, whose data for its definition (ξ_i , α_i and G_f) was obtained by

fitting the post-cracking response recorded in the uniaxial tensile tests carried by Moreno *et al.* (2014).

Table 4-1: Bond-slip law's parameters used in the proposed models

Data source / **Specimen's name**	**Bond-slip law's parameters**									
	δ_1	δ_2	δ_3	δ_4	τ_0	τ_1	τ_m	τ_R	β_1	β_2
	(mm)	(mm)	(mm)	(mm)	(MPa)	(MPa)	(MPa)	(MPa)	(-)	(-)
Baena *et al.* 2011: GFRP-RC member										
13-170	0.60	2.0	6.5	12.0	3.0	11.5	17.5	3.0	0.30	0.75
16-170	0.35	1.8	5.5	12.5	3.0	14.0	17.0	5.5	0.35	0.75
19-170	0.45	1.9	5.0	10.0	2.5	11.0	14.5	4.0	0.40	0.75
Moreno *et al.* 2014: Steel-HyFRC member										
HyFRC	0.10	1.0	2.0	11.0	3.0	8.0	14.0	5.6	0.40	0.40

Table 4-2: Geometry and material properties of the test specimens from the literature

Name of specimen	**Geometry**			**Reinforcement**			**Concrete (or FRC)**					
	s	L_{eff}	$a \times a$	*Dia.* (ρ)	E_s | E_f	ε_{sy} | ε_{fu}	f_{ct}	f_{cm}	E_c	ξ_1, ξ_2, ξ_3	$\alpha_1, \alpha_2, \alpha_3$	G_f
	(mm)	(mm)	(mm²)	(mm) (%)	(GPa)	(%)	(MPa)	(MPa)	(GPa)			N/mm
Baena *et al.* 2011: GFRP-RC member												
13-170	1300	1200	170×170	13.7(0.51)	37.6	2.05	1.75	48.4	27.3	-	-	0.14[1]
16-170	1300	1200	170×170	16.9(0.71)	41.7	2.47	2.58	48.1	27.3	-	-	0.14[1]
19-170	1300	1200	170×170	19.1(0.99)	40.7	1.60	2.10	56.2	33.3	-	-	0.15[1]
Moreno *et al.* 2014: Steel-HyFRC member												
HyFRC[2]	1041	813	127×127	16 (1.2)	192.2	0.23	2.30	31.0	31.3[3]	0.004,0.014,0.14 (0.006,0.021,0.14)[4]	0.74, 0.85,0.22 (0.56,0.78,0.22)[4]	5.5[5]

[1] Fracture energy calculated according to recommendations of Model Code 2010;
[2] Average results of 4 tested specimens by Moreno *et al.* 2014;
[3] Not reported by author; calculated according to the recommendations of Model Code 2010;
[4] The values in parentheses correspond to the strict contribution of fibers (see Figure 4-10a);
[5] Calculated by measuring the area under the experimental stress-strain curve and assuming for the crack band width the value of 197mm, as reported by Moreno *et. al* 2012).

In case of analytical model, the contribution of fibers are obtained by subtracting the concrete softening from the given post-cracking response of "HyFRC" (Moreno *et al.* 2012). The concrete softening is obtained by using the bi-linear diagram recommended by CEB-FIB Model Code 2010. Figure 4-10a shows the contribution of fibers, and the total post-cracking stress-strain diagram of "HyFRC" that is used in the analytical model and FE model, respectively. In Figure 4-10b, Figure 4-11a, b and c the experimental results are compared to those obtained by the proposed analytical and FE models. By giving the relevant input data that defines the material properties of concrete, reinforcing bar, and the bond-slip law's parameters, the models predict well the experimental results. Moreover, Figure 4-10c and Figure 4-11d compare the crack pattern obtained experimentally (in red) and numerically (in blue). The FE model predicts fairly in an acceptable way the experimental

crack pattern registered in the GFRP-RC specimens. However, in the simulation of the tensile response of "HyFRC" the crack pattern obtained by FE model showed some differences in terms of number of cracks and crack spacing since the model is not simulating the influence of fiber distribution and orientation on the post-cracking behavior of "HyFRC". To take these aspects into consideration, more sophisticated models should be used, like the one detailed in (Cunha *et al.* 2011).

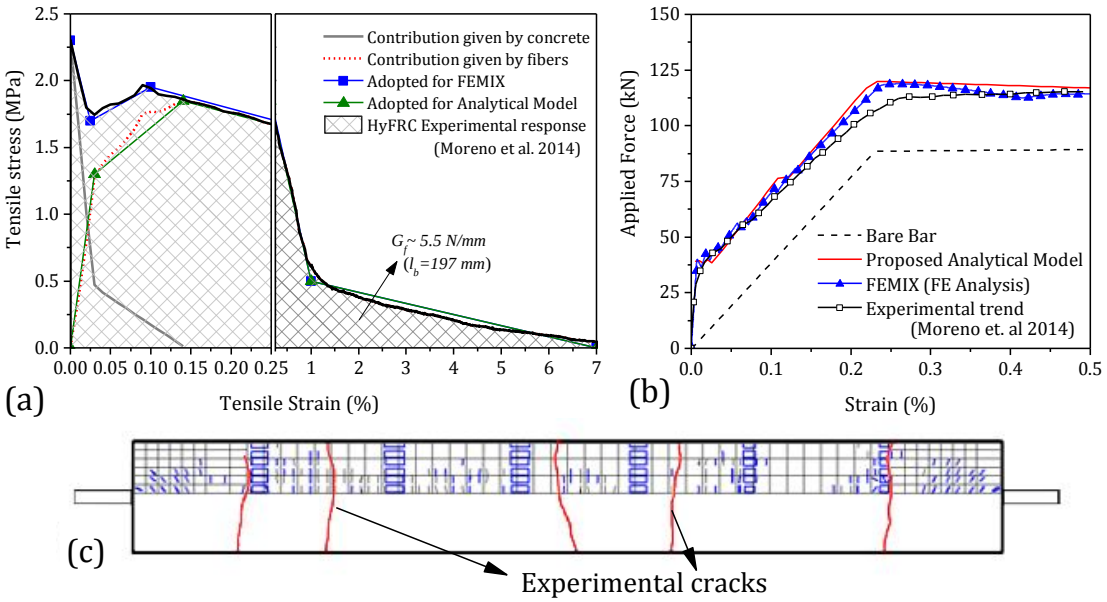

Figure 4-10: (a) Uniaxial tensile response of "HyFRC" developed by Moreno *et al.* in 2012, (b) Comparison between theoretical and experimental results, and (c) Comparison between the experimental and numerical crack patterns at the member mean strain of 0.2%

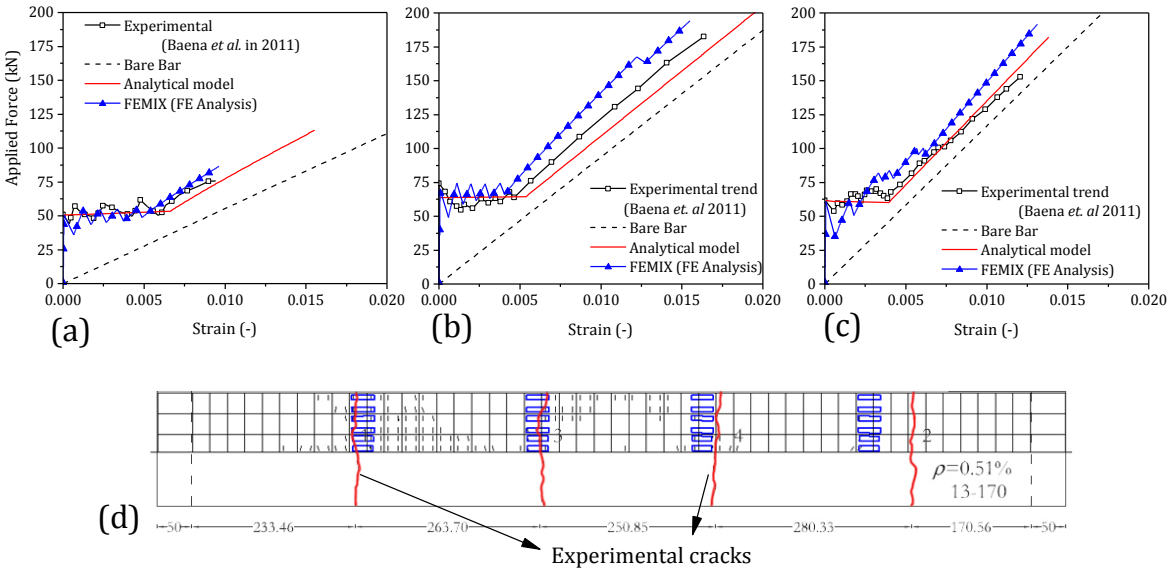

Figure 4-11: Comparison between theoretical and experimental results (Baena *et al.* 2011) for the specimen: (a) 13-170, (b) 16-170, (c) 19-170, and (d) Comparison between the experimental and numerical crack patterns of specimen 13-170

4.5 Parametric study

By using the proposed analytical model, two groups of parametric studies, A and B, are carried out to evaluate the influence of the main model parameters on the variations of tensile stress of reinforcing bars due to their bond interaction to surrounding concrete, which is defined as tension-stiffening effect $f_{r,TS}$ hereafter. For this purpose, a FRC tensile member containing FRP and steel bars in a symmetric arrangement in the concrete section is considered to be subjected to direct tension load. The effective embedded length of the reinforcing bars (L_{eff}) is assumed equal to 1000 mm. The properties of the adopted FRP bars correspond to the type of ribbed GFRP bars previously used in the bond tests (Chapter 3) were considered in this parametric study. The typical properties of mild steel that is being used in construction industry are also taken for the steel bars in this study.

Table 4-3: Values of parameters adopted for parametric studies of Group A

Study	FRP [1]			Steel [2]			ρ [3] (%)	Type [4]	Concrete (or FRC)					
	d_b	n_F	ρ_F	d_b	n_s	ρ_s			f_{ct}	E_c	f_{cm}	ξ_1,ξ_2,ξ_3	$\alpha_1,\alpha_2,\alpha_3$	G_f
	(mm)		(%)	(mm)		(%)			(MPa)	(GPa)	(MPa)			(N/mm)
1	4×Ø8	2.0	0.65	**Ø12**	6.7	**0.37**	**1.02**	PC	3.0	30	50			0.14
2	4×Ø8	2.0	0.65	**Ø14**	6.7	**0.50**	**1.15**	PC	3.0	30	50			0.14
3	4×Ø8	2.0	0.65	**Ø16**	6.7	**0.65**	**1.30**	PC	3.0	30	50			0.14
4	4×Ø8	2.0	0.65	**Ø20**	6.7	**1.02**	**1.48**	PC	3.0	30	50			0.14
5	4×Ø8	2.0	0.65	**Ø25**	6.7	**1.60**	**2.25**	PC	3.0	30	50			0.14
6	**4×Ø8 + Ø16**	2.0	**1.30**	-	-	-	**1.30**	PC	3.0	30	50			0.14
7	-	-	-	**4×Ø8 + Ø16**	6.7	**1.30**	**1.30**	PC	3.0	30	50			0.14
8	4×Ø8	2.0	0.65	Ø16	6.7	0.65	1.30	**FRC1**	3.0	30	50	**0.03,0.06,0.2**	**0.3,0.50,0.17**	**3.81**
9	4×Ø8	2.0	0.65	Ø16	6.7	0.65	1.30	**FRC2**	3.0	30	50	**0.02,0.05,0.2**	**0.5,0.67,0.33**	**6.21**
10	4×Ø8	2.0	0.65	Ø16	6.7	0.65	1.30	**FRC3**	3.0	30	50	**0.01,0.04,0.2**	**0.67,0.83,0.50**	**8.61**

[1] Young's modulus of FRP bar and its ultimate tensile strain are 60 GPa and 1.67%, respectively;
[2] Young's modulus of steel bar and its yielding tensile strain are 200 GPa and 0.3%, respectively;
[3] Total reinforcement ratio: $\rho_F + \rho_s$;
[4] PC: Plain Concrete with no fibers.

Finally, three types of FRCs (named FRC1, FRC2 and FRC3), with different values of mode I fracture energy (G_f), are considered to be representative of a concrete mix with different volume fraction of fibers. Figure 4-12 compares the post-cracking behavior of FRC1, 2 and 3 in terms of the parameter α *versus* ξ as they were defined earlier in Figure 4-4b, and the respective values are given in Table 4-3. The contribution of fibers after

cracking is simply defined by using the same four-linear post-cracking response of FRC shown in Figure 4-12, but having the first point starts at (0, 0), that is null values for the both α and ξ (see dotted line in Figure 4-12). This represents in a simple manner how the pullout force by fibers starts increasing from null value while the crack is opening (or increase in crack strain).

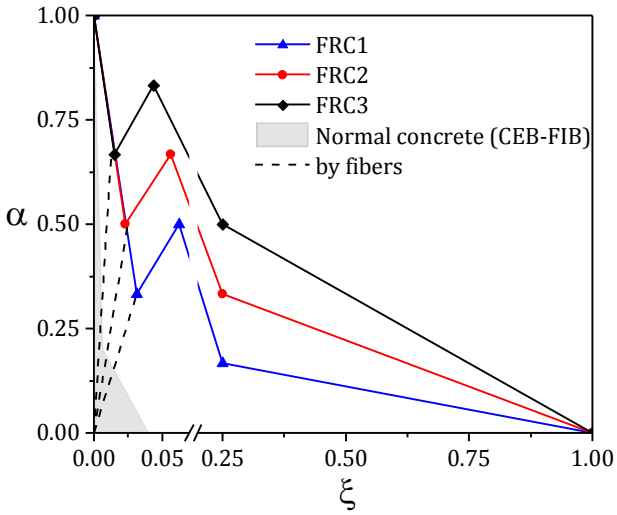

Figure 4-12: Comparison between the post-cracking responses of the adopted FRCs for the parametric studies 8 to 10

4.5.1 Studies of Group A

Group A includes 10 different studies that are focused on the influence of the steel *versus* FRP reinforcement ratio (*i.e.* ρ_s / ρ_F) and concrete fracture energy mode I, G_f. Although different bars' diameter are used in Group A, the bond-slip law's parameters are kept constant in order to neglect the effect of bond-slip law's parameters in these studies. Table 4-3 reports the properties of the used materials in Studies 1 to 10. The values that define the bond-slip relationship for these studies are indicated in the first row of Table 4-4.

Studies 1 to 5: the steel reinforcement ratio, ρ_s, is varied by adopting different steel bars in terms of diameter (Ø12, 14, 16, 20 and 25 mm), while the properties of concrete and GFRP reinforcement ratio (4Ø8 GFRP) are kept constant. Plain concrete (without fibers) is used in these studies.

Studies 6 to 7: the reinforcement arrangement of Study 3 (*i.e.* 4×Ø8 GFRP + 1×Ø16 steel) with a total reinforcement ratio of $\rho = \rho_s + \rho_F = 1.30\%$ is adopted in these studies, but for

Study 6, ρ_s is assumed to be null, which means no steel bars are used (*i.e.* (4×Ø8+1×Ø16) GFRP), while in Study 7 no GFRP bars are applied (*i.e.* (4×Ø8+1×Ø16) Steel).

Studies 8 to 10: the hybrid reinforcement of Study 3 is used for studies 8 to 10, but the G_f varies by taking FRC type 1, 2 and 3.

Table 4-4: Values of bond-slip parameters adopted in parametric studies (Group A and B)

Study	Bond-slip law's parameters																	
	Steel								GFRP									
	τ_0	τ_1	τ_m	τ_R	δ_1	δ_2	δ_3	δ_4	τ_0	τ_1	τ_m	τ_R	δ_1	δ_2	δ_3	δ_4	K_1	K_2
	(MPa)	(MPa)	(MPa)	(MPa)	(mm)	(mm)	(mm)	(mm)	(MPa)	(MPa)	(MPa)	(MPa)	(mm)	(mm)	(mm)	(mm)		
1-10	2.5	10.0	18.0	7.0	0.10	0.8	1.2	5.0	1.5	8.0	15.0	2.0	0.50	1.50	3.0	7.0	16.0	7.0
11	2.5	10.0	18.0	7.0	0.10	0.8	1.2	5.0	1.5	8.0	15.0	2.0	**0.20**	**1.20**	3.0	7.0	**40.0**	7.0
12	2.5	10.0	18.0	7.0	0.10	0.8	1.2	5.0	1.5	8.0	15.0	2.0	**0.30**	**1.30**	3.0	7.0	**26.7**	7.0
13	2.5	10.0	18.0	7.0	0.10	0.8	1.2	5.0	1.5	8.0	15.0	2.0	**0.40**	**1.40**	3.0	7.0	**20.0**	7.0
14	2.5	10.0	18.0	7.0	0.10	0.8	1.2	5.0	1.5	8.0	15.0	2.0	0.50	**1.00**	3.0	7.0	16.0	**14.0**
15	2.5	10.0	18.0	7.0	0.10	0.8	1.2	5.0	1.5	8.0	15.0	2.0	0.50	**2.00**	3.0	7.0	16.0	**4.7**
16	2.5	10.0	18.0	7.0	0.10	0.8	1.2	5.0	1.5	8.0	15.0	2.0	0.50	**2.50**	3.0	7.0	16.0	**3.5**

4.5.2 Studies of Group B

Group B includes 6 studies, 11th to 16th, that aim to assess the influence of the bond-slip law's parameters of GFRP bars on the variation of $f_{r,TS}$. The type of concrete, the reinforcement ratio and arrangement are those adopted in Study 3. Note that the bond-slip law's parameters of steel bar are constant in the analysis of Group B. Table 4-4 includes the bond-slip law's parameters adopted in all the studies. As shown in Figure 4-13, the alteration of the stiffness of the pre-peak branches can be simulated by changing the power value of β_1 with a bond-slip diagram similar to the one adopted in the FE model (Figure 4-3b), which has already been used by many authors (Baena *et al.* 2013, Lee *et al.* 2013, Sena Cruz 2004, and Focacci *et al.* 2000).

Studies 11 to 13: the stiffness of the first and second linear branches of $\tau-\delta$ diagram (shown in Figure 4-3a) are defined as K_1 and K_2, respectively. Then, they are calculated by

$$\begin{cases} K_1 = \dfrac{\tau_1}{\delta_1} \\ K_2 = \dfrac{(\tau_m - \tau_1)}{(\delta_2 - \delta_1)} \end{cases} \tag{4-38}$$

In Studies 11 to 13, the value of K_1 is varied by changing the value of δ_1 (Figure 4-13a). However, the value of δ_2 is adjusted in order to keep the value of K_2 constant and equals to the value defined in Study 3. In this case, δ_2 is calculated by

$$\delta_2 = \frac{(\tau_m - \tau_1)}{K_2} + \delta_1 \tag{4-39}$$

The values of τ_1 and τ_m are those adopted in Study 3, since the concrete compressive strength (f_{cm}) is considered equal in all studies, and considering that the bond strength of a bar-concrete interface is commonly presented as function of $\sqrt{f_{cm}}$.

Studies 14 to 16: the value of K_2 is varied by changing only the value of δ_2 (Figure 4-13b). The other parameters are the same adopted in Study 3.

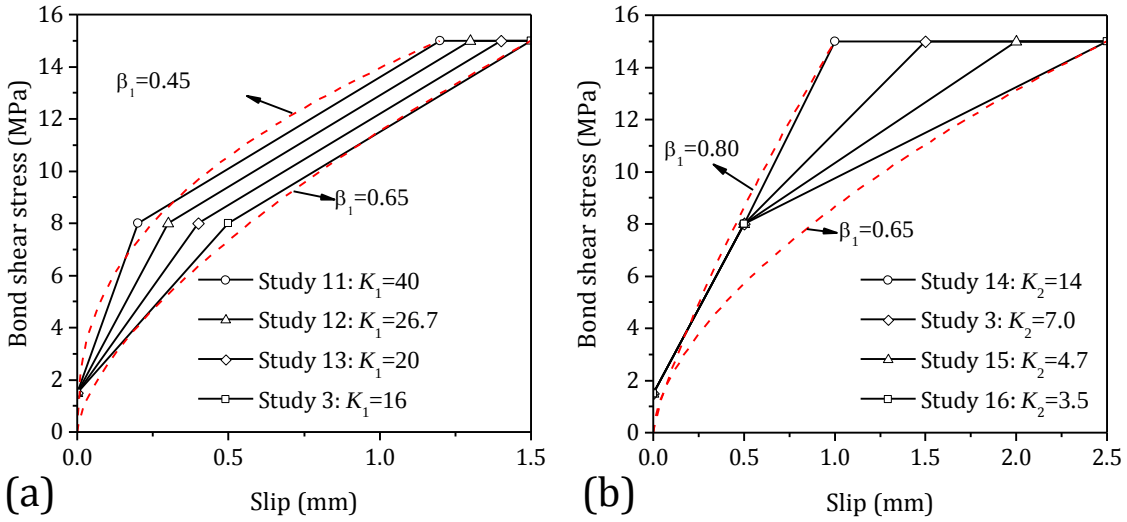

Figure 4-13: Concept of changing the stiffness of the first and second branches of bond-slip constitutive law: (a) K_1, and (b) K_2

4.5.3 Results and discussion

The tension-stiffening effect, $f_{r,TS}$, is defined as the portion of tensile stress of reinforcing bars at crack section that is carried by the surrounding concrete due to the bond behavior of reinforcing bars. Based on this definition, $f_{r,TS}$ is determined by:

$$f_{r,TS} = \frac{1}{A_c}(F_r - F_{bare}) \tag{4-40}$$

where F_{bare} is the tensile force of bare bars (un-bonded bars):

$$F_{bare} = (E_s A_s + E_F A_F)\bar{\varepsilon} \tag{4-41}$$

being $\bar{\varepsilon}$ the mean strain of member, if the elastic deformation of FRC between cracks is neglected, the mean value is simply obtained by:

$$\bar{\varepsilon} = \frac{\bar{w}_{cr}}{\bar{L}_{cr}} + \bar{\varepsilon}_{cr} \tag{4-42}$$

where $\bar{L}_{cr}$ and $\bar{w}_{cr}$ are obtained according to Eqs. (4-31) and (4-32), respectively, and $\bar{\varepsilon}_{cr}$ is the elastic mean strain of member at cracking point. By substituting Eq. (4-34) into Eq. (4-40), $f_{r,TS}$ becomes

$$f_{r,TS} = \begin{cases} \rho_s E_s(\varepsilon_s^{cr} - \bar{\varepsilon}) + \rho_F E_F(\varepsilon_F^{cr} - \bar{\varepsilon}) & \varepsilon_s^{cr} \le \varepsilon_{sy} \\ \rho_s(\sigma_{sy} - E_s\bar{\varepsilon}) + \rho_F E_F(\varepsilon_F^{cr} - \bar{\varepsilon}) & \varepsilon_s^{cr} > \varepsilon_{sy} \end{cases} \tag{4-43}$$

Hereafter the normalized tensile stress, $f_{r,TS}/f_{ct}$, is used being f_{ct} the concrete tensile strength.

4.5.3.1 Normalized $f_{r,TS}/f_{ct}$ versus member's mean strain

Figure 4-14a and b present the results of the parametric study of group A (studies 1 to 5, and 8 to 10), and Figure 4-14c and d show the results obtained from the parametric study of group B (studies 11 to 16), both in terms of $f_{r,TS}/f_{ct}$ *versus* mean strain of the member (*i.e.* $\bar{\varepsilon}$), which is calculate by Eq. (4-42). In accordance with the tension-stiffening responses obtained from the results of the parametric study, a multi-linear diagram presented in Figure 4-15 can be proposed for tension-stiffening model of concrete (or FRC) member reinforced by hybrid FRP/steel bars. This diagram can be defined by three coefficients, namely ζ_j, ψ_i, and η_i (*i*= 1 to 3, *j*=1 to 4 and *j*= 1 to 5) where:

- Values of $\zeta_j \varepsilon_{cr}$ define the level of concrete tensile strain (ε_{ct}) due to the tension-stiffening effects, in which ζ_1 corresponds to the concrete crack tensile strain at the beginning of the primary *crack formation stage*, ζ_2 corresponds to the concrete

tensile strain at the initiation of steel yielding at crack section while ζ_3 defines the concrete tensile strain equals to steel yielding strain (*i.e.* $\varepsilon_{ct} = \varepsilon_{sy} \approx 30\varepsilon_{cr}$), ζ_4 defines the concrete crack tensile strain corresponding to reinforcing bar's slip (δ_{cr}) at the end of the elastic bond phase (δ_1), and finally, ζ_5 defines the concrete tensile strain at rupture of FRP bar;

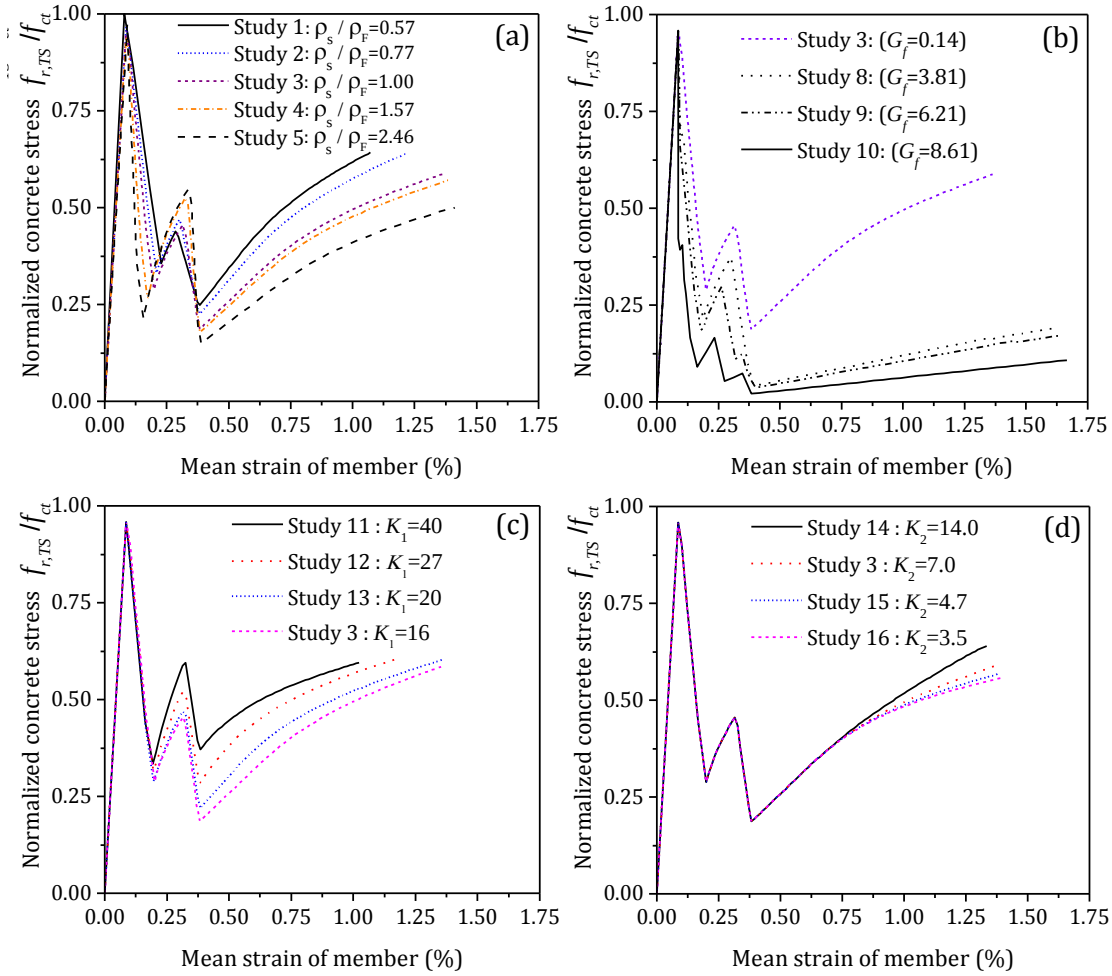

Figure 4-14: Influence of the following parameters on the normalized tensile stress *versus* mean strain of the member: (a) steel to FRP reinforcement ration , (b) Mode I FRC fracture energy , (c) K_1 , and (d) K_2

- Values of $\psi_i f_{ct}$ define the level of concrete tensile stress (σ_{ct}) due to the tension stiffening, in which ψ_1 to ψ_4 define the crack tensile stress corresponding to ζ_1 to ζ_4, respectively;

- Values of $\eta_i E_c$ define the stiffness of the ascending linear branches of the model (pseudo-hardening stages), in which η_i corresponds to the axial stiffness of the reinforcing bars, as well as their bond stiffness by $\tau - \delta$ diagram.

By fitting the proposed diagram to the tension-stiffening responses shown in Figure 4-14, the variation of these coefficients *versus* the parametric variables of ρ_s / ρ_F, G_f, K_1 and K_2 are determined, and plotted in Figure 4-16.

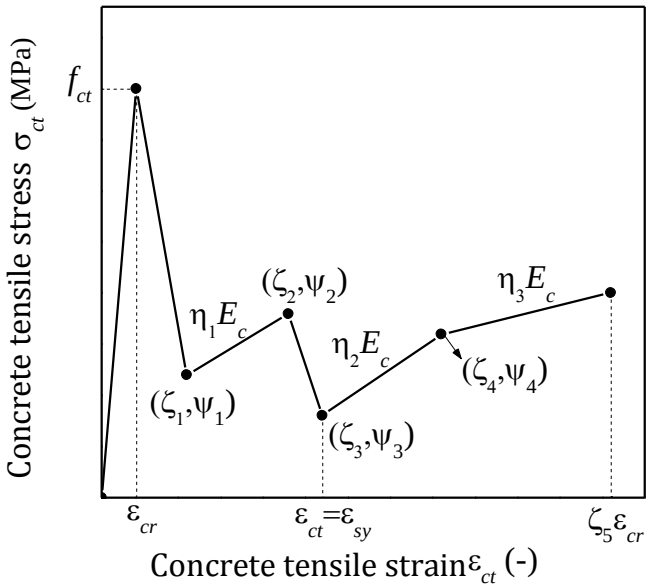

Figure 4-15: Tension-stiffening model proposed for hybrid FRP/steel reinforcing system

Effect of increasing the steel reinforcement ratio **(** ρ_s/ρ_F **)**: when the steel reinforcement ratio increases, the average crack spacing ($\bar{L}_{cr}$), as well as the bond length (L_b) decreases. Hence, by increasing the slip of reinforcing bars at crack section, the difference between ε_r^{cr} and ε_r^m in Eq. (4-16) for both FRP and steel bars decreases, and based on Eq. (4-42), the mean value of $\bar{\varepsilon}$ approaches to the value of ε_r^{cr}. Therefore, the tension-stiffening effect calculated by Eq. (4-43) decreases. This was evidenced from the obtained results plotted in Figure 4-14a, as well as the decrease in the value of coefficients ψ_i *versus* ρ_s / ρ_F in Figure 4-16. Before yielding of steel bar, by increasing ρ_s, η_1 increase due the increase in the axial stiffness of the steel bars. However, after yielding of the steel, the value of η_2 and η_3 decrease due to the significant drop in the axial stiffness of steel bar

at cracked section, as well as the increase in its bond stiffness (by Eq. (4-25)). Additionally, when $(\varepsilon_r^{cr} - \bar{\varepsilon})$ decreases, the coefficients ζ_2 and ζ_5 increase, in which ζ_2 gets closer value to $\varepsilon_{sy} \approx 30\varepsilon_{cr}$, and ζ_5 to the level of strain at the rupture of FRP ($\varepsilon_{fu} \approx 167\varepsilon_{cr}$).

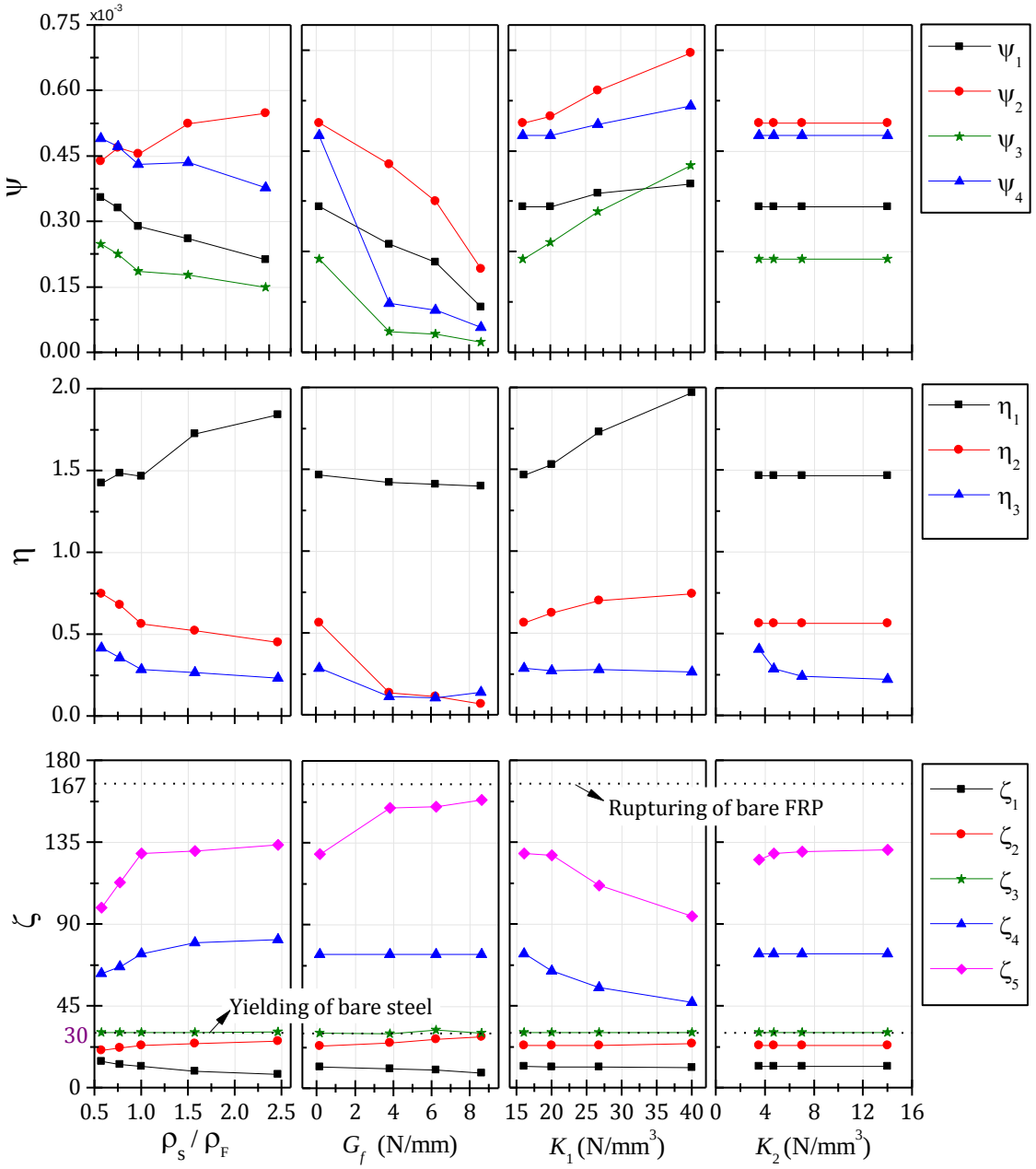

Figure 4-16: The variation of the tension-stiffening model coefficients *versus* the parametric variables

Effect of increasing the fracture energy of FRC: when of the mode I fracture energy of concrete (G_f) increases, the number of cracked sections in the member increases significantly, leading to a smaller average crack spacing. Therefore, similar to what already

explained, the $(\varepsilon_r^{cr} - \bar{\varepsilon})$ parcel of Eq. (4-43) decreases with the increase of the slip at cracked section. Since in these studies the reinforcement ratios (ρ_F and ρ_s) are constant, the decrease in the tension-stiffening effect calculated by Eq. (4-43) is more noticeable (comparing the obtained results in Figure 4-14a and Figure 4-14b). The same tendency that was previously obtained for ψ_i , η_i and ζ_j when ρ_s is increased, is also obtained with the increase of G_f . However, in the present studies the η_1 is almost constant since the axial stiffness of the steel bar does not change (see Figure 4-16, variation of the model coefficient *versus* G_f).

Effect of increasing the stiffness of elastic bond phase of FRP bar **(** K_1 **)**: by increasing the stiffness of the elastic branch of bond law assumed for FRP bar (*i.e.* K_1), the tension-stiffening effect of reinforcing bars increases. This can be evidenced by the obtained results shown in Figure 4-14c, as well as the increase in coefficient ψ_i *versus* the variation of K_1 in Figure 4-16. When K_1 increases, the parcel $(\varepsilon_r^{cr} - \varepsilon_r^m)$ of Eq. (4-16) increases, and considering that $\varepsilon_r^m \cong \bar{\varepsilon}$ (Eq. (43)), the $f_{r,TS}$ determined from Eq. (4-43) also increases. On the other hand, if the parcel $(\varepsilon_F^{cr} - \bar{\varepsilon})$ increases, FRP bar attains its ultimate strain (ε_{Fu}) at lower level of the concrete crack tensile strain, which can be seen by the variation of ζ_4 *versus* K_1 in Figure 4-16. Additionally, η_1 and η_2 increase with K_1 , while η_3 is not significantly affected for the variation of this parameters because for $\varepsilon_{ct} > \zeta_3 \varepsilon_{cr}$ the slip of FRP bars at crack section is not in its elastic bond phase.

Effect of increasing the stiffness of hardening bond phase of FRP bars **(** K_2 **)**: for the material properties and the bond-slip relationship adopted in this study, Figure 4-14d shows that K_2 has a negligible effect on the variation of tension stiffening $f_{r,TS}$. Only the stiffness of the third linear branch (η_3) is influenced by the variation of K_2 . This is due to the fact that for the concrete cracking strain greater than $\zeta_3 \varepsilon_{cr}$, the slip of FRP bar at crack section is beyond the elastic bond phase of the bond diagram, and consequently it is influenced by the value of K_2 .

4.5.3.2 Total force versus the average crack width and the mean strain

In Figure 4-17a the total force *versus* the average crack width (*i.e.* $\bar{w}_{cr}$) obtained in the studies 6 and 7, corresponding to the GFRP-RC and Steel-RC tensile member, are compared to the hybrid GFRP-Steel RC tensile member of Study 3. The enhancement in terms of crack width by adding steel reinforcement to the GFRP-RC member is observable. Note that the same total reinforcement ratio of 1.3% was adopted for the three studies. However, after yielding of steel, the crack width increases considerably due to the significant loss in the steel axial stiffness, as well as its bond to concrete.

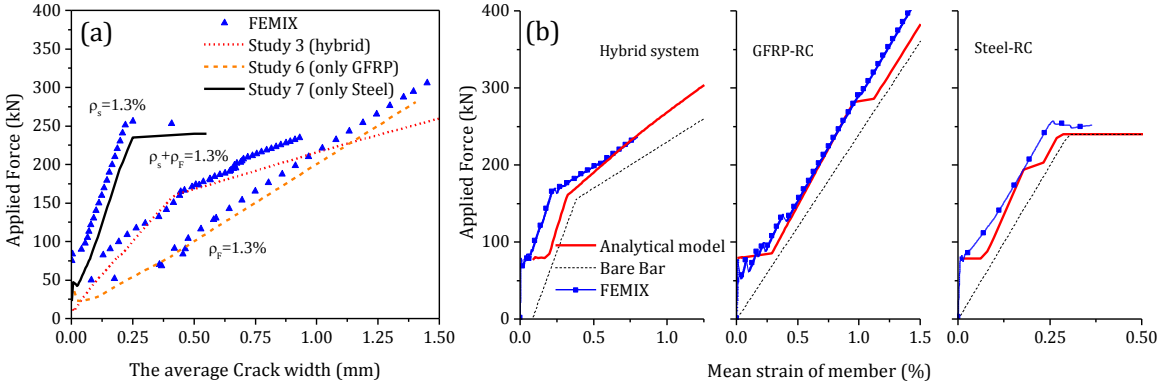

Figure 4-17: GFRP-RC, Steel-RC and hybrid GFRP-Steel RC member: (a) Total force *versus* the average crack width and (b) Total force *versus* the mean strain

In addition to the analytical results obtained from the parametric studies of 3, 6 and 7, FE analysis were carried out by using FEMIX, and the results obtained from the simulation are compared with the analytical ones in terms of the total force *versus* average crack width and mean strain, which are plotted in Figure 4-17a and b, respectively. The average crack width in the FE model was obtained by computing the average value of inelastic deformation of the integration points at the location of the main cracks for different load combinations. The inelastic deformation of the integration points was calculated by multiplying the crack tensile strain in loading direction by the crack band width (l_b). As a results, a good agreement between both models was achieved.

4.5.3.3 Post-cracking response of FRC including tension-stiffening effect

In case of modeling of RC members, if the bond-slip behavior of reinforcing bars and concrete is not simulated, the tension-stiffening effect due to the reinforcements is normally

performed through the concrete tensile stress-strain relationship in order to get more accurate results. This is the same concept when S- FRC or FRP reinforced FRC members are simulated. The tension-stiffening of FRP and steel bars due to their bond behavior with FRC should be included in the post-cracking behavior of FRC, which is normally obtained by uniaxial tensile tests. In this context, if the tension-stiffening response obtained from the parametric studies of 8 to 10, shown in Figure 4-14b, is added to the respective post-cracking response of FRCs, shown in Figure 4-12, the total post-cracking response of hybrid FRP/steel reinforced FRC including the tension-stiffening effect of the reinforcing bars is attained. Figure 4-18 compares the post-cracking response of FRC1, 2 and 3 with and without the tension stiffening effect. This figure is plotted in terms of dimensionless coefficient of α *versus* ξ, where the black dots show the failure of FRP bars corresponding to the attainment of the ultimate tensile strain adopted for FRP bars (see Table 4-3). The post-cracking response of hybrid reinforced FRC is appropriate to be used in the finite elemental or sectional analysis where the interfacial bond behavior between reinforcing bar and FRC is ignored.

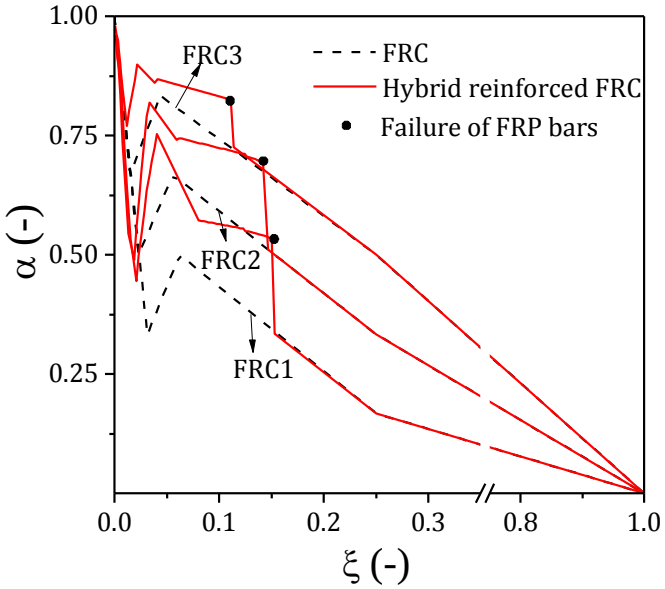

Figure 4-18: Post-cracking response of FRC including the tension-stiffening effect

4.6 Summary and conclusion

In the present work, the tension-stiffening effect due to the bond interaction between a

hybrid reinforcement system composed by fiber reinforced polymer (FRP) and steel bars and surrounding fiber reinforced concrete (FRC) was theoretically investigated through an explicit analytical formulation. The analytical model is based on the bond-slip behavior of the reinforcing bars and the surrounding FRC, as well as the post-cracking response of FRC in tension. The tension-stiffening effect was also investigated by employing 2D interface finite elements using a constitutive model that simulates the bond behavior of reinforcing bars and concrete. This interface was used to connect 2D Cable elements to 2D Plane Stress finite elements, which simulate concrete employing a multi-directional smeared crack approach. With a basis of the results from the proposed model, the following conclusion can be drawn:

1) The two analytical and numerical models showed a good agreement with some recent experimental tests available in the literature in case of GFRP reinforced tensile member and S-FRC tensile member, leading to show their capability to address to the tension-stiffening effect of such reinforced members;
2) The post-yielding of steel bar as well as the loss in its bond to concrete was modeled through an empirical coefficient. This gives possibility of modeling the decrease in tension stiffening effect of steel-RC element after yielding of steel bar;
3) Based on the results of parametric study, increasing in mode I fracture energy of FRC will reduce the tension-stiffening effect by reinforcing bars in reinforced FRC members. This is attributed to the fact that the higher fracture energy results in higher number of cracks and lower crack spacing, and consequently, lower bond length. If the bond length decreases, tension stiffening significantly decreases. On the other hand, the higher fracture energy decrease the average crack width, which is beneficial for serviceability limit state requirements;
4) An improve in terms of crack width and load carrying capacity can be observed for the hybrid FRP-steel reinforced FRC member if the steel reinforcement ratio increases. However, after yielding of the steel bar, this hybrid system showed the

higher average crack width when it compares with the FRP reinforced FRC member without steel bar (in case of the same total reinforcement ratio for both reinforced member);

5) The tension-stiffening effect of hybrid steel/GFRP reinforced FRC element was introduced as a modified crack stress-strain diagram of FRC in which a fracture energy higher than its original value was adopted before rupturing strain of GFRP. This modification is based on the properties of the reinforcing bars and their bond-slip characterizations. The modified crack tensile stress-strain diagram is functional to be used in the sectional or finite elemental analysis of hybrid FRP/steel reinforced FRC elements where no attempt is made to simulate the effect of bond-slip behavior of the reinforcing bars.

It should be noticed that the influence of concrete cover, reinforcing bar's diameter, and concrete splitting are not considered in the proposed model. However, their effectiveness can be simply added to the model if the relevant bond-slip law including those effect is adopted in the model. In addition, the discrete crack analysis proposed in this study may not be functional for cement-based composite materials that exhibits strain-hardening behavior after cracking.

Notations

a	width of concrete tensile member's cross section	f_{cm}	the mean value of concrete (or FRC) compressive strength
A_c	area of concrete member cross section	f_{ct}	concrete (or FRC) tensile strength
A_s	area embedded steel bar's cross section	$f_{r,TS}$	tension-stiffening effect due to the reinforcing bars
A_F	area embedded FRP bar's cross section	F	value of pullout force transferred by bond length of reinforcing bar
A_{fr}	area of steel fiber's cross section	F_{bare}	tensile force of bare bar
C_1	first integration constant for the elastic phase	F_F	value of pullout force transferred by bond length of FRP bar
C_2	second integration constant for the elastic phase	F_r	value of pullout force transferred by bond length of either steel or FRP bar
C_3	first integration constant for the hardening bond phase	F_s	value of pullout force transferred by bond length of steel bar
C_4	second integration constant for the hardening bond phase	G_f	mode I fracture energy of concrete (or FRC)
C_5	first integration constant for the plastic bond phase	J_{fr}	constant in the governing differential equation with unknown $\delta(x)$ for steel fibers
C_6	second integration constant for the plastic bond phase	J_F	constant in the governing differential equation with unknown $\delta(x)$ for FRP bar
C_7	first integration constant for the softening bond phase	J_r	constant in the governing differential equation for either FRP or steel bar
C_8	second integration constant for the softening bond phase	J_s	constant in the governing differential equation with unknown $\delta(x)$ for steel bar
C_9	first integration constant for the frictional bond phase	K_1	stiffness of the first linear branch in bond-slip relation
C_{10}	second integration constant for the frictional bond phase	K_2	stiffness of the second linear branch in bond-slip relation
C_e	constant value for the elastic phase	K_b	modified factor for bond shear stress of steel bar due to its yielding phase
C_f	constant value for the frictional bond phase	$K_{un/re}$	slop of the unloading/reloading branch of bond-slip relation
C_h	constant for the hardening bond phase	l_{fr}	length of steel fibers
C_{so}	constant for the softening bond phase	L_b	bond length of reinforcing bar
C_p	constant for the plastic bond phase	L_{cr}	crack spacing
d_b	diameter of embedded bar	$\bar{L}_{cr}$	the average crack spacing in the analysis procedure
E_c	Young's modulus of concrete (or FRC) material	L_{eff}	the effective embedded length of the reinforcing bars in concrete tensile member
E_F	Young's modulus of FRP bar	L_{tr}	transferred bond length corresponding to whatever value of the slip at crack section
E_{fr}	Young's modulus of steel fibers	L_{tr}^e	transferred bond length undergoes only elastic bond phase
E_s	Young's modulus of steel bar	L_{tr}^f	transferred bond length undergoes only frictional bond phase

Notations

L_{tr}^{h}	transferred bond length undergoes only hardening bond phase	α_i	residual tensile stress factors define the post-cracking behavior of FRC ($i=1,2,3$)
L_{tr}^{p}	transferred bond length undergoes only plastic bond phase	β_1	factor defines the post-peak behavior of bond-slip relation used in numerical model
L_{tr}^{pre}	transferred bond length due to prestress in the embedded reinforcing bars	β_2	factor defines the post-peak behavior of bond-slip relation used in numerical model
L_{tr}^{so}	transferred bond length undergoes only softening bond phase	γ	constant entering the governing differential equation for the softening phase
n_{cr}	number of crack along the concrete tensile member counted in the crack analysis	δ	relative slip between reinforcing bar and surrounded concrete (or FRC)
n_F	modular ratio between FRP and concrete (or FRC) material	δ_1	first value of slip corresponding to the initial bond shear stress
n_s	modular ratio between steel and concrete (or FRC) material	δ_2	second value of slip corresponding to peak of local bond stress slip relation
P_F	perimeter of FRP bar's cross section	δ_3	third value of slip corresponding to peak of local bond stress slip relation
P_{fr}	perimeter of steel fiber's cross section	δ_4	slip corresponding to the start of friction phase in the local bond stress slip relation
P_r	perimeter of either FRP or steel bar's cross section	δ_{cr}	slip of embedded reinforcing bar at crack section
P_s	perimeter of steel bar's cross section	δ_{fr}	slip of steel fibers at crack section
S	total length of the experimental tensile member	δ_{ir}	slip remains in the interface when the applied load is totally removed
u_c	concrete deformation at concrete-FRC or concrete-steel bar interface	δ_m	the maximum slip reached during the loading phase
u_F	FRP bar's deformation at FRP-concrete (or -FRC) interface	$\delta_r(x)$	slip distribution of reinforcing bar either FRP or steel bar
u_s	steel bar's deformation at steel-concrete (or -FRC) interface	$\bar{\varepsilon}$	mean strain of reinforced concrete tensile member
V_{cr}	cracking force of concrete (or FRC) tensile member	ε_c	concrete (or FRC) tensile strain
$(V_c)_{fr}$	The total force that is transferred to the concrete matrix by the steel fibers	$\bar{\varepsilon}_{cr}$	the elastic mean strain of member at cracking point
$(V_c)_r$	The total force that is transferred to the concrete matrix by the reinforcing bars	ε_{fr}	tensile strain of steel fibers at crack section
$(V_c)_t$	The total force that is transferred to the concrete matrix by the reinforcements	ε_{fu}	the ultimate tensile strain of FRP bar at failure
w_{cr}	crack mouth opening at crack section	ε_F	FRP bar's tensile strain
w_{cu}	the ultimate crack opening corresponding to zero residual tensile stress in concrete or FRC	ε_F^{pre}	pre-strain of FRP bar due to prestressing
$\bar{w}_{cr}$	average crack width in the crack analysis procedure	ε_n^{cr}	crack tensile strain of concrete (or FRC) in numerical model

Notations

ε_r^{cr}	tensile strain of FRP (or steel) bar at crack section	σ_{ct}^{cr}	crack tensile stress of concrete (or FRC)
ε_s	steel bar's tensile strain	σ_n^{cr}	concrete crack tensile stress of concrete (or FRC) in the numerical model
ε_{sh}	strain of mild steel at the initiation of the hardening phase in its direct tensile behavior	σ_F	FRP bar's tensile stress
ε_s^{pre}	pre-strain of steel bar due to prestressing	σ_s	steel bar's tensile stress
ε_{sy}	Yielding strain of steel bar	σ_{sy}	yield stress of steel bar
ζ_i	factors define the proposed tension-stiffening model ($i=1,2,3,4,5$)	$\tau(\delta)$	local bond shear stress-slip relationship
η_i	factors define the slopes in the proposed tension-stiffening model ($i=1,2,3$)	τ_0	initial bond shear stress
λ_1	constant entering the governing differential equation for elastic bond phase	τ_1	bond shear stress at the beginning of the hardening bond phase
λ_2	constant entering the governing differential equation for hardening bond phase	τ_F	bond shear stress of FRP bar
ξ_i	crack opening factors define the post-cracking behavior of FRC ($i=1,2,3$)	τ_m	peak stress of the local bond shear stress-slip relationship
ρ	reinforcement ratio	$\tau_r(x)$	bond shear stress distribution over bond length for either FRP or steel bar
ρ_F	FRP reinforcement ratio	τ_R	residual bond shear stress in the local bond-slip relationship
ρ_s	steel reinforcement ratio	τ_s	bond shear stress of steel bar
σ_c	tensile stress of concrete	τ_s^{mod}	modified bond shear stress of steel bar due to initiation of its yielding phase
σ_{cf}	the local tensile stress of concrete due to the force transferred by the steel fibers at cracked section	ψ_i	factors define the proposed tension-stiffening model ($i=1,2,3,4$)

Chapter 5

5 HYBRID GFRP/STEEL REINFORCED HPFRC PRESTRESSED BEAM

5.1 Introduction

The chapter investigates the structural behavior of I-shaped cross-sectional beams flexurally reinforced by hybrid prestressed steel strand and glass fiber reinforced polymer (GFRP) bars, and made by High Performance Fiber Reinforced Concrete (HPFRC) for eliminating steel stirrups since they are quite susceptible to corrosion. Combining prestressed GFRP bars of relatively low elasticity modulus, but immune to corrosion (positioned with a small concrete cover), with prestressed steel strand (with higher concrete cover to avoid corrosion), a good compromise in terms of reinforcement effectiveness, ductility, durability and cost competitiveness can be obtained. The steel strand aids also to assure the necessary flexural strengthening of the beams if GFRP bars become ineffective in case of fire occurrence. This work presents and discusses the results obtained from the experimental study of the beams flexurally tested under monotonic loading conditions. Additionally, the predictive performance of the available formulation in the design codes for the case of Fiber Reinforced Concrete (FRC) and FRP reinforced Concrete (FRP-RC) was assessed to be used for the proposed hybrid system.

5.2 Experimental program

The experimental program is described hereafter has been conducted at the laboratory of

the Structural Division (LEST) of the Civil Engineering Department of University of Minho in Portugal funded by National Funds through FCT—Portuguese Foundation for Science and Technology under the project reference PTDC/ECM/105700/2008, and named "DURCOST: Innovation in reinforcing systems for sustainable pre-fabricated structures of higher durability and enhanced structural performance".

5.2.1 Material properties

The materials used in the fabrication of the I-Beam specimens were GFRP bar and steel strand as longitudinal reinforcements, and high performance self-compacting concrete mix reinforced by hooked steel fibers (90 kg/m^3).

5.2.1.1 Steel strand and GFRP bars

Two types of longitudinal reinforcements, composed of FRP and steel materials, was used in the present experimental study: ribbed surface GFRP bar of 12 mm diameter; 9 and 15 nominal size of steel strand of Grade 1725 (formed by uncoated seven-wires), which is normally used for pre-tensioned or post-tensioned in construction industry. The GFRP bar's ribs have a constant height of 6% of bar diameter and rib's spacing of about 8.5 mm. Some nominal mechanical properties of the reinforcements, based on the information given by the manufacturers, are included in Table 5-1. These two reinforcements are shown in Figure 5-1a, and their typical tensile stress-strain diagram are compared in Figure 5-1b.

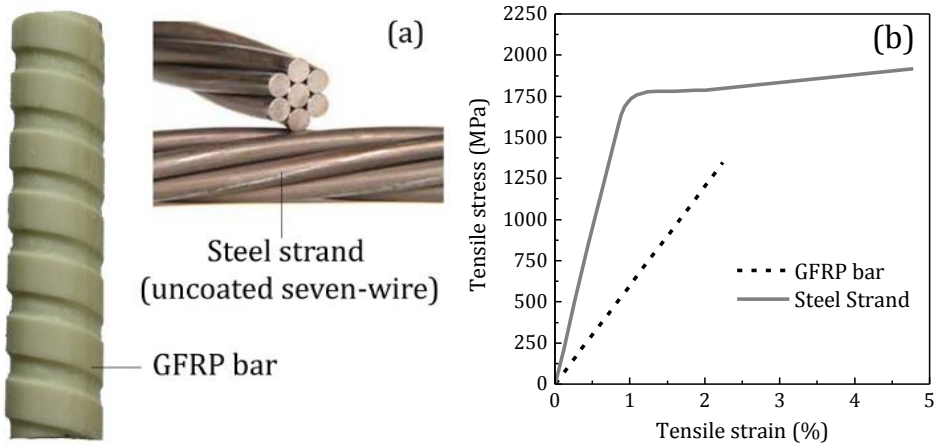

Figure 5-1: GFRP bar and steel strand: (a) comparison between their appearance and (b) comparison between their stress-strain curves

Table 5-1: Nominal properties of the longitudinal reinforcements used in the present study

Type	diameter (mm) ϕ_f ,ϕ_s	Cross section area (mm²) A_f ,A_s	Young's Modulus (GPa) E_f ,E_s	Yielding strain (%) ε_{sy}	Yielding stress (MPa) f_{sy}	Ultimate stress (MPa) f_{fu},f_{su}	Ultimate strain (%) ε_{fu},ε_{su}	Weight per 1m (gr/m)
Steel strand 15	15.2	139.4	187.5	0.85	~1600	~1900	>3.5	1094
Steel strand 9	9.5	51.6	187.5	0.85	~1600	~1900	>3.5	405
GFRP bar	13.1	134.7	60.0	-	-	1350	2.25	317

5.2.1.2 High Performance FRC (HPFRC)

The HPFRC used in the present experimental program was prepared based on the mix method developed by Soltanzadeh *et al.* (2015). The used materials were cement, CEM I 42.5R, fly ash class F, limestone filler, superplasticizer, water, three types of aggregates (containing fine and coarse river sand, and crushed granite) and hooked end steel fibers of 35 mm in length, aspect ratio of 64 and yield stress of 1100 MPa. The geometrical properties of hooked steel fibers and its tensile strength are reported in Table 5-2. More details about the designed mix and the properties of mixed material can be found in the work published by Soltanzadeh *et al.* (2015). The mix compositions is given in Table 5-3.

Table 5-2: Geometrical properties of hooked steel fibers

Fiber diameter (ϕ_{sf})	h_{sf}	l'	l''	l_{sf}	l_{sf}/ϕ_{sf}	Tensile strength
(mm)	mm	mm	mm	(mm)	(-)	(N/mm²)
0.55	1.8	~23	4	35	64	[1224-1446]

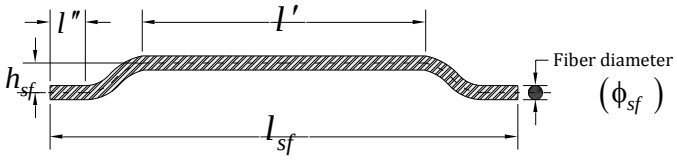

Table 5-3: HPFRC compositions (Soltanzadeh *et al.* 2015)

Cement (kg/m³)	Fly ash (kg/m³)	Limestone filler (kg/m³)	Water (Litr/m³)	SP* (Litr/m³)	Fine sand (kg/m³)	River Sand (kg/m³)	Coarse Aggregate (kg/m³)	ST** (kg/m³)
462	138	139	208	16	99	697	503	90

* SP: Superplastizier; ** ST: Steel fiber.

Compressive strength:

Since to produce all the I-Beam specimens it was necessary to execute ten HPFRC mix

batches, the compressive strength of each mix batch was obtained using HPFRC cylinders of Ø150×300 mm according to ASTM C39. The average results of the compressive test for different HPFRC batches in terms of the compressive strength are summarized in Table 5-4. In addition, three cylinder specimens was tested using deformation controlled manner in order to capture the whole stress-strain response of HPFRC in compression. The average curve of these stress-strain responses will be later used in the numerical simulation described in Chapter 6.

Table 5-4: The compressive strength and the elastic Young's modulus of HPFRC

	Mix Batch	**Number of specimens**	**Compressive strength** (f_c') (MPa)	**Elastic Young's modulus** (E_c) (GPa)	**Age** (days)
Group A	M1	2	70.55	33.9	49
	M2	1	72.59	34.5	53
	M3	3	69.71	34.9	76
	M4	1	70.14	35.1	69
Group B	M5	3	76.94	37.2	70
	M6	3	72.09	35.3	99
	M7	3	80.96	36.7	98
	M8	3	66.77	34.0	97
	M9	3	78.73	36.5	130
	M10	3	76.89	36.1	126
	Total/Average	25	73.13 (CoV=6%)	35.4 (CoV=3%)	-
	M11 *	3	65.10	30.02	28

* HPFRC mix batch to characterize the properties at 28th days of curing.

Elastic Young's modulus:

The same cylinder specimens that were used to measure the compressive strength was utilized to measure the elastic Young's modulus of HPFRC in compression. This test was carried out according to ASTM C469 where the cylinders were experienced the compressive load up to 40% of its ultimate load. The ultimate compressive load was estimated based on the primarily compressive test that had been executed to characterize the developed HPFRC (Soltanzadeh *et al.* 2015). The elastic Young's modulus of HPFRC batches are included in Table 5-4.

Flexural strength:

In regards to the behavior of HPFRC in tension, which is the behavior most benefited by fiber reinforcement, five simply supported notched beams of 150×150 mm2 cross section and 600 mm in length were subjected to three point loading conditions to characterize and classify of the post-cracking response of HPFRC according to CEB-FIP Model Code 2010. Nominal values of the flexural properties of HPFRC can be determined by considering the diagram of the applied force (F) *versus* the Crack Mouth Opening Displacement (*CMOD*). Parameters, $f_{R,j}$, representing the residual flexural tensile strength, are evaluated from the $F-CMOD$ relationship, as follows:

$$f_{R,j} = \frac{3}{2}\frac{F_j l}{b_n h_{sp}^{\ 2}} \tag{5-1}$$

where F_j is the applied load corresponding to $CMOD_j$ ($CMOD_1 = 0.5$ mm, $CMOD_2 = 1.5$ mm, $CMOD_3 = 2.5$ mm and $CMOD_4 = 3.5$ mm), l is the beam's span, while b_n and h_{sp} is the width of the cross section and the distance between the notch tip and the top of the specimen, respectively. Figure 5-2a shows the geometry of notched beam test setup. In addition, the results of the notched beam tests in terms of the applied load (*F*) *versus* CMOD are plotted in Figure 5-2b. The residual flexural tensile stress parameters of HPFRC are included in Table 5-5.

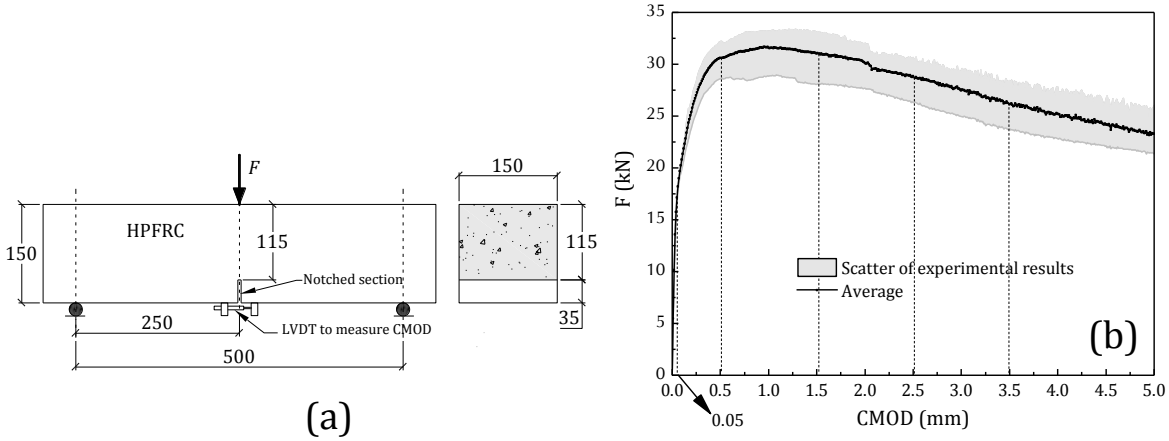

Figure 5-2: (a) Notched beam test setup and geometry, and (b) *F-CMOD* results

Table 5-5: The residual flexural tensile stress parameters of HPFRC

Notched beam Specimens ID.	Residual flexural tensile strength parameters								Limit of proportionality*	
	$CMOD_1$=0.5		$CMOD_2$=1.5		$CMOD_3$=2.5		$CMOD_4$=3.5			
	F_1 (kN)	$f_{R,1}$ (MPa)	F_2 (kN)	$f_{R,2}$ (MPa)	F_3 (kN)	$f_{R,3}$ (MPa)	F_4 (kN)	$f_{R,4}$ (MPa)	F_L (kN)	$f_{ct,L}$ (MPa)
B1	30.34	11.47	30.13	11.39	27.60	10.43	24.27	9.18	15.64	5.91
B2	32.06	12.12	32.70	12.36	29.76	11.25	27.17	10.27	16.12	6.13
B3	30.79	11.64	30.93	11.69	28.22	10.67	25.32	9.57	14.26	5.39
B4	31.40	11.87	32.28	12.20	29.77	11.26	26.41	9.99	15.62	5.91
B5	28.65	10.83	28.03	10.60	25.88	9.78	23.15	8.75	16.23	6.14
Average:	**30.65**	**11.59**	**30.81**	**11.65**	**28.25**	**10.68**	**25.26**	**9.55**	**15.57**	**5.90**

* Calculated by Eq. (5-1) for *CMOD*=0.05 (RILEM TC 162-TDF).

5.2.2 Beams: manufacturing, geometry, reinforcements and pre-stress level

A total of ten I-shaped cross-sectional HPFRC beams reinforced by passive or prestressed GFRP bars, and passive or prestressed steel strand was simply supported and subjected to four-point bending test under monotonic and fatigue loading conditions. The experimental variables were the reinforcement ratio of hybrid GFRP/steel strand and the level of prestress in GFRP bars (*i.e.* P_{pf}). Note that the prestress level of GFRP bars (*i.e.* f_f^{pre}) is calculated as a percentage of its ultimate tensile stress (*i.e.* f_{fu}), and prestress level of steel strand (*i.e.* f_s^{pre}) is calculated as a percentage of its yielding stress (f_{sy}):

$$f_f^{pre} = P_{pf} \times f_{fu} \tag{5-2}$$

$$f_s^{pre} = P_{ps} \times f_{sy} \tag{5-3}$$

where P_{pf} and P_{ps} are the percentage of prestress in GFRP bar and steel strand, respectively.

The tests were carried out in two groups. The Group A included four prestressed I-Beams reinforced by non-prestressed GFRP bars and prestressed steel strand, while the Group B was composed by six prestressed I-Beams where the prestressed force was applied to both reinforcements. In each group, a non-prestressed beam was casted as a reference beam. The identification, reinforcement data, and the prestress level applied to both types of bars are indicated in Table 5-6. Additionally, dimension of the beams and their reinforcement details are shown in Figure 5-3. In Group B, IB7 and IB9 beams (with the same configurations as IB6 and IB8, respectively) as well as IB10 were subjected to fatigue loading conditions.

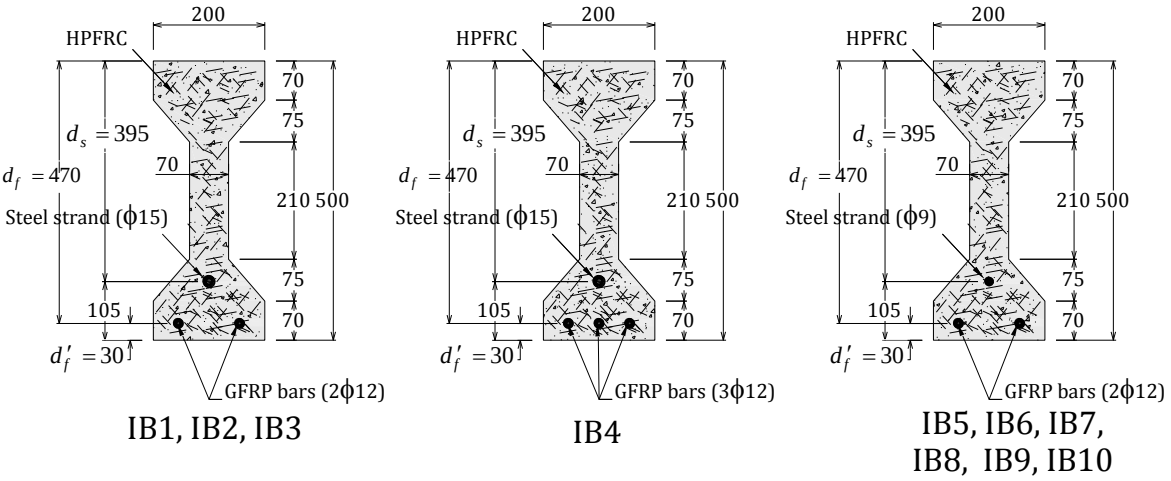

Figure 5-3: Dimension and reinforcing configuration of the specimens (dimension in mm)

Table 5-6: The beam identification, the reinforcement content and the prestress level

	Specimen ID	Mix batches	$\frac{a}{d_{f,eq}}$ [1]	ρ_f [2]	ρ_s [3]	At jacking			
						f_s^{pre}	f_f^{pre}	N_{ps} [4]	N_{pf} [5]
				(%)	(%)	(MPa)	(MPa)	(kN)	(kN)
Group A	IB1	M1	3.48	0.29	0.18	0.0	0.0	0.0	0.0
	IB2	M2	3.48	0.29	0.18	400	0.0	55.6	0.0
	IB3	M3	3.48	0.29	0.18	800	0.0	111.2	0.0
	IB4	M4	3.42	0.43	0.18	800	0.0	111.2	0.0
Group B	IB5	M5	3.62	0.29	0.07	0.0	0.0	0.0	0.0
	IB6	M6	3.62	0.29	0.07	800	200	41.3	53.8
	IB7 [6]	M7	3.62	0.29	0.07	800	200	41.3	53.8
	IB8	M8	3.62	0.29	0.07	800	400	41.3	107.6
	IB9 [6]	M9	3.62	0.29	0.07	800	400	41.3	107.6
	IB10 [6]	M10	3.62	0.29	0.07	800	540	41.3	145.3

[1] The parameter is the shear span, and is defined later by Eq. (5-41);
[2] GFRP bar reinforcement ratio: $\rho_f = A_f / bd_f$;
[3] Steel strand reinforcement ratio: $\rho_s = A_s / bd_s$;
[4] Prestressed force due to the steel strand;
[5] Prestressed force due to the GFRP bars;
[6] reserved to be subjected to fatigue loading conditions.

The manufacturing processes of prestressed HPFRC I-beams reinforced by GFRP bars and steel strand is briefly described as the following steps, and schematically illustrated in Figure 5-4:

a) The beam framework of 4 m length was placed in the Prestressing line;
b) GFRP bars and steel strand were crossed along the framework, and passed through the holes that had been made at two extremities of the mold. The holes were located in accordance with the height level of the reinforcements from the bottom surface of the beam as shown in Figure 5-3.

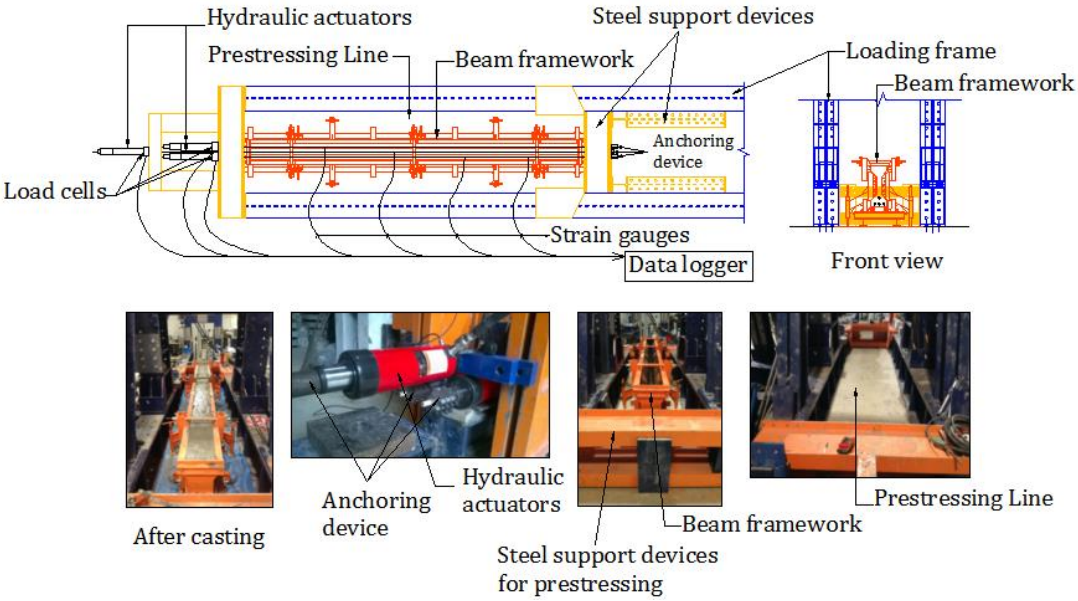

Figure 5-4: Prestressing process of the beam specimens

c) The bars and strand were pulled out by using three hydraulic actuators from one side of the prestressing line, while they were anchored at opposite side. The amount of pre-strain was controlled by the values given by the strain gauges that were previously installed on the reinforcements as well as the load cell at the location of the actuators. For group A of the specimens with non-prestressed GFRP bars, the plastic spacers were used to hold GFRP bars to their position at the bottom of the framework;

d) HPFRC mix batch was prepared and placed inside the frame work, and it was cured for three days;

e) The framework was removed;

f) The applied pre-strain in the reinforcements was released, while the value of strain gauges and load cells were being monitored by a data logger, being able to control the rate of releasing, which was about 0.1 kN/sec for all the specimens. This monitoring was continued after releasing to measure the possible loss of pre-strain;

g) Two days after releasing, the measuring instruments were unplugged, the reinforcements were cut, and finally the beam was taken out from the prestress line and stored for the testing day.

5.2.3 Test setup and monitoring system

The beam specimens were subjected to a four-point bending test configuration by using a servo-hydraulic actuator of 500 kN loading capacity under monotonic loading condition. The points loading distance (indicated by "bending zone" in Figure 5-5) was 750 mm for the Group A of the beams, while this value was decreased to 500 mm for the Group B. The tests were displacement-controlled by imposing a speed of 0.01 mm/sec to the piston of the actuator. Five Linear Variable Differential Transducers (LVDTs) were installed along the span length of the beam, according to the schematic representation in Figure 5-5. This figure also includes the disposition of the seven strain gauges installed on the materials for measuring their strain during loading (indicated as 'SG' for GFRP bars, 'SGst' for steel strand, and 'SGc' for HPFRC in Figure 5-5).

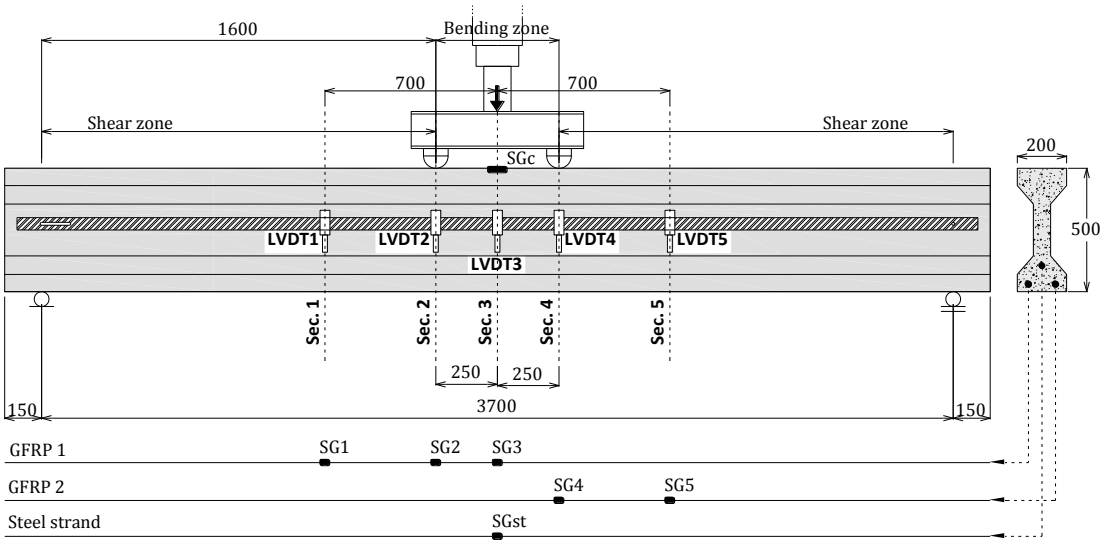

Figure 5-5: Test setup and measuring instruments used in the experimental study

Three photos of final installation of these three types of strain gauges are shown in Figure 5-6. The test setup and the other measuring instruments are shown in Figure 5-5. It should be noticed that a total of six additional strain gauges were installed at two extremities of GFRP bar and steel strand to study the distribution of pre-strain in this region during the releasing (the respective analysis will be discussed later in Section 5.2.6).

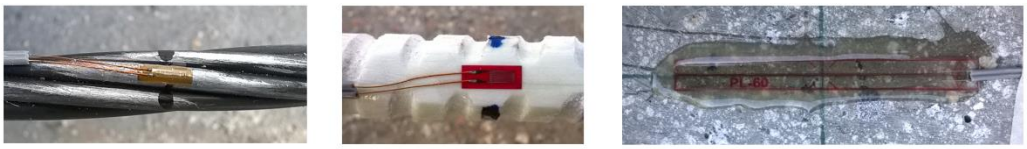

Figure 5-6: Photos of the installation of the strain gauges on the materials: steel strand (SGst), GFRP bars (SG), and HPFRC (SGc)

5.2.4 Test procedure

All the beam specimens in group A, *i.e.* IB1 to 4, plus three beams in group B, *i.e.* IB5, 6 and 8, were subjected to monotonic loading conditions, while the remained three beams of group B, *i.e.* IB7, 9 and 10, were subjected to the Constant-Amplitude (CA) fatigue loading condition. The monotonic loading template was displacement-controlled manner, where the speed of the actuator moving in the tests was controlled at 0.01 mm/sec. Prior to the mid span displacement magnitude of 15 mm (which corresponds to the value of about $S/250$ defined as the maximum beam deformation at serviceability limit state, being S beam span), six pauses of 60 sec (sustained loading condition) were arranged for measuring *CMOD* of the formed cracks at the level of the reinforcing bars by using a microscope device with $1/20$ mm of measuring precision. After the sixth pause, the loading was continued with the same speed until the failing of the specimens. The template of this monotonic loading condition is shown in Figure 5-7a.

The CA fatigue loading template included three stages, which were all loaded-controlled manner. In the first stage, the load was monotonically applied with rate of 0.2 kN/sec until reaching $F_{\max}$, which will be explained later in Section 5.4.6. The second stage was the sinusoid loading condition, in which one million loading cycles were applied considering the constant loading amplitude of 30 kN within 0.5 sec for each cycle (meaning 2 Hz of frequency). After one million cycles, in third stage, the load was monotonically removed with the rate of 0.5 kN/sec. The CA fatigue loading template is shown in Figure 5-7b. For each fatigue beam, the CA fatigue loading template was repeated twice. Hence, a total of two million sinusoid loading cycles of 2 Hz frequency was applied to the fatigue beam specimens of IB7, 9 and 10.

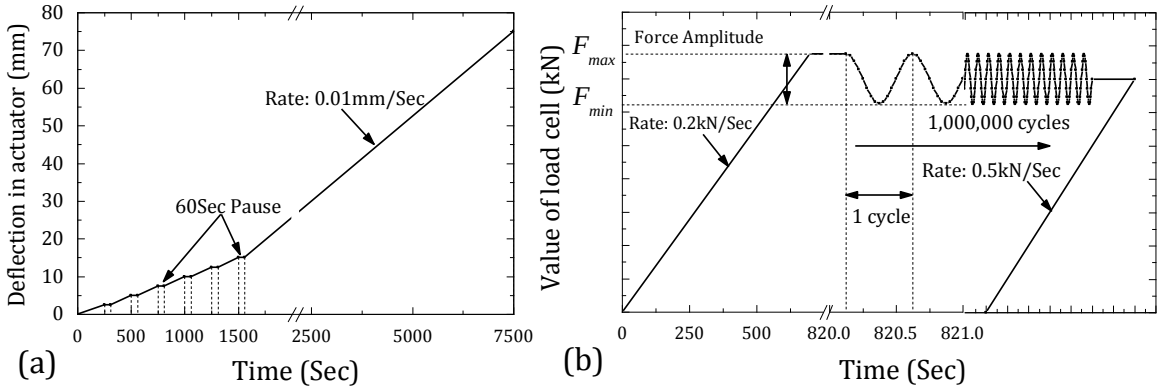

Figure 5-7: Template of (a) the monotonic loading condition, and (b) CA fatigue loading condition

5.2.5 Pre-strain loss of the reinforcements

In Group A, the prestress force was controlled using only the force value registered in the load cell (no strain gauge was installed on the steel strand), while in the Group B the prestressing process was performed by monitoring both the force in the load cell and the strain recorded in the strain gauges installed on the reinforcements. Table 5-7 includes the average results of the pre-strain of the reinforcements recorded by the strain gauges at pulling, releasing, and testing days.

Table 5-7: Pre-strain loss of the prestressed beams for the group B of specimens

Beam ID	Design Prestress Level [1]	Design pre-strain level [2]	Reinforcing line	Average value of strain in the reinforcements ε_s^{pre} and ε_f^{pre} at					Loss	Prestress level [3] P_{ps} or P_{pf}
				Pulling	→ days	Releasing	→ days	Testing day		
	(%)	(%)		(%)		(%)		(%)	(%)	(%)
IB6	50	0.43	Steel	0.44	4	0.41	95	0.40	9	47
	15	0.34	GFRP 1	0.35	4	0.33	95	0.30	14	13
	15	0.34	GFRP 2	0.37	4	0.36	95	0.32	14	14
IB7	50	0.43	Steel	0.46	4	0.45	94	0.41	11	48
	15	0.34	GFRP 1	0.35	4	0.34	94	0.30	14	13
	15	0.34	GFRP 2	0.36	4	0.34	94	0.31	14	14
IB8	50	0.43	Steel	0.45	4	0.44	93	0.41	9	48
	30	0.68	GFRP 1	0.68	4	0.65	93	0.58	15	25
	30	0.68	GFRP 2	0.69	4	0.67	93	0.60	13	26
IB9	50	0.43	Steel	0.45	4	0.42	126	0.40	11	47
	30	0.68	GFRP 1	0.69	4	0.67	126	0.60	13	26
	30	0.68	GFRP 2	0.68	4	0.63	126	0.58	15	25
IB10	50	0.43	Steel	0.45	4	0.44	122	0.41	9	48
	40	0.90	GFRP 1	0.94	4	0.88	122	0.83	11	37
	40	0.90	GFRP 2	0.93	4	0.86	122	0.81	14	36
							Average:	Steel	9.8%	
								GFRP	13.6%	

[1] It is defined as the value in percentage that is calculated by dividing the nominal prestress value in the reinforcements by the yield stress in case of steel strand and by the ultimate tensile stress in case of GFRP bar;

[2] It is defined as the strain value in percentage calculating by multiplying the design prestress level by the yield strain in case of steel strand and the ultimate tensile strain in case of GFRP bar;

[3] It is calculated according to the value of prestress in the reinforcements after the possible losses.

The pre-strain losses in the reinforcements were computed based on the measured values of strain at pulling and testing days. These pre-strain losses (indicated in Table 5-7) are mainly due to the elastic deformation of HFRRC beams, creep and shrinkage of HPFRC, and the relaxation of the reinforcements. The average pre-strain loss at the day of testing was about 13.6% and 9.8% regarding the pre-strain at the pulling day for GFRP bars and steel strand, respectively. Additionally, the value of prestress in steel strand and GFRP bars after the strain losses (*i.e.* P_{ps} and P_{pf}) is reported in last column of Table 5-7, and will be used later in the theoretical formulation.

5.2.6 Transferred bond length of reinforcements due to the prestress

The prestressed force of the reinforcement was released after three days of curing. During the releasing process, the prestressed force is transferred to the surrounding HPFRC through the transferred bond length (L_{tr}^{pre}) of each reinforcement due its bond behavior with HPFRC. When the applied prestressed force is totally released, the reinforcement's tensile strain at the beginning of L_{tr}^{pre} ($x = 0$) is null, while the strain beyond the L_{tr}^{pre} ($x \geq L_{tr}^{pre}$) is equal to ε_r^{pre} being the subscript "*r*" representative of the tensile strain due to prestressing for either steel strand or GFRP bars. In order to evaluate experimentally the value of L_{tr}^{pre}, a total of three strain gauges were installed on the steel strand as well as GFRP line 2 near to the extremity of the beams at loading side (Figure 5-8a). These strain gauges were designated by letter a, b and c and installed, respectively, at section distanced 50, 100 and 150 mm from the end section in IB7, IB9 and IB10 (Figure 5-8a). The values of tensile strain measured by these strain gauges are plotted in Figure 5-8a in terms of strain *versus* the distance from the extremity of the beam (loading side of the beam where the actuators were located). By the relevant boundary condition that was presented in Eq. (4-29) in Chapter 4, the IBL algorithm described in Annex 4B can be employed to obtain the distribution of the tensile strain of the prestressed reinforcing bars after releasing. By fitting the obtained theoretical diagram to the results measured by the strain gauges, the bond-slip constitutive law of each reinforcing bar can be calibrated. This calibration can be only done for the elastic and hardening bond phases

(as discussed in Chapter 4) due to the limited value of prestressed force. However, the calibrated bond-slip laws will be still relevant for future crack analysis procedure in this chapter. The results of this calibration in terms of bond-slip constitutive law for GFRP bars and steel strand is plotted in Figure 5-8b.

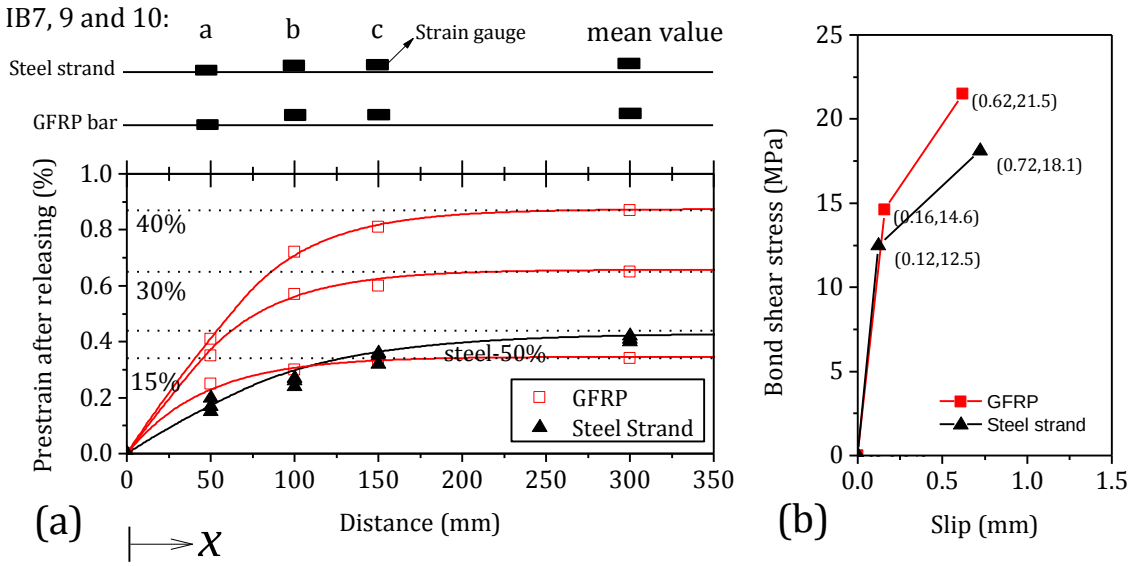

Figure 5-8: Transferred bond length due to the prestressed force; (a) distribution of tensile strain of reinforcements, and (b) calibrated bond-slip law

5.3 Theoretical investigation

In this section, nominal flexural strength, as well as moment-deflection and moment-crack width responses of the tested beams were theoretically investigated. A new concept of balanced reinforced ratio was defined for the proposed hybrid system in this study in order to establish a design criteria for addressing different flexural response of the HPFRC prestressed beams. Due to the complex behavior of the HPFRC I-beams under flexure-shear mechanism, and also many involved parameters that should be known to understand their shear behavior, the nominal shear strength of the beams was evaluated through a simplified flexure-shear mechanism that is based on an unified approach dealing with the moment-rotation presented by Oehlers *et al.* (2011). Moreover, the formulation recommended by CEB-FIB model code 2010 for calculation of the nominal shear strength of FRC beams reinforced by conventional steel reinforcements and without shear reinforcements was used to predict the shear resistance of the tested beams. These results were compared with the

experimental results in the Section 5.4.

Finally, using the bond model previously presented in Chapter 3, and considering the concepts of tension-stiffening of the hybrid FRC system discussed in Chapter 4, the crack spacing of the tested beams was theoretically determined. By employing the FBL model described earlier in Chapter 4 (presented in Annex 4B), and considering the compatibility of deformation at crack section based on the moment rotation approach (Visintin 2012), the crack width of the beam under service load condition was predicted for each step of the applied moment. The calculated theoretical crack width was validated by the *CMOD* measured during the monotonic tests.

5.3.1 Balanced reinforcement ratio

For conventional steel reinforced RC beams, the balanced steel reinforcement ratio, *i.e.* ρ_{sb}, is a condition that beam fails by crushing of concrete in compression and yielding of steel in tension simultaneously. For FRP reinforced RC beams, the balanced FRP reinforcement ratio, ρ_{fb}, is a condition that the beam fails by crushing of concrete and rupture of FRP reinforcement simultaneously. When these two cases are combined in hybrid reinforced beams, the balanced reinforcement ratio is defined as a failure condition in which concrete crushing, yielding of steel, and rupture of FRP occur at the same time. However, this situation is almost impractical. Therefore, the balanced reinforcement ratio may be defined as a situation that concrete crushing in compression and rupture of FRP bars happen simultaneously, while the steel reinforcement has already yielded. From this standpoint, the hybrid balanced reinforcement ratio of FRP/steel RC beam, ρ_{hb}, is calculated using the following equation (Leung and Balendran 2003, Lau and Pam 2010):

$$\rho_{fb} = \alpha_1 \beta_1 \frac{f_c'}{f_{fu}} \frac{E_f \varepsilon_c'}{E_f \varepsilon_c' + f_{fu}} - m_s \rho_s \qquad (5\text{-}4)$$

where α_1 and β_1 are the parameters defining the rectangular stress block, as illustrated in Figure 5-9. The parameter α_1 is the ratio between the equivalent average concrete compressive stress and the concrete compressive strength, f_c', while the parameter β_1 is a

factor relating the depth of equivalent rectangular concrete compressive stress block to neutral axis depth., c (c_b in the balanced conditions). The parameter ε_c' in Eq. (5-4) is the concrete compressive strain corresponding to f_c' (it is assumed equal to 0.0035). The parameters f_{fu} and E_f are the ultimate tensile stress and Young's modulus of FRP bar, respectively (Table 5-1). Moreover, the second term on the right side of Eq. (5-4) intends to simulate the presence of yielded steel reinforcement in the balanced section, in which m_s is

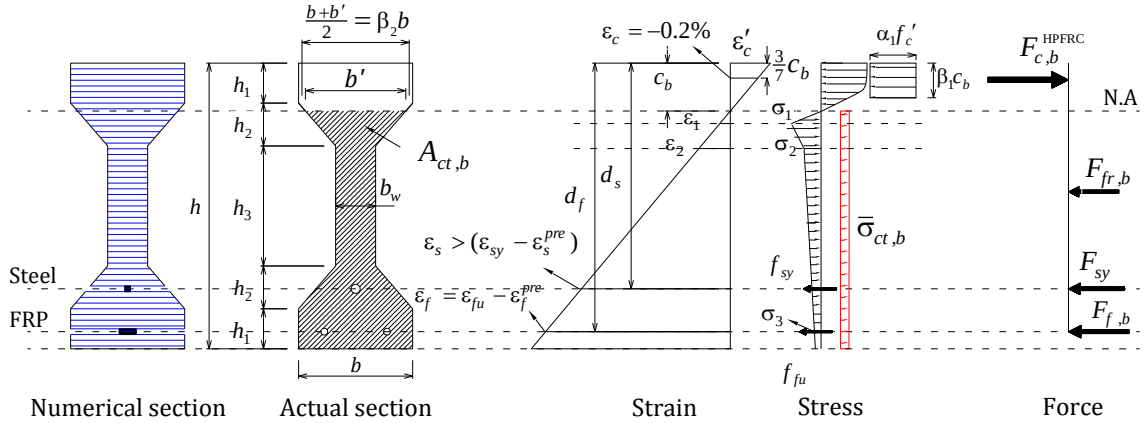

Figure 5-9: Balanced section of HPFRC beam reinforced by hybrid prestressed steel and FRP bars (not to scale)

$$m_s = \frac{d_s}{d_f}\frac{f_{sy}}{f_{fu}} \tag{5-5}$$

where d_s and d_f are the internal arm of steel and FRP reinforcement, respectively, as represented in Figure 5-3. For the case of hybrid GFRP/steel reinforced HPFRC prestressed beams, Eq. (5-4) has to be modified by considering the effect of prestressing in FRP and steel, as well as the post-cracking response of HPFRC. By assuming that plane section remains plane during the loading process of the beam (Bernoulli), the strain compatibility shown in Figure 5-9 allows determination of the c_b/d_f ratio in terms of the installed strains at the balanced section:

$$\frac{c_b}{d_f} = \frac{\varepsilon_c'}{\varepsilon_c' + \varepsilon_{fu} - \varepsilon_f^{pre}} \tag{5-6}$$

where ε_f^{pre} is the average pre-strain of FRP bar reported previously in Table 5-7. Note that the possible losses of pre-strain due to the creep and shrinkage of HPFRC, elastic shortening

of HPFRC, and *etc.* are all included in the value of ε_f^{pre}. From the equilibrium condition at balanced section of the hybrid HPFRC beam, the compressive force due to HPFRC, $F_{c,b}^{HPFRC}$, is in static balance with the tensile force due to the yielded steel strand, F_{sy}, tensile force due to the FRP bars at the balanced condition, $F_{f,b}$, and tensile force due to the fibers at balanced section condition, $F_{fr,b}$. Hence

$$F_{c,b}^{HPFRC} = F_{sy} + F_{f,b} + F_{fr,b} \tag{5-7}$$

with

$$F_{c,b}^{HPFRC} = \alpha_1\beta_1\beta_2 f_c' c_b b \tag{5-8}$$

where β_2 is the parameter that takes into account the particular geometry of the adopted I shape cross section, giving by

$$\beta_2 = \begin{cases} 1 & c_b \le h_1 \\ 1 - \dfrac{c_b - h_1}{2bh_2}(b - b_w) & h_1 < c_b \le h_2 \end{cases} \tag{5-9}$$

The tensile force of reinforcing bars are

$$F_{sy} = \rho_s d_s b f_{sy} \tag{5-10}$$

$$F_{f,b} = \rho_f d_f b f_{fu} \tag{5-11}$$

Therefore, by substituting Eqs. (5-8), (5-10) and (5-11) into Eq. (5-7), and dividing the both sides of the equation by d_f, Eq. (5-7) becomes

$$\alpha_1\beta_1\beta_2 f_c' \frac{c_b}{d_f} b = \rho_f b f_{fu} + \rho_s \frac{d_s}{d_f} b f_{sy} + \frac{F_{fr,b}}{d_f} \tag{5-12}$$

By considering an equivalent average value of crack tensile stress of HPFRC over the distance $h - c_b$ at the balanced section (*i.e.* $\bar{\sigma}_{ct,b}^{cr}$ shown in Figure 5-9), $F_{fr,b}$ becomes

$$F_{fr,b} = \bar{\sigma}_{ct,b}^{cr} A_{ct,b} \tag{5-13}$$

where $A_{ct,b}$ is the tensile area of the section as shown in Figure 5-9, and it is derived by

$$A_{ct,b} = A_g - c_b(\beta_2 b) \tag{5-14}$$

where A_g is the gross area of HPFRC beam section. Eq. (5-14) can be rewritten as follow

$$A_{ct,b} = \left(\rho_c - \frac{c_b}{d_f} \beta_2 \right) b d_f \tag{5-15}$$

with

$$\rho_c = \frac{A_g}{b d_f} \tag{5-16}$$

Therefore, Eq. (5-13) becomes

$$F_{fr,b} = \bar{\sigma}_{ct,b}^{cr} \left(\rho_c - \frac{c_b}{d_f} \beta_2 \right) b d_f \tag{5-17}$$

By substituting Eq. (5-17) into Eq. (5-12), and taking c_b / d_f from Eq. (5-6), the value of ρ_f in Eq. (5-12) is found as the balanced reinforcement ratio in hybrid FRP/steel HPFRC prestressed beam, giving by

$$\rho_{hb} = \alpha_1 \beta_1 \beta_2 \left(\frac{f_c'}{f_{fu}} + m_{fr} \right) \frac{\varepsilon_c'}{\varepsilon_c' + \varepsilon_{fu} - \varepsilon_f^{pre}} - m_s \rho_s - m_{fr} \rho_c \tag{5-18}$$

where

$$m_{fr} = \frac{\bar{\sigma}_{ct,b}^{cr}}{f_{fu}} \tag{5-19}$$

The value of $\bar{\sigma}_{ct,b}^{cr}$ can be estimated by considering the stress-strain diagram of HPFRC in tension (*i.e.* $\sigma_{ct} - \varepsilon_{ct}$) similar to the recommendations by RILEM TC 162-TDF for design purpose of fiber reinforced concrete (FRC). This stress-strain diagram is plotted in Figure 5-10a for compressive strain and in Figure 5-10b for tensile strain. The mathematical expression of this diagram is given by:

$$\sigma_c(\varepsilon_c) = \begin{cases} E_c \varepsilon_c & \varepsilon_c \le \varepsilon_{cp} \\ f_c' & \varepsilon_c > \varepsilon_{cp} \end{cases}, \qquad \sigma_{ct}(\varepsilon_{ct}) = \begin{cases} E_c \varepsilon_{ct} & 0 \le \varepsilon_{ct} \le \varepsilon_1 \\ \sigma_1 + \dfrac{\sigma_2 - \sigma_1}{\varepsilon_2 - \varepsilon_1} \cdot (\varepsilon_{ct} - \varepsilon_1) & \varepsilon_1 < \varepsilon_{ct} \le \varepsilon_2 \\ \sigma_2 + \dfrac{\sigma_3 - \sigma_2}{\varepsilon_3 - \varepsilon_2} \cdot (\varepsilon_{ct} - \varepsilon_2) & \varepsilon_2 < \varepsilon_{ct} \le \varepsilon_3 \end{cases} \tag{5-20}$$

Where ε_c and ε_{ct} are, respectively, the compressive and tensile strain of HPFRC, while ε_{cp} defines the threshold of plastic limit for HPFRC in compression (shown in Figure 5-10a), which is taken as f_c'/E_c . Further, σ_1 , σ_2 and σ_3 are calculated based on the residual flexural tensile strength, which were obtained based on the residual tensile strength from the

notched beam bending test (see Table 5-5), giving by the following equations:

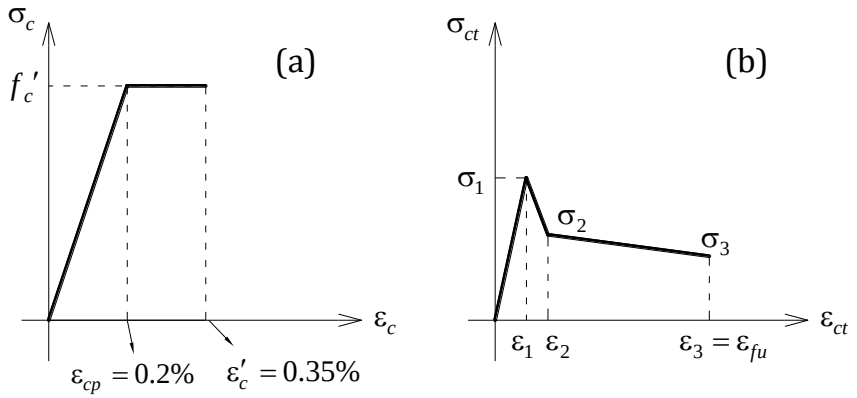

Figure 5-10: Stress-strain diagram for design purpose of FRC material based on recommendation of RILEM in (a) compression, and (b) tension

$$\sigma_1 = 0.7 f_{ct,L} \tag{5-21}$$

$$\sigma_2 = 0.45 f_{R,1} \kappa_h \tag{5-22}$$

$$\sigma_3 = 0.37 f_{R,4} \kappa_h \tag{5-23}$$

where κ_h is the size factor that is

$$\kappa_h = 1.0 - 0.6 \frac{h - 125}{475} \tag{5-24}$$

and it is calculated $\kappa_h = 0.53$ for case of this study. The strain values of ε_1, ε_2 and ε_3 are calculated using the following equations (RILEM TC 162-TDF):

$$\varepsilon_1 = \frac{\sigma_1}{E_c} \tag{5-25}$$

$$\varepsilon_2 = \varepsilon_1 + 0.01\% \tag{5-26}$$

$$\varepsilon_3 \approx \varepsilon_{fu} = \frac{f_{fu}}{E_f} \tag{5-27}$$

where ε_{fu} is the ultimate tensile strain of FRP bar. Note that the average values were included in Table 5-4 are used for E_c and f_c', and the average values were included in Table 5-5 for $f_{ct,L}$, $f_{R,1}$ and $f_{R,4}$. The stress-strain diagram defined in Eq. (5-20) is plotted in Figure 5-11 for the developed HPFRC. As shown, the crack tensile strain is only defined up to the tensile strain at failing of FRP bars (*i.e.* $\varepsilon_3 \approx \varepsilon_{fu}$). Based on this diagram, the

average crack tensile stress of HPFRC at the balanced section can be estimated by

$$\bar{\sigma}_{ct,b}^{cr} = \frac{1}{2}(\sigma_2 + \sigma_3) = \frac{\kappa_h}{2}(0.45 f_{R,1} + 0.37 f_{R,4}) \quad (5\text{-}28)$$

In the balanced section condition, the compressive strain is $\varepsilon_c = \varepsilon_{cp} = 0.2\%$ at level of $\frac{3}{7}c_b$ measured from the top surface (RILEM TC 162-TDF), as shown in Figure 5-9. Therefore, the equivalent rectangular HPFRC stress block in compression can be defined by $\beta_1 = 3/7 + (1/2)(4/7) = 0.714$, if $\alpha_1 = 1$.

In order to verify the reliability of Eq. (5-18) to calculate the balanced reinforcement ratio, ρ_{hb}, a sectional analysis is carried out by using a software named DOCROS (Design Of CROss Section) that calculates the moment–curvature relation as well as the strain distribution along the section by taking into account the constitutive laws of the materials, the kinematic and the equilibrium conditions (more detail about this analysis can be found from the study carried out by Varma *et. al.* 2013, Barros *et al.* 2006, and Taheri *et al.* 2011). For this purpose, the cross section was discretized in layers of 5 mm (Numerical section shown in Figure 5-9), and the constitutive model of the intervening materials (shown in Figure 5-11) were assigned to their respective layers. In this software, the compressive stress strain relationship is simulated according to the model proposed by Barros *et al.* (2008), and the post-cracking response of HPFRC was defined based on the average tensile stress-crack opening diagram obtained by an inverse analysis technique using the *F-CMOD* response of the notched beam tests. The inverse analysis consisted in applying a numerical strategy similar to the one described in the work carried out by Cunha (2010). This inverse analysis will be described later in Chapter 6. The average 4-linear diagram of the stress-crack opening from this inverse analysis is plotted in Figure 5-11c. The stress-crack opening diagram is converted to the stress-strain diagram by considering the structural characteristic length l_{cs} (CEB-FIB Model Code 2010). Based on the Model Code 2010, this value can be taken as the smaller value of the average crack spacing and the distance between the neutral axis and the tensile side of the section. For case of the tested beams, l_{cs} is taken as the average final crack spacing (*i.e.* S_{cr}) that is computed later in Section 5.3.5. This stress-strain diagram is

plotted in Figure 5-11b, and it is compared with the one recommended by RILEM. Additionally, the tensile stress-strain of the steel strand and GFRP bars are plotted in Figure 5-11d and e, respectively. The respective values that define the aforementioned diagrams of HPFRC in tension are included in Table 5-8. The hybrid balanced reinforcement ratio, ρ_{hb}, was found by changing the value of ρ_f in DOCROS software for a situation that the compressive strain at top surface was $\varepsilon_c' = 0.0035$, and simultaneously the tensile strain of FRP bars was ε_{fu}. Note that the values of pre-strain (see Table 5-7) were assigned to the respective layers for FRP bars and steel strand, which results in negative value for curvature at the initiating of the analysis.

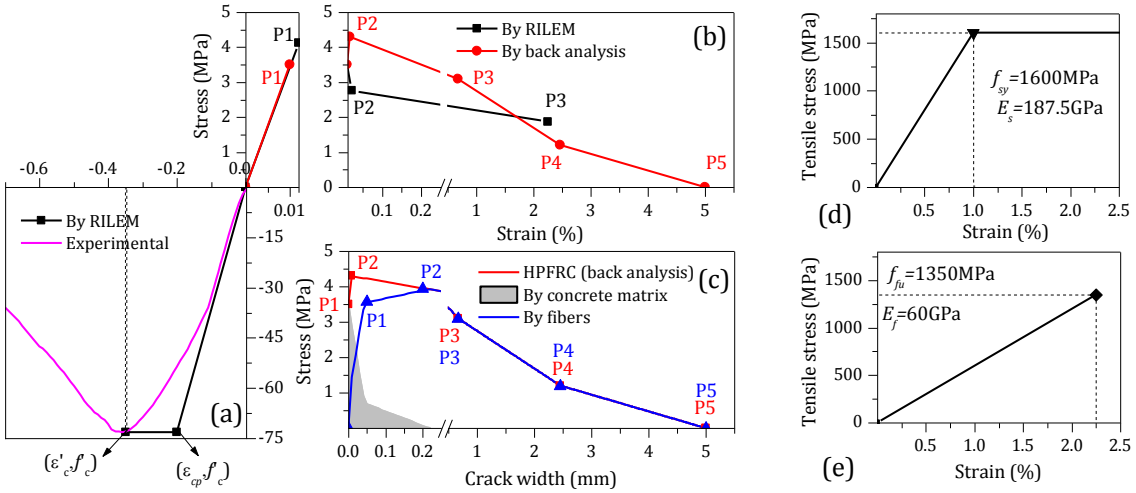

Figure 5-11: Constitutive laws of the materials: (a) HPFRC compressive stress-strain, (b) crack tensile stress-strain of HPFRC, (c) crack tensile stress-crack opening of HPFRC, (d) tensile stress-strain of steel strand, and (e) tensile stress-strain of GFRP bar

Table 5-8: The values that define the stress-strain and stress-crack opening relationship of HPFRC (see Figure 5-11a, b and c)

	Point 1		**Point 2**		**Point 3**		**Point 4**		**Point 5**	
	Strain (%)	**Stress (MPa)**	**Strain (%)**	**Stress (MPa)**	**Strain (%)**	**Stress (MPa)**	**Strain (%)**	**Stress (MPa)**	**Strain (%)**	**Stress (MPa)**
By RILEM	0.012	4.13	0.022	2.76	2.25	1.87	-	-	-	-
By inverse analysis (total response)	0.010	3.50	0.017	4.30	0.68	3.10	2.47	1.20	5.00	0.0
	Point 1		**Point 2**		**Point 3**		**Point 4**		**Point 5**	
	CMOD (mm)	**Stress (MPa)**	**CMOD (mm)**	**Stress (MPa)**	**CMOD (mm)**	**Stress (MPa)**	**CMOD (mm)**	**Stress (MPa)**	**CMOD (mm)**	**Stress (MPa)**
By inverse analysis (total response)	0.0	3.50	0.007	4.30	0.67	3.10	2.46	1.20	5.00	0.0
By inverse analysis (By fibers)	0.05	3.57	0.20	3.95	0.67	3.10	2.46	1.20	5.00	0.0

The calculated values of the balanced reinforcement ratio of the experimental beams by

Eq. (5-18) and by the sectional analysis using DOCROS software are written in Table 5-9. According to the results, the first three specimens in Group A (*i.e.* IB1, 2, and 3) are nearly balanced-reinforced beams, while the last specimen in this group is over-reinforced. Besides, the beams in group B are all under-reinforced.

Table 5-9: The balanced reinforcement ratio of the tested beams

Group	Specimen ID	ρ_f	ρ_s	β_2	ε_f^{pre}	By Eqs. (5-6) and (5-18)		By DOCROS		Over/under reinforced
						c_b	ρ_{hb}	c_b	ρ_{hb}	
		(%)	(%)	(-)	(%)	(mm)	(%)	(mm)	(%)	
A	IB1	0.29	0.18	1.00	0.0	63.3	0.25	66.2	0.23	~Balanced
	IB2	0.29	0.18	1.00	0.0	63.3	0.25	66.2	0.23	~Balanced
	IB3	0.29	0.18	1.00	0.0	63.3	0.25	66.2	0.23	~Balanced
	IB4	0.43	0.18	1.00	0.0	63.3	0.25	66.2	0.23	Over
B	IB5	0.29	0.07	1.00	0.0	63.3	0.36	66.2	0.33	Under
	IB6,7	0.29	0.07	0.99	0.31	71.8	0.43	75.1	0.40	Under
	IB8,9	0.29	0.07	0.95	0.59	81.8	0.49	86.1	0.48	Under
	IB10	0.29	0.07	0.90	0.82	92.4	0.53	98.2	0.56	Under

The balanced reinforcement ratio increase by increasing the amount of prestress in FRP bars, but, it is not influenced by the amount of the prestress in the steel reinforcement. This is due to the fact that the yielding of steel always occurs prior to the concrete crushing or FRP bar rupturing. As mentioned earlier in Chapter 2, the presence of prestressed steel reinforcements in the hybrid system is to increase the serviceability requirements of FRP reinforced beams as well as providing the minimum structural requirements in the case of failing of FRP reinforcements due to the high temperature (e.g. fire).

5.3.2 Nominal flexural strength

If the hybrid reinforced HPFRC prestressed beam is under-reinforced, *i.e.* $\rho_f < \rho_{fb}$, a tension-controlled section condition occurs as a result of FRP bars rupture before crushing of HPFRC in compression (*i.e.* $\varepsilon_f = \varepsilon_{fu}$ and $\varepsilon_c < \varepsilon_c' = 0.0035$). Conversely, if $\rho_f \geq \rho_{fb}$, a compression-controlled section condition occurs in which the HPFRC crushes with no failure of the FRP bars (*i.e.* $\varepsilon_f < \varepsilon_{fu}$ and $\varepsilon_c = \varepsilon_c' = 0.0035$). Note that in both cases, it is assumed that the steel strand has already yielded. These two nominal flexural failing conditions are illustrated in Figure 5-12. If the linear distribution of strain along the depth of the section is adopted (Bernoulli assumption), the calculation of the nominal flexural

strength incorporates two unknown parameters: the level of neutral axis (*i.e.* c) and the tensile strain of FRP bars for condition 1, or the compressive strain of HPFRC for condition 2. The depth of neutral axis, *i.e.* c, can be efficiently approximated by equalizing the variation of force between the section at the nominal failing condition and the balanced failing condition:

$$(F_c^{\text{HPFRC}} - F_{c,b}^{\text{HPFRC}}) \cong \left(F_f - F_{f,b}\right) + \left(F_{fr} - F_{fr,b}\right) \tag{5-29}$$

where F_c^{HPFRC} and F_{fr} are the compressive force and the tensile force assured by HPFRC at nominal failing condition, while F_f represent the tensile force due to FRP bars at this section. Note that it is assumed that the steel already yielded, hence, the tensile stress variation in this reinforcement is null. Eq. (5-29) can be written as follow:

$$m_1 f_c'(\beta_2 b)(c - c_b) \cong m_2 f_{fu} b d_f (\rho_f - \rho_{fb}) + \bar{\sigma}_{ct,b}^{cr} (\beta_2 b)(c - c_b) \tag{5-30}$$

where m_1 and m_2 are the modification factors that take into account, respectively, the change of HPFRC compressive rectangular stress block and the tensile stress of FRP bar, at the nominal failing condition with respect to the balanced failing conditions. Eq. (5-30) becomes

$$c = c_b + \gamma\left(\rho_f - \rho_{fb}\right) \tag{5-31}$$

with

$$\gamma = \frac{m_2 f_{fu}}{\beta_2 (m_1 f_c' - \bar{\sigma}_{ct,b}^{cr})} d_f \tag{5-32}$$

where c_b and ρ_{fb} can be calculated by Eqs. (5-6) and (5-18), respectively. The definition of the modification factors, m_1 and m_2 are not straightforward since they are dependent on the depth of neutral axis, c. But, in order to proceed with the calculation of c, they can be approximated by the following equations, depending on the ratio between ρ_f and ρ_{hb}:

$$m_1 = \begin{cases} (1 + \rho_f / \rho_{hb})\beta_1 & \rho_f \le \rho_{hb} \\ \beta_1 & \rho_f > \rho_{hb} \end{cases}, \quad m_2 = \begin{cases} 1 & \rho_f \le \rho_{hb} \\ \rho_{hb} / \rho_f & \rho_f > \rho_{hb} \end{cases} \tag{5-33}$$

where the parameter β_1 corresponds to the compressive strain of ε_c', and the parameter β_2 is calculated for the value of c_b from Eq. (5-9).

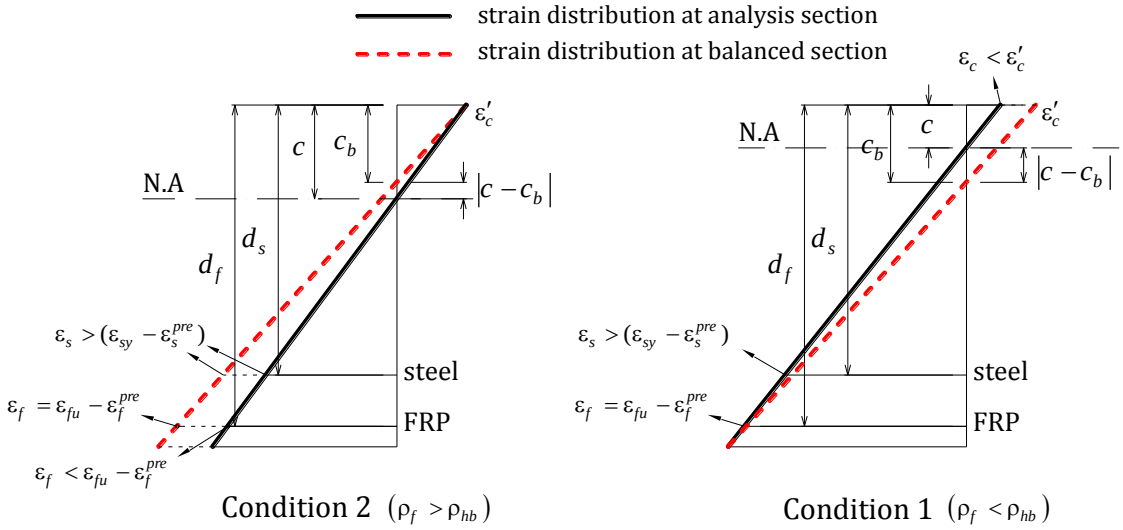

Figure 5-12: Nominal flexural failing conditions of strain being over- or under-reinforced condition for hybrid FRP/steel reinforced HPFRC prestressed beams

By having obtained the value of c, the nominal flexural strength of the hybrid FRP/steel reinforced HPFRC prestressed beam, M_n, is calculated under the following two conditions:

Condition 1 ($\rho_f < \rho_{hb}$): considering the strain compatibility, the concrete compressive strain at top surface is

$$\varepsilon_c = \frac{\varepsilon_{fu} - \varepsilon_f^{pre}}{(d_f - c)} c \tag{5-34}$$

Since the tensile strain of FRP equals to its ultimate value, the average tensile stress of HPFRC is taken to be equal to the respective value at the balanced section (*i.e.* $\bar{\sigma}_{ct,b}^{cr}$, from Eq. (5-28)). Hence, the nominal flexural strength can be determined by summation of moments about the centroid of HPFRC rectangular stress block, giving

$$M_n = F_{sy} \cdot (d_s - \frac{\beta_1 c}{2}) + F_{fu} \cdot (d_f - \frac{\beta_1 c}{2}) + \bar{\sigma}_{ct,b}^{cr} (A_g - c \cdot \beta_2 b) \cdot (d_{fr} - \frac{\beta_1 c}{2}) \tag{5-35}$$

where β_2 is given by Eq. (5-9) for the value c that replaces c_b, and the coefficient β_1 that defines the rectangular HPFRC stress block in compression is calculated based on the following equation, depending on ε_c:

$$\beta_1 = \begin{cases} \frac{1}{2} \frac{E_c \varepsilon_c}{f_c'} & \varepsilon_c \le \varepsilon_{cp} \\ \left(1 - \frac{1}{2} \frac{\varepsilon_{cp}}{\varepsilon_c}\right) & \varepsilon_{cp} < \varepsilon_c \le \varepsilon_c' \end{cases} \le 0.714 \tag{5-36}$$

In addition, the parameter d_{fr} is computed based on different configurations of HPFRC tensile area with the depth of neutral axis, as shown in Figure 5-13. The calculation of d_{fr} is given in Annex 5A. However, as a simpler way, d_{fr} may be given by

$$d_{fr} = \frac{1}{2}(h + c) \tag{5-37}$$

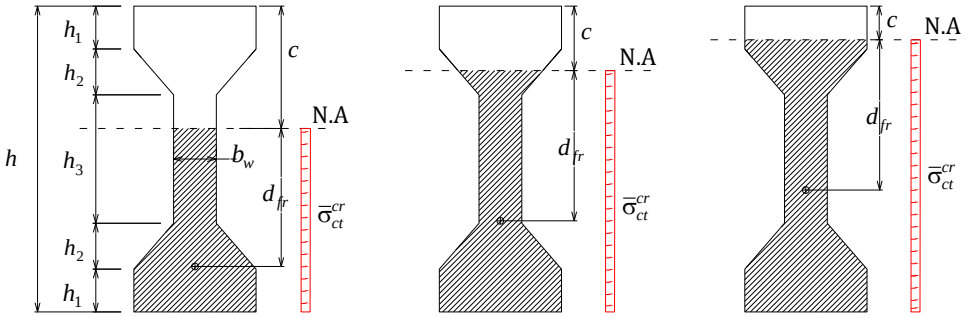

Figure 5-13: different configuration of HPFRC tensile area with variation of the depth of the neutral axis

Condition 2 ($\rho_f > \rho_{fb}$): considering the similar triangles, the tensile strain of FRP bars is determined as

$$\varepsilon_f = \left(\frac{d_f}{c} - 1\right)\varepsilon_c' + \varepsilon_f^{pre} \tag{5-38}$$

Under this condition, the average tensile stress of HPFRC (*i.e.* $\bar{\sigma}_{ct}^{cr}$) can be given by Eq. (5-39), which is based on the average tensile stress of HPFRC between σ_2 and the tensile stress σ_{ct} for $\varepsilon_{ct} = \varepsilon_f$ in Eq. (5-20):

$$\bar{\sigma}_{ct}^{cr} = \frac{1}{2}\left[2\sigma_2 + (\sigma_3 - \sigma_2)\left(\frac{\varepsilon_f - \varepsilon_2}{\varepsilon_{fu} - \varepsilon_2}\right)\right] \tag{5-39}$$

Hence, the nominal flexural strength, M_n, can be determined by summation of moments about the centroid of rectangular HPFRC stress block, giving

$$M_n = F_f \cdot \left(d_f - \frac{\beta_1 c}{2}\right) + F_{sy} \cdot \left(d_s - \frac{\beta_1 c}{2}\right) + \bar{\sigma}_{ct}^{cr}\left(A_g - c \cdot \beta_2 b\right) \cdot \left(d_{fr} - \frac{\beta_1 c}{2}\right) \tag{5-40}$$

where $\beta_1 = 0.714$, and β_2 is determined by Eq. (5-9) for value of c instead of c_b. The calculated values of the nominal flexural strength of the tested beams by Eq. (5-35) or (5-40)

are included in Table 5-10.

Table 5-10: The nominal flexural strength of the tested beams

Specimen ID	By using the proposed analytical formulation					By DOCROS	
	c	ε_f	Maximum HPFRC strain		By Eq. (5-35) or (5-40)		
			Tension ε_{ct}	Compression ε_c	M_n	M_n	M_y *
	(mm)	(%)	(%)	(%)	(kN.m)	(kN.m)	(kN.m)
IB1	66.89	2.11	2.23	0.35	269.9	256.8	214
IB2	66.89	2.11	2.23	0.35	269.9	257.1	202
IB3	66.89	2.11	2.23	0.35	269.9	256.8	189
IB4	79.45	1.72	1.84	0.35	302.3	296.3	242
IB5	57.02	2.25	2.41	0.31	222.7	218.8	165
IB6,7	59.23	2.25	2.09	0.29	225.9	220.8	155
IB8,9	63.85	2.25	1.78	0.26	228.8	222.9	175
IB10	70.86	2.25	1.46	0.23	226.7	224.4	190

* It is obtained using DOCROS software, which correspond to yield initiation in the steel strand for tensile stress of about 1600 MPa at the bending zone.

Moreover, by performing a sectional analysis using the DOCROS software, the nominal flexural strength (M_n) of the tested beams can be calculated, considering the two aforementioned conditions. If the beam is under-reinforced, reaching FRP bar to its ultimate tensile strain is stop condition criteria in the analysis. On the other hand, if the beam is over-reinforced, reaching the compressive strain of HPFRC at top layer to the value of 0.35% is the stop condition. The results of this analysis is also written in Table 5-10. The results of the nominal flexural strength from the proposed equations are in a good agreement with the results by DOCROS. Additionally, the values of the depth of neutral axis calculated by Eq. (5-31) are quite close to those determined by DOCROS. This proofs that the analytical formulation is an efficient tool for design purposes.

5.3.3 Nominal shear strength

The RC beams are normally designed based on their nominal flexural strength, but, they can only reach their flexural strength if shear reinforcements are enough to resist the possible external shear forces. The shear resistance is normally provided by internal steel or FRP stirrups, or external shear reinforcements such as NSM FRP laminates (Dias and Barros 2013), FPR sheets (Norris *et al.* 1997) or ETS bars (Breveglieri *et al.* 2015). However, in the present research study, HPFRC with 90 kg/m^3 steel fibers was utilized to resist the shear force and no other shear reinforcements were used.

The nominal shear strength of HPFRC is analyzed based on a fracture mechanism approach, which accounts for the fact that HPFRC prestressed beam fails in shear due to the propagation of a critical diagonal crack (named as CDC). By analyzing this crack through the equilibrium equations as well as compatibility relationships for the respective deformations, the maximum shear force that carried by the prestressed beam before its failure is determined, and it can be considered as the nominal shear strength, *i.e.* V_n.

For the loading configuration adopted in this study, the effective shear zones can be considered as two gray areas highlighted in Figure 5-14. These areas can be identified using the equivalent depth of the beam, *i.e.* $d_{f,eq}$, as shown in Figure 5-14. The value of $d_{f,eq}$ is defined as the distance between the top surface of HPFRC and the centroid of equivalent longitudinal reinforcements at the bottom, giving by

$$d_{f,eq} = \frac{n_r \rho_s d_s + \rho_f d_f}{\rho_{f,eq}} \tag{5-41}$$

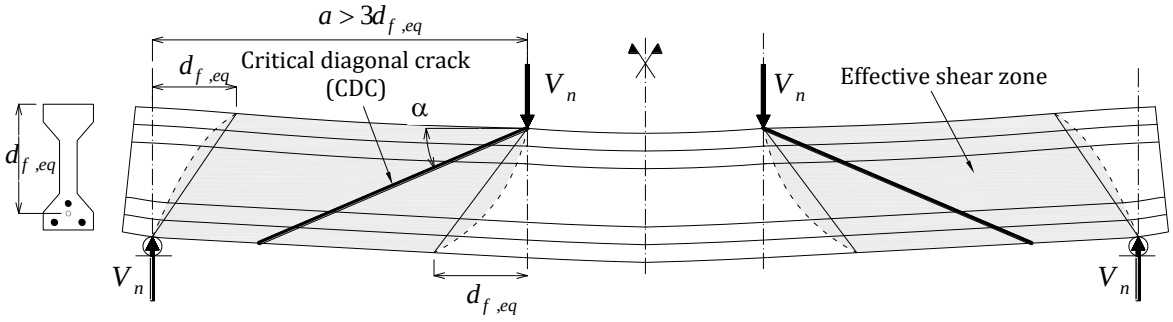

Figure 5-14: The critical diagonal crack (CDC) in shear span for the loading configuration of the tested beams

where the parameter $\rho_{f,eq}$ is the effective reinforcement ratio

$$\rho_{f,eq} = n_r \rho_s + \rho_f \tag{5-42}$$

with

$$n_r = \frac{E_s}{E_f} \tag{5-43}$$

For relatively long shear span, $a > 3d_{f,eq}$, the CDC may be taken as a diagonal line with an inclination of α in respect to the longitudinal axis of the beam, as shown in Figure 5-14.

5.3.3.1 Flexure-shear mechanism

To analyze the CDC, a flexure-shear mechanism similar to the one discussed by Oehlers *et al.* 2010 can be followed. The internal forces that are acting over the CDC are shown in Figure 5-15. The line 'OA' in this figure is the compressive part, and line 'OB' is the CDC face. The value of c_v defines the depth of the neutral axis where the longitudinal strain is null (*i.e.* point 'O'). The internal forces shown in this figure have to be in static balance with the external shear force and its moment. It is easier to consider the line 'OC' instead of 'OA' for deriving the equilibrium equations. Hence, in the vertical direction

$$V = F_{fr,n}\cos\alpha + F_{fr,v}\sin\alpha + F_{c,v} \tag{5-44}$$

where $F_{c,v}$ is the resultant of tangential force at the compressive zone along the line 'OC'. This component is negligible since the value of c_v becomes small at the failure stage. The force $F_{fr,n}$ is the resultant of normal tensile force due to the steel fibers at tensile zone of the crack, while $F_{fr,v}$ is the tangential force of HPFRC over the line 'OB'.

Additionally, the horizontal equilibrium condition leads to:

$$F_{fr}\sin(\alpha-\varphi) + F_f + F_s = F_{c,n} \tag{5-45}$$

where φ is the angle between the total resultant of the residual force due to the HPFRC (*i.e.* $F_{fr} = \sqrt{{F_{fr,n}}^2 + {F_{fr,v}}^2}$) and the corresponding normal component (*i.e.* $F_{fr,n}$) as shown in Figure 5-15. More details about the angle of φ will be discussed later in Section 5.3.3.2. Further, $F_{c,n}$ is the compressive force of HPFRC normal to the line 'OC' shown in Figure 5-15, which may be obtained by the equivalent rectangular stress block using Eq. (5-8). F_f and F_s are the tensile force of the FRP bars and steel strand respectively, giving by

$$F_f = \left(\varepsilon_f + \varepsilon_f^{pre}\right)E_f\rho_f bd_f = \left(\varepsilon_f + \varepsilon_f^{pre}\right)E_f A_f \tag{5-46}$$

$$F_s = \begin{cases}\left(\varepsilon_s + \varepsilon_s^{pre}\right)E_s\rho_s bd_s = \left(\varepsilon_s + \varepsilon_s^{pre}\right)E_s A_s & \varepsilon_s \le \varepsilon_{sy} - \varepsilon_s^{pre} \\ f_{sy}\rho_s bd_s = f_{sy}A_s & \varepsilon_s > \varepsilon_{sy} - \varepsilon_s^{pre}\end{cases} \tag{5-47}$$

where the parameters in the above equations were all defined previously in Section 5.3.2.

Note that the constitutive laws plotted in Figure 5-11d and Figure 5-11e are used for defining the behavior of the longitudinal reinforcement in tension.

Finally, if it is assumed that the compressive wedge 'OAC' becomes small at the failure stage, the summation of moment about the centroid of this compressive wedge can be expressed as the following equation:

$$F_f\left(d_f-\frac{\beta_1 c_v}{2}\right)+F_s\left(d_s-\frac{\beta_1 c_v}{2}\right)+F_{fr,n}\left(d_{fr}-\frac{\beta_1 c_v}{2}\right)\text{cossec}(\alpha)=V\left(a-c_v\cot\alpha\right) \quad (5\text{-}48)$$

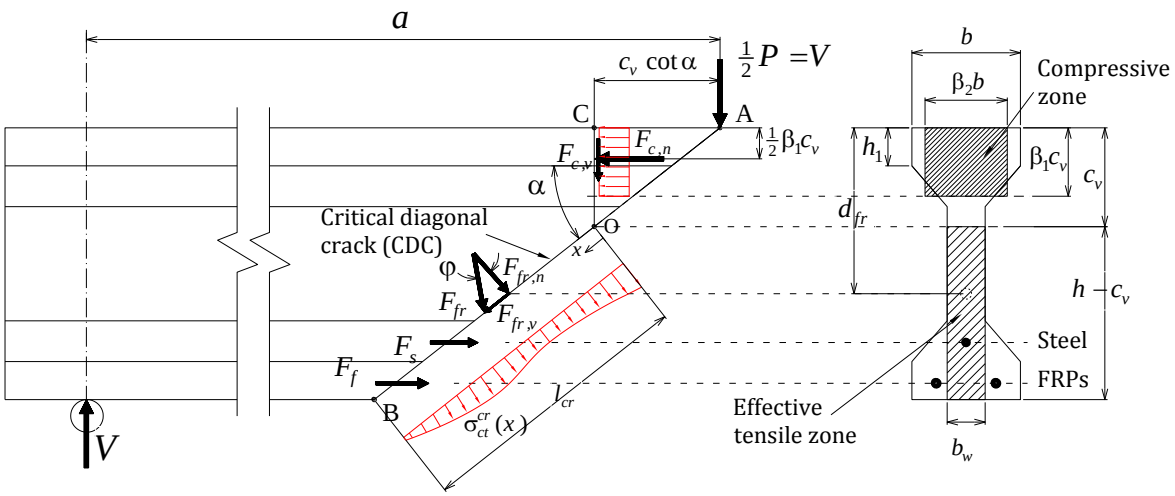

Figure 5-15: Illustration of internal forces acting over the critical diagonal crack (CDC)

where a is shear span, d_{fr} is depth of $F_{fr,n}$ as illustrated in Figure 5-15, which is calculated by Eq. (5-59). The parameter V is the reaction of the applied load at location of the beam support being equal to the half value of the total applied load (*i.e.* P) due to the static balanced condition of the whole beam. The coefficient β_1 defines the depth of the equivalent HPFRC stress block as previously defined in 5.3.2 (assuming linear distribution of compressive strain along 'OC'). Note that the moment due to $F_{fr,v}$ is assumed to be negligible based on the assumption that the compressive wedge of 'OAC' becomes small at the failure stage.

According to the above equilibrium equations, two scenarios can be theoretically taken place at the failure stage:

1) By increasing the shear force in shear span, the crack tip (near to point 'O') grows through the compressive zone in order to provide larger crack face (*i.e.* c_v is getting

smaller), leading to increase the residual tensile force of HPFRC in order to resist the external shear force (as it will be also discussed in Section 5.3.4.1). On the other hand, the compressive force increases significantly since the compressive zone is becoming smaller. The failure can be assumed when the balanced force in the horizontal direction (Eq. (5-45)) is no longer satisfied. Therefore, the maximum shear resistance is attained when the compressive force reaches its maximum value

$$F_{c,n} = (\beta_1 c_v)(\beta_2 b) f_c' \tag{5-49}$$

where $\beta_1 = 0.714$ using the bi-linear law for concrete in compression as plotted in Figure 5-10, and $\beta_2 = 1$ for $c < h_1$;

2) While the crack tip grows through the compressive zone, the crack width becomes wider at the location of the longitudinal reinforcements due to the imposed rotation to the CDC by the applied moment. The second scenario is when the longitudinal reinforcements reach their ultimate tensile strain prior to the maximum value of the concrete in compression. This scenario seems realistic if very low reinforcement ratio is utilized. However, the lower reinforcement ratio leads to more possibly having the failing of the beam in the pure bending zone rather than in shear span.

In order to determine the nominal shear strength, the equilibrium equations (*i.e.* Eqs. (5-44), (5-45), and (5-48)) are solved for value of V by considering the first scenario. Such analysis incorporates many unknown parameters that becomes complex to solve. Therefore, the compatibility relationships among the deformations of the intervening materials are required to reduce the number of unknown parameters.

In a flexure-shear crack, due to the existence of shear stress over the crack plane and its variation along the crack, the crack plane does not remain plane. It is assumed that the maximum crack opening occurs at the junction between web and flange due to the lower thickness of the beam, as well as its higher shear stress concentration when it compares with the bottom flange. Therefore, it is more realistic to consider the variation of crack width along the crack face as two linear profiles. This adopted deformation profile is illustrated in Figure 5-16, where the maximum crack opening, *i.e.* w_{cr}, takes place at the above indicated

transition zone, while the crack width at the bottom of the flange can be defined as $\beta_3 w_{cr}$, where $0<\beta_3 \leq 1$. Hence, the variation of the crack width along the flexure-shear crack plane is defined by

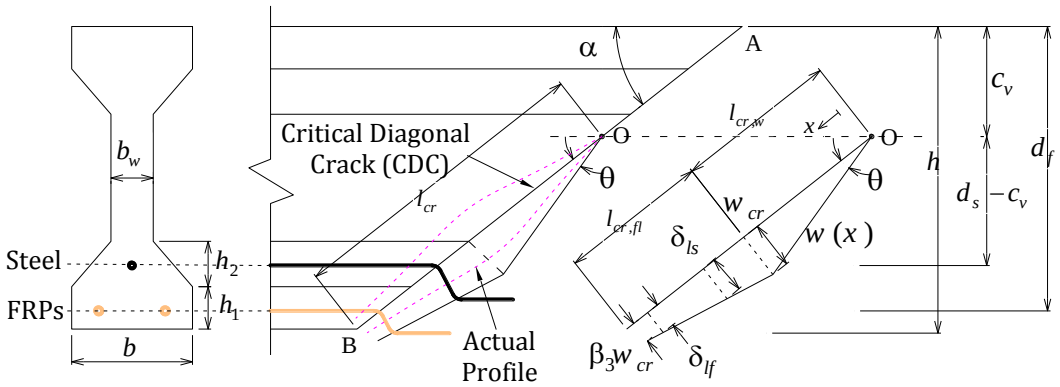

Figure 5-16: Compatibility of the tensile deformations along the CDC

$$w(x)=\begin{cases}\dfrac{w_{cr}}{l_{cr,w}}\cdot x & 0\leq x \leq l_{cr,w} \\ w_{cr}-\dfrac{(1-\beta_3)w_{cr}}{l_{cr,fl}}(x-l_{cr,w}) & l_{cr,w}<x\leq l_{cr}\end{cases} \tag{5-50}$$

with the following definition:

$$l_{cr}=(h-c_v)\,\mathrm{cossec}(\alpha) \tag{5-51}$$

$$l_{cr,fl}=(h_1+h_2)\,\mathrm{cossec}(\alpha) \tag{5-52}$$

and

$$l_{cr,w}=l_{cr}-l_{cr,fl} \tag{5-53}$$

where x origins from point 'O' toward the CDC (line 'OB' in Figure 5-16). The relation between the crack width and the slip of the reinforcements can be determined by

$$\delta_s=\frac{1}{2}w\left(x_s=(d_s-c_v)\,\mathrm{cossec}(\alpha)\right) \tag{5-54}$$

$$\delta_f=\frac{1}{2}w\left(x_f=(d_f-c_v)\,\mathrm{cossec}(\alpha)\right) \tag{5-55}$$

where δ_f and δ_s are the slip of FRP bars and steel strand, respectively, at the CDC. The slip of the longitudinal reinforcements can be calculated, by imposing w_{cr}. Once these slips are obtained, the FBL model (Annex 4B) is employed to calculate the tensile strain of the

reinforcements taking into account the bond-slip behavior of the reinforcements, which was calibrated in Section 5.2.6. Note that the bond length is taken as the final crack spacing, which will be discussed later in Section 5.3.5. Alternatively, the tensile strain of the longitudinal reinforcements can be simply calculated by dividing the slip by the crack spacing. This means a linear slip distribution over the crack spacing is assumed. By having obtained the tensile strain of FRP bars, *i.e.* ε_f , and the tensile strain of steel strand, *i.e.* ε_s , from the FBL model, their tensile force are computed by Eqs. (5-46) and (5-47). Moreover, the value of $F_{fr,n}$ in Eq. (5-44) can be determined by

$$F_{fr,n} = b_w \int_0^{l_{cr}} \omega \sigma_{ct}^{cr}(w(x))dx \tag{5-56}$$

where $\sigma_{ct}^{cr}(w(x))$ is the normal tensile stress of HPFRC as function of the crack width, which can be determined from direct tensile test (or in-direct tensile test using back analysis technique). The coefficient ω takes into account the degradation of the normal tensile stress due to existence of shear stresses over the crack, which is described in 5.3.3.2.

In addition, the tangential force of HPFRC over the line 'OB' (*i.e.* $F_{fr,v}$) is determined by

$$F_{fr,v} = \begin{cases} \bar{\tau}_{cr}^{m} b_w l_v & w(x) \le w_a \\ F_{fr,n} \tan\varphi & w(x) > w_a \end{cases} \tag{5-57}$$

where $\bar{\tau}_{cr}^{m}$ is the mean crack shear stress, which is effectively due to the frictional behavior of the crack face, and w_a is a limit value of crack opening over which the frictional stress can be assumed almost null for $w(x) > w_a$. Consequently, l_v is defined as a distance of the diagonal crack that the frictional behavior due to the crack surface is still active, given by

$$l_v = \frac{w_a}{w_{cr}} l_{cr,w} \tag{5-58}$$

Finally, the value of d_{fr} in Eq. (5-48) can be determined by the following integral:

$$d_{fr} = c_v + \frac{\int_0^{l_{cr}} \omega \sigma_{ct}^{cr}(w(x))x dx}{\int_0^{l_{cr}} \omega \sigma_{ct}^{cr}(w(x))dx} \sin\alpha \tag{5-59}$$

By substituting Eq. (5-44) into Eq. (5-48), and Eq. (5-49) into Eq. (5-45), a set of two nonlinear equation is obtained in which the unknown parameters are the values of c_v and w_{cr} for the predefined values of α, φ, ω, $\bar{\tau}_{cr}^{m}$, w_a and β_3. A numerical procedure is employed to solve this set of non-linear equations. The algorithm for solving the equations to derive the value of the nominal shear strength, V_n, is presented in Annex 5B. For this purpose, the 4-linear stress-crack opening law ($\sigma_{ct}^{cr} - w$) plotted in Figure 5-17 is used for modeling the post-cracking behavior of HPFRC in tension.

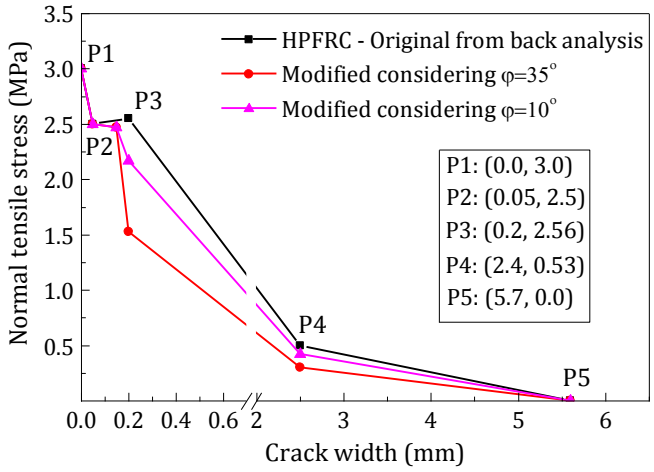

Figure 5-17: Normal tensile stress *versus* crack opening obtained from the back analysis of the notched beam specimens taken from the web plate of the tested I-beams (from Chapter 6)

The original diagram shown in Figure 5-17 is obtained from the back analysis of the *F-CMOD* results of a series of notched beam bending tests that were carried out using the notched beam specimens taken from the HPFRC web plate of the I-beam specimens after the bending test (the un-cracked part of the web plate at the two extremities). More details about these series of notched beam tests, and the respective results of the back analysis will be given later in Chapter 6. Furthermore, the obtained $\sigma_{ct}^{cr} - w$ diagram may not be directly used for the analysis of the CDC, since the crack sliding due to the existing shear stress at crack face influences this diagram. This phenomena is discussed in the next section where the parameters of φ and ω are defined.

5.3.3.2 Definition of φ and ω

For case of HPFRC crack with no tangential force, and tensile force normal to the crack plane as shown in Figure 5-18a, the area under the curve of tensile force *versus CMOD* (or w) can be defined as the total fracture energy that is consumed in the direction normal to the fracture surface. The normal crack tensile stress (*i.e.* σ_{ct}^{cr}) is calculated by dividing the tensile force by the area of the crack plane in which the normal tensile stress *versus* crack width ($\sigma_{ct}^{cr} - w$) is obtained. The area under this diagram is typically defined as the mode I fracture energy (*i.e.* G_f^I) to propagate a tensile crack of unit area.

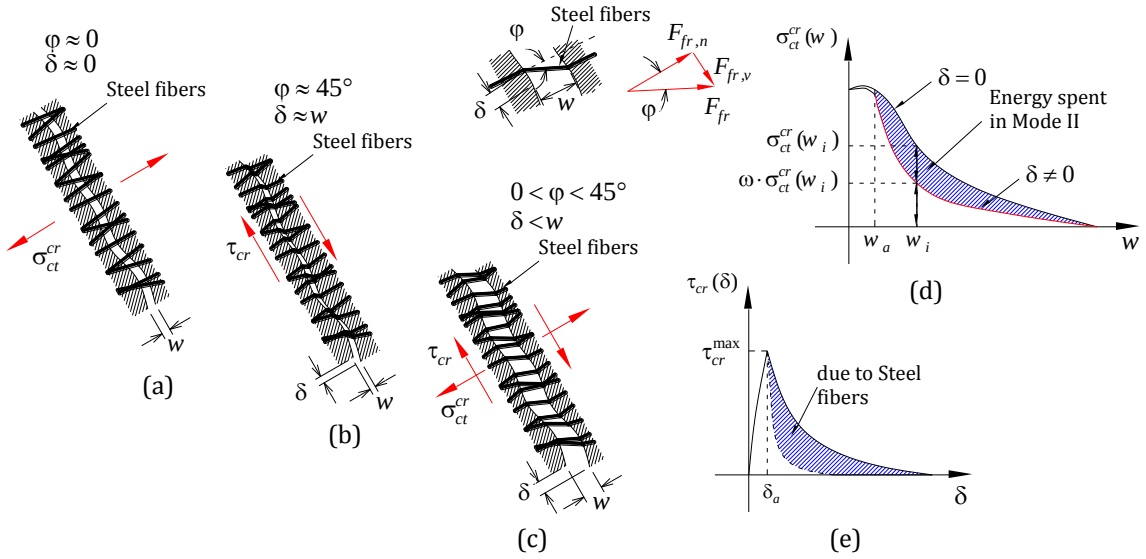

Figure 5-18: Concept of angle φ in HPFRC crack: (a) without tangential force, (b) with only tangential force, (c) with both tangential and normal force, (d) degradation of normal tensile stress-crack opening diagram due to the sliding, and (e) increase in the Mode II fracture energy

For the case shown in Figure 5-18b, the crack is under only shear force, however, due to the elongation and slipping of the steel fibers, splitting of the surrounding paste at the exit point of the fibers, as well as the frictional behavior of crack surface (e.g. overlapping of aggregates), the crack is always opening while it is sliding (δ). After a certain crack opening of w_a , it can be assumed that the crack opening is only due to the slipping and elongation of the steel fibers, and frictional behavior due to the roughness of crack face does not anymore exist. Hence, in an idealized manner, the resultant of residual tensile force of the crack has the same inclination with the fibers in respect to the crack plane. Therefore, the

angle φ may be defined as follow:

$$\varphi = \arctan\left(\frac{\delta}{w}\right) \quad (w > w_a) \tag{5-60}$$

Based on the shear tests carried out by Soltanzadeh *et al.* (2015) on the same type of HPFRC, it has been obtained that the average value of δ and w are almost equal for the same level of applied shear force, leading to define $\varphi \cong 45°$ (see Figure 5-19).

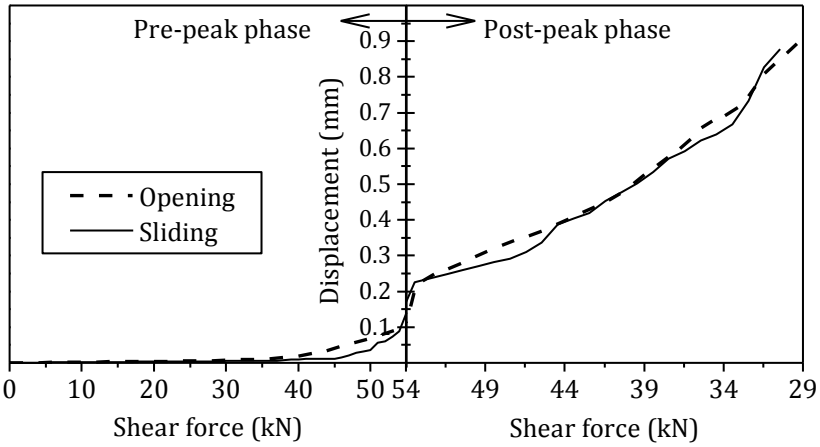

Figure 5-19: Average sliding and opening *versus* the average shear force (based on the results obtained by Soltanzadeh *et al.* 2015 from a direct shear test)

Furthermore, if the crack is under the shear force and the tensile force simultaneously (as shown in Figure 5-18c), the rate of opening is higher than sliding, which leads to have the value of φ ranged between $0 < \varphi < 45°$ for $w > w_a$. Typically, $\sigma_{ct}^{cr} - w$ diagram obtained from direct tensile test is considered for the case that $\varphi = 0$ and $\delta = 0$, hence, the resultant of residual tensile force due to the fibers is assumed normal to the crack face (*i.e.* $F_{fr,n}$). However, when $\delta \neq 0$, the normal residual tensile force cannot be calculated from the original $\sigma_{ct}^{cr} - w$ response where $\delta = 0$, since the fibers are inclined due to the sliding, and consequently they have a tangential component along the crack face. Therefore, after crack opening of w_a, the normal tensile force decreases based on the angle of φ, which is estimated from Eq. (5-60). Based on what shown in Figure 5-18d, the value of tangential over the infinitesimal tensile area of dA_{ct} for $w = w_i$ (when $\delta \neq 0$) can be expressed by

$$dF_{fr,n} = \omega(\varphi)\sigma_{ct}^{n}(w_i)dA_{ct} \qquad (w_i > w_a) \tag{5-61}$$

Based on the expression given in Figure 5-18d (for $\delta \neq 0$), the value of tangential over the infinitesimal tensile area of dA_{ct} is given by

$$dF_{fr,v} \cong \sigma_{ct}^{n}(w_i)dA_{ct} - \omega(\varphi)\sigma_{ct}^{n}(w_i)dA_{ct} = (1-\omega(\varphi))\sigma_{ct}^{n}(w_i)dA_{ct} \quad (w_i > w_a) \qquad (5\text{-}62)$$

where ω is a coefficient that takes into account the reduced portion of the normal tensile stress of steel fibers due to the sliding. On the other hand, based on the definition of φ

$$dF_{fr,v} = \tan\varphi dF_{fr,n} \qquad (5\text{-}63)$$

Hence, substituting Eqs. (5-61) and (5-62) into Eq. (5-63) leads to derive

$$\omega(\varphi) = \frac{1}{1+\tan\varphi} \qquad (5\text{-}64)$$

In fact, ω is a coefficient that takes into account the reduced portion of the Mode I fracture energy that is spent in Mode II for $w > w_a$ (see diagram of $\sigma_{ct}^{cr} - w$ and $\tau_{cr} - \delta$ in Figure 5-18d and Figure 5-18e, respectively). The mode II fracture energy (*i.e.* G_f^{II}) is defined as the area under the curve of crack shear stress *versus* sliding for unit of area. For case of Steel Fiber Reinforced Concrete (SFRC), this energy is not independent from the Mode I, and it can be accounted as the fracture energy due to the frictional behavior of crack face (*i.e.* $G_{f,a}^{II}$) for $w < w_a$ (e.g. aggregate interlocking), plus a portion of G_f^{I}, giving

$$G_f^{II} \cong G_{f,a}^{II} + \left[1-\omega(\varphi)\right]G_f^{I} \qquad (5\text{-}65)$$

More studies are required with respect to the definition of angle φ, and the coefficient of ω. However, in the present work, the nominal shear strength of the beams are analyzed for intermediate values of φ ranged $\varphi \in [10° - 35°]$ where $w_a = 0.15$ mm. Note that the value of w_a is taken from the average crack opening at the peak shear force in the direct shear tests carried out by Soltanzadeh *et al.* (2015) on the same type of HPFRC.

Based on the adopted values of φ and w_a, the modified diagrams of $\sigma_{ct}^{cr} - w$ are plotted in Figure 5-17. Since the diagram is defined by means of 4 linear branches, the modification factor, ω, is multiplied by the crack tensile stress values at the connection points of these lines (*i.e.* P1 to P4). Note that the modification procedure is based on this assumption that

most of the fibers are pulled out, hence, the same value of ultimate crack opening is adopted.

5.3.3.3 Results of the flexure-shear analysis

The results of the nominal shear strength based on the proposed flexure-shear analysis are plotted in Figure 5-20 and Figure 5-21, for group A and B of the test specimens, respectively.

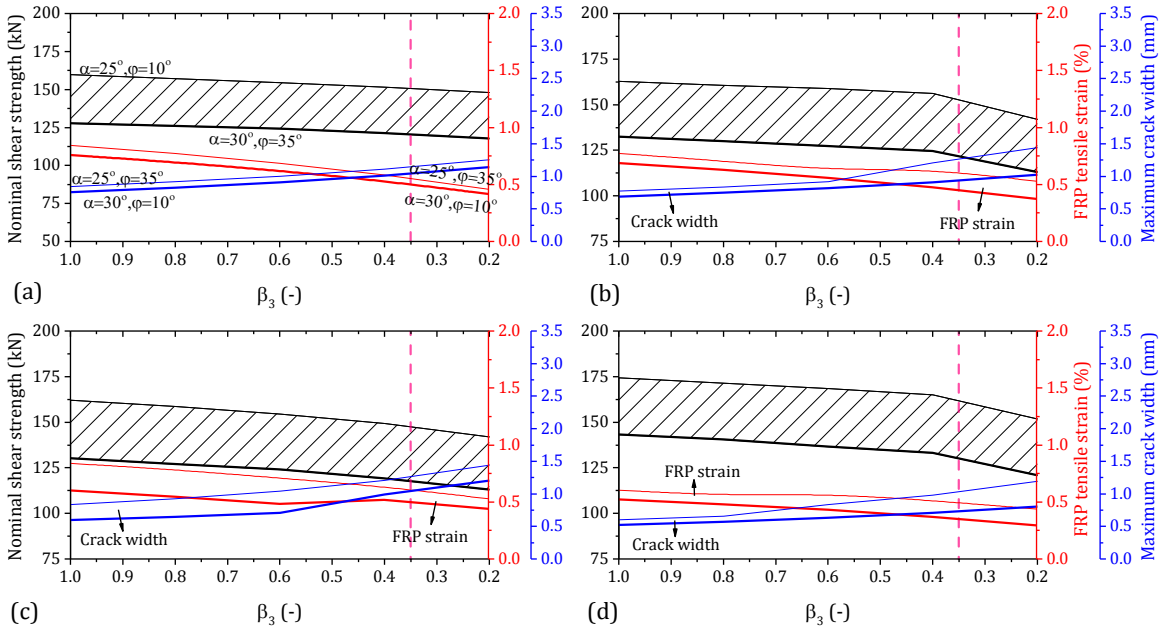

Figure 5-20: Results of the flexure-shear analysis: (a) IB1, (b) IB2, (c) IB3, and (d) IB4

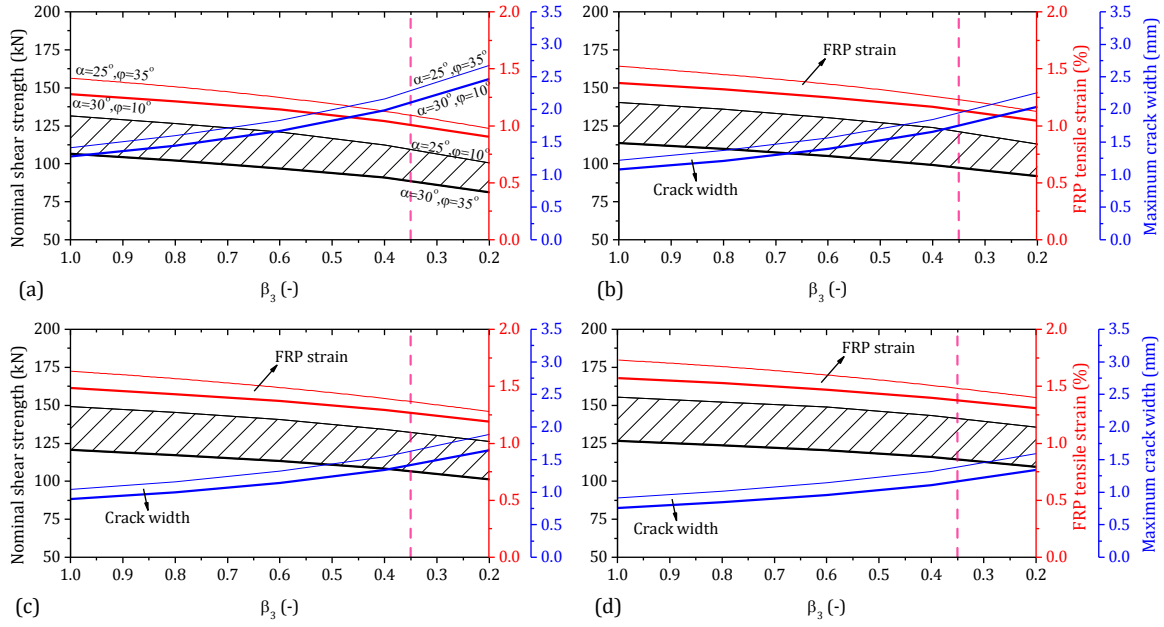

Figure 5-21: Results of the flexure-shear analysis: (a) IB5, (b) IB6, (c) IB8, and (d) IB10

In these figures, the nominal shear strength is plotted *versus* the parameter β_3, for

different range values of α, φ. The effectiveness of $\bar{\tau}_{cr}^{m}$ was not so significant on the nominal shear strength due to the small length of l_v at the failure stage. Hence, $\bar{\tau}_{cr}^{m}$ is empirically taken as constant value of 1.0 MPa (Baghi 2015). The average computed values of c_v corresponding to whatever value of β_3 for different tested beams is plotted in Figure 5-22a and b.

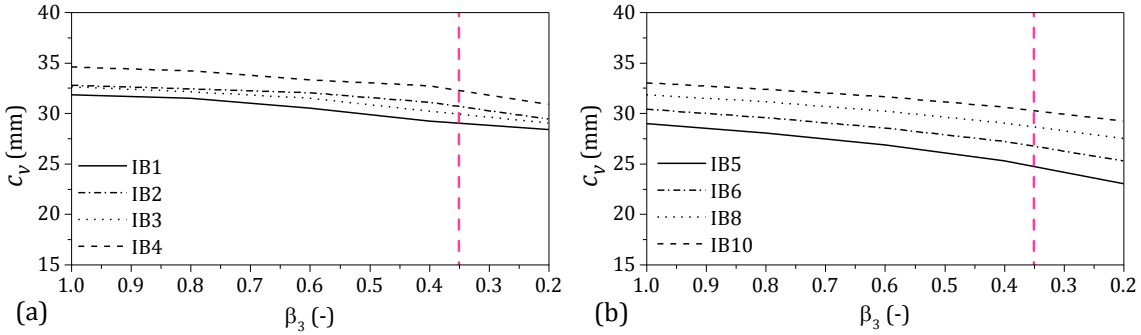

Figure 5-22: The average depth of the neutral axis obtained from the flexure–shear analysis: (a) IB1, IB2, IB3, and IB4, (b) IB5, IB6, IB8, and IB10

5.3.3.4 Nominal shear strength of FRC by Model Code 2010

In the lack of formulation in the available guidelines to calculate the nominal shear strength of the hybrid FRP/steel reinforced HPFRC prestressed beams proposed in this study, the recommendation by CEB-FIB Model Code 2010, which applies to prestressed or none-prestressed FRC beams containing conventional steel reinforcement, is used to predict the shear capacity of the beam specimens:

$$V_n = \left\{ \frac{0.18}{\gamma_c} \cdot k \cdot \left[100 \cdot \rho_{f,eq} \cdot \left(1 + 7.5 \cdot \frac{f_{Ftu}}{f_{ct}} \right) . f_c' \right]^{1/3} + 0.15 \cdot \sigma_c^{pre} \right\} b_w d_{f,eq} \qquad (5\text{-}66)$$

where σ_c^{pre} is the average compressive stress acting over the gross section due to the prestressed force:

$$\sigma_c^{pre} = \frac{N_{ps} + N_{pf}}{A_g} \qquad (5\text{-}67)$$

where N_{ps} and N_{pf} are, respectively, the axial forces due to prestress in steel strand and FRP bars, which have been given in Table 5-6. The parameters $d_{f,eq}$ and $\rho_{f,eq}$ were previously defined in Eqs. (5-41) and (5-42), respectively. The coefficient k is derived by

$$k = 1 + \sqrt{\frac{200}{d_{f,eq}}} \leq 2 \tag{5-68}$$

Additionally, the parameter f_{Ftu} is the characteristic value of the ultimate residual tensile strength for HPFRC, and determined by (CEB-FIB Model Code 2010)

$$f_{Ftu} = f_{Fts} - \frac{w_u}{CMOD_3}(f_{Fts} - 0.5f_{R,3} + 0.2f_{R,1}) \geq 0 \tag{5-69}$$

where

$$f_{Fts} = 0.45f_{R,1} \tag{5-70}$$

and w_u is the maximum crack opening accepted for structural design, which is set to be 1.5 mm (CEB-FIB Model Code 2010). By substituting Eq. (5-70) to Eq. (5-69), f_{Ftu} is simply obtained as follow:

$$f_{Ftu} = 0.06f_{R,1} + 0.3f_{R,3} \tag{5-71}$$

Meanwhile, f_{ct} in Eq. (5-66) is assumed equal to $0.7f_{ct,L}$ (RILEM TC 162-TDF). The partial safety factor, *i.e.* γ_c, is taken 1.0 since the formulation is used to predict experimental results, and average data for the material properties is used. The results of nominal shear strength obtained by Eq. (5-66) and the respective values of the parameters defined in this equation are included in Table 5-11. , the maximum moment supported by the tested I-beams in the present study, can be taken as the minimum value between M_n and M_v, where M_v is the maximum moment corresponding to the nominal shear strength. For the case of the loading configuration adopted in this study, M_v is given by

$$M_v = V_n \cdot a \tag{5-72}$$

where a is the shear span of the beam. The calculated values of M_v for the tested beams are included in Table 5-11. Based on the results for all the beams $M_v < M_n$, which shows that the beams would have been failed in shear. These results will be compared with the values obtained from the experimental tests in Section 5.4 and further discussion in this respect will be given in order to highlight the benefits of prestress level in this type of structural system.

Table 5-11: Nominal shear strength of the tested beams by CEB-FIB Model Code 2010

Specimen ID	$d_{f,eq}$	$\rho_{f,eq}$	k	f_{ct}	f_{Ftu}	σ_c^{pre}	V_n	M_v	V_{cd} *	M_{cd} **
	(mm)	(%)	(-)	(MPa)	(MPa)	(MPa)	(kN)	(kN.m)	(kN)	(kN.m)
IB1	424	2.40	1.69	4.13	3.90	0.0	98.6	145.4	49.5	73.0
IB2	424	2.40	1.69	4.13	3.90	0.83	102.3	150.9	53.2	78.5
IB3	424	2.40	1.69	4.13	3.90	1.65	106.0	156.3	56.8	83.8
IB4	431	2.79	1.68	4.13	3.90	1.65	112.8	166.3	60.3	88.9
IB5	442	1.40	1.67	4.13	3.90	0.0	85.5	136.8	42.6	68.2
IB6,7	442	1.40	1.67	4.13	3.90	1.42	92.1	147.4	49.5	79.2
IB8,9	442	1.40	1.67	4.13	3.90	2.14	95.5	152.7	52.8	84.5
IB10	442	1.40	1.67	4.13	3.90	2.73	98.2	157.1	55.6	89.0

* the shear resistance of the member without fibers;
** calculated by Eq. (5-72), replacing V_n by V_{cd}.

5.3.4 Theoretical deflection

In order to predict theoretically the maximum deflection of the tested beams, two methods are followed in this study:

1) The beam is discretized in Euler-Bernoulli beam element of 2 nodes. Then, the moment-curvature relationship that was obtained from DOCROS software is assigned to each element to compute the flexural stiffness by using a matrix displacement approach. This analysis procedure is done by using Def-DOCROS analysis software, which is described in detail elsewhere (Barros *et al.* 2005 and Varma 2013);
2) Using a direct method similar to the one suggested by ACI318, and it was followed by subsequent ACI guidelines for concrete structures reinforced by FRP bars (ACI440-1R), and prestressed concrete structures with FRP tendons (ACI440-4R). Based on this method, an effective moment of inertia (I_{eff}) of the beam section is determined using moment of inertia of the cracked section (I_{cr}) at flexural failing, which corresponds to the nominal flexural strength (M_n). This method is explained in this section.

Based on the traditional mechanics of material, the maximum deflection of the tested beam determined by

$$D_{\max} = \frac{M_a}{6E_c I_g}\left(\tfrac{3}{4}L^2 - a^2\right) \tag{5-73}$$

where I_g is the gross moment of inertia of un-cracked section. Further, L and a are, respectively, the beam span and beam shear span. ACI suggests to replace I_g in Eq. (5-73)

by an effective moment of inertia (I_{eff}) of cracked beam to obtain its deflection in inelastic stage, giving by (ACI440-1R):

$$I_{eff} = \begin{cases} I_g & M_a \le M_{cr} \\ I_{cr} + \left(\beta_d I_g - I_{cr}\right)\left(\dfrac{M_{cr}}{M_a}\right)^3 & M_a > M_{cr} \end{cases} \tag{5-74}$$

where β_d is a factor that takes into account the relatively smaller tension stiffening effect when FRP reinforcements are used, giving by

$$\beta_d = \frac{1}{5}\left(\frac{\rho_f}{\rho_{fb}}\right) \le 1.0 \tag{5-75}$$

In Eqs. (5-73) and (5-74), the parameter M_a is the maximum moment of the beam for each level of loading, and M_{cr} is the cracking moment that can be calculated by

$$M_{cr} = \frac{2(f_{ct} + \sigma_{c,m}^{pre})I_g}{h} \tag{5-76}$$

where $\sigma_{c,m}^{pre}$ is the compressive stress introduced in the bottom surface of the beam's cross section due to the eccentrically applied prestress force:

$$\sigma_{c,m}^{pre} = \sigma_c^{pre} + \frac{M_p h}{2I_g} \tag{5-77}$$

with

$$M_p \cong N_{ps}\left(d_s - \tfrac{1}{2}h\right) + N_{pf}\left(d_f - \tfrac{1}{2}h\right) \tag{5-78}$$

The concept of the proposed effective moment of inertia (I_{eff}) by Eq. (5-74) is schematically illustrated in Figure 5-23a (shown by dotted-line) for a concrete member reinforced with FRP bars (FRP-RC). Before reaching the cracking moment, *i.e.* $M_a < M_{cr}$, it is assumed that $I_{eff} = I_g$. After crack initiation, I_{eff} decreases with the increase of the ratio between the cracking moment and the applied moment (i.e M_{cr}/M_a), getting the moment of inertia of the cracked section I_{cr} at the flexural failing.

According to the ACI 440-1R-06 design guidelines for concrete structure reinforced with FRP bars, the moment of inertia of the cracked section (*i.e.* I_{cr}) can be determined by

$$I_{cr} = \frac{bc^3}{3} + n_f A_f (d_f - c)^2 \tag{5-79}$$

where n_f is ratio between the modulus of elasticity of FRP bars and the modulus of elasticity of concrete (E_f / E_c). However, in this study, the moment of inertia of the cracked hybrid FRP/steel reinforced HPFRC prestressed beam at failure is determined by calculating the curvature of the cracked section, giving by

$$I_{cr}^{h} = \frac{M_n}{E_c \chi_{cr}^{h}} = \frac{M_n (d_f - c)}{E_c (\varepsilon_f - \varepsilon_f^{pre})} \tag{5-80}$$

with ε_f given by

$$\varepsilon_f = \begin{cases} \varepsilon_{fu} & \rho_f \le \rho_{fb} \\ \left(\dfrac{d_f}{c} - 1\right)\varepsilon_c' + \varepsilon_f^{pre} & \rho_f > \rho_{fb} \end{cases} \tag{5-81}$$

where χ_{cr} is the respective curvature corresponding to the nominal flexural strength (*i.e.* M_n).

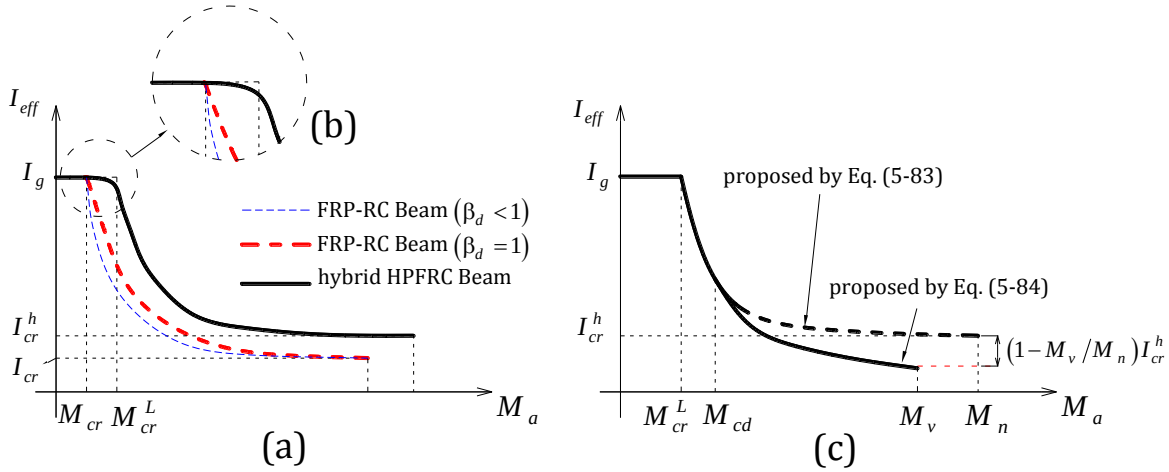

Figure 5-23: (a) Effective moment of inertia *versus* the maximum applied moment, (b) decreasing pattern of the effective moment of inertia at cracking initiation, and (c) effect of flexure-shear crack propagation of HPFRC on the decrease in the effective moment of inertia

The nominal flexural strength can be calculated using Eq. (5-35) or Eq. (5-40) depending on being under or over-reinforced section conditions, respectively. Note that in the above equation, the value of c is computed using Eq. (5-31), which is the level of neutral axis for $M_a = M_n$ in the bending zone.

The effective moment of inertia presented in Eq. (5-74) by ACI is relevant for reinforced

concrete beams and not reinforced HPFRC beams. For case of plain concrete in FRP-RC beam, the tensile stress of concrete drops to almost zero after crack initiation (following typical tension-softening of plain concrete), which introduces significant loss in the effective moment of inertia, I_{eff} , after crack initiation. Additionally, the axial stiffness of FRP bars, as well as their bond performance to plain concrete are normally lower than conventional steel bars. Therefore, the tension-stiffening exhibited by FRP bars at crack initiation is less than steel bars. For this reason, the ACI committee 440 recommends the coefficient β_d that is defined by the simple relation given in Eq. (5-75) depending on the ratio ρ_f / ρ_{fb} , in which the decrease level of the effective moment of inertia is governed by the coefficient β_d , as illustrated in Figure 5-23a.

Conversely, for the case of hybrid reinforced HPFRC beam, HPFRC material provides high residual tensile stress after crack initiation (normally following a slight tension-hardening branch in its direct tensile behavior as shown by P2 in Figure 5-11b and c), which reduces the decreasing rate of the effective moment of inertia at cracking stage. This trend in both FRP-RC beam and hybrid HPFRC beam is schematically compared in Figure 5-23b. Due to this difference, the function that reduces the effective moment of inertia, presented in Eq. (5-74), cannot be directly used for case of hybrid HPFRC beam when $M_a > M_{cr}$. In order to adjust Eq. (5-74) for this type of beams, the concrete tensile strength (*i.e.* f_{ct}) is recommended to be replaced by the limit of proportionality, $f_{ct,L}$, which is included in Table 5-5, and calculated using Eq. (5-1) for F_j corresponding to $CMOD = 0.05\,\text{mm}$ in the standard notched beam test. Hence, the cracking moment is replaced by M_{cr}^{L} , which is computed by the following equation

$$M_{cr}^{L} = \frac{2(f_{ct,L} + \sigma_{c,m}^{pre}) I_g}{h} \tag{5-82}$$

The difference between considering M_{cr} or M_{cr}^{L} in Eq. (5-74) can be realized from the schematic illustration given in Figure 5-23a and b. With this strategy, the effective moment of inertia is assumed I_g for $M_a \le M_{cr}^{L}$, which introduces a slight error in calculation of

deflection for $M_{cr} < M_a \le M_{cr}^{L}$, however, it gives accurate results for $M_a > M_{cr}^{L}$, as it will be discussed later in Section 5.4. Based on the above explanation, the following equation is proposed for the calculation of the effective moment of inertia in case of the proposed hybrid system:

$$I_{eff}^{h} = \begin{cases} I_g & M_a \le M_{cr}^{L} \\ I_{cr}^{h} + \left(\beta_d I_g - I_{cr}^{h}\right)\left(\dfrac{M_{cr}^{L}}{M_a}\right)^3 & M_a > M_{cr}^{L} \end{cases} \quad (5\text{-}83)$$

where the value of β_d is recommended to be assumed unit value for case of the hybrid HPFRC beams proposed in this study. It should be noticed that I_{eff}^{h} is also influenced by the propagation of flexure-shear cracks in shear span, as it is discussed in the next section.

5.3.4.1 Effect of shear crack propagation on the effective moment of inertia

For case of reinforced FRC beams without shear reinforcements, the effective moment of inertia of the member calculated by Eq. (5-83) is influenced by the propagation of shear cracks in the effective flexure-shear zones (as defined in Figure 5-14). This is attributed to the fact that the average curvature of HPFRC beam in shear span gets higher magnitude rather than when the beam with no fibers, and it is shear reinforced with steel stirrups. This can be explained by the following two aspects:

- When compared to the conventional beams of plain concrete shear reinforced with steel stirrups, FRC beams do not including steel stirrups, as is the case of the present beams, develop larger curvature for the same applied moment. Figure 5-24a and b evidence this effect, where for assuring force equilibrium in the crack section of a FRC beam, the neutral axis needs to progress further due to the tensile softening character of the post-tensile behavior of FRC instead of the tensile hardening effect provided by steel stirrups;
- In the shear span of FRC beams, the shear component in the crack face promotes the occurrence of micro-spalling of the paste at the exit point of the fibers (Cunha *et al.* 2010), whose occurrence introduces an instantaneous increase of crack

opening with a direct consequence on the decrease of the post-cracking tensile capacity of the cracked section (Figure 5-24a, typical tension-softening diagram with shear force).

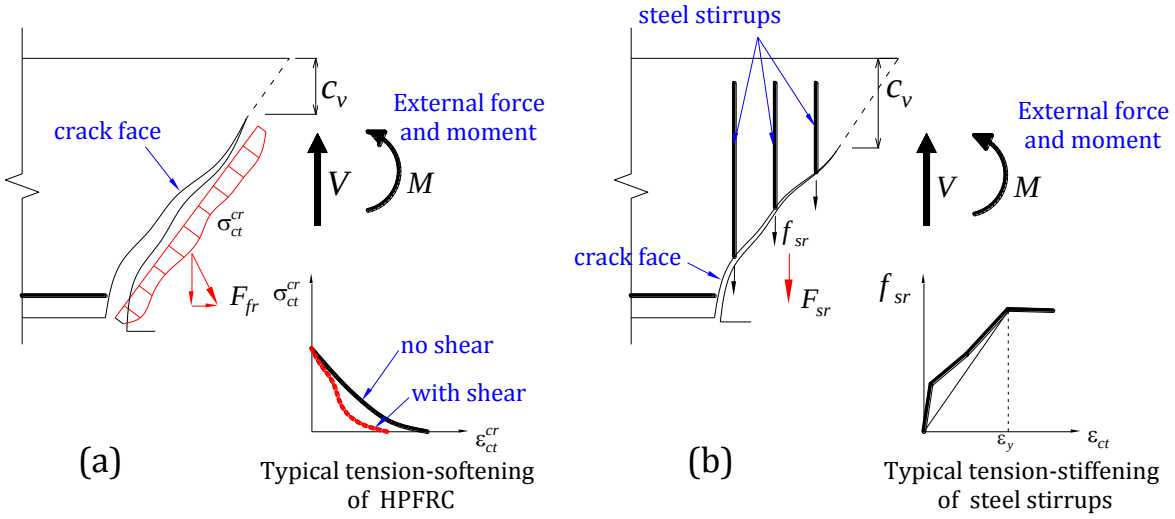

Figure 5-24: Comparison between the depth of neutral axis in a flexure-shear zone for (a) hybrid HPFRC beam with no conventional shear reinforcements, and (b) FRP-RC beam reinforced in shear by steel stirrups

While experimental results are not available for more reliable approach, the decrease level in the moment of inertia caused by these effects are simulated by the second linear parcel introduced in Eq. (5-83) for $M_a > M_{cd}$, where M_{cd} defines the applied moment corresponding to the nominal shear strength of the beam only due to the concrete (*i.e.* V_{cd}). This can be taken as the values recommended by the CEB-FIB Model code 2010 calculated in Table 5-13, however, it should not be obviously taken smaller than M_{cr}^{L}. This reduction is schematically illustrated in Figure 5-23c. The modified equation of the effective moment of inertia for HPFRC reinforced beams considering the increase in the curvature of beam due to the cracks in shear span may be given by

$$I_{eff}^{h} = \begin{cases} I_g & M_a \le M_{cr}^{L} \\ I_{cr}^{h} + \left(I_g - I_{cr}^{h}\right)\left(\dfrac{M_{cr}^{L}}{M_a}\right)^3 & M_{cr}^{L} < M_a \le M_{cd} \\ I_{cr}^{h} + \left(I_g - I_{cr}^{h}\right)\left(\dfrac{M_{cr}^{L}}{M_a}\right)^3 - \beta_{sh}\left(\dfrac{M_a}{M_{cr}^{L}}\right) & M_a > M_{cd} \end{cases} \quad (5\text{-}84)$$

The parameter β_{sh} takes into account the rate of the linear decrease in I_{eff}^{h} with increasing the maximum applied moment. The minimum value of I_{eff}^{h} at failure may be defined based on the ratio of M_v/M_n :

$$I_{eff}^{h}\,(M_a = M_v) = \left(\frac{M_v}{M_n}\right) I_{cr}^{h} \qquad \text{where } M_v \le M_n \tag{5-85}$$

When $M_v > M_n$, the minimum value of I_{eff}^{h} at failure can be equal to I_{cr}^{h} from Eq. (5-80). The coefficient β_{sh} can be obtained by substituting Eq. (5-85) into Eq. (5-84) for $M_a = M_v$:

$$\beta_{sh} = \left[\left(1-\frac{M_v}{M_n}\right) I_{cr}^{h} + \left(I_g - I_{cr}^{h}\right)\left(\frac{M_{cr}^{L}}{M_v}\right)^3\right]\left(\frac{M_{cr}^{L}}{M_v}\right) \tag{5-86}$$

5.3.5 Theoretical crack spacing

The average crack spacing of the hybrid FRP/steel HPFRC prestressed beams (*i.e.* S_{cr}) can be obtained through a crack analysis procedure that takes into account the bond behavior between the reinforcements and surrounding HPFRC. It is assumed that the first crack occurs at section 'A' in the bending region as shown in Figure 5-25 for a total applied load P_{cr}, which creates the cracking moment of M_{cr}. For a value of crack width at the level of FRP bars (*i.e.* w_f), the slip of FRP bars can be assumed as half value of the crack width:

$$\delta_f = \frac{w_f}{2} \tag{5-87}$$

If it is assumed that section remains plain after rotation of θ, similar to compatibility of deformation by the moment-rotation approach discussed by Oehlres *et al.* (2010) and Barros *et al.* (2015), the slip of steel strand becomes

$$\delta_s = \frac{w_s}{2} = \left(\frac{d_s - c}{d_f - c}\right)\delta_f \tag{5-88}$$

where c is the depth of the neutral axis, and δ_s is slip of steel strand at the crack section. Once the values of δ_f and δ_s are obtained, the transferred bond length of the longitudinal reinforcing bars (*i.e.* $L_{tr,f}$ and $L_{tr,s}$), as well as the distribution of the tensile strain, stress,

and bond shear stress over this length can be obtained using the 'IBL algorithm' (Annex 4A), which was previously described in Chapter 4. The bond-slip relationships that were calibrated in Section 5.2.6 for steel strand and FRP bars, are now used for calculation of the transferred bond length. The magnitude of slip at this stage deals with small values, hence, the transferred bond length can be computed using the following equation, which is based on the analytical bond model described in Chapter 3 for the bond solution in the elastic bond phase (see Figure 3-13 in Chapter 3):

$$L_{tr,r} = \frac{1}{\lambda_r}\operatorname{arccosh}\left(\frac{\delta_r + C_e}{C_e}\right) \tag{5-89}$$

with

$$\frac{1}{\lambda_r{}^2} = \frac{\delta_{1,r}}{(\tau_{1,r} - \tau_{0,r})J_r} \tag{5-90}$$

$$C_e = \frac{\tau_{0,r}\, J_r}{\lambda_r{}^2} \tag{5-91}$$

where J_r is the ratio between the perimeter ($\pi\phi_r$) and axial stiffness of the reinforcing bar (*i.e.* E_rA_r). The subscript 'r' defines the parameters for either steel strand or FRP bar. The parameters $\delta_{1,r}$, $\tau_{0,r}$ and $\tau_{1,r}$ define the elastic bond phase of the bond-slip constitutive law of the reinforcements (see Figure 3-13 in Chapter 3).

The second crack occurs when the tensile strain of HPFRC due to the tension-stiffening effect of the reinforcements (*i.e.* fibers, FRP bars and steel strand) in the HPFRC tensile prism at bottom flange of the beam (see Figure 5-25) reaches its cracking strain (*i.e.* ε_{cr}). This crack occurs at Section B, as shown in Figure 5-25, for the reason that the tensile force transferred to the surrounding HPFRC due to the bond behavior of the reinforcements is maximum at this section, which is located at $x = 0$ where x origins from the beginning of L_{tr} ($L_{tr} = \max\{L_{tr,s}, L_{tr,f}\}$) towards section A as illustrated in Figure 5-25. As shown in this figure, two tensile prisms in accordance with the recommendations by CEB-FIB Model Code 2010 are considered to calculate the crack spacing. The first one comprises almost all area of the bottom flange including both longitudinal reinforcements, while the

second is considered only the effective tensile area around the GFRP bars, which is the closer reinforcement to the maximum tensile surface. The crack spacing is the smaller value that is calculated considering these two tensile prisms. The average tensile strain of these two tensile prisms can be given as follow:

$$\varepsilon_{ct1} = \frac{P_s + P_f}{E_c A_{p1}} + \frac{\bar{\sigma}_{fr}(\delta_s + \delta_f)}{E_c} \tag{5-92}$$

$$\varepsilon_{ct2} = \frac{P_f}{E_c A_{p2}} + \frac{\bar{\sigma}_{fr}(w_f)}{E_c} \tag{5-93}$$

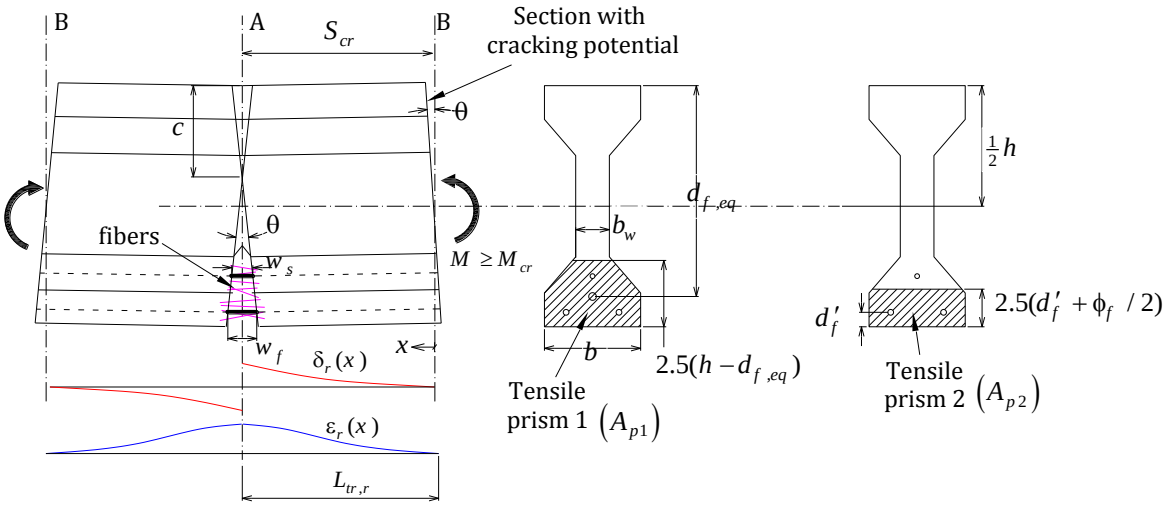

Figure 5-25: Illustration of the effective tensile area of the beam and the crack spacing

where A_{p1} and A_{p2} are the cross-section area of the first and second tensile prisms shown in Figure 5-25, and $\bar{\sigma}_{fr}$ is the average tensile stress in the tensile prism due to the tension–stiffening effect of the steel fibers at the crack section. This value can be computed using the 4-linear law plotted in Figure 5-11c in which the tension-softening law due to concrete matrix is subtracted by the obtained post-cracking law for HPFRC. The respective values define in this diagram is included in Table 5-8. The parameter P_s and P_f are the maximum tensile force transferred to the tensile prism due to bond behavior of the steel strand and FRP bars, respectively, which are given by

$$P_f = \pi\phi_f \int_0^{L_{tr,f}} \tau_f(x)dx = \varepsilon_f E_f A_f \tag{5-94}$$

$$P_s = \pi\phi_s \int_0^{L_{tr,s}} \tau_s(x)dx = \varepsilon_s E_s A_s \tag{5-95}$$

where $\tau_s(x)$ and $\tau_f(x)$ define the distribution of bond shear stress of the steel strand and FRP bars, respectively over L_{tr}. Additionally, ε_s and ε_f are the tensile strains of the steel strand and FRP bars, respectively, at Section A. For $\delta_s \le \delta_{1,s}$ and $\delta_f \le \delta_{1,f}$, the tensile strain in the reinforcing bars at section "A" can be obtained by the following equation (based on Eqs. (3-4) and (3-7) from Chapter 3):

$$\varepsilon_r = C_1^e \lambda_r e^{\lambda_r L_{tr,r}} - C_2^e \lambda_r e^{-\lambda_r L_{tr,r}} \tag{5-96}$$

where

$$C_1^e = \left[\delta_r + C_e \cdot \left(1 - e^{-\lambda \cdot L_{tr,r}}\right)\right] \cdot \frac{1}{e^{\lambda_r \cdot L_{tr,r}} - e^{-\lambda_r \cdot L_{tr,r}}} \tag{5-97}$$

$$C_2^e = C_e - C_1^e \tag{5-98}$$

By substituting Eqs. (5-94) and (5-95) into Eqs. (5-92) and (5-93), and considering the cracking strain (*i.e.* $\varepsilon_{cr} = f_{ct}/E_c$) of HPFRC for both values of ε_{ct1} and ε_{ct2}, the tensile strain of FRP bars corresponding to the cracking of section B is given by the two following equations for the adopted prism 1:

$$\varepsilon_f = \frac{A_{p1}}{E_f A_f}\left(f_{ct} - \bar{\sigma}_{fr}(\delta_s + \delta_f)\right) - n_r \frac{A_s}{A_f}\varepsilon_s \tag{5-99}$$

and for the adopted prism 2:

$$\varepsilon_f = \frac{A_{p2}}{E_f A_f}\left[f_{ct} - \bar{\sigma}_{fr}(w_f)\right] \tag{5-100}$$

where n_r is given by Eq. (5-43). Based on the above equations, the primary crack spacing can be calculated through a trial and error procedure in which for a given value of δ_f, the tensile strain of FRP calculated by Eq. (5-96) and Eq. (5-99) (or Eq. (5-100)) must be equal. Hence, the calculated value of L_{tr} by Eq. (5-89) can be considered as the primary crack spacing. Moreover, to calculate δ_s from Eq. (5-88), the value of c is unknown. This value can be computed by using the equilibrium conditions over the crack section. However, the slip of steel strand (*i.e.* δ_s) can be efficiently estimated as a constant portion of the slip in FRP bars (*i.e.* δ_f). Based on Eq. (5-88), the relation between δ_s/δ_f and c is plotted in

Figure 5-26 or the value of c ranged $c_n < c \leq \frac{1}{2}h$, where c_n is the depth of neutral axis corresponding to the nominal flexural failing of the beam, and it is given by Eq. (5-31) (see Table 5-10 for calculated values of for the tested beams). As shown in this figure, the variation of δ_s/δ_f *versus* the depth of neutral axis is not so significant. Therefore, the slip in steel strand can be on average taken as 75% of the slip in FRP bars.

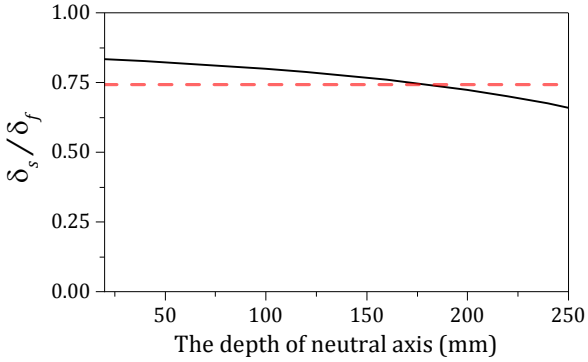

Figure 5-26: The ratio between the slip in steel strand and slip in FRP bar *versus* the depth of neutral axis

A simple algorithm presented in Annex 5C is employed for the trial and error procedure of calculating the primary crack spacing. The calculated values of S_{cr} for the tested beams are included in Table 5-12.

Table 5-12: Results of the analysis to calculate the crack spacing

Specimen ID	M_{cr}	First prism			Second prism			S_{cr}	S_{cr} **	S_{cr}^{RILEM} ***
		w_f	ε_f *	L_{tr}	w_f	ε_f *	L_{tr}			
	(kN.m)	(mm)	(%)	(mm)	(mm)	(%)	(mm)	(mm)	(mm)	(mm)
IB1	25.7	0.051	0.058	392	0.042	0.048	190	190	95	97
IB2	39.3	0.051	0.058	392	0.042	0.048	190	190	95	97
IB3	53.0	0.051	0.058	392	0.042	0.048	190	190	95	97
IB4	53.0	0.048	0.055	386	0.039	0.045	182	182	91	77
IB5	25.7	0.052	0.059	302	0.042	0.048	190	190	95	97
IB6,7	52.1	0.052	0.059	302	0.042	0.048	190	190	95	97
IB8,9	67.9	0.051	0.058	306	0.042	0.048	190	190	95	97
IB10	80.4	0.051	0.057	308	0.042	0.048	190	190	95	97

* The tensile strain of FRP bars at primary cracking stage excluding the amount of pre-strain in the bar, this value is equivalent with the tensile strain of FRP bar at "crack formation stage", which is discussed in the next section where the value of crack width is calculated;
** The secondary crack spacing taken by the half value of the primary crack spacing;
*** calculated by Eq. (5-101) based on the recommendation by RILEM TC 162-TDF.

The secondary crack spacing can be taken as the half value of the primary crack spacing (if applicable) for the reason that the midway section between two consecutive cracks theoretically has the highest degree of force that is transferred by the bond behavior between

the reinforcements and concrete. The possibility of having secondary cracking stage or additional cracking stage can be verified through the same analysis procedure, however, at this time, the FBL algorithm, which was described in Chapter 4 and presented in Annex 4B, has to be employed. This verification is done by using the algorithm that will be described in Section 5.3.6, where the crack width for each level of the applied moment is calculated. In fact, after first cracking stage, the tensile strain of the prisms due to the bond behavior of the reinforcing bars are calculated by taking the difference value between the strain of reinforcing bars at crack section and the midway section between two consecutive cracks.

In addition to the above crack analysis approach, the crack spacing may be calculated by using the equation recommended by RILEM TC 162-TDF for case of FRC beams reinforced by conventional steel bars, but, replacing the respective values of steel bars by those for FRP bars. Hence, the equation becomes

$$S_{cr}^{\text{RILEM}} = \left(50 + 0.25 k_1 k_2 \frac{A_{p2}\phi_f}{A_f}\right)\left(\frac{50}{l_{sf} / \phi_{sf}}\right) \qquad (5\text{-}101)$$

where l_{sf} and ϕ_{sf} are the length and diameter of the hooked steel fibers, which was reported in Table 5-2. The parameter ϕ_f is the FRP bar's diameter. The coefficients k_1 and k_2 are the factors that take into account, respectively, the bond quality and the form of strain distribution. Based on the recommended values by RILEM TC 162-TDF, $k_1 = 0.8$ for having good bond quality, and $k_2 = 0.5$ for bending condition. The calculated values of the crack spacing by Eq. (5-101) are included in Table 5-12. The crack spacing calculated by using Eq. (5-101) are close to those obtained as the secondary crack spacing using the proposed analysis procedure. Due to the good bond quality obtained between the utilized GFRP bars and FRC in this study (discussed in Chapter 3), the recommendation in terms of crack width and crack spacing for FRC beams reinforced by steel bars may be effectively used for case of FRC beams reinforced by GFRP bars.

5.3.6 Theoretical crack width

In order to predict theoretically the value of crack width for the I-beam specimens, two

methods are followed in this study:

1) Using moment-rotation approach and mechanics based beam hinge model in the bending zone discussed by Visintin *et al.* (2012) and by Barros *et al.* (2015), as well as employing the bond model developed in Chapter 3 and 4 of this study. This method is briefly explained in the present section;
2) Using the equations recommended by RILEM TC 162-TDF for case of FRC beam reinforced by steel bars as well as the design crack width recommended by ACI 440-1R-06 for case of FRP-RCs.

The obtained crack width by these two methods are compared with those values obtained from the tests in the next section.

5.3.6.1 Moment-rotation approach and mechanics based beam hinge model

A rotation of θ at cracked section 'A' as shown in Figure 5-27 is considered in the bending zone. For the idealized tensile and compressive deformation at section 'A' shown in this figure, the following compatibility conditions can be derived:

$$\delta_f = \frac{w_f}{2} = \frac{w_{cr}}{2}\frac{(d_f - c)}{(h - c)} \tag{5-102}$$

$$\delta_s = \frac{w_s}{2} = \frac{w_{cr}}{2}\frac{(d_s - c)}{(h - c)} \tag{5-103}$$

where w_f and w_s are the crack mouth opening at level of FRP bars and the steel reinforcement, respectively. Additionally, the maximum compressive deformation at top surface becomes:

$$D_{cm} = \frac{c}{(h - c)} w_{cr} \tag{5-104}$$

where w_{cr} is the crack mouth opening at the bottom surface. On the other hand, the longitudinal equilibrium condition leads to derive

$$F_c = F_{fr} + F_f + F_s \tag{5-105}$$

where F_f and F_s are, respectively, the tensile forces due to the FRP bars and steel strand, which are calculated from the values of tensile strains obtained by employing the 'FBL

model' (Annex 4B) for input values of $\delta_f/2$ and $\delta_s/2$, respectively, where the bond length equals to $S_{cr}/2$. The bond-slip law calibrated in Section 5.2.6 is adopted in this model.

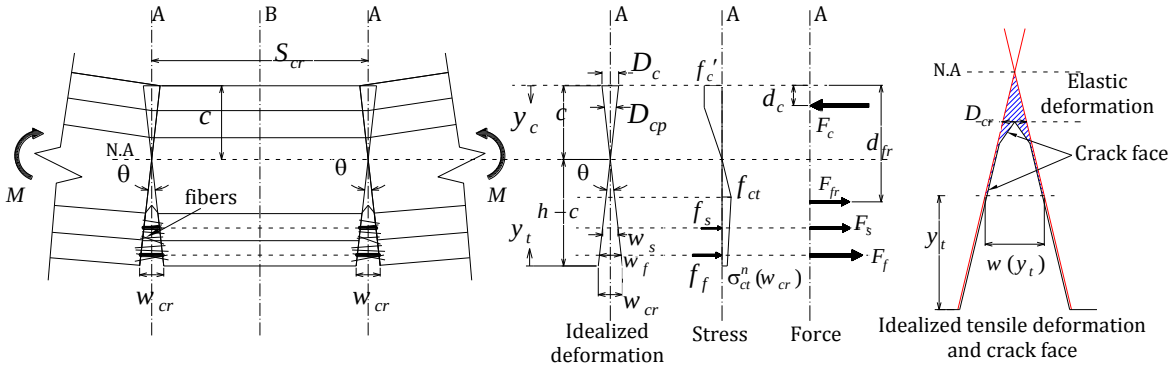

Figure 5-27: Mechanics based beam hinge model and the idealized deformation, stresses, and forces along the crack section

By assuming linear deformation profile in compression, and considering the bi-linear constitutive law previously presented in Figure 5-11a for the behavior of HPFRC in compression, the compressive force, F_c, becomes

$$F_c = \int_0^c b(y_c)\sigma_c(y_c)dy_c \tag{5-106}$$

with the following definitions:

$$b(y_c) = \begin{cases} b & y_c \le h_1 \\ b - (b - b_w)(y_c - h_1)/h_2 & h_1 < y_c \le h_2 \\ b_w & h_2 < y_c < h \end{cases} \tag{5-107}$$

$$\sigma_c(D_c(y_c)) = \begin{cases} f_c' & D_c(y_c) > D_{cp} \\ E_c D_c(y_c) & D_c(y_c) \le D_{cp} \end{cases} \tag{5-108}$$

where y_c is defined in Figure 5-27, and it origins from the top surface. The parameter D_{cp} is the compressive deformation corresponding to the threshold of the plastic phase adopted in the bi-linear law of HPFRC in comparison (see Figure 5-11a), estimating by

$$D_{cp} \cong \varepsilon_{cp} S_{cr} \tag{5-109}$$

Furthermore, $D_c(y_c)$ defines the linear compressive deformation profile, and it is given by

$$D_c(y_c) = D_{cm} - (D_{cm}/c)y_c \tag{5-110}$$

and the tensile force due to HPFRC, *i.e.* F_{fr}, can be given by

$$F_{fr} = \int_0^{(h-c)} b(y_t)\sigma_{ct}(w(y_t))dy_t \tag{5-111}$$

with the following definition in accordance with the linear tensile deformation profile shown in Figure 5-27:

$$w(y_t) = w_{cr} - w_{cr}/(h-c)y_t \tag{5-112}$$

where w is the linear function of crack width along the section. The parameter y_t has its origin from the bottom surface, as shown in Figure 5-27. The parameter $b(y_t)$ is computed using Eq. (5-107), replacing y_c by y_t. Further, $\sigma_{ct}(w(y_t))$ defines the tensile stress diagram of HPFRC at crack section as function of the crack width.

At the right side of Figure 5-27, the elastic and inelastic tensile deformation profile at the crack section are compared using an adequate magnification. As shown, moving from the crack tip toward the bottom surface (*i.e.* $y_t = 0$), the total tensile deformation is effectively due to the inelastic deformation (crack opening) as the elastic deformation can be assumed almost null. However, for the tensile deformation less than D_{cr} (*i.e.* $w(y_t) < D_{cr}$), which defines the maximum elastic tensile deformation corresponding to the concrete tensile strength, the deformation is only due to the elastic behavior of HPFRC, and consequently, inelastic tensile deformation is null. The parameter D_{cr} may be estimated by

$$D_{cr} \cong \varepsilon_{cr} S_{cr} \tag{5-113}$$

where ε_{cr} is the cracking strain of HPFRC, and it can be taken as the value written in Table 5-8 (Point 1 in Figure 5-11b). Hence, $\sigma_{ct}(w(y_t))$ is given by

$$\sigma_{ct}(w(y_t)) = \begin{cases} E_c \cdot w(y_t)/S_{cr} & w(y_t) \le D_{cr} \\ \sigma_{ct}^{cr}(w(y_t)) & w(y_t) > D_{cr} \end{cases} \tag{5-114}$$

where $\sigma_{ct}^{cr}(w(y_t))$ is the crack tensile stress of HPFRC, and it is defined based on the 4-linear stress-crack diagram that was previously presented in Figure 5-11c.

In addition to the longitudinal equilibrium condition, summation of the moment about the top surface of the section to derive the following equation:

$$M_a = F_c d_c + F_f d_f + F_s d_s + F_{fr} d_{fr} \tag{5-115}$$

where d_c and d_{fr} are, respectively, the internal arm of the resultant of the compressive and

tensile force due to HPFRC in respect to the top surface (as shown in Figure 5-27) with the following mathematical expression

$$d_c = \frac{\int_0^c \sigma_c(y_c) y_c dy_c}{\int_0^c \sigma_c(y_c) dy_c} \tag{5-116}$$

$$d_{fr} = h - \frac{\int_0^{(h-c)} \sigma_{ct}(w(y_t)) y_t dy_t}{\int_0^{(h-c)} \sigma_{ct}(w(y_t)) dy_t} \tag{5-117}$$

Eqs. (5-105) and (5-115) are solved for the unknown parameters of w_f (or w_{cr}) and c. For this purpose, a numerical procedure is employed in which for each given value of w_f, the value of c is calculated by solving Eq. (5-105). Hence, the respective moment (M_a) is calculated using Eq. (5-115). To calculate the tensile and compressive force due to HPFRC, the presented integrals in the above equations are solved by discretizing the beam to thin layers (e.g. 5 mm), similar to the numerical section adopted for DOCROS software. The solving procedure is presented in the algorithm given in Annex 5D. Note that the solving procedure requires predefinition of the crack spacing (*i.e.* S_{cr}). At the beginning, this value is defined as the primary crack spacing written in Table 5-12 for case of the second tensile prism. In consequence, the possibility of forming the second crack at midway section between two consecutive cracks is verified by calculating the tensile strain of the second HPFRC tensile prism using Eq. (5-93). At this stage, P_f is computed by the following equation

$$P_f = \left(\varepsilon_f - \varepsilon_f^m\right) E_f A_f \tag{5-118}$$

where ε_f^m is the tensile strain of GFRP bars at the midway section between two consecutive cracks (*i.e.* at distanced $S_{cr}/2$ from the crack section) as it was previously introduced in Chapter 4. This value is obtained as the output value of the FBL model described in Annex 4B. If the tensile strain of the second HPFRC prism calculated by Eq. (5-93) reaches the cracking strain (*i.e.* ε_{cr}), another crack is formed, and consequently the crack spacing is taken as its half value for the further increment of the crack width (w_f) in the crack analysis

procedure. Due to the relatively large distance between the FRP and steel longitudinal reinforcements (~75 mm), the first HPFRC tensile prism, which includes both FRP and steel reinforcements (as shown in Figure 5-25), is not the effective tensile area to detect the secondary crack section. As a general case, the maximum tensile force transferred to the first tensile prism by both FRP and steel longitudinal reinforcements can be computed as follow:

$$P = P_f + P_s = \left(\varepsilon_f - \varepsilon_f^m\right) E_f A_f + \left(\varepsilon_s - \varepsilon_s^m\right) E_s A_s \tag{5-119}$$

where ε_f^s is the tensile strain of steel strand at the midway section between two consecutive cracks, which can be obtained as the output value of the FBL model.

5.3.6.2 Design crack width by codes

ACI 440-1R-06, guideline for design of FRP RCs, recommends the following equation for the calculation of crack width:

$$w_f = 2\frac{f_f}{E_f}\beta k_b \sqrt{d_f'^2 + \left(\frac{s}{2}\right)^2} \tag{5-120}$$

where d_f' and s are FRP bar's concrete cover and spacing, respectively. Further, the parameter β is defined as the ratio of distance between neutral axis and tension face to distance between neutral axis and centroid of reinforcement. The factor k_b takes into account the degree of bond between FRP bars and surrounding concrete. According to ACI440-1R-06, the value of k_b is ranged from 0.6 to 1.7 depending on the bond degree.

RILEM TC 162-TDF recommends the design crack width calculating by multiplying the average value of tensile strain of the reinforcing bars by the crack spacing. Though, the recommendation is for case of FRC beams reinforced by conventional steel bars, the same strategy may be suitable for case of the present study, replacing the respective parameters of steel bars by those from GFRP bars. Hence, the design crack width becomes:

$$w_k = w_f = \beta \bar{\varepsilon}_f S_{cr}^{\text{RILEM}} \tag{5-121}$$

where β is a coefficient relating the average crack width to the design value, which is set unit value to compare with the measured crack width from the tests. The parameter $\bar{\varepsilon}_f$ is the mean value of GFRP bar's stain over the crack spacing, given by

$$\bar{\varepsilon}_f = \frac{f_f}{E_f}\left[1 - k_3 k_4 \left(\frac{\sigma_{sr}}{f_f}\right)^2\right] \quad (5\text{-}122)$$

where f_f is the tensile stress of GFPR bars at crack section (excluding prestress). The coefficient k_3 and k_4 are factors taking into account, respectively, the bond quality and the duration of the loading or of repeated loading which both set equal to 1 for case of this study. Further, the value of σ_{sr} is the tensile stress of GFRP bars calculated on the basis of a cracked section under loading conditions causing first cracking. This value can be calculated using equation recommended by CEB-FIB Model Code 2010, depending on the adopted HPFRC tensile prism. In case of adopting A_{p1} :

$$\sigma_{sr} = \frac{(f_{ct} - f_{Fts})}{\rho_{eff}}(1 + n_f \rho_{eff}) \quad \text{where} \quad \rho_{eff} = \frac{A_f + A_s}{A_{p1}} \quad (5\text{-}123)$$

and in case of A_{p2}

$$\sigma_{sr} = \frac{(f_{ct} - f_{Fts})}{\rho_{eff}}(1 + n_f \rho_{eff}) \quad \text{where} \quad \rho_{eff} = \frac{A_f}{A_{p2}} \quad (5\text{-}124)$$

where n_f is the modular ratio between GFRP bars and concrete (HPFRC for case of this study, *i.e.* E_f / E_c). The value of f_{Fts} was previously defined in Eq. (5-70), and it equals to $0.45 f_{R,1}$. However, $0.45 f_{R,1}$ is greater than f_{ct} for case of HPFRC in the current study, hence, the parcel $(f_{ct} - f_{Fts})$ in Eq. (5-123) is taken null, meaning that the tensile stress of FRP bars at "crack formation stage" is almost negligible. In the current study, for the calculation of $\bar{\varepsilon}_f$ from Eq. (5-122), it is proposed that σ_{sr} is calculated using the following equation:

$$\sigma_{sr} = E_f \varepsilon_{f,cfs} \quad (5\text{-}125)$$

where $\varepsilon_{f,cfs}$ is the tensile strain of GFRP bars at "*crack formation stage*" (CEB-FIB Model Code 2010), and it can be taken as the tensile strain of FRP bars obtained from the analysis procedure described in the previous section to calculate the primary crack spacing. The computed values for the tested I-beams are included in Table 5-12. Based on the calculated values in this table, the tensile stress of GFRP bars at "*crack formation stage*" in average is about 30 MPa, which is definitely small.

The obtained results of the crack width in terms of $w_f - f_f$ diagram will be compared with those obtained by the experiments in the next section.

5.4 Results and discussion

The experimental results of the tested I-beams are presented and discussed in this section on the following aspects:

i. Flexural strength and failure modes;
ii. Force-deflection response;
iii. Ductility;
iv. Cracking behavior;
v. Tensile strain of the reinforcing bars.

Moreover, the experimental results are compared to the respective results obtained from the theoretical investigation in order to evaluate the capability of the theoretical formulation to predict the structural behavior of the proposed hybrid reinforcing system.

Finally, the results of the fatigue tests on specimens IB7, 9 and 10 are presented at the end of this section, where and the influence of this loading condition on the structural performance of the hybrid HPFRC prestressed I-beams is discussed. The loss of both the material's strength and flexural stiffness of the tested beams due to the fatigue loading condition is determined.

5.4.1 Flexural strength and failure mode

The maximum experimental moment (*i.e.* $M_{u,\exp}$) carried by the tested beams was calculated from the respective maximum load (*i.e.* $P_{\max}$) that was registered during the monotonic tests, giving by

$$M_{u,\exp} = \frac{1}{2} a \cdot P_{\max} \tag{5-126}$$

The calculated values of $M_{u,\exp}$ are included in Table 5-13 for group A and B of the specimens. With the aim of the results obtained from DOCROS software, the theoretically values of the maximum applied moment that reasons yielding in the steel strand (defined as

M_y) are calculated and included in the last column in Table 5-10 for the tested beams. By comparing between $M_{u,\exp}$ and M_y, it may be stated that the steel strand reached the yielding stress for the group B of the specimens (with the exception of IB5 as the reference beam), while no beam in group A experienced the maximum applied moment greater than M_y. For this reason, the failing of the beams in group A was "*shear failure*", while the failing of the prestressed I beams in group B was "*flexo-shear failure*" with the exception of reference IB5 as indicated in Table 5-13. It should be noticed that it was unlikely to have the strain gauge "SGst" installed on the steel strand working up to the steel yielding strain of about 1% ($\varepsilon_{sy} \cong 1\%$). Consequently, the steel yielding strain could not be evidenced by means of the strain gauge "SGst" during the test.

Table 5-13: Nominal flexural and shear strength of the tested beams

Beam ID				By CEB-FIB		Flexure-shear analysis [4]								
	$M_{u,\exp}$	M_{SLS} [1]	D_y [3]	V_n	M_v	V_n	M_v	ε_f	w_{cr}	c_v	M_n	$\frac{M_{u,\exp}}{M_n}$	Steel yielded?	Mode of failure
	(kN.m)	(kN.m)	(mm)	(kN)	(kN.m)	(kN)	(kN.m)	(%)	(mm)	(mm)	(kN.m)			
IB1	175	111	36	67.5	99.6	118	174	0.75	1.55	27	257	0.74	No	Shear failure
IB2	179	119	32	71.3	105.1	123	181	0.60	1.45	28.5	257	0.76	No	Shear failure
IB3	180	132	31	74.9	110.5	130	192	0.50	1.30	30	257	0.76	No	Shear failure
IB4	142	135	30	79.6	117.4	137	202	0.45	1.15	31	296	0.59	No	Shear failure
IB5	148	100	38	58.6	93.8	97	155	1.10	2.30	25	219	0.67	No	Shear failure
IB6	186	128	23	65.2	104.3	106	170	1.25	1.80	26.5	221	0.84	Yes	Flexo-shear failure
IB7	171 [2]	116	23	65.2	104.3	106	170	1.25	1.80	26.5	221	0.77	Yes	Flexo-shear failure
IB8	201	147	21	68.5	109.6	117	187	1.35	1.60	28.5	223	0.90	Yes	Flexo-shear failure
IB10	210 [2]	157	20	71.3	114.1	125	200	1.45	1.40	30	224	0.94	Yes	Flexo-shear failure

[1] Calculated from the experimental results of force-deflection corresponding to the mid span deflection of about $L/250$~15 mm;
[2] Obtained from the monotonic test after two million fatigue cycles;
[3] mid span deflection calculated by Def-DOCROS, which corresponds to M_y from Table 5-10;
[4] The average values from the results plotted in Figure 5-20, Figure 5-21, and Figure 5-22.

Additionally, the final crack pattern and the failing mode of the tested beams are illustrated in Figure 5-28 for group A, and in Figure 5-29 for group B (Note that the taken photos of the failure modes of the tested beams are all given in the Annex 5E). As shown in these two figures, all the beams failed by the propagation of diagonal crack in the shear span starting from the bottom flange toward the loading point, with the exception of IB4 (over-reinforced condition). IB4 was failed by progressing a shear crack from the loading point through the transition zone between the flange and web of the beam for the maximum applied moment less than the value registered for IB3 beam. The premature rupture of the IB4 beam

was mainly caused by the increase of the flexural reinforcement, since this increased the stiffness of the bottom flange of the beam, as well as the dowel effect. These two factors contributed for the higher resistance of the flange zone to be crossed by a shear crack, which promoted its propagation at the interface between bottom flange and web. Since this interface had no stirrups resisting to these in-plane shear stresses, and the percentage of fibers giving effective contribution for shear resistance was relatively small (the fibers have the tendency to get a horizontal direction in accordance to the work carried out by Abrishambaf *et al.* (2013), a premature failure occurred in this beam.

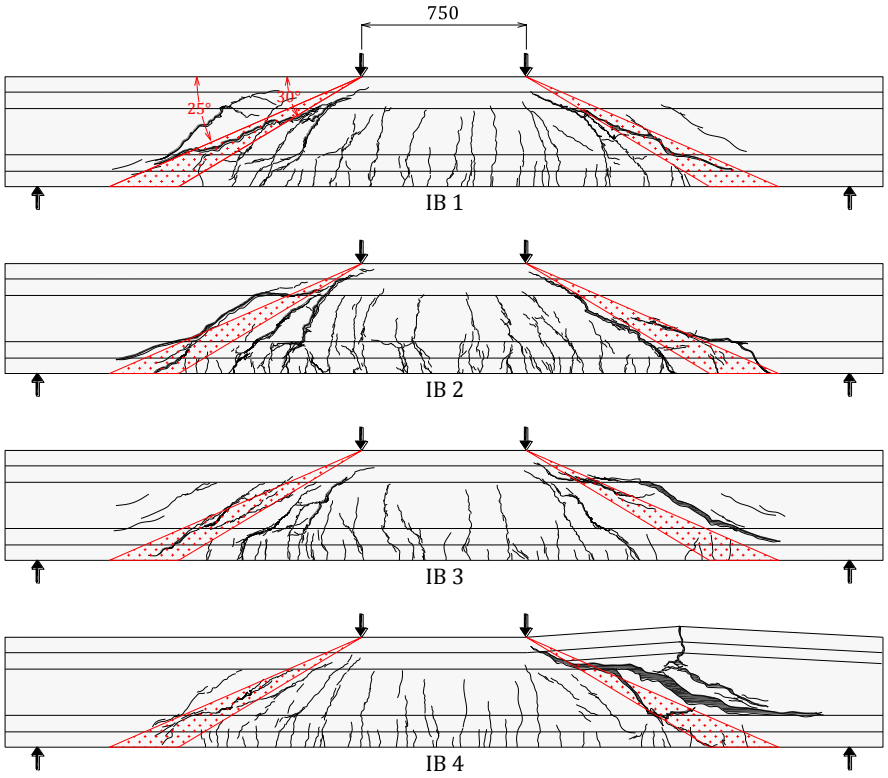

Figure 5-28: Ultimate crack pattern and failure mode of the tested beams in group A

Moreover, the adopted range for the angle of the CDC (*i.e.* $\alpha = 25° \text{ to } 30°$) in the flexure-shear analysis is illustrated in Figure 5-28 and Figure 5-29. It can be fairly accepted that the experimental failure crack is in the adopted range of α (except IB4). In order to determine the nominal shear strength (*i.e.* V_n) from the proposed crack analysis in Section 5.3.3.1, whose results were plotted in Figure 5-20 and Figure 5-21, a proper value of β_3 shall be taken. Based on the adopted bi-linear profile for tensile deformation of the CDC shown in

Figure 5-16, the parameter β_3 is defined as the ratio between the crack mouth opening of HPFRC at the level of GFRP bars and the crack mouth opening at the connection of the bottom flange and the web plate. This definition is not straightforward since the values of crack opening at CDC are unknown.

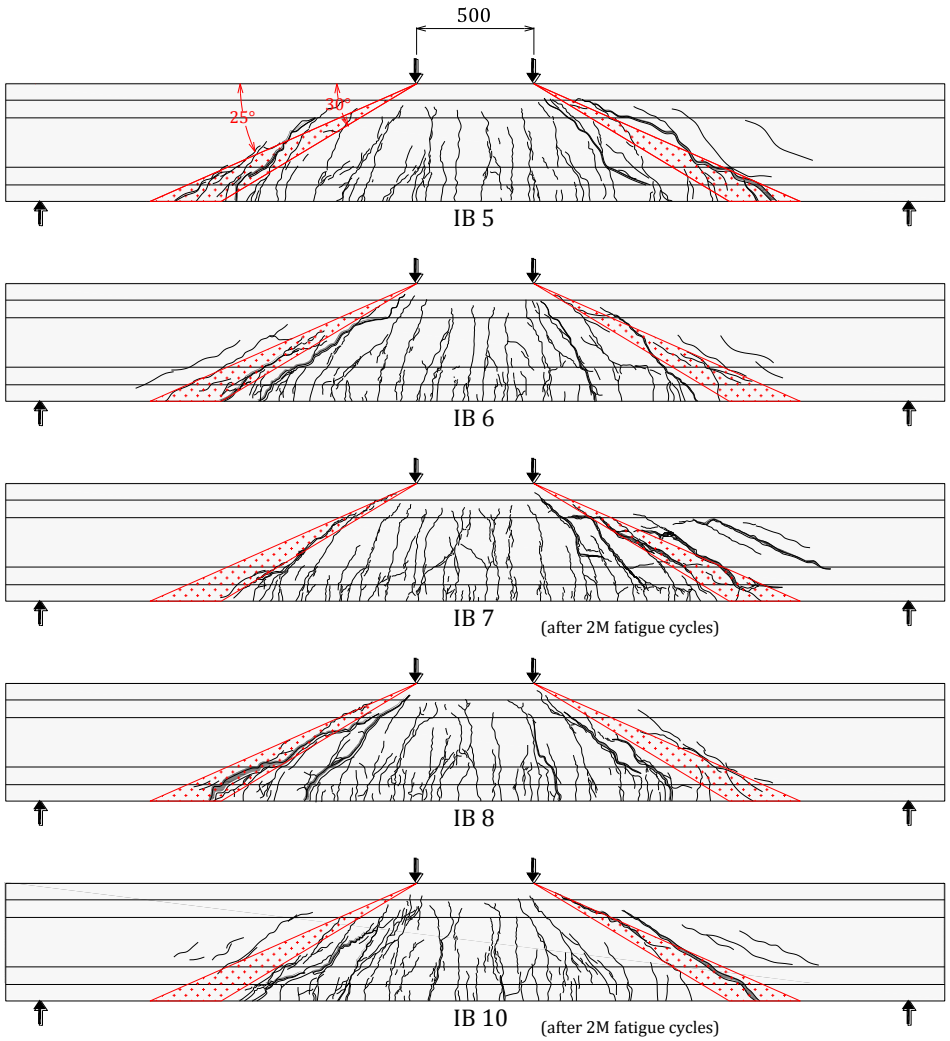

Figure 5-29: Ultimate crack pattern and failure mode of the tested beams in group B

In order to proceed with the definition of β_3 for design purpose, it is proposed to be computed based on geometry adopted for beam cross section. A proposal is given in Figure 5-30 in terms of different tensile deformation profile at the CDC for two typical geometries adopted for beam's cross section in RC applications. As shown in this figure, the parameter β_3 is recommended unit value (*i.e.* $\beta_3 = 1$) for T-shaped cross section, the following equation is proposed for case of I-shaped cross section:

$$\beta_3 = \frac{b_w}{b} \qquad (= 0.35 \text{ for case of this study}) \qquad (5\text{-}127)$$

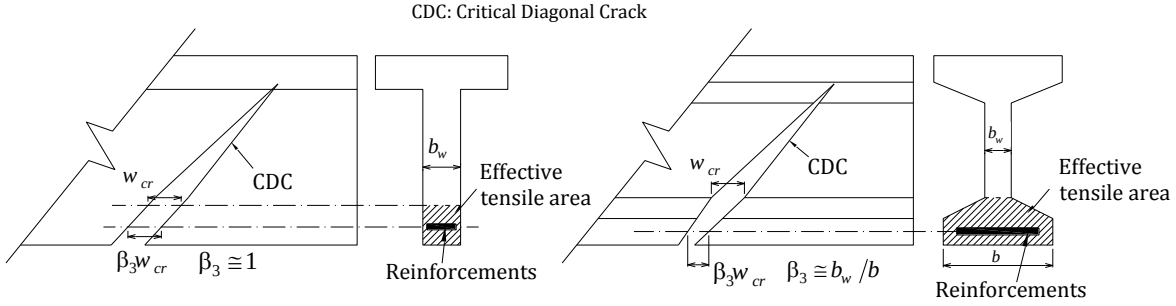

Figure 5-30: Definition of parameter β_3 based on the typical geometries adopted for cross section in RC beam applications

Based on the results obtained from the flexure-shear analysis (plotted in Figure 5-20 and Figure 5-21), the nominal shear strength tends to decreases when β_3 decreases. Hence, considering the definition given in Eq. (5-127), an increase in the bottom flange width decreases the shear capacity of HPFRC I-beams (for beam without shear reinforcements). Based on this, T-shaped is proposed to be optimized beam's cross section in terms of carrying shear loads, even though, it is not the optimized section with respect to flexural capacity, when I-shaped is considered for comparison purposes. The obtained nominal shear strength, V_n and its corresponding moment (*i.e.* M_v), as well as the respective values of the maximum crack width, tensile strain of GFRP, and the depth of neutral axis at failure (*i.e.* c_v) are included in Table 5-13. These results have been extracted from the results of the flexure-shear analysis plotted in Figure 5-20, Figure 5-21, and Figure 5-22 in Section 5.3.3.3 for $\beta_3 = 0.35$ (see the vertical dotted-line in these figures).

In addition to these results, the calculated nominal shear strength based on Eq. (5-66) by the Mode Code 2010 (*i.e.* Eq. (5-66)) are included in Table 5-13. In Figure 5-31, the maximum moment that was reached during the monotonic test ($M_{u,\exp}$) is compared with the nominal flexural strength (*i.e.* M_n) in Section 5.3.2, as well as M_v from the flexure-shear analysis, and M_v from Eq. (5-66) by Model Code 2010. The equation by CEB-FIB underestimates the moment capacity of the beams in shear span, however, the range of the nominal flexural strength calculated by the flexure-shear crack predicts with an acceptable

accuracy the results of the tested beams, mainly, the group B of the specimens that are all under-reinforced. Due to the unexpected failing of IB4, both results overestimate the shear capacity of this beam. IB1, IB2 and IB3 reached about 75% of their nominal flexural strength (M_n) in which no significant change that was observed by increasing the prestress level of the steel strand. On the other hand, increase in the level of prestress in GFRP bars showed significant influence on increasing the flexure-shear strength of the tested beams in group B, in which the non-prestressed beam, IB5, reached about 67% of its nominal flexural strength at the bending zone, while this value was about 94% for IB10 with 40% of prestress in GFRP bars. Note that the amount of prestress level in steel strand was 50% for all the prestressed specimens in group B.

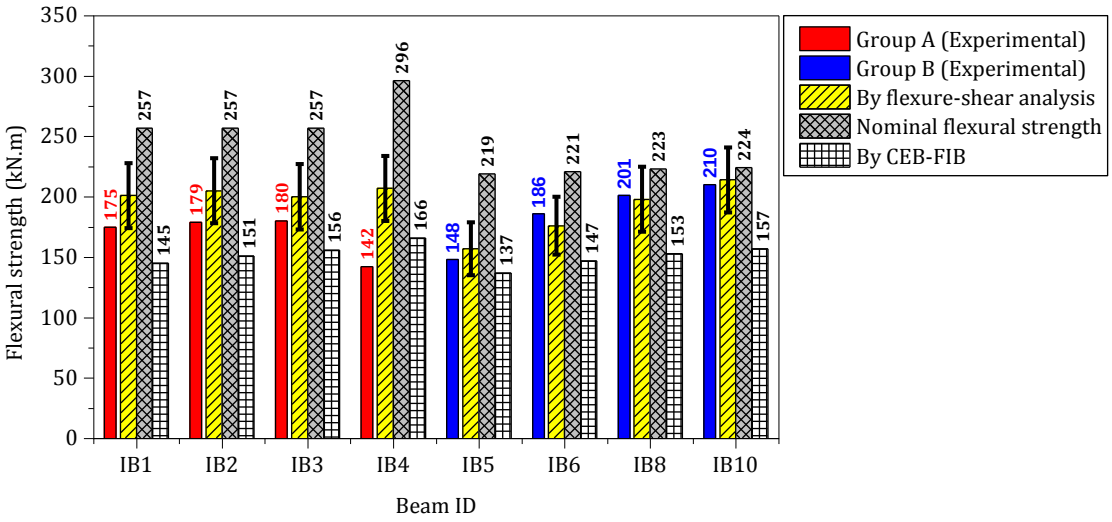

Figure 5-31: Comparison between the experimental and theoretical flexural strength of the tested beams

5.4.2 Force-deflection response

In this section, the flexural stiffness of the tested beams is discussed by comparing their force-deflection response at mid span, as well as the concept of the effective moment of inertia that was previously presented in Section 5.3.4.

5.4.2.1 Effective moment of inertia

The experimental effective moment of inertia (*i.e.* $I^{h}_{eff,\exp}$) of the tested beams is calculated using Eq. (5-73) and taking the experimental results of the applied moment *versus*

mid span deflection. Hence, the experimental effective moment of inertia becomes

$$I_{eff,\exp}^{h} = \frac{(\frac{3}{4}L^2 - a^2)}{6E_c} \frac{M_a}{D_{\max}} \tag{5-128}$$

where $M_a/D_{\max}$ is taken from the test results. The calculated results are plotted in Figure 5-32a for group A, and in Figure 5-32b for group B. These figures evidence that the increase of the flexural stiffness of the beams with the applied prestress level. Although the tested beams showed different load carrying capacities, the ultimate $I_{eff,\exp}^{h}$ at failure was almost same for all the beams (see the graph with higher magnification in Figure 5-32). This means that the ultimate $I_{eff,\exp}^{h}$ is not influenced by the level of prestress in the reinforcements. In fact, the cracking moment is the main benefited aspect by the increase of the prestress level applied to the reinforcements.

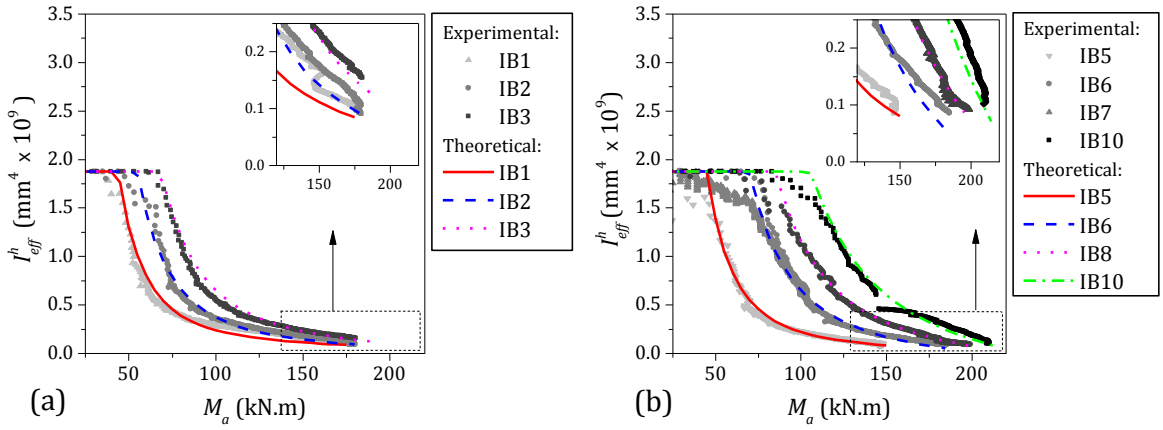

Figure 5-32: Comparison between the theoretical and experimental effective moment of inertia: (a) group A, and (b) group B

Additionally, the $I_{eff}^{h} - M_a$ relationship according to Eq. (5-84) is plotted in Figure 5-32. As shown, the proposed equation can predict with an acceptable accuracy the experimental results in terms of $I_{eff}^{h} - M_a$. The coefficient β_{sh} was defined to consider the effect of shear crack propagation on the effective moment of inertia. In order to show the influence of this factor, the experimental $I_{eff} - M_a$ of IB6 (as example), is compared with the corresponding theoretical results by Eq. (5-84) for $\beta_{sh} = 0$, and for β_{sh} by Eq. (5-86). By comparing the experimental variation of $I_{eff,\exp}^{h}$ with theoretical I_{eff}^{h} for $\beta_{sh} = 0$, after a certain value of

applied moment, $I^{h}_{eff,\exp}$ starts decreasing with a higher rate rather than the theoretical I^{h}_{eff}. In fact, when the applied shear load in shear span gets higher value than about the shear strength of concrete beam, V_{cd} concrete without fibers, the effective moment of inertia of the beam starts increasing with a higher rate of magnitude. In Table 5 11, the value of V_{cd} was obtained about 50kN for IB6, which gives M_{cd} = 80 kN.m as indicated in Figure 5-33. When I^{h}_{eff} is determined by considering the coefficient β_{sh} obtained from Eq. (5-83), a good agreement between the theoretical and experimental trends is ensured.

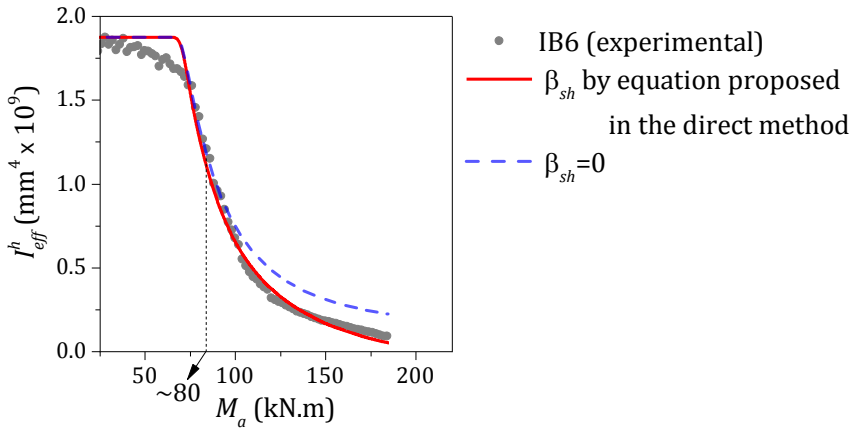

Figure 5-33: Effect of coefficient β_{sh} on the calculation of the effective moment of inertia

5.4.2.2 Force-deflection up to service load

The applied force *versus* mid span deflection obtained from the tested beams is plotted in Figure 5-34 up to the mid span deflection of 15 mm, which equals to about $L/250$, and it is typically defined as the limited deflection for service loads (ACI318-08). The increase in the service load by increasing in the prestress level is observable from this figure. In addition to the experimental results, the force-deflection response at mid span from the Def-DOCROS software, and by Eq. (5-73) for $I_g = I^{h}_{eff}$, which is designated as "direct method", are shown in this figure. Note that in calculation of the theoretical deflection by using the direct method, the value of M_v was calculated by adopting the value of V_n from the results of the flexure-shear analysis (included in Table 5-13). Up to mid span deflection of about 9 mm, the precision of both theoretical approaches to predict the crack initiation is acceptable for all the tested beams in groups A and B. As mentioned earlier, using the concept of limit of

proportionality ($f_{ct,L}$) is quite relevant to estimate the crack initiation response of HPFRC prestressed beams.

For mid span deflection between 9 to 15 mm (or service moment, M_{SLS} included in Table 5-13), the precision of both theoretical approaches to predict the results from group B was acceptable. On the other hand, the results from Def-DOCROS overestimated the results of beams in group A, while the experimental results were captured well using the direct method (except IB5). This is mainly due to the different loading point configurations adopted for test specimens in groups A and B (750 mm loading distance for group A and 500 mm for group B). Due to the lower shear span in group A rather than group B, the effect on the beam curvature by the propagation of shear cracks occurred for a lower value of mid span deflection. Therefore, the results from Def-DOCROS, which did not consider this effect, overestimated the experimental results for mid span deflection between 9 to 15 mm.

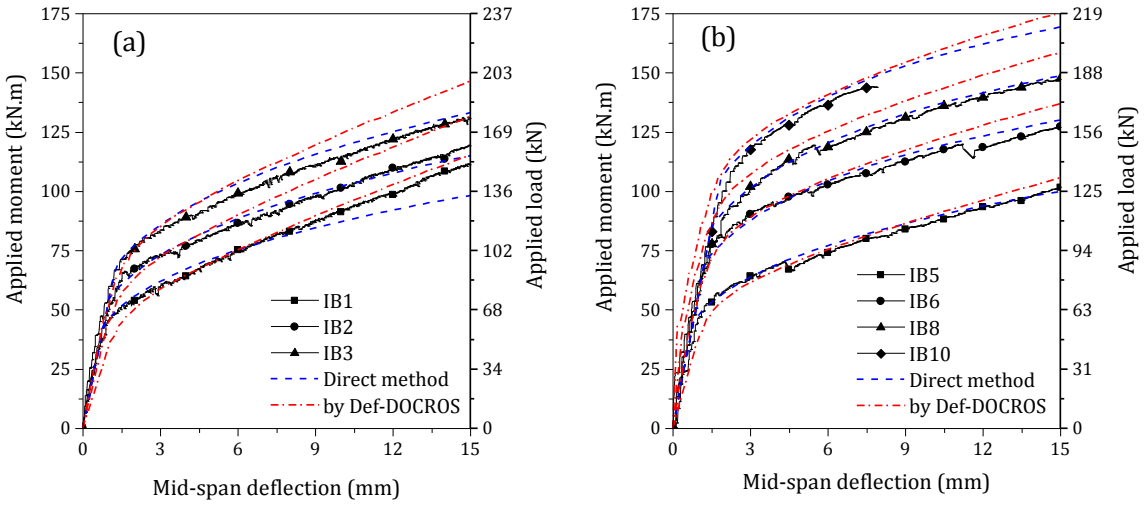

Figure 5-34: Applied moment *versus* mid span deflection up to the serviceability limit state: (a) group A, (b) group B

The difference between the experimental force-deflection response of IB1 and the corresponding response from Def-DOCROS was exceptionally less than the difference between this experimental response and the one by the direct method. This was due to the fact that the applied load in IB1 specimen was not distributed uniformly to the two loading points during the test. This non-uniform response is more visible in the total force-deflection response of IB1, as it will be shown in the next section.

5.4.2.3 Total force-deflection response

The force-deflection response up to the failure at mid span is plotted in Figure 5-35 and Figure 5-36, respectively, for groups A and B. In addition to the experimental results, the force-deflection response from the Def-DOCROS software, and the results obtained by the direct method, are shown in these figures. The direct method, which is based on the proposed effective moment of inertia by Eq. (5-84), estimates with an acceptable accuracy the force-deflection response of the beams up to the ultimate stage. However, the force-deflection response obtained by Def-DOCROS overestimated the experimental responses. This is due to the fact that the numerical model does not simulate the shear stiffness degradation occurred during the loading process in the matrix displacement method that it is based on the work carried out by Barros *et al.* (2005).

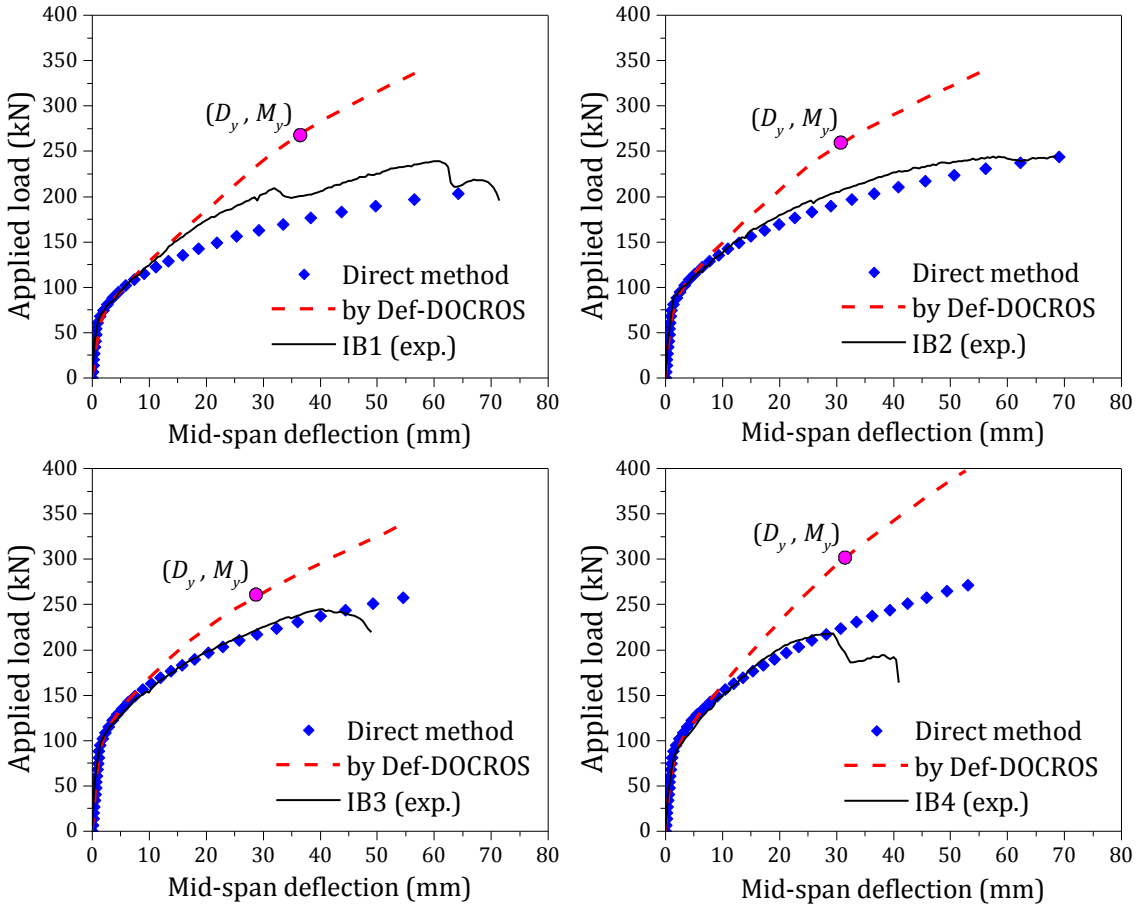

Figure 5-35: Applied force *versus* mid span deflection of the tested beams in group A

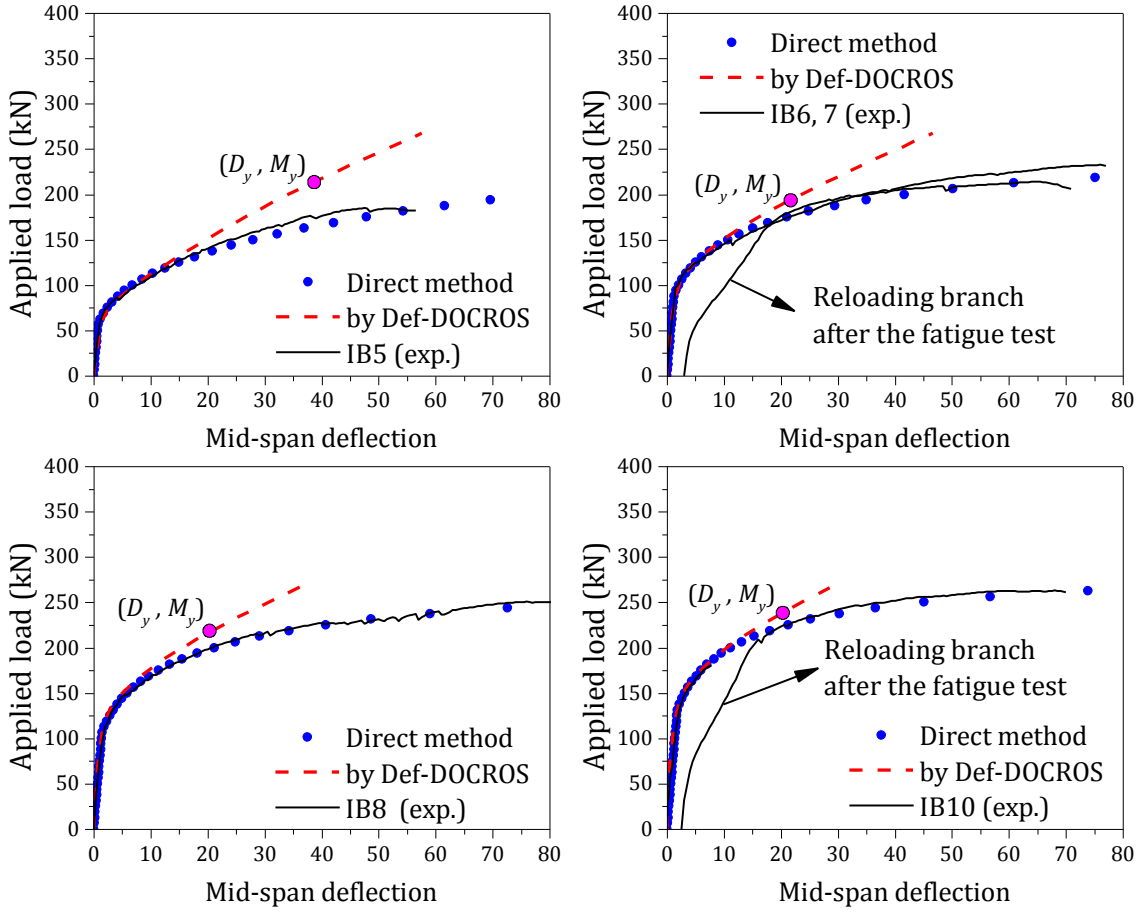

Figure 5-36: Applied force *versus* mid span deflection of the tested beams in group B

The experimental force-deflection response recorded from IB1 showed asymmetrical behavior comparing to the other beams in group A. As shown in Figure 5-35 for IB1, a great load drops was observed in the recorded force-deflection response. The reason of this abnormal behavior is due to non-uniform distribution of the applied load in the two loading points. In this test, a critical diagonal crack was formed firstly at one side of the beam's shear span, which resulted in a loading drop at mid span deflection of about 30 mm. Afterward, the applied load started to increase again, leading to form another critical diagonal crack at another side of the beam's shear span, which resulted in the second load drop, and finally the failure of the beam. Figure 5-37a and b show the critical diagonal shear cracks at two sides of the beam for IB1, which did not occur simultaneously. This non-uniform behavior can be mainly due to a poor HPFRC casting process and/or intensely different fiber distribution and orientation between the shear zones. As a consequence of these deficiencies, the different HPFRC flexural stiffness can be attained at the cracked sections in theses shear

zones, which may cause asymmetrical behavior of the whole system. It should be noticed that in some cases, this phenomena can be beneficial as, for example, in the case of specimen IB1, the higher load carrying capacity was attained in IB1 when compared to the results from the direct method. However, in general, attaining the minimum requirements for HPFRC strength and fibers distribution in all part of RC structure should be always under control.

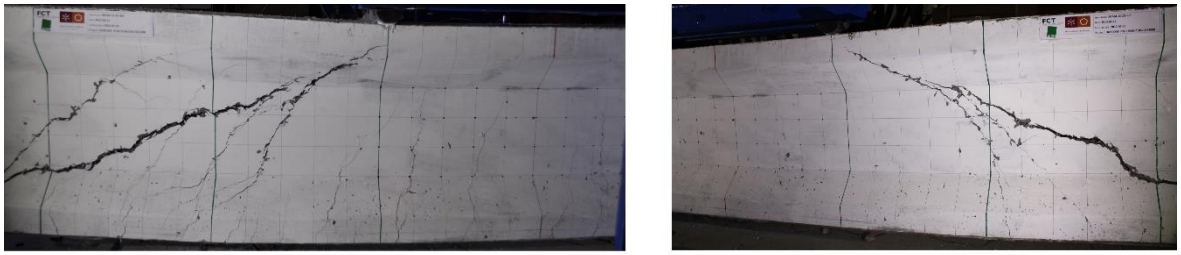

Left side (239 kN) Right side (208 kN)

Figure 5-37: Critical diagonal shear crack in IB1 at left and right sides of beam in shear span

Furthermore, the theoretical "yielding point" that is defined as the theoretical maximum moment of the beam and its corresponding mid span deflection at yield initiation of the steel strand, being respectively, M_y and D_y, is demonstrated in Figure 5-35 and Figure 5-36 for all tested beams. Note that M_y was obtained as the output results from DOCROS software that was included in Table 5-10, while D_y was obtained as the output results from Def-DOCROS software whose values were included in Table 5-13. As mentioned earlier, none of the beams in group A was carried the applied moment higher than M_y. Conversely, the maximum applied moment for the beams in group B (with the exception of IB5 as the reference beam) was higher than M_y, meaning that steel strand yielded for this group of specimens. This gave higher ductility to the beams in group B as it is discussed in the next section.

5.4.3 Ductility and deformability

Deformability is an important aspect for determining the safety of FRP prestressed beams. Since FRP bars are brittle materials, a care should be taken to ensure sufficient warning for these structures. Based on the deformability-approach that was previously defined in Chapter 2, and firstly proposed by Jaejer *et al.* (1997), ductility of FRP-RCs can

be measured taking into account the following effects:

1) The strength effect nominated by C_s, and defined as the ratio between the flexural strength of the beam at ultimate limit stage (ULS) and service limit stage (SLS):

$$C_s = \frac{M_u}{M_{SLS}} \tag{5-129}$$

where M_{SLS} is the applied moment corresponding to SLS for mid span deflection being equal to $L/250$ (included in Table 5-13), and M_u is the maximum moment that carried by the beam at ultimate limit stage;

2) The deformation effect nominated by C_d, and it is defined as the ratio between the maximum deflection of the beam at ULS and SLS:

$$C_d = \frac{D_u}{L/250} \tag{5-130}$$

where D_u is the maximum deflection that corresponds to the peak load in the force-deflection response.

The ductility index is defined by multiplying these two factors. The calculated ductility index (*i.e.* μ), as well as the strength and deformation effects of the tested beams are compared using three column charts presented in Figure 5-38. To understand better the ductility improvements of the tested beams, the *deformation* and *strength effects* calculated by using the force-deflection response obtained from the Def-DOCROS software are also presented in these figures. The reason of this comparison is that Def-DOCROS was developed for simulating the behavior of elements failing in bending. Therefore, the force-deflection response of the I-beams from Def-DOCROS is only governed by flexural deformation of the beam. Hereafter, the force-deflection response of beam by Def-DOCROS is known as "*reference response*".

5.4.3.1 Strength effect

From Figure 5-38a, the *strength effect* C_s, calculated from the experimental force-deflection response are totally lower than the respective value calculated from the *"reference response"*. By increasing the prestress level of the beam, the difference between these two

values becomes smaller in which for IB10 with the highest amount of prestress level the difference is almost negligible.

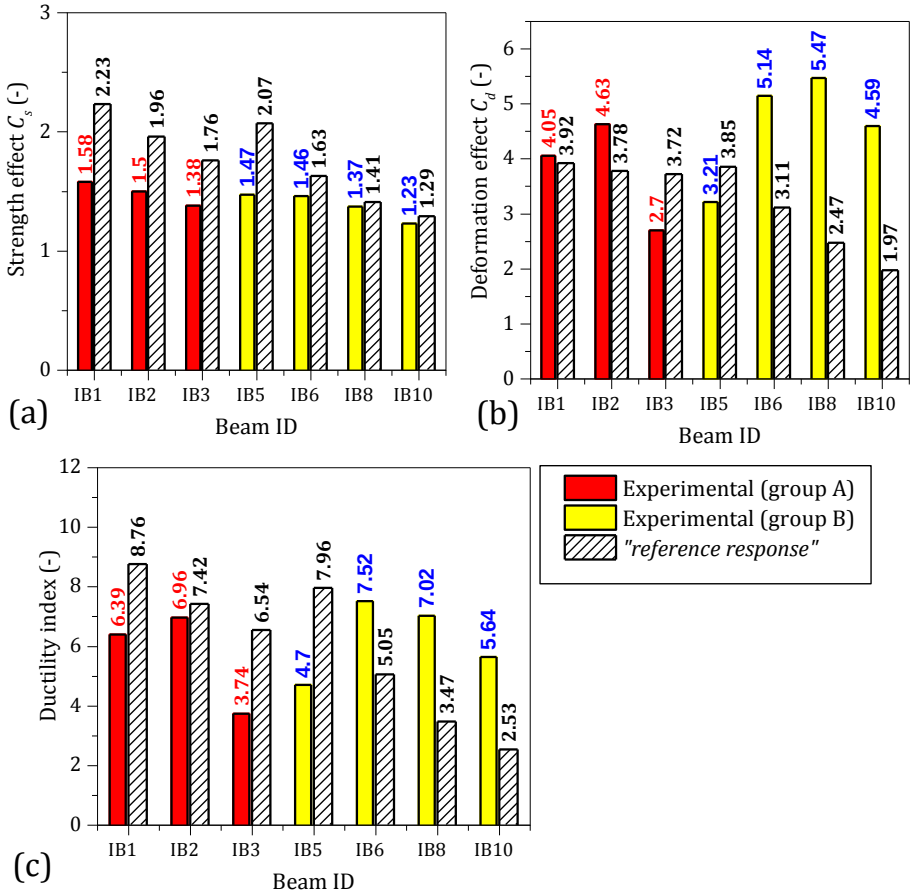

Figure 5-38: Comparison between the ductility index of the tested beams with the reference response by Def-DOCROS: (a) strength effect, (b) deformation effect, and (c) ductility index

5.4.3.2 Deformation effect

In Figure 5-38b, the *deformation effect* C_d, that is calculated from experimental force-deflection response are compared with those obtained from the *"reference response"*. With an exception of the non-prestressed I-beams, C_d increases for all the prestressed I-beams. This increase is much higher for the case of under-reinforced beams in group B, in which the value of C_d from the experiments is about two times higher than the calculated C_d from the *"reference response"*.

5.4.3.3 Ductility index

The ductility index, μ, of the tested beams is compared with the ones obtained from the *"reference response"*. As shown in Figure 5-38c, the ductility corresponding to elements

governed by flexural deformation was not attained in over-reinforced beams (group A), while it was exceeded in the under-reinforced beams (group B). In fact, the prestressed IB6, IB8 and IB10 can exhibit enough deformation at the ultimate stage before failing with no loss of the strength. This can be a great achievement in terms of structural performance of the proposed hybrid HPFRC prestressed beams, in which the beams behaves efficiently similar to its *"reference response"* up to the service loads, afterward, at ultimate limit stage, the progressive degradation of beam curvature in the flexure-shear region introduces higher deformation to the global response of the beam, while the beam can maintain the flexural strength.

5.4.4 Cracking behavior

To analysis the cracking behavior of the tested beams, the obtained crack pattern and the measured value of CMOD are evaluated under service load. From what was discussed in the previous sections, the under-reinforced I-beams in group B showed better structural performance rather than the beams in group A. For this reason, the cracking analysis is restricted to group B of the specimens in the next sections.

5.4.4.1 Crack pattern

The crack patterns of IB5, IB6 and IB8 at mid span deflection of about 15 mm are compared in Figure 5-39. Based on the experimental crack pattern, the following results can be remarked:

- The cracking length of the tested beams decreases with the increase of the prestress force of the reinforcements at the same level of deflection at mid span. The cracking length is simply defined by the distance between two beam's sections at two sides of the shear zones that are remained uncracked, and it may be experimentally approximated by the distance between the last two formed cracked at two sides of the beam, as shown in Figure 5-39. The decrease in the cracking length is due to the fact that the prestress in reinforcing bars increases the cracking moment of the beam because of the initial confinement and negative camber that imposes by the applied

prestress force;

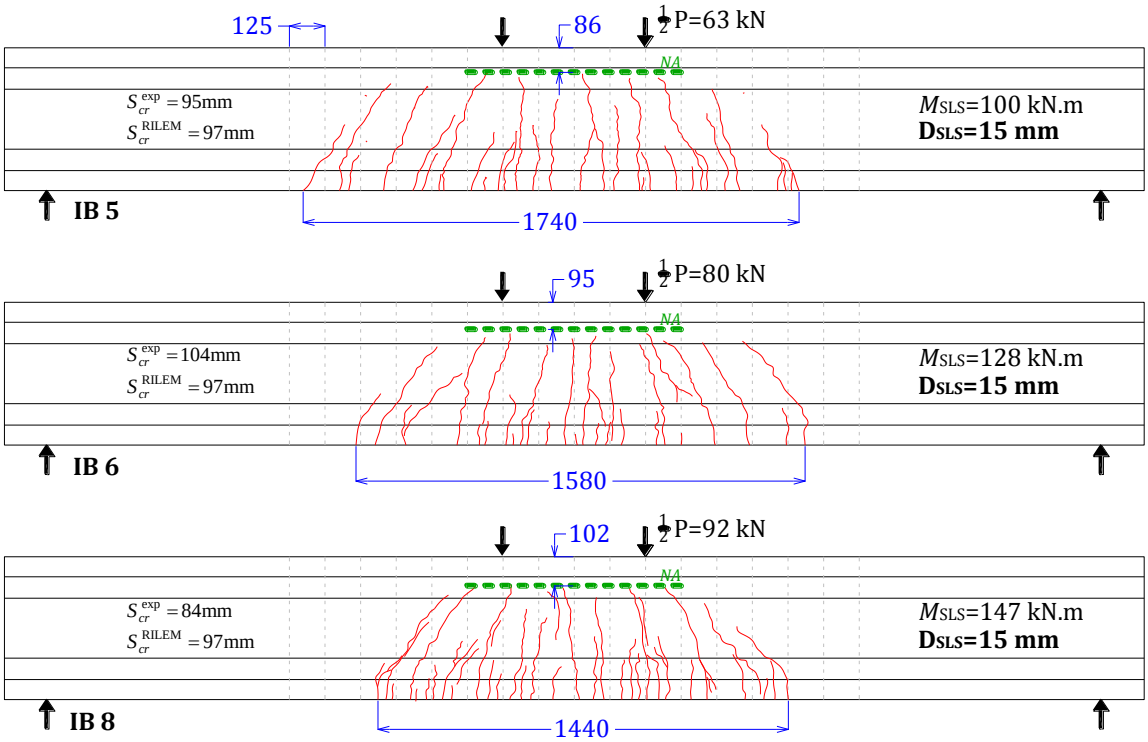

Figure 5-39: Crack pattern of the monotonically tested beams for the mid span deflection corresponding to SLS

- The prestress level of the longitudinal reinforcements showed no significant effect on crack spacing of the beams. The average crack spacing measured for IB5, IB6, and IB8 is written in Figure 5-39 (indicated as S_{cr}^{exp}). The measured crack spacing is in good agreement with the final crack spacing proposed by the analysis procedure in Section 5.3.5 (the values were included in Table 5-12), as well as the crack spacing recommended by RILEM from Eq. (5-101);
- The theoretical level of the neutral axis obtained by DOCROS at SLS is illustrated in Figure 5-39 using a bold dashed-line. On the other hand, the position of crack tips in the constant moment region can approximately represent the experimental depth of the neutral axis in this region. As it is observed, the theoretical and experimental crack pattern are in a good agreement. This may proof that assuming linear distribution of strain (Bernoulli assumption) up to SLS is quit acceptable for the proposed hybrid system in this study.

5.4.4.2 Crack width

The value of maximum crack with, *i.e.* w_f , *versus* the average tensile stress of GFRP bars, *i.e.* ε_f , are plotted in Figure 5-40 for IB5, IB6, IB8 and IB10. The average tensile stress of GFRP bars were obtained using the recorded strain by means of the installed strain gauges SG2, SG3 and SG4 at bending zone. Note that the results of IB10 are from the monotonic test before the fatigue load cycles.

Additionally, the theoretical $w_f - f_f$ obtained from the crack analysis procedure described in Section 5.3.6 and designated as "proposed model", is plotted in Figure 5-40 for IB5, IB6, IB8 and IB10. The proposed model is based on the moment-rotation approach and mechanics based beam hinge model (discussed by Visintin *et al.* 2012 and by Barros *et al.* 2015) that considers the bond-behavior of the reinforcing bars, as well as the post-cracking behavior of HPFRC. As shown in Figure 5-40, the model predicts with a good accuracy the experimental value of the crack width up SLS. On the other hand, based on the equation given by ACI, a wide range of crack width is obtained for FRP-RCs depending on the adopted value for k_b (see the plotted pattern in Figure 5-40). As shown, the highest accuracy is obtained when $k_b = 0.6$, which represents a good bond degree between GFRP bars and HPFRC. However, this equation may be modified in order to take into account explicitly the effect by the HPFRC residual tensile stress after cracking and the HPFRC-FRP bond strength in the calculation of crack width. Additionally, the equation given by RILEM in case of Steel-FRC beams is plotted in Figure 5-40. As shown, this equation predicts well the experimental results of crack width. In this equation, also, the bond quality between GFRP and HPFRC was taken as the highest value by giving 1.0 to the parameter k_3.

Finally, by using the proposed model, the theoretical curve of the applied moment *versus* the crack width (*i.e.* $M_a - w_f$) for IB8 is compared in Figure 5-41 (as an example) with the case when HPFRC is replaced by plain concrete. Note that the same concrete compressive strength is adopted, and the bi-linear concrete softening law recommended by Model Code 2010 is taken into account for the behavior of plain concrete in tension. Based in this comparison, the value of crack width significantly increases in case of the plain concrete

prestressed beam for the same level of applied moment. The difference between these two theoretical curves in Figure 5-41 may reveal the contribution by steel fibers at crack section to maintain the crack narrower. It should be noticed that the same bond-slip behavior is adopted for GFRP bars and steel strand in the analysis.

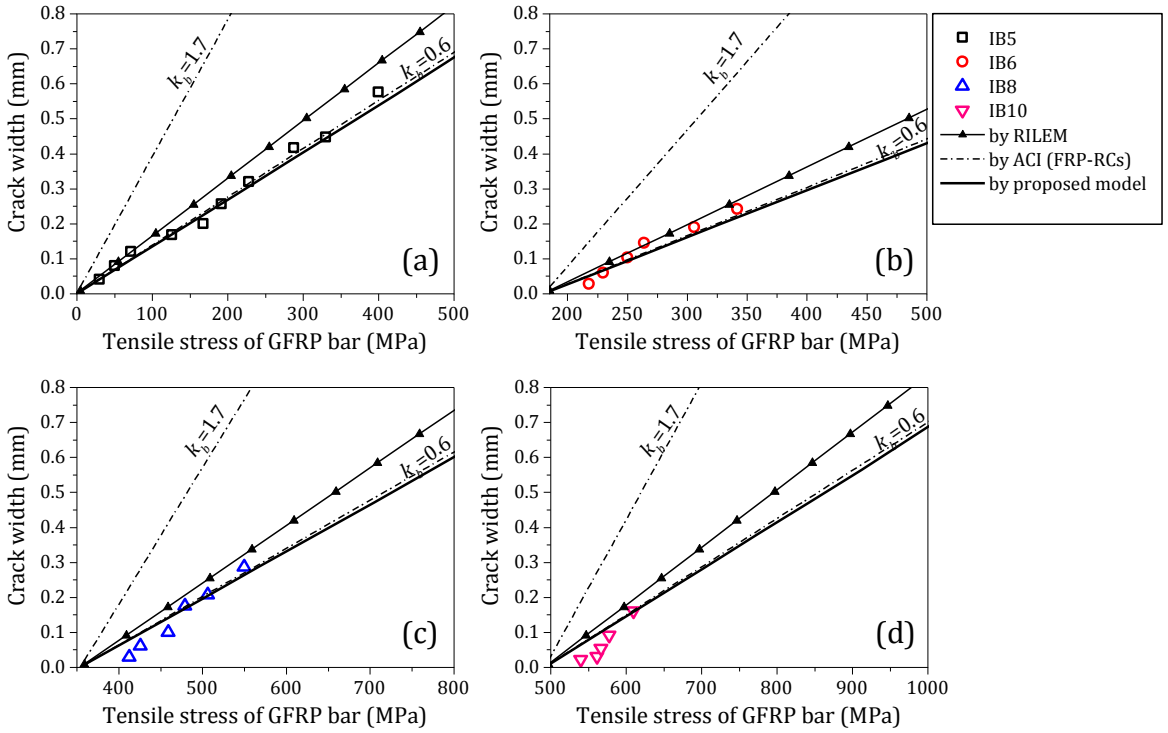

Figure 5-40: Comparison between the theoretical and experimental crack width up to SLS

The bond behavior between reinforcing bars and FRC is commonly better than bond between bars and plain concrete for the same level of the compressive strength. However, this effect was not taken into account in the analysis presented in Figure 5-41, since for the range of the bar's slip at SLS, the difference between bond quality of bar-concrete and bar-FRC may not be significant. In fact, the significant damage occurred in the bar-FRC interface when slipping of bar is in the *plastic*, *softening* or *frictional* bond phases (Figure 3-13 in Chapter 3), and the steel fibers can effectively influence the debonding progress by bridging the cracks at interface. Therefore, for the small range of slip at SLS, the bond-slip behavior of bar-concrete and bar FRC may be almost similar for the same class of the concrete compressive strength

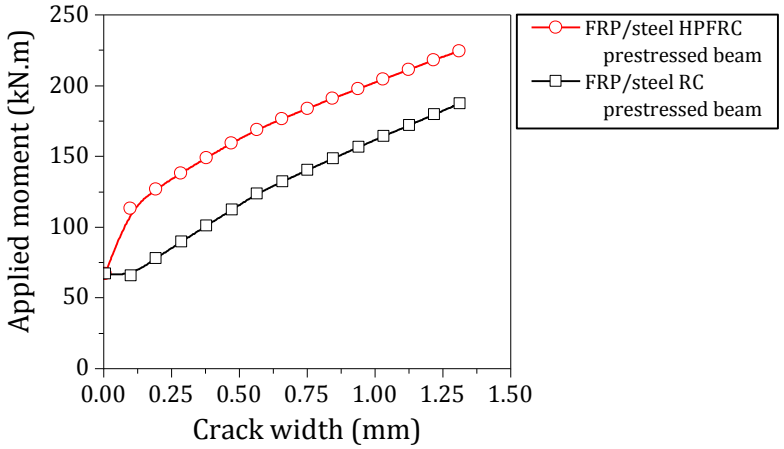

Figure 5-41: Comparison between the applied moment *versus* crack width of hybrid FRP/steel RC and HPFRC prestressed beams

5.4.5 Strain results

The tensile train of GFRP bars measured by the strain gauges SG2, SG3 and SG4 (see Figure 5-5) are plotted in Figure 5-42 for IB5, IB6, IB8 and IB10. Additionally, the compressive strain of HPFRC measured by SGc (see Figure 5-6) at mid span section is presented in Figure 5-42.

It was unlikely to have the strain gauge of steel strand working for the strain values greater than the yielding strain because of the section configuration of this steel strand. The steel strand is formed by seven steel wires (see Figure 5-1), hence, the average value of strain by these seven wires can be a good representative of the strain value in steel strand. But, the strain gauges was installed only on a single wire as shown in Figure 5-6, and it was quite impractical to have many of them installed at the same section. As an example, the recorded strain by this strain gauge for IB8 is plotted in Figure 5-42c. As shown, for the value of strain higher than about 0.8%, which is close to its yielding strain, the data logger started recording abnormally higher rate of increase in this strain gauge, and in short time after, the strain gauge was failed. The same happened for this strain gauge in IB6, and unfortunately, the strain gauge of steel strand was failed at the beginning of the test in IB5 and IB10. Besides, the strain gauges for GFRP bars worked in a better way, and much higher range of strain was measured for GFRP bars before failing of the beams.

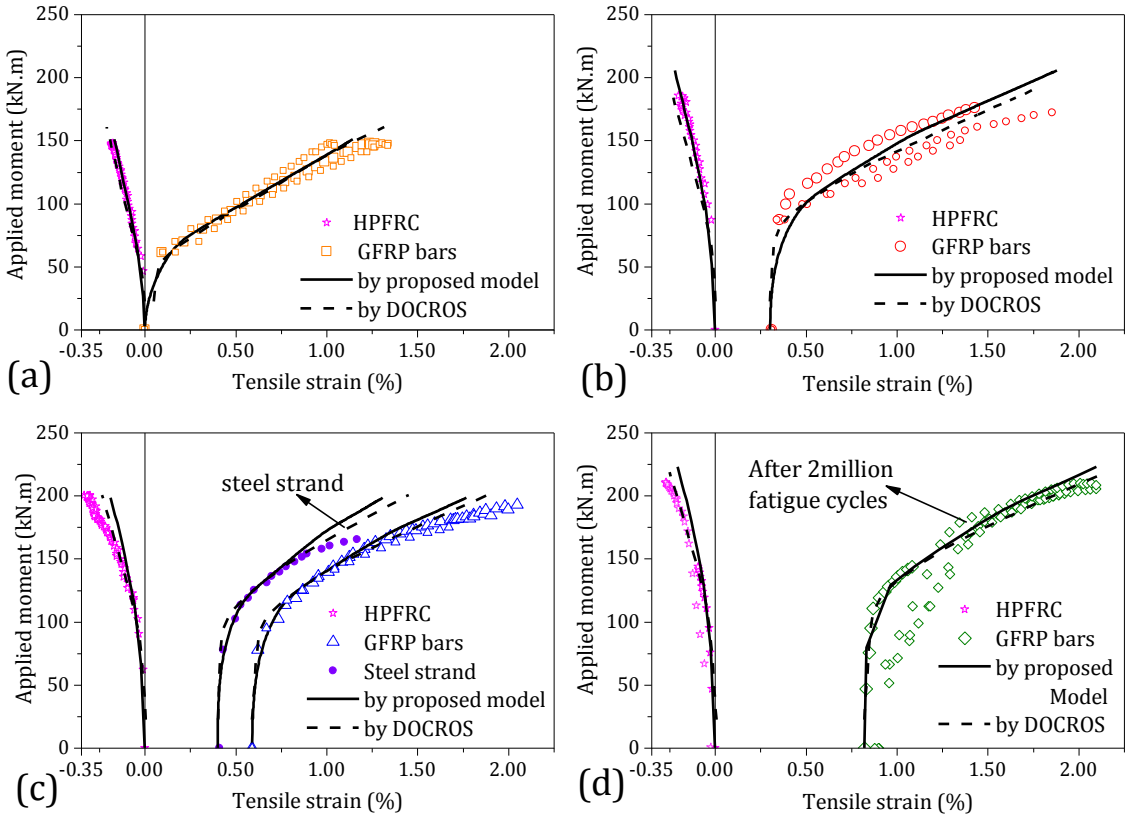

Figure 5-42: Tensile strain of the longitudinal reinforcements and compressive strain of HPFRC at mid span during the monotonic tests: (a) IB5, (b) IB6, (c) IB8, and (d) IB10

The measured values of tensile strain at SLS, the maximum recorded value of strain before failing of the I-beams for both GFRP bars and steel strand, and the value of compressive strain of HPFRC at mid span measured by SGc are all included in Table 5-14.

Table 5-14: Tensile strain of the longitudinal reinforcements as well as the compressive strain of HPFRC at service limit state and failing stage

Beam ID	GFRP bars			Steel strand			HPFRC		
	ε_f^{SLS} *	ε_f **	$\varepsilon_f/\varepsilon_{fu}$	ε_s^{SLS} *	ε_s **	$\varepsilon_s/\varepsilon_{sy}$	ε_c^{SLS} *	ε_c **	$\varepsilon_c/\varepsilon_c'$
	(%)	(%)	(-)	(%)	(%)	(-)	(%)	(%)	(-)
IB5	0.49	1.05	0.47	-	-	-	0.093	0.180	0.51
IB6	0.81	1.90	0.84	0.74	-	-	0.077	0.190	0.54
IB8	1.09	2.13	0.95	0.82	1.17	1.17	0.120	0.320	0.91
IB10	-	2.12	0.95	-	-	-	-	0.270	0.77

* value of strain at service limit state;
** the last value of strain recorded during the monotonic test.

For case of IB8 and IB10, the tensile strain of about 2.12% was recorded for GFRP bars in the bending zone, which is about 95% of its ultimate tensile strain as reported by the manufacturer (written in Table 5-1). Note that the tensile strain reported in Table 5-14, and plotted in Figure 5-42, is the total tensile strain of reinforcements including the initial pre-

strain due to the prestressing process. In addition to the experimental results, the theoretical values of the applied moment *versus* the strain obtained from DOCROS software, as well as the respective values obtained from the proposed model in section 5.3.6 are plotted in Figure 5-42. As shown, both models captured with an accepted accuracy the experimental trends. However, for high level of the applied moment near to the failing point, the measured strain showed higher increasing rate rather than the theoretical values (see the plotted curves in Figure 5-42b, c and d). This is mainly due to:

1) Decrease in the Young's modulus of GFRP bars for the high level of strain near to the ultimate tensile strain. In fact, the stress-strain behavior of GFRP bar is not perfectly linear elastic up to failing. Based on the results reported by manufacturer, there is slight decrease in the stiffness of this diagram when the strain approaches to its ultimate value;
2) Occurrence of the higher deformation effect in the tested I-beams when it compares with the "reference response" from Def-DOCROS. This concept will be discussed in the next section.

5.4.5.1 Higher longitudinal tensile strain at the vicinity of failure stage

As already mentioned in Section 5.4.3.2, the tested beams showed higher deformation effect rather the "*reference response"* by Def-DOCROS. This higher deformation effect resulted in the higher curvature in the beam, led to impose an extra deformation to the reinforcing bars at the mid span. Note that this higher deformation effect was imposed from the shear span to the mid span. The difference between the effective curvature (*i.e.* χ_{eff}) of the beam, and the curvature calculated by DOCROS (which was used as the input data for Def-DOCROS) in the constant moment region for the same level of applied moment is a relevant parameter to modify the value of strain of the longitudinal bars at mid span section. The effective curvature, χ_{eff} , can be calculated by means of the effective moment of inertia (*i.e.* I_{eff}^{h}):

$$\chi_{eff} = \frac{M_a}{E_c I_{eff}^{h}} \tag{5-131}$$

The value of tensile strain of GFRP bars can be simply modified by adding the following value to the calculated tensile strain by DOCROS:

$$\Delta\varepsilon_f = \Delta\chi\left(d_f - c\right) = \left(\chi_{eff} - \chi_D\right)\left(d_f - c\right) \tag{5-132}$$

where χ_D and c are, respectively, the calculated curvature and the level of neutral axis by DOCROS, which correspond to the applied moment of M_a. This modification by Eq. (5-132) has been implemented to the results obtained by DOCROS for the case of IB8 (as an example), and it is plotted in Figure 5-43. As can be seen, by considering the effect that is due to the higher deformability caused by the higher curvature in the shear span, it fits the modified tensile strain of GFRP bars to the experimental measurement of strain. Note that this modification is relevant only for the high value of the applied moment near to the failing stage of beam, where the beam curvature significantly increased.

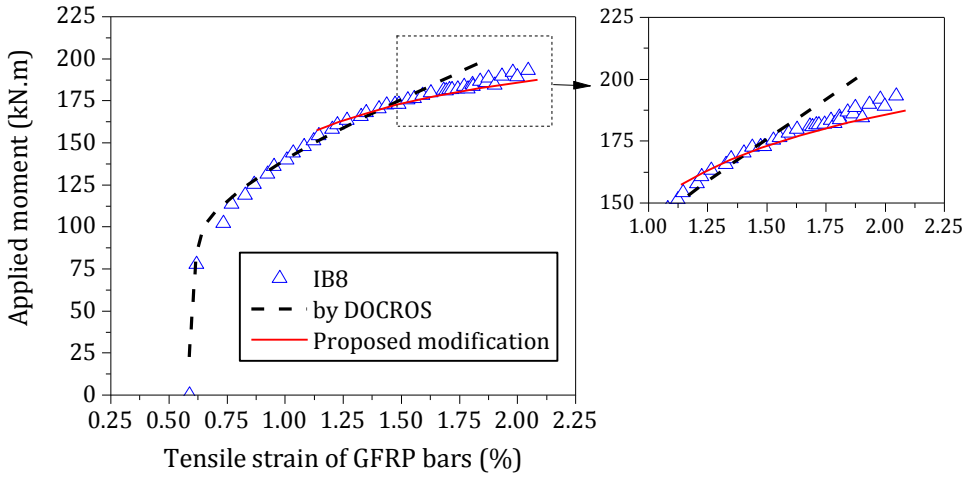

Figure 5-43: Comparison between the modified tensile strain of GFRP bars and the measured values during the test

5.4.5.2 Difference between moment-rotation and moment-curvature approach

Based on the results of strain that was presented in Figure 5-42, a slight difference is observed between the theoretical trend by DOCROS and by the proposed model described in Section 5.3.6, which is based on the moment-rotation approach. The main difference of these two models is related to the assumption of the deformation profiles along the section. In DOCROS, a linear strain profile is adopted along the section, in which the crack tensile strain of HPFRC and the tensile strain of reinforcing bars are assumed equal at the level of

reinforcements. However, for the proposed model, a linear deformation profile is adopted along the section, in which the half value of tensile deformation of HPFRC at crack section (*i.e.* half of crack mouth opening) is taken as the bar's slip. By having this slip at crack section, the tensile strain of the reinforcing bars is obtained by solving their governing bond formulation, which was previously described using two FBL and IBL models in Chapter 4. Therefore, the strain profile at the crack section is not necessarily linear. Note that the crack spacing (*i.e.* S_{cr}) is taken as the bond length (*i.e.* L_b) in FBL model (Annex 4B). On the other hand, the crack tensile stress in the model was calculated using directly the tensile stress-crack width diagram of HPFRC plotted in Figure 5-11. However, the crack tensile stress of HPFRC in DOCROS software is calculated by the converted stress-crack width diagram to stress-strain diagram using the concept of an effective crack band width that is taken equal to the crack spacing, which is named as the structural characteristic length, l_{cs}, by Model Code 2010. Although the models consider two different strain profile at crack section, the results of these two models are close, and are in good agreement with the test results. This is attributed to the fact that when l_{cs} is taken as S_{cr} for converting the stress-crack width to stress-strain for HPFRC, it means the tensile strain of the reinforcement over S_{cr} is considered constant, which, consequently, introduces a linear distribution profile of bar's slip over the crack spacing:

$$\varepsilon_{ct}^{cr} = \varepsilon_r = \frac{w_{cr}}{S_{cr}} \tag{5-133}$$

where ε_{ct}^{cr} is the crack tensile strain of HPFRC at the level of reinforcements. On the other hand, the distribution of slip obtained by FBL model over the crack spacing is properly close to the adopted linear distribution by Eq. (5-133). To understand better this concept, the distribution of the slip and the tensile strain of the GFRP bar over the crack spacing by FBL model are compared, respectively, in Figure 5-44a and b with the respective distribution considered in DOCORS model. As shown, the distribution of slip of reinforcement between two consecutive cracks can be sufficiently taken linear. However, a slight difference is observed by assuming a constant tensile strain of bar over the crack spacing.

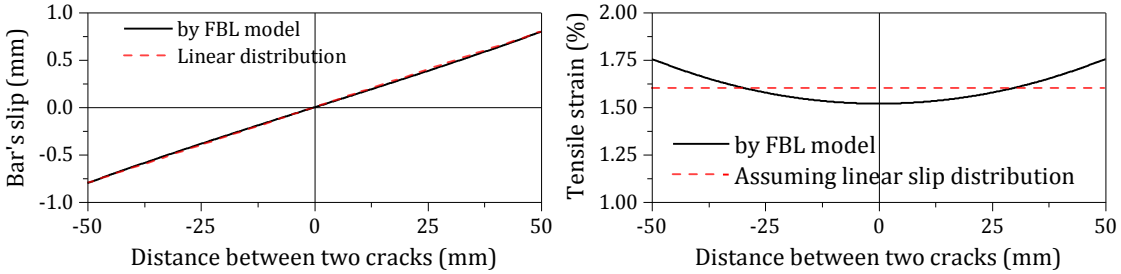

Figure 5-44: Distribution of slip and tensile strain of GFRP bars over the crack spacing

5.4.6 Fatigue results

The beams IB7, IB9 and IB10 were subjected to the fatigue loading conditions based on the loading template presented in Figure 5-7b. A total of 2 million cycles of sinusoid Constant-Amplitude (CA) loading conditions with 2Hz frequency was planned to apply to the beam specimens. It is unlikely that fatigue will be a problem in the un-cracked beam since the stress ranges in the prestressed GFRP bars and steel strand under repeated loading are small. Additionally, it was impractical to implement with high frequency the fatigue cycles starting from elastic to in-elastic domain due to the great loss of flexural stiffness, which leads to a high magnitude of deformation. Therefore, the range of fatigue cycles was selected in the elasto-cracked at service loading conditions. The maximum applied load was calculated based on the total flexural strength of the monotonically tested beams (*i.e.* IB6 and IB8). However, for IB10; the theoretical force-deflection response was taken into account, since there was no corresponding specimen submitted to monotonic load conditions. The value of maximum applied load in the fatigue cycles (*i.e.* F_{max} shown in Figure 5-7) was taken about 70% of the peak applied load in the monotonic test (about 90% of the maximum service moment M_{SLS}), while the minimum value of the applied load (*i.e.* F_{min} shown in Figure 5-7) was about 55% of the peak applied load. Based on this range, a constant amplitude of 30kN was determined for all the specimens. The range of the applied moment during the fatigue cycles is schematically illustrated in Figure 5-45. Furthermore, the amplitude of applied moment and load during the fatigue cycles are written in Table 5-15.

Based on the adopted loading amplitude, the range of strain in the intervening materials at the beginning of the fatigue cycles were measured by means of the installed strain gauges.

These calculated values are included in Table 5-16. With an exception of IB9, which failed after about 1.82 million cycles, IB7 and IB10 successfully carried 2 million fatigue cycles at 2Hz. After these cycles, the beam was unloaded, and monotonically tested up to its failure. Unfortunately, the strain gauge of steel strand failed at the beginning of the test for IB10, and no strain was measured during fatigue cycles for the steel strand.

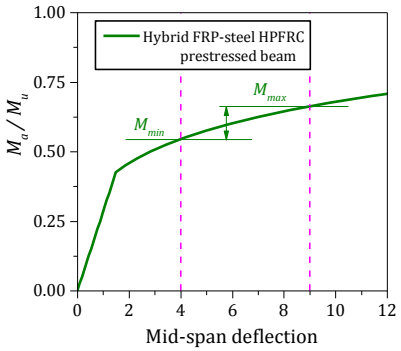

Figure 5-45: The range of applied moment during the fatigue cycles: normalized applied moment *versus* mid span deflection

Table 5-15: Range values of the applied moment and load during the fatigue cycles

Beam ID	M_{SLS}	$M_{\min}$ [1]	$M_{\max}$ [2]	M_u	$F_{\min}$ [3]	$F_{\max}$ [4]	$M_{\min}/M_u$	$M_{\max}/M_u$	$M_{\min}/M_{\max}$
	(kN.m)	(kN.m)	(kN.m)	(kN.m)	(kN)	(kN)	(-)	(-)	(-)
IB7	125	100	124	186	125	155	0.54	0.67	0.81
IB9	147	112	136	201	140	170	0.56	0.68	0.82
IB10	157	120	144	212	150	180	0.57	0.68	0.84

[1] the minimum applied moment during the fatigue cycles, corresponding to $F_{\min}$;
[2] the maximum applied moment during the fatigue cycles, corresponding to $F_{\max}$;
[3] the minimum applied moment during the fatigue cycles;
[4] the maximum applied moment during the fatigue cycles.

Table 5-16: The lower and upper value of strain in the material, and the beam curvature at the beginning of fatigue cycle

Beam ID	**GFRP bars**			**Steel strand**			**HPFRC**			**Flexural stiffness**			
	ε_f^{l} *	ε_f^{u} *	R **	ε_s^{l}	ε_s^{u}	R	ε_c^{l}	ε_c^{u}	R	χ_{eff}^{l}	χ_{eff}^{u}	χ_u ***	R
	(%)	(%)	(-)	(MPa)	(MPa)	(-)	(MPa)	(MPa)	(-)	(mm^{-1})	(mm^{-1})	(mm^{-1})	(-)
IB7	0.45	0.56	0.8	1022	1162	0.88	24.2	29.0	0.83	3.7e-6	7.9e-6	6.0e-5	0.47
IB9	456	511	0.81	1087	1125	0.87	29.2	34.6	0.86	3.4e-6	6.9e-6	5.7e-5	0.50
IB10	553	703	0.79	-	-	-	32.3	40.7	0.79	3.6e-6	7.9e-6	5.4e-5	0.46

* superscript "*l*" indicates lower stress limit, while "*u*" is for upper stress limit during the first fatigue cycle;
** Factor *R* is defined as the ratio between the lower strength and upper strength during the fatigue cycles;
*** Curvature of beam at failing (ultimate static curvature).

In Figure 5-46, the evolution of the strain *versus* the number of fatigue cycles is plotted for the tensile strain of GFRP bar and steel strand at mid span, as well as the compressive strain of HPFRC on top surface. As shown In Figure 5-46a, the strain in the prestressed GFRP bars has increased with the number of cycles. The different strain gradient due to the

different prestress level is observable for the tested beams. The same increasing rate was obtained for the tensile strain of GFRP bars in IB7 and IB10 under the fatigue cycles. However, the rate of this increase was higher in IB9. The evolution of strain in steel strand is shown in Figure 5-46b for IB7 and IB9. The strain of strand increases with the number of fatigue cycle in IB7, however, in IB9, the value of strain gauge abnormally showed a decrease tendency by increasing the number of cycles. The two following reasons might be the answer to this abnormal behavior:

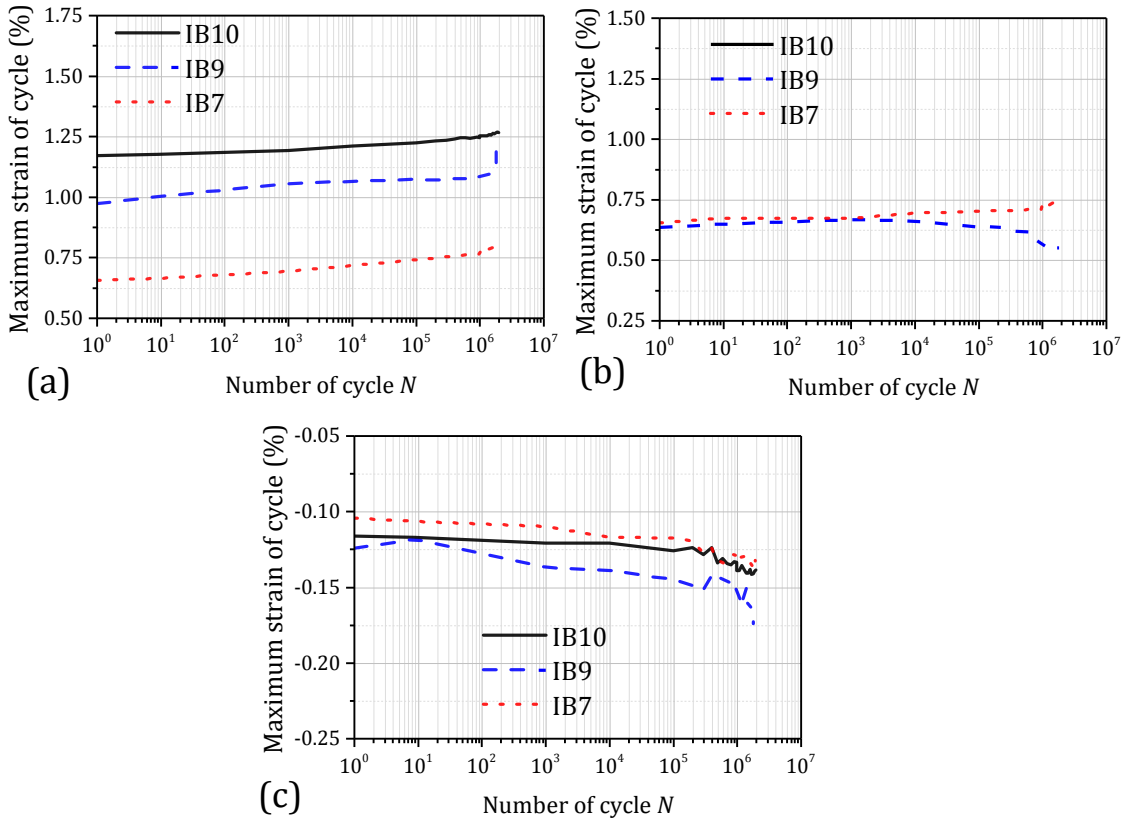

Figure 5-46: Strain evolution of the intervening materials in hybrid steel/GFRP HPFRC prestressed beams: (a) GFRP bar, (b) Steel strand, and (c) HPFRC (compressive strain)

1) It might be possible that the wire with the strain gauge installed on, locally yielded near to the mid span section, hence, the stress level, and consequently strain decreased for this wire. Since this beam was unexpectedly failed before termination of 2 million cycles, the early yielding of the steel strand at least in one or two wires might be the reason;
2) Secondly, based on the results obtained from the monotonic tests, it was almost unlikely to have this strain gauge working near or after its yielding phase due to the

section configuration of strand. Note that the yield initiation is between about 0.8% and 1% reported by the manufacturer. Therefore, the abnormal results of strain might be a sign of failure in the strain gauge;

The obtained results in terms of the compressive strain of HPFRC is plotted in Figure 5-46c. The absolute value of this strain showed an increasing tendency as obtained for the tensile strain of longitudinal reinforcement. As shown in the figure, the compressive strain of HPFRC showed higher strain gradient in IB9 comparing with the other two beams, as the same approach obtained from the strain results of GFRP bar and steel strand in IB9.

Additionally, the degradation of flexural stiffness of the prestressed I-beams is evaluated in terms of increase in the effective curvature of the beam (*i.e.* χ_{eff}). The effective curvature of the beam can be simply calculated by

$$\frac{M_a}{E_c I_{eff}^h} = \chi_{eff} = \frac{6D_{mid}}{\left(\frac{3}{4}S^2 - a^2\right)} \tag{5-134}$$

where D_{mid} is vertical deflection of mid span section measured by LVDT3 (see Figure 5-5). The upper and lower effective curvature at the beginning of the fatigue cycles are included in Table 5-16. It should be noticed that the ultimate curvature reported in Table 5-16 was determined from the results of the monotonic tests taking the ultimate deflection corresponding to the peak applied load at mid span section. Figure 5-47 compares the degradation of the flexural stiffness of the fatigue specimens. As shown, the stiffness of IB9 showed a significant decrease during the fatigue cycles. In fact, to compare with the other two fatigue beams, this beam abnormally lost its stiffness, which might be due to an uncommon failure of GFRP bar or steel strand. Because, in IB10 that the range of stress of GFRP bars was even higher than IB9, no sign of failure was observed after two million fatigue cycles.

As Figure 5-48 shows, IB9 failed in bending followed by the abrupt tensile rupture of the GFRP bars. No sign of failure in shear span was detected since the crack pattern was almost the same since the beginning of fatigue cycles. This can be confirmed that the beam failed due to its significant stiffness loss at mid span, which results in the tensile failure of

the longitudinal reinforcements at mid span. Based on the obtained results of the flexural stiffness shown in Figure 5-47, after 2 million fatigue cycles, in total, IB7 has lost about 8% of its stiffness comparing to the static case (*i.e.* monotonic load), and this value was about 5% for IB10.

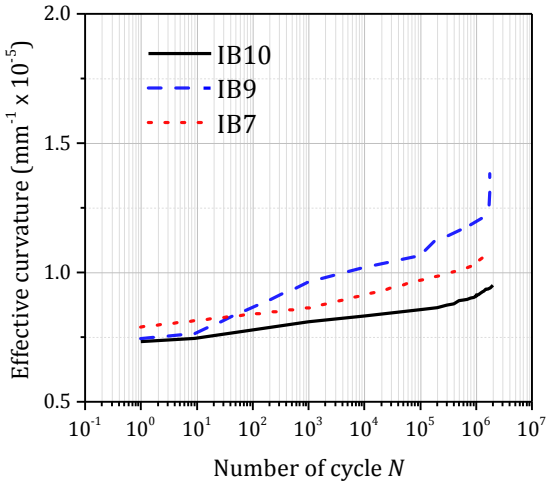

Figure 5-47: Evolution of the effective curvature of the tested beam under the fatigue loading condition

Figure 5-48: Failure of specimen IB9 after about 1.82 Million of fatigue cycles

The beams IB7 and IB10 were subjected to monotonic test after the fatigue cycles. The monotonic response of these two beams are plotted in Figure 5-49. The force-deflection response of IB6, which has the same configuration of IB7, as well as the theoretical force-deflection response predicted for IB10 by using the direct method, are compared in Figure 5-49. It is versified that IB6 and IB7 showed a slight decrease in terms of flexural strength. On the other hand, IB10 showed no loss in the flexural strength and ductility index when compared to the theoretical curve by the direct method. It should be noticed that the reloading branch plotted in Figure 5-49 was recorded by means of the data logger when the

beam was unloading in accordance with the reloading template shown in Figure 5-7b.

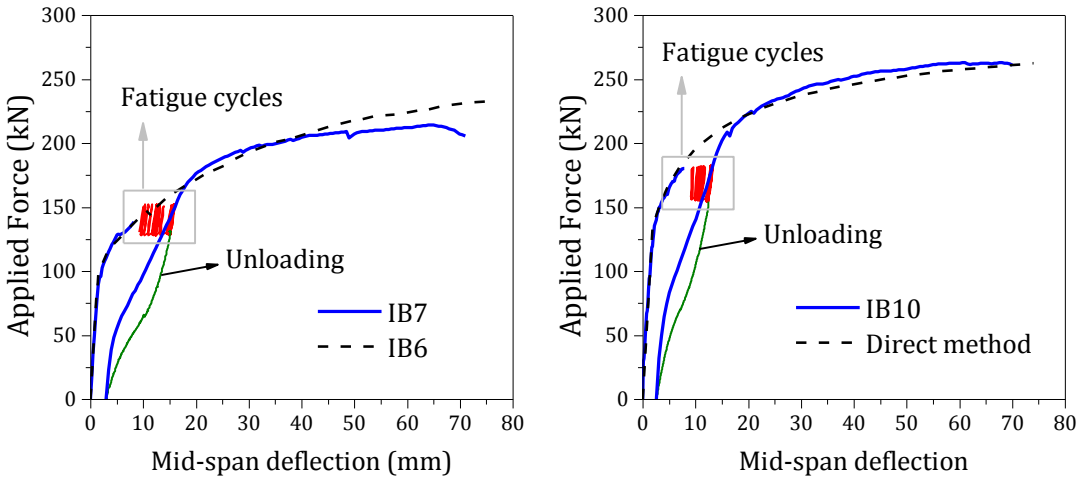

Figure 5-49: Force-deflection response of IB7 and IB10 from the monotonic tests after 2 million of fatigue cycles

5.5 Summary and conclusion

In this chapter, the structural performance of prestressed HPFRC I-shaped cross sectional beams reinforced by hybrid steel strand and GFRP bars was experimentally and theoretically investigated. The tested beams were categorized in two main test groups. The first group of the tested beams included three beams with nearly balanced reinforced condition and one beam with over-reinforced condition, while the second group included six beams with under-reinforced condition. The tested beams were subjected to monotonic and fatigue four-point loading conditions. The structural response of the tested beams including, cracking, deformation, reinforcement strain, and HPFRC strain in compression were monitored during the tests. In addition to the experiments, a comprehensive analytical formulation was developed in order to address theoretically the structural responses of the hybrid reinforced beams. Based on the obtained results from both analytical and experimental research activities, the following remarks can be drawn:

- Since no HPFRC crushing in compression or rupture of FRP bar in tension occurred at the failure stage of the tested beams, it can be concluded that none of the beams reached their maximum flexural capacity. However, by increasing in the amount of prestressed in the longitudinal reinforcements, the load carrying

capacity increased at both SLS and ULS conditions, in which the I-beam with the highest prestressing level (*i.e.* IB10) could reach 94% of its maximum nominal flexural strength. The strain of GFRP bars for this prestressed beam was about 95% of its nominal ultimate strain at the failure stage;

- Although all tested beam failed in the shear zone through propagation of a critical diagonal crack at shear span, a very ductile behavior, particularly for second group of the beams (under-reinforced beams) was observed. This ductility was measured by multiplying the strength effect by the deformation effect, which were firstly defined by Jaejer *et al.* (1997). The calculated ductility index from the experimental force-deflection was compared to the ductility index calculated by means of the "*reference response*", which was based on the force-deflection response governed by flexural deformation only (obtained from Def-DOCROS software). This comparison showed that the ductility of the under-reinforced prestressed beam was significantly increased in respect to the corresponding values by the "*reference response*". This can be a great achievement in terms of ductility for the beams reinforced by prestressed FRP bars, where are categorized as RC beams with brittle failure mode;
- The shear failure process in case of beams in the present study was not as brittle as what is typically known for concrete beams failing in shear, since the proposed system could carry the load up to a very high deflection at mid-span section. During the crack formation process in the HPFRC, high amount of fracture energy in both mode I and mode II was released, resulting shear resisting at the flexure-shear zones. This fracture energy was spent while HPFRC cracks were opening and sliding (*i.e.* propagation of shear cracks), and at the same time the applied load was gradually increasing. This behavior of HPFRC under flexure-shear fracture mechanism gives high deformability to the prestressed beams similar to deformability that is typically obtained in conventional steel RC beams after yielding of longitudinal steel bars;

- No significant loss was observed in the flexural stiffness of the beams with 15% and 40% of prestress level in GFRP bars (IB6 and IB10) after two million fatigue loading cycles. However, for the beam with 30% prestress level in GFRP bars (IB9), the beam failed after about 1.8 million loading cycles. Unfortunately, due to the limited amount of the specimen in this series, no straight conclusion can be drawn from the obtained results;
- The prestressing in the longitudinal reinforcements increased the load carrying capacity at both SLS and ULS stages. At SLS, the load carrying capacity and other structural response of the prestressed beams were captured well by the results obtained using DOCROS sectional analysis software. The linear strain profile for each section of the beam is the fundamental assumption in the analysis by this software. However, at ULS, the results from this section analysis overestimated the experimental results. In case of ULS, the proposed direct method to calculate the maximum deflection response of the beam, which is a modified version of the direct method recommended by ACI code, can be an accurate alternative. This method is based on the calculation of the effective moment of inertia of the tested beams. The results from this method were promising when compared with the experimental force-deflection responses;
- The flexure-shear analysis proposed in the present study was capable of predicting the shear strength of the tested beam with acceptable accuracy for design purpose. The proposed analysis was based on the mode I fracture energy of HPFRC material, and also considers its interaction with the mode II fracture energy, which is fundamental in elements governed by the mixed fracture modes, such is the case of the tested beams;

Notations

a	shear span of beam	D_{cp}	HPFRC compressive deformation corresponding to onset of the plastic phase
$A_{ct,b}$	tensile area of beam's cross section under level of neutral axis at balanced condition	D_{cr}	tensile deformation of HPFRC in direct tension that causes cracking
A_f	area of GFRP bar's cross section	D_{mid}	mid span deflection of tested beams
A_g	gross area of HPFRC beam's cross section	D_u	mid span deflection at peak force-deflection response of the tested beam
A_s	area of steel strand's cross section	D_y	mid span deflection corresponding to yielding of steel strand
A_{p1}	the first effective tensile area of hybrid reinforced HPFRC beam's cross section	E_c	Young's modulus of HPFRC material
A_{p1}	the second effective tensile area of hybrid reinforced HPFRC beam's cross section	E_f	Young's modulus of GFRP bar
b	width of bottom flange in HPFRC beam's cross section	E_s	Young's modulus of steel strand
b_n	width of beam in the notched beam bending tests	f_c'	the compressive strength of HPFRC
b_w	width of web in HPFRC beam's cross section	f_{ct}	HPFRC tensile strength
c	the depth of neutral axis	$f_{ct,L}$	limit of proportionality calculated for CMOD =0.05 mm in standard notched beam test
c_b	the depth of neutral axis at the balanced section condition	f_f^{pre}	prestress of GFRP bar
c_n	the depth of neutral axis at nominal flexural failing condition (corresponding to M_n)	f_{fu}	the ultimate tensile stress of GFRP bars
c_v	the depth of neutral axis in a flexure-shear crack in shear span	f_{Fts}	the residual flexural stress of HPFRC defined by Model Code 2010
C_1^e	first integration constant for the elastic phase	f_{Ftu}	the residual flexural stress of HPFRC defined by Model Code 2010
C_2^e	second integration constant for the elastic phase	$f_{R,j}$	the residual flexural stresses of HPFRC defined by Model Code 2010 ($j=1,2,3,4$)
C_d	the strength effect in calculation of ductility index	f_s^{pre}	prestress of steel strand
C_s	the deformation effect in calculation of ductility index	f_{su}	the ultimate tensile stress of steel strand
d_f	the arm of tensile force of GFRP bars at HPFRC beam's cross section	f_{sy}	yielding stress of steel strand
d_f'	HPFRC concrete cover of GFRP bars (measured from bottom surface of section)	F_c	the resultant of compressive force at cracked HPFRC beam's cross section
$d_{f,eq}$	the arm of tensile force of equivalent GFRP bars at HPFRC beam's cross section	$F_{c,b}$	the resultant of compressive force at balanced cracked HPFRC beam's cross section
d_{fr}	the arm of the resultant of the residual tensile force by fibers at beam's cross section	$F_{c,n}$	the resultant of compressive force in horizontal direction at a flexure-shear crack
d_s	the arm of tensile force of steel strand at HPFRC beam's cross section	$F_{c,v}$	the resultant of compressive force in vertical direction at a flexure-shear crack
D_{cm}	maximum compressive deformation at top HPFRC beam's cross section	F_f	the tensile force of GFRP bars at cracked HPFRC beam's cross section

Notations

$F_{f,b}$	the tensile force of GFRP bars at balanced cracked HPFRC beam's cross section	$I_{eff,\exp}^{h}$	The experimental effective moment of inertia of hybrid GFRP/steel HPFRC beam
F_j	the applied force in notched beam test corresponding to $f_{R,j}$	J_r	constant in the governing differential equation for either GFRP or steel bar
$F_{\max}$	the maximum applied force in the fatigue loading template	k	the factor in calculation of nominal shear strength of beam by Eq. (5-66)
$F_{\min}$	the minimum applied force in the fatigue loading template	k_1	the factors that take into account the bond quality (Eq. (5-101))
F_{fr}	the resultant of tensile force at cracked HPFRC beam's cross section (due to fibers)	k_2	the factors that take into account the form of strain distribution (Eq. (5-101))
$F_{fr,b}$	the resultant of tensile force at balanced cracked FRC beam's cross section by fibers	k_3	factors taking into account the bond quality (Eq. (5-122))
$F_{fr,n}$	the resultant of tensile force by fibers in normal direction to crack plane	k_4	factors taking into account the duration of the loading or of repeated loading (Eq. (5-122))
$F_{fr,v}$	the resultant of tensile force in tangential direction to crack plane	k_b	the factors that take into account the bond quality (Eq. (5-120))
F_s	the tensile force of steel strand bars at cracked HPFRC beam's cross section	l	span of the standard notched beam test
F_{sy}	yielding force of steel strand	l'	the length of un-hooked part of the steel fiber
G_f^I	the mode I fracture energy	l''	the length of hooked part of the steel fiber
G_f^{II}	the mode II fracture energy	l_{cs}	characteristic length defined by Model Code 2010
$G_{f,a}^{II}$	the portion of the mode II fracture energy due to frictional behavior of fracture surface	l_{cr}	the length of the flexure-shear crack
h	height of I shaped HPFRC beam's cross section	$l_{cr,fl}$	the length of the flexure-shear crack crossing flange of the beam
h_1	height of the flanges in I shaped HPFRC beam's cross section	$l_{cr,w}$	the length of the flexure-shear crack crossing web of the beam
h_2	height of the flanges in I shaped HPFRC beam's cross section	l_{sf}	total length of hooked steel fiber
h_3	height of the web in I shaped HPFRC beam's cross section	l_v	the length of a flexure-shear crack with activated frictional stresses
h_{sf}	the hook height of the utilized steel fibers	L	span of the I shaped hybrid HPFRC prestressed beam
h_{sp}	height of the notched section in the standard notched beam benign test	L_b	bond length of reinforcing bar
I_{cr}	the moment of inertia of cracked FRP-RC beam's cross section	L_{tr}	transferred bond length corresponding to whatever value of the slip at crack section
I_{cr}^{h}	the moment of inertia of cracked hybrid FRP/steel HPFRC beam's cross section	$L_{tr,f}$	transferred bond length of GFRP bar corresponding to the slip at crack section
I_{eff}	the effective moment of inertia of FRP-RC beam	$L_{tr,r}$	transferred bond length of either GFRP or steel strand corresponding to the slip at crack section
I_{eff}^{h}	the effective moment of inertia of hybrid GFRP/steel HPFRC beam	$L_{tr,s}$	transferred bond length of steel strand corresponding to the slip at crack section
I_g	the moment of inertia of uncracked hybrid GFRP/steel HPFRC beam	m_s	factor to calculate balanced reinforcement ratio by Eq. (5-18)

Notations

m_{fr}	factor to calculate balanced reinforcement ratio by Eq. (5-18)	S_{cr}^{RILEM}	crack spacing calculated by Eq. (5-101)
m_1	modified factor to calculate the depth of neutral axis by Eq. (5-31)	R	factor defines the ratio between the lower strength and upper strength in fatigue cycles
m_2	modified factor to calculate the depth of neutral axis by Eq. (5-31)	V	the applied shear force in shear span of beam
M_a	the maximum applied moment carried by I shaped HPFRC beam at each level of loading	V_{cd}	the shear resistance of beam due to only concrete
M_{cr}	the cracking moment of I shaped HPFRC beam	V_n	the nominal shear strength of hybrid reinforced HPFRC prestressed beam
M_{cd}	the moment corresponding to V_{cd}	w	crack width at cracked section
M_{cr}^{L}	the cracking moment of I shaped HPFRC beam calculated, replacing f_{ct} by $f_{ct,L}$	w_a	the limited crack width in which for $w > w_a$ the frictional shear stress of crack face is null
M_n	the nominal flexural strength of beam	w_f	crack width at the level of GFRP bars at cracked section
M_p	moment due to the eccentrically applied prestress force	w_k	design crack width
M_{SLS}	the applied moment corresponding to $L/250$	w_u	the ultimate crack width with null value of crack tensile stress
M_u	the peak applied moment in moment-deflection response of beam	α	the angle of the critical diagonal crack (CDC) in the flexure-shear analysis
$M_{u,\text{exp}}$	the peak applied moment in moment-deflection response of the tested beams	α_1	the parameter define the rectangular HPFRC compressive stress block of at crack section
M_v	the moment corresponding to V_n	β	coefficient relating the average crack width to the design value
M_y	the applied moment corresponding to yield initiation of steel strand	β_1	the parameter define the rectangular HPFRC compressive stress block of at crack section
n_r	the ratio between the Young's modulus of steel strand and GFRP bar	β_2	parameter that takes into account the particular geometry of the adopted I shape cross section
n_f	the ratio between the Young's modulus of GFRP bar and HPFRC	β_3	the factor defines the bi-linear tensile deformation of the flexure-shear crack
N_{fp}	axil prestressed force applied to beam due to GFRP bars	β_d	factor that takes into account the relatively smaller tension stiffening effect of FRP bars
N_{sp}	axil prestressed force applied to beam due to steel strand	β_{sh}	factor that takes into account the crack shear propagation in the proposed direct method
P_f	the maximum tensile force transferred due to bond behavior of the GFRP bars	γ	factor to calculate the depth of neutral axis by Eq. (5-31)
$P_{\max}$	the peak applied force in force-deflection response of the tested beams	γ_c	safety factor in calculation of the nominal shear strength by Eq. (5-66)
P_s	the maximum tensile force transferred due to bond behavior of the steel strand	δ_f	slip of GFRP bar at cracked section
s	horizontal distance between GFRP bars at beam's cross section	δ_s	slip of steel strand at cracked section
S_{cr}	crack spacing	ε_1	the first strain point in the proposed tensile stress-strain diagram of HPFRC by RILEM

Notations

ε_2	the second strain point in the proposed tensile stress-strain diagram of HPFRC by RILEM	θ	rotation at the crack section due to the opening
ε_3	the third strain point in the proposed tensile stress-strain diagram of HPFRC by RILEM	κ_h	the size factor defined by Eq. (5-24)
ε_c	HPFRC compressive strain	λ_r	constant entering the governing differential equation for elastic bond phase
ε_c'	HPFRC compressive strain corresponding to its compressive strength	μ	ductility index of beam
ε_{cp}	HPFRC compressive strain at onset of its plastic behavior	ρ_c	defined by Eq. (5-16)
ε_{ct}	HPFRC tensile strain	ρ_{eff}	effective reinforcement ratio
ε_{ct1}	mean tensile strain in the first adopted HPFRC tensile prism	ρ_f	GFRP reinforcement ratio
ε_{ct2}	mean tensile strain in the second adopted HPFRC tensile prism	ρ_{fb}	FRP balanced reinforcement ratio
ε_{cr}	cracking strain of HPFRC	$\rho_{f,eq}$	equivalent GFRP reinforcement ratio
ε_f	tensile strain of GFRP bars	ρ_{hb}	hybrid balanced reinforcement ratio
$\bar{\varepsilon}_f$	mean tensile strain of GFRP bars at distance between two consecutive cracks	ρ_s	steel strand reinforcement ratio
$\varepsilon_{f,cfs}$	the tensile strain of GFRP bars at "crack formation stage"	σ_1	the first stress point in the proposed tensile stress-strain diagram of HPFRC by RILEM
ε_f^l	lower limit of GFRP bar tensile strain during the first fatigue cycle	σ_2	the second stress point in the proposed tensile stress-strain diagram of HPFRC by RILEM
ε_f^m	tensile strain of FFRP bar at midway section between two consecutive cracks	σ_3	the third stress point in the proposed tensile stress-strain diagram of HPFRC by RILEM
ε_f^{pre}	pre-strain of GFRP bars	σ_{ct}	tensile stress of HPFRC
ε_{fu}	the ultimate tensile strain of GFRP bars	$\bar{\sigma}_{ct}^{cr}$	equivalent average value of crack tensile stress of HPFRC
ε_f^u	upper limit of GFRP bar tensile strain during the first fatigue cycle	$\bar{\sigma}_{ct,b}^{cr}$	equivalent average value of crack tensile stress of HPFRC at balanced condition
ε_s	tensile strain of steel strand	σ_c^{pre}	average compressive stress acting over the gross section due to the prestressed force
ε_s^l	lower limit of steel strand tensile strain during the first fatigue cycle	$\sigma_{c,m}^{pre}$	average compressive stress over the section due to the prestressed force and its moment
ε_s^{pre}	pre-strain of steel strand	$\bar{\sigma}_{fr}$	the average tensile stress in the HPFRC tensile prisms by the tension–stiffening of fibers
ε_{su}	breaking tensile strain of steel strand	σ_{sr}	tensile stress of reinforcements at crack formation stage defined by Eq. (5-125)
ε_s^u	upper limit of steel strand tensile strain during the first fatigue cycle	τ_{cr}^m	the mean crack shear stress effectively due to the frictional behavior of the crack face
ε_{sy}	yielding strain of steel strand	φ	the angle between $F_{fr,n}$ and F_{fr} defined in the flexure-shear analysis

Notations

χ_D	the obtained curvature by DOCROS	χ_u	the effective curvature of beam at peak load in force-deflection response
χ_{cr}^{h}	the curvature of cracked section corresponding to M_n	ω	coefficient takes into account the degradation of the normal tensile stress due to existence of shear stresses over the crack
χ_{eff}	the effective curvature of beam	ϕ_f	diameter of GFRP bars
χ_{eff}^{l}	lower limit of beam curvature during the first fatigue cycle	ϕ_s	diameter of steel strand
χ_{eff}^{u}	upper limit of beam curvature during the first fatigue cycle	ϕ_{sf}	diameter of steel fibers

Chapter 6

6 NUMERICAL SIMULATION

6.1 Introduction

In this chapter, numerical simulations are carried out to address the structural behavior of the hybrid GFRP/steel reinforced HPFRC prestressed beams, and to introduce a reliable method to design this reinforcing system. For this purpose, a 2D model using Concrete Smeared Crack (CSC) approach, as well as a 3D model using Concrete Damage Plasticity (CDP) approach are employed to simulate the fracture mechanism of HPFRC after cracking. The CDP model also accounts for the nonlinear behavior of HPFRC in compression. An elasto-plastic model is used for simulating the steel strand, while a linear elastic behavior up to the ultimate tensile strain is assigned for tensile behavior of GFRP bars. The results obtained from these numerical simulations will be compared with those obtained by the experimental tests, which are presented in Chapter 5.

Additionally, a 2D numerical simulation of two series of notched beam tests is implemented using back analysis technique in order to obtain the stress-crack width diagram of HPFRC that is being used for the tension softening behavior of HPFRC in both 2D/CSC and 3D/CDP models. The 2D/CSC numerical simulations were carried out using FEMIX program (Sena Cruz *et. al* 2007), while, the 3D/CDP simulations were carried out using Abaqus.

In this chapter, a brief description of CSC and CDP model approaches for concrete is

firstly given in Sections 6.2 and 6.3, respectively. Afterward, the back analysis to obtain the crack stress-CMOD of the HPFRC material will be described in Section 6.4. Finally, the numerical 2D and 3D simulations of the prestressed beams and their respective results will be presented and compared with the experimental results in Sections 6.5 and 6.6.

6.2 Concrete Smeared Crack (CSC) approach

Bazant and Oh (1983) firstly used the concept of "*smeared cracking"* as they modeled concrete by using a fracture process employing a band of smeared crack with a fixed length (named as crack band width l_b). The basic assumption of smeared crack modelling of concrete is to decompose the concrete strain, after crack initiation, into an elastic (*i.e.* strain associated to the elastic concrete between cracks) and an inelastic components (strain component associated to the crack face) at each material sampling point (e.g. Gauss integration point within the frame work of a finite element model). The smeared crack approach, in general, is a modelling approach that is used for reinforced concrete elements, in which the concrete behavior is modeled independently of the reinforcing rebars. Then, the effect associated to the interaction between concrete and rebars is typically modeled by introducing "tension stiffening" in the tensile behavior of concrete or, sometimes, changing its axial stiffness of the tensile rebars. Alternatively, this interaction can be modeled employing interfacial finite elements that connect concrete element to bar's element, and using a constitutive model that simulates the bond behavior between them.

6.2.1 Crack detection

A simple Rankine criterion is used to detect crack initiation. This states that a crack forms when the maximum principal tensile stress attains the concrete tensile strength. This crack detection criterion is shown in Figure 6-1 for plane stress element.

When a crack occurs, its orientation is stored for the subsequent calculations. After crack initiation, the CSC implemented into FEMIX allows the formation of more cracks, if the following conditions are satisfied simultaneously:

1) The principal stress in the integration point reaches the actual concrete tensile

strength;

2) The angle between the direction of the existing cracks and the direction of the new crack is higher than a user-defined threshold value (threshold angle α_{th}).

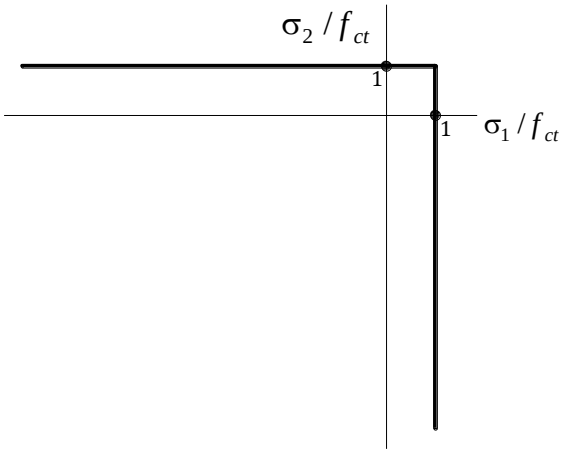

Figure 6-1: Rankine criterion for crack detection in plane stress state

In this multi-directional fixed smeared crack model, when a new crack is formed in the cracked material point, the fracture energy that is assigned to the new crack is calculated by the following equation (Barros, 1995):

$$G_f^{new} = (G_f - G_{f,a})\left(\frac{\alpha_{th}}{\pi/2}\right)^{p_2} + G_{f,a} \tag{6-1}$$

where p_2 is a parameter that, currently, can be taken the values of 1, 2 or 3, α_{th} is the angle (in radians) between the new and the previous cracks, and $G_{f,a}$ is the available fracture energy of the previously formed crack. This value is calculated subtracting the fracture energy consumed by the previously formed crack, G_f^{pre}, from the total given fracture energy, limited by the critical fracture energy defined elsewhere (Barros 1995):

$$G_{f,a} = G_f - G_f^{pre} \tag{6-2}$$

The following crack status define the behavior of each crack: "opening", "closing", "fully opened", and completely closed (Barros 1995).

6.2.2 Fracture mode I process

In case of an element in 2D plane stress state, two deformation components are considered for a formed crack line: the normal and tangential deformations represented by,

respectively, opening (*i.e.* w) and sliding (*i.e.* δ) components, as shown in Figure 6-2a for case of FRC. Since a smeared crack approach is adopted, a crack should be regarded as a smeared crack band. Therefore, the respective strain components are derived by means of "crack band width" (*i.e.* l_b), meaning that normal crack strain (*i.e.* ε_{ct}^{cr}) is computed dividing w by l_b , and the tangential strain (*i.e.* γ^{cr}) is computed dividing δ by l_b . The crack band width in FEMIX is calculated based on the geometry of FE mesh characteristics in order to assure that the results are not dependent of the mesh refinement. This value can be assumed equal to the square root of the area of the finite element for plane stress element, but in the present simulations the first option was adopted.

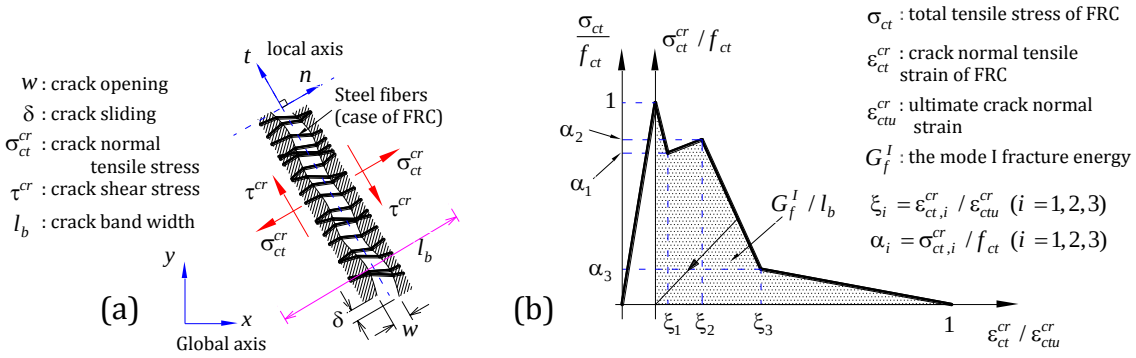

Figure 6-2: (a) deformation components of crack in concrete or FRC, and (b) tension-softening diagram of concrete or FRC

The incremental behavior of the residual stresses *versus* the respective value of crack strain is typically defined as constitutive law of crack. The component of this constitutive law that defines the crack opening process ('Tension softening' or "tension stiffening"), is simulated by the stress-strain diagram shown in Figure 6-2b, where the crack normal strain and the crack normal stress are normalized by, respectively, the ultimate crack normal strain and concrete tensile strength.

It should be noticed that in adopted CSC model (NLMM104 in FEMIX), the behavior of HPFRC in compression is considered linear and elastic.

6.2.3 Fracture mode II process

Cracking behavior is predominantly influenced by crack opening process that is based on the mode I fracture energy, tensile strength and shape of the tensile stress *vs*. crack width

relationship. However, to allow the simulation of structures governed by the mixed mode fracture mechanisms, such is the case of the beams tested in the present work, the crack sliding behavior and its dependence on the crack opening process should be modeled as accurately as possible. The crack shear behavior is governed by the Mode II fracture mechanism, and mainly two available methods in the literature are proposed to simulate the Mode II fracture behavior, both of them available in FEMIX.

6.2.3.1 Shear retention factor

Although the crack initiation is based on Mode I fracture only, post cracking behavior also depends on the Mode II fracture process. Based on the experimental evidences, the crack shear stress transfer depends on the crack opening evolution. Therefore, the crack shear modulus, D_{II}^{cr}, is defined as function of the crack opening, according to Eq. (6-3), where β_{cr} is the shear retention parameter obtained according to Eq. (6-4) that depends on the actual crack normal strain (ε_{ct}^{cr}) and the ultimate crack normal strain (ε_{ctu}^{cr}). In Eq. (6-3), the parameter G_c is the shear modulus of un-cracked and cracked concrete, while in Eq. (6-4) the parameter p_1 defines the decrease rate of β_{cr} in terms of the ε_{ct}^{cr} variation:

$$D_{II}^{cr} = \frac{\beta_{cr}}{1-\beta_{cr}} G_c \tag{6-3}$$

$$\beta_{cr} = \left(1 - \frac{\varepsilon_{ct}^{cr}}{\varepsilon_{ctu}^{cr}}\right)^{p_1} \tag{6-4}$$

The parameter p_1 can be taken as 1, 2 or 3, which, respectively, represents linear, quadratic and cubic shear retention power law. When crack is closed (*i.e.* $\varepsilon_{ct}^{cr} = 0$), a full interlock is assumed for the crack, while for $\varepsilon_{ct}^{cr} \geq \varepsilon_{ctu}^{cr}$ the crack is completely opened and shear stress cannot anymore be transferred between both faces of the crack.

6.2.3.2 Shear softening law

The previous approach based on the concept of shear retention factor is appropriate for concrete structures where cracking process is predominantly influenced by the fracture mode I parameters, such is the case of structures failing in bending. To simulate the concrete

structures that are supposed to fail by the propagation of critical shear cracks, the shear retention factor does not assure accurate results (Ventura-Gouveia 2011). For attending for these cases, FEMIX has a constitutive model where a shear softening diagram is proposed to simulate the fracture mode II process (Ventura-Gouveia 2011). In this approach, the crack tangential deformation is simulated independently from its crack normal deformation, by using the shear softening diagram shown in Figure 6-3 (Ventura-Gouveia 2011).

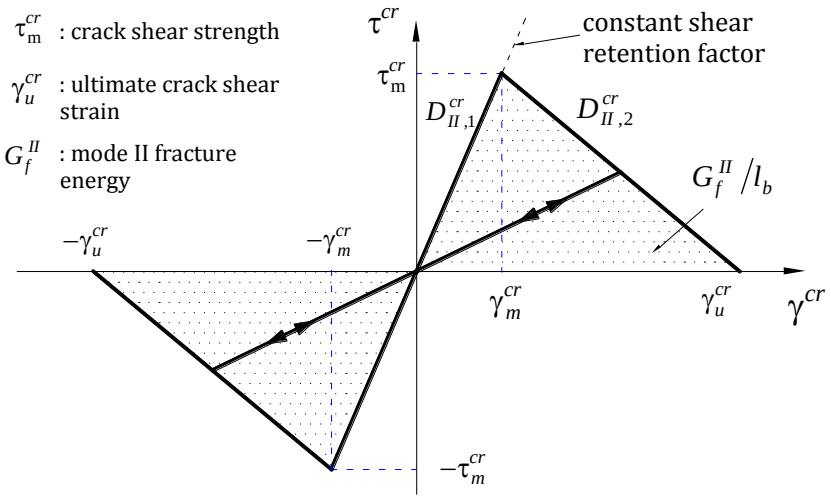

Figure 6-3: Shear softening diagram

The crack shear stress increases linearly until the crack shear strength is reached (τ_m^{cr}), afterward, it is followed by a descending branch (softening) up to the ultimate crack shear strain (γ_u^{cr}). Several authors demonstrated the good applicability of this approach for RC elements failing in shear (Ventura-Gouveia 2011, Barros *et al.* 2013, Breveglieri 2015, Baghi 2015), therefore it will be also used for simulating the beams tested experimentally in the scope of the present thesis.

6.3 Concrete Damage Plasticity (CDP) approach

The CDP model available in Abaqus provides a general capability to capture the effects of irreversible damage associated with the failure mechanisms that occur in concrete and other quasi-brittle materials. Even though it is primarily developed for the analysis of reinforced concrete structures, it can be also applied to modeling of plain concrete. In this chapter, the model will be used to simulate the behavior of reinforced HPFRC beams that

was detailed in Chapter 5. The CDP model in Abaqus is based on the plastic-damage modeling approach proposed by Lubliner *et al.* (1989) and by Lee and Fenves (1998). The CDP model uses concepts of isotropic damaged elasticity in combination with isotropic tensile and compressive plasticity to represent inelastic behavior of concrete, and it is designed for applications in which concrete is subjected to monotonic, cyclic, or dynamic loading conditions. However, the CDP model is only applicable for concrete under low confining pressure, because the brittle behavior of concrete disappears when the confining pressure is sufficiently large to prevent crack propagation. Modeling the behavior of concrete under large hydrostatic pressures is out of the scope of the CDP model. A brief description about the CDP model is given in the following subsections.

6.3.1 Uniaxial tension and compression behavior

The CDP model assumes two stages in uniaxial tensile and compressive behavior of concrete: elastic and plastic responses. The material starts within its linearly elastic behavior up to the "*failure stress*" in tension, which can be defined as the stress at crack initiation (*i.e.* σ_{t0}), and initiation of "*yield stress*" in compression (*i.e.* σ_{c0}). The *failure stress* in uniaxial tensile, and *yield stress* in uniaxial compressive behavior of concrete is shown in Figure 6-4. When the *failure stress* or *yield stress* is reached, the stress-strain relation is defined independently for tension and compression as follows:

$$\sigma_{ct} = (1-d_t)E_c(\varepsilon_{ct} - \varepsilon_{ct}^{pl}) \tag{6-5}$$

$$\sigma_{c} = (1-d_c)E_c(\varepsilon_{c} - \varepsilon_{c}^{pl}) \tag{6-6}$$

where ε_{ct}^{pl} and ε_{c}^{pl} are the plastic strains, respectively, in tensile and compression domains. The parameters d_t and d_c are the damage parameters (ranged between 0 and 1) to define the degradation of the elastic stiffness of the material after initiation of the in elastic deformation (as shown in Figure 6-4). Note that the uniaxial stress-strain curves are converted into stress *versus* plastic-strain curves in the model after occurrence of inelastic deformation.

The tensile plastic strain is calculated using:

$$\varepsilon_{ct}^{pl} = \varepsilon_{ct} - \frac{d_t}{(1-d_t)}\frac{\sigma_{t0}}{E_c} \tag{6-7}$$

while the plastic strain in compression is obtained from:

$$\varepsilon_{c}^{pl} = \varepsilon_{c} - \frac{d_c}{(1-d_c)}\frac{\sigma_{c0}}{E_c} \tag{6-8}$$

where σ_{c0} is the compressive stress the threshold of the plastic behavior of concrete in compression as shown in Figure 6-4. More sophisticated aspects are considered in the uniaxial behavior of concrete under cyclic and dynamic loading conditions, however, the details about this type of behavior are not given in this study since no cyclic behavior is intended to model. In a general form, multiaxial stress-strain relation can be written as follow:

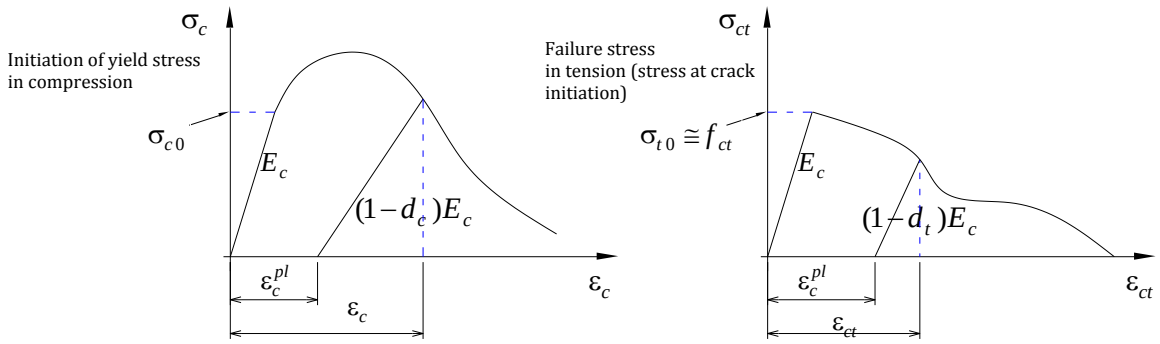

Figure 6-4: Response of concrete to uniaxial loading in compression (left) and tension (right)

$$\bar{\sigma} = \frac{\sigma}{(1-d)} = E_c\left(\varepsilon - \varepsilon^{pl}\right) \tag{6-9}$$

where d is the stiffness reduction variable, σ and ε are the stress and strain tensors of concrete, while $\bar{\sigma}$ is the equivalent stress tensor.

6.3.2 Yield surface

In multiaxial conditions, the *yield stress* is presented as a "*yield surface*" (conceptually, this should be named "*failure surface*" for tension, however, for sake of brevity, the *yield surface* is also adopted for tensile behavior). The CDP model uses a yield condition based on the yield function proposed by Lubliner *et al.* (1989) and incorporates the modifications proposed by Lee and Fenves (1998) to account for different evolution of strength under

tension and compression. This *yield surface* can be considered by means of a relationship between the equivalent pressure stress, named as p, and the Von Mises equivalent deviatoric stress, named as q, which is known as $p-q$ plane (known also as *meridian plane*) shown in Figure 6-5a, and they are given by:

$$p = -\frac{1}{3}\sigma : \mathrm{I} \tag{6-10}$$

$$q = \sqrt{\frac{3}{2} S : S} \tag{6-11}$$

where I is the identity matrix, σ is the concrete stress tensor, and S is derived by

$$S = p\,\mathrm{I} + \sigma \tag{6-12}$$

Note that the symbol ":" is Frobenius inner product in matrix multiplications.

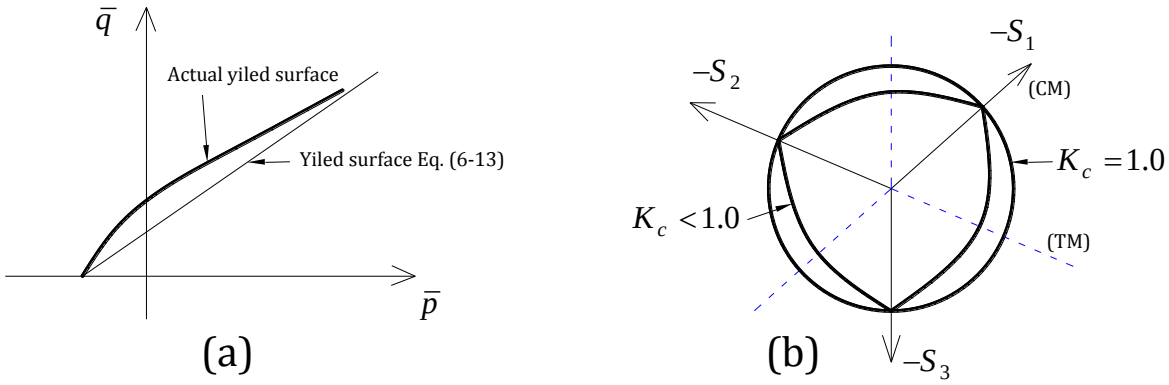

Figure 6-5: Illustrative of the failure surfaces in: (a) *p-q* plane, and (b) the deviatoric plane for compression, corresponding to different values of K_c

In the $p-q$ plane, the *yield surface* is defined in a general form as follow:

$$F(\bar{\sigma}, \varepsilon^{pl}) = \frac{1}{1-\alpha}(\bar{q} - 3\alpha\bar{p} + \beta\langle\hat{\sigma}_{\max}\rangle - \gamma\langle\hat{\sigma}_{\max}\rangle) - \bar{\sigma}_c\left(\varepsilon_c^{pl}\right) \le 0 \tag{6-13}$$

with the following definition:

$$\alpha = \frac{(\sigma_{b0}/\sigma_{c0}) - 1}{2(\sigma_{b0}/\sigma_{c0}) - 1}; (0 \le \alpha \le 0.5) \tag{6-14}$$

$$\beta = \frac{\bar{\sigma}_c\left(\varepsilon_c^{pl}\right)}{\bar{\sigma}_t\left(\varepsilon_t^{pl}\right)}(1-\alpha) - (1+\alpha) \tag{6-15}$$

where

$\hat{\sigma}_{\max}$: is the maximum principal effective stress. Note that the Macauley bracket $\langle\cdot\rangle$ is defined by $\langle x\rangle = \frac{1}{2}(|x|+x)$;

$(\sigma_{b0}/\sigma_{c0})$: is the ratio of initial biaxial compressive yield stress to initial uniaxial compressive yield stress;

The coefficient γ takes part in the *yield surface* only for stress states of triaxial compression, *i.e.* $\hat{\sigma}_{\max} < 0$. This coefficient can be determined by comparing the yield conditions along the *tensile* and *compressive meridians*. The *tensile meridian* (TM) and *compressive meridian* (CM) for $\hat{\sigma}_{\max} < 0$ are defined as a particular form of Eq. (6-13), given as follows:

$$\left(\frac{2}{3}\gamma+1\right)\bar{q} - (\gamma+3\alpha)\,\bar{p} = (1-\alpha)\bar{\sigma}_c \qquad \text{(TM)} \qquad (6\text{-}16)$$

$$\left(\frac{1}{3}\gamma+1\right)\bar{q} - (\gamma+3\alpha)\,\bar{p} = (1-\alpha)\bar{\sigma}_c \qquad \text{(CM)} \qquad (6\text{-}17)$$

If the ratio between the *tensile meridian*, *i.e.* $\bar{q}_{\text{TM}}$, to that of the *compressive meridian*, *i.e.* $\bar{q}_{\text{CM}}$, is assumed as $K_c = \bar{q}_{TM}/\bar{q}_{CM}$, then, K_c is given by

$$K_c = \frac{\gamma+3}{2\gamma+3} \qquad (6\text{-}18)$$

being K_c constant is not in contrast with experimental evidence (Lubliner *et al.* 1989). Therefore, the coefficient γ is evaluated as

$$\gamma = \frac{3(1-K_c)}{2K_c-1} \qquad (6\text{-}19)$$

The parameter K_c ranges between 0.5 and 1.0. For $K_c = 2/3$, which is typical for concrete, γ becomes 3.0. The typical *yield surface* considered by CDP is shown in Figure 6-5 in the deviatoric plane for different value of K_c. It should be noticed that the parameters to define this *yield surface* for concrete can be adopted for the HPFRC, since for the current content of fibers applied in practical applications, only the post peak tensile and compressive residual strength capacity is increased with the efficiency of the reinforcement mechanisms of fibers bridging the formed cracks, but the shape of the *yield surface* does not

change significantly. For the specific case of $\hat{\sigma}_{max} = 0$, Eq. (6-13) is the well-known Drucker-Prager failure surface, which was firstly developed for soils.

6.3.3 Flow potential

The most important aspect of the plastic behavior in CDP modelling is the incremental behavior of the plastic strain (or stress) beyond the *yield surface*, and it is defined as plastic flow potential. The CDP model assumes the Drucker-Prager hyperbolic function (named as G) for flow potential of the *yield surface*, which is derived by

$$G = \sqrt{(e \cdot f_{ct} \tan\psi)^2 + \bar{q}^2} - \bar{p} \tan\psi \qquad (6\text{-}20)$$

where ψ is the dilation angle measured in the $p-q$ plane at high confining pressure, and e is a parameter, referred to as the eccentricity, that defines the rate at which the function G approaches the asymptote (the flow potential tends to a straight line as the eccentricity tends to zero). A hardening potential *flow rule* is schematically illustrated in Figure 6-6a for the Drucker-Prager hyperbolic function in $p-q$ plane. A non-associated flow rule is adopted the dilation angle, ψ, and the material friction angle, β, are different. The definition of material friction angle is also given in Figure 6-6a. In fact, the direction of the incremental equivalent plastic strain, $d\varepsilon^{pl}$, is not perpendicular to the *yield surface* in case of non-associated flow rule.

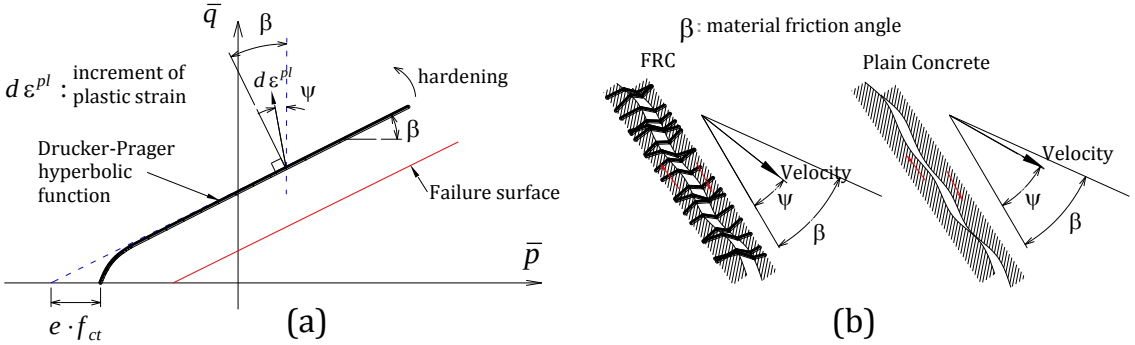

Figure 6-6: (a) Schematic illustration of a hardening non-associated flow potential considered in CDP modeling approach, and (b) The physical interpretation of the dilation angle associated with sliding along fracture surface (Modified from Zhao and Cai 2010)

For case of plain concrete, the dilation angle is recommended being between 30 and 40 degrees (Ren *et al.* 2014). Later in this chapter, it will be shown that for HPFRC material (or

FRC in general), smaller values in this interval best fit the experimental results. In order to understand better the concepts behind the parameters ψ and β, their physical interpretation is shown in Figure 6-6b on a fracture surface in case of normal and fiber-reinforced concrete. It should be noticed that the parameters ψ, e, α and K_c are the main input variables to identify the CDP model in Abaqus.

6.4 Inverse analysis to obtain post-cracking behavior of HPFRC

Typically, the diagram of stress-crack opening or stress-strain diagram, as well as the mode I fracture energy of HPFRC are obtained by performing direct tensile test (e.g. using dogbone specimen as shown in Figure 6-7c). However, in the lack of data available from this test setup, the stress-crack opening relationship of HPFRC (or FRC material in general) can be obtained by simulating numerically indirect tensile tests (e.g. splitting test and notched beam bending test as shown, respectively, in Figure 6-7a and b), performing a back analysis technique that fits, as accurately as possible, the experimental results obtained in these tests (for instance the total applied force *vs*. deflection or CMOD in case of notched beam bending tests). In the back analysis, the stress-crack width diagram, as well as the mode I fracture energy of FRC are the input variables in the model to reach a desired error between the experimental and numerical curves. In this study, due to the lack of data available from the direct tensile test of HPFRC, the stress-crack width law is obtained by means of a back analysis technique using the experimental force-CMOD response from notched beam bending tests.

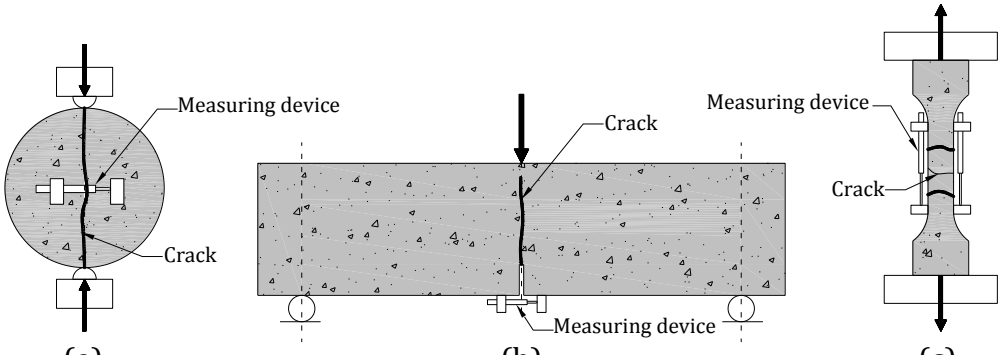

Figure 6-7: Typical test setups to measure tensile stress *versus* crack opening for FRC materials: (a) splitting test, (b) notched beam bending test, and (c) dogbone test

6.4.1 Notched beam bending tests

A total of two series of notched beam bending tests, composed of 5 specimens per each series, was carried out to characterize the post-cracking behavior of the HPFRC. The first series of these tests was similar to the standard notched beam bending test setup recommended by CEB-FIB Model Code 2010, and the obtained force-*CMOD* curves are those presented in Section 5.2.1.2 in Chapter 5.

The second series of test was carried out with notched beam specimens that were cut from the undamaged parts of both extremities of the tested HPFRC I-beams. The geometry of this series of notched beam test is shown in Figure 6-8. The results of the five notched beam bending tests with these specimens, in terms of the normalized applied force *versus CMOD*, is plotted in Figure 6-9b, and it is compared with the same results obtained from the standard notched beam tests (*i.e.* first series plotted in Figure 6-9a). The calculated value of the residual flexural tensile stress parameters of the second series of notched beam test are included in Table 6-1. As shown in Figure 6-9b, the scatter of the results for specimens taken from HPFRC web plate of the I-Beam specimens is much higher than the standard notched beam specimens. This is due to significant difference of steel fiber distribution and orientation between these two series of notched beam specimens. When a smaller fracture surface of FRC material is analyzed (like the case of HPFRC web plate in I-Beam specimens), the post-cracking behavior is significantly influenced by the number and orientation of fibers crossing this fracture surface. Therefore, the fracture energy of FRC material is significantly influenced by the location of the fracture surface at HPFRC web plate. The homogeneity and isotropy are two fundamental assumptions in almost all the available macro scale models for cement-based materials. However, for FRC materials, their post-cracking behavior strongly depends on the geometry of the specimen, rheology characteristics, and casting conditions.

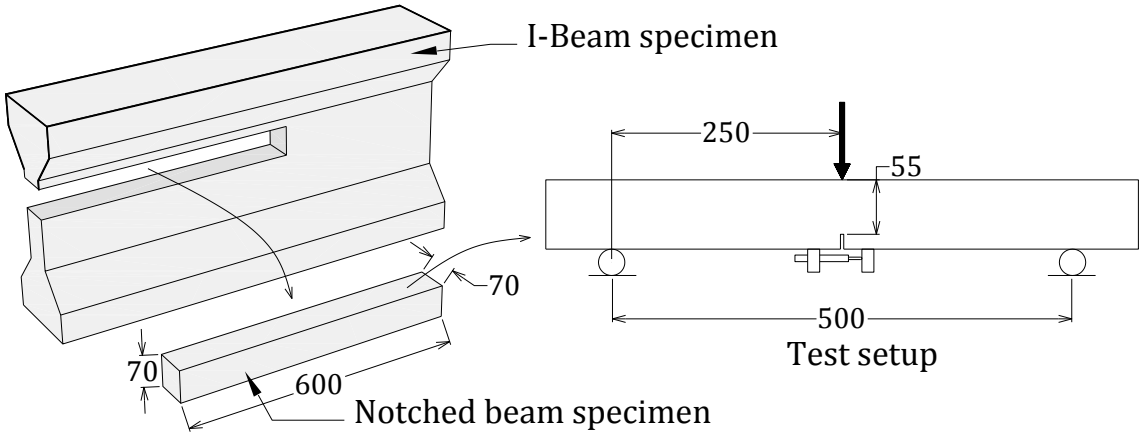

Figure 6-8: (a) the location that notched beam specimens were taken, and (b) Notched beam bending test setup for second series

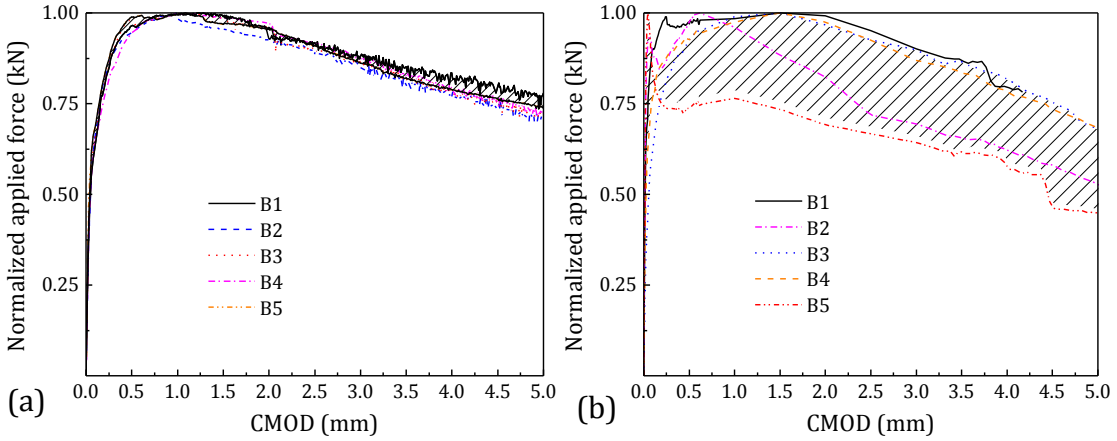

Figure 6-9: Normalized applied force *versus CMOD* obtained from the notched beam tests: (a) first series (standard test), and (b) second series

Table 6-1: The residual flexural tensile stress parameters of the second series of notched beam bending test

Notched beam Specimens ID.	Residual flexural tensile strength parameters								Limit of proportionality*	
	$CMOD_1$=0.5		$CMOD_2$=1.5		$CMOD_3$=2.5		$CMOD_4$=3.5			
	F_1 (kN)	$f_{R,1}$ (MPa)	F_2 (kN)	$f_{R,2}$ (MPa)	F_3 (kN)	$f_{R,3}$ (MPa)	F_4 (kN)	$f_{R,4}$ (MPa)	F_L (kN)	$f_{ct,L}$ (MPa)
B1	2.35	8.31	2.42	8.57	2.30	8.14	2.09	7.42	1.85	6.56
B2	1.65	5.84	1.50	5.31	1.22	4.32	1.11	3.93	1.58	5.62
B3	3.35	11.87	3.62	12.82	3.35	11.86	3.12	11.05	1.71	6.04
B4	3.31	11.57	3.59	12.71	3.32	11.76	2.99	11.59	2.31	8.18
B5	1.21	4.29	1.20	4.25	1.09	3.86	1.00	3.55	1.62	5.77
Average:	**2.37**	**8.37**	**2.47**	**8.73**	**2.25**	**7.99**	**2.06**	**7.51**	**1.81**	**6.43**

* Calculated by Eq. (5-1) in Chapter 5 for *CMOD*=0.05.

6.4.2 Strategies to perform the inverse analysis

In order to obtain more reliable results from the inverse analysis, the following strategy was adopted:

- The inverse analysis is performed by considering the force-*CMOD* response of each individual notched beam specimen. This helps to consider not only the values obtained by the experimental test, but also the real shape of the experimental curve, which represents the real behavior of the fracture surface at notched section for each specimen. In other word, the average result of force-*CMOD* response of HPFRC is not used in the analysis;
- The force-*CMOD* response of each individual specimen will be analyzed separately in three distinguished stages: stage 1, 2 and 3 that correspond, respectively, to *CMOD* of 0 to 0.2, 0.2 to 1, and 1 to 5 mm;
- For each phase, the difference between the numerical and experimental curves is minimized for a desired value of error;
- The previous steps conducted to a scatter of results in terms of crack tensile stress *versus* crack opening, as well as a range of values for Mode I fracture energy.

Figure 6-10 briefly describes the procedure of the adopted inverse analysis to determine the properties that define the post-cracking tensile behavior of HPFRC. As shown, in the first stage, three parameters are changed in the analysis: tensile strength (*i.e.* f_{ct}) and the slope of the first linear branch (*i.e.* ξ_1, α_1). The numerical results are fitted to the respective experimental results up to *CMOD*=0.2 mm. In the second stage, the slope of the second linear branch (*i.e.* ξ_2, α_2) is changed while the rest of the parameters are kept constant. The difference between the numerical and experimental curves are minimized in the range of *CMOD*=[0.2-1.0] mm. At this point, if the response from the first stage changed, the values of ξ_1 and α_1 are modified while the slope of the first linear branch is kept constant. Finally, in the third stage, the slope of the third linear branch is changed while the difference between the experimental and numerical curves are minimized in range of *CMOD*=[1.0-5.0] mm. At this point, if the numerical curves in the second stage changed, the values of ξ_2 and α_2 are modified while the slope of the second linear branch is kept constant. It should be noticed that the last linear branch did not have influence on the numerical results of force-*CMOD* up to *CMOD*=5.0 mm. Therefore, no verification was made for the ultimate crack opening. The

ultimate crack opening should be less than the effective bond length of steel fibers (fiber length~ 30 mm), which is about 25% of total fiber length according to the literature (Wang 1989). The empirical value of 5 mm was taken for the ultimate crack opening.

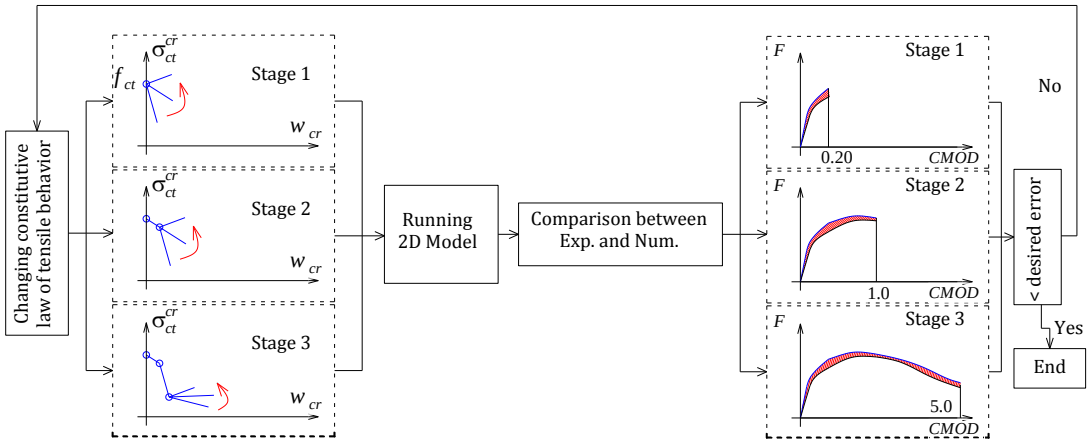

Figure 6-10: Procedure of the back analysis to reach the post-cracking tensile response of HPFRC

6.4.3 2D model used in the back analysis of the notched beam tests

The geometric and meshing details of the models that were used to simulate the two series of notched beam bending tests are illustrated in Figure 6-11. Eight-node Plane Stress FEs were employed to simulate HPFRC, with a Gauss-Legendre (G-L) integration scheme of 2×2. The diagram composed of four-linear branches, shown in Figure 6-2b, was used to simulate the post-cracking tensile behavior of HPFRC. Note that in the back analysis, the compressive behavior of HPFRC was assumed linear-elastic.

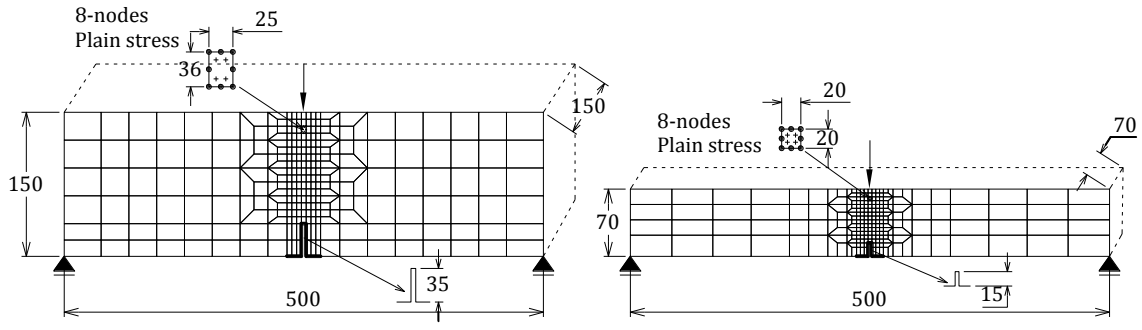

Figure 6-11: Geometry, mesh and boundary conditions of the numerical modelling of notched beam bending tests

6.4.4 Results of the inverse analysis

Based on the procedure explained in the previous sections, the obtained results in terms

of applied force *versus CMOD* are plotted in Figure 6-12 and Figure 6-13, respectively, for the first and second series of notched beam bending tests. Additionally, the respective parameters that define the obtained 4-linear diagram of HPFRC post-cracking response (5 points) are written in Table 6-2. Note that all analysis were performed with FEMIX computer program.

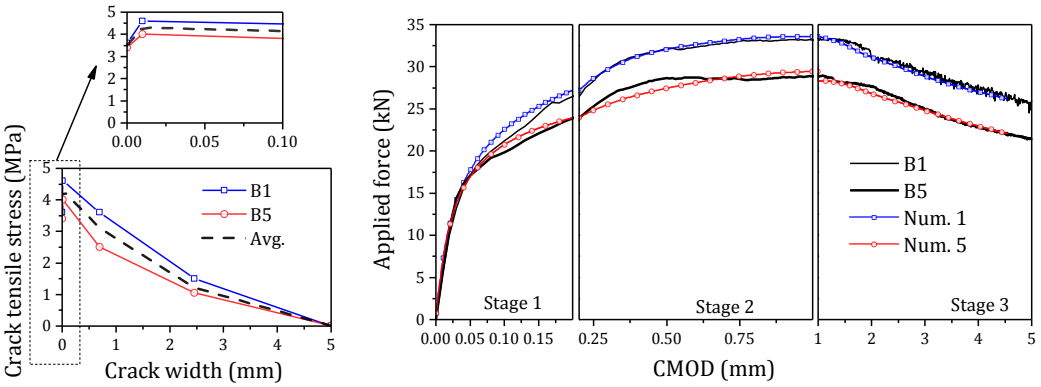

Figure 6-12: Results of the back analysis for first series of notched bending beam tests: (a) obtained stress-crack width, (b) the respective comparison between the experimental and numerical results

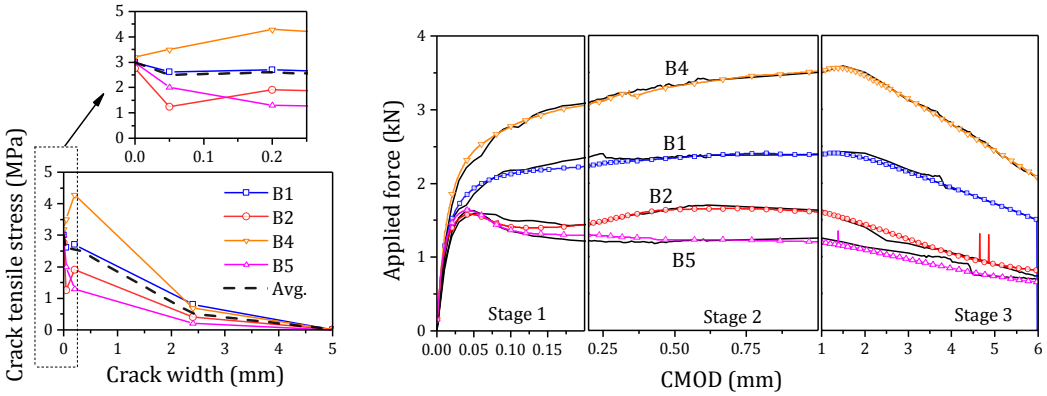

Figure 6-13: Results of the back analysis for second series of notched beam bending tests: (a) stress-crack width, (b) the comparison between the experimental and numerical results

Table 6-2: The values that define the post-cracking behavior of HPFRC (unit: N, mm)

Series	Beam ID	Point 1	Point 2		Point 3		Point 4		Point 5	
		f_{ct}	ξ_1	α_1	ξ_2	α_2	ξ_3	α_3	w_u *	G_f^I
First series	**B1**	3.5	0.0013	1.31	0.091	1.03	0.33	0.37	5.0	10.44
	B5	3.5	0.0013	1.14	0.091	0.71	0.33	0.31	5.0	8.20
	Average	3.5	0.0013	1.23	0.091	0.89	0.33	0.34	5.0	9.38
Second series	**B1**	3.0	0.007	0.90	0.03	0.90	0.32	0.27	5.0	6.52
	B2	2.8	0.007	0.50	0.03	0.68	0.32	0.14	5.0	3.96
	B4	3.2	0.007	1.13	0.03	1.34	0.32	0.22	5.0	8.18
	B5	3.0	0.007	0.73	0.03	0.43	0.32	0.07	5.0	2.59
	Average	3.0	0.007	0.73	0.03	0.87	0.32	0.17	5.0	5.28

*The ultimate crack opening.

6.4.5 Post-cracking behavior of HPFRC

Based on the results of the back analysis, the obtained post-cracking responses of HPFRC is plotted in Figure 6-14a and b, respectively, for the first and second series of the notched beam tests. The scatter of the results from the smaller notched beam specimens (second series), which were cut from the undamaged part of the I-beam specimens, is higher than those by the standard notched beam bending tests (first series). The average fracture energy obtained from the standard notched beam bending tests (G_f =8.0N/mm) is about two times of the average value for the second series (G_f =4.0N/mm). This attributes to the fact when the analysis focuses on a smaller fracture surface, the fracture energy will strongly depend on the fiber distribution and orientation, as well as the number of fibers per unit area. In addition, the casting procedure might be another reason of this fact. This confirms that in the simulation of FRC structures, the isotropic assumption for FRC post-cracking behavior is too arguable, since this behavior strongly depends on the fiber distribution and orientation. Assigning an unique value for fracture energy (*i.e.* G_f) to all FRC elements in a FE model of FRC structure may overestimate (in case of higher fracture energy) or underestimate (in case of lower fracture energy) the global behavior of the structure.

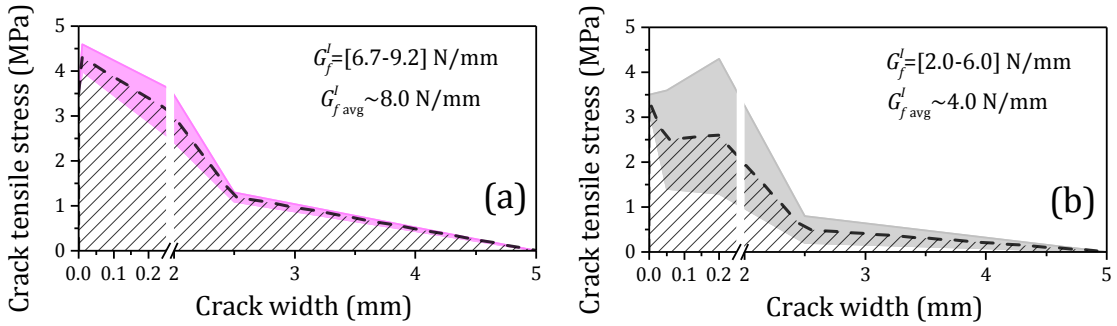

Figure 6-14: Post-cracking behavior of HPFRC from the back analysis of: (a) first series, and (b) second series of notched beam bending specimens

6.5 Numerical simulations of hybrid HPFRC prestressed beams

The description of the FE models employed for the numerical simulations of the experimental hybrid HPFRC prestressed I-Beams is given in the present section. This description includes details of the adopted FE mesh, boundary conditions, and the respective

constitutive laws and parameters that define the models. The numerical simulations are carried out in form of both 2D and 3D modelling. The 2D models are based on the CSC modeling approach, while 3D models are based on CDP modeling approach. The 2D model is described in Section 6.5.1, and 3D model in Section 6.5.1.3. Afterward, a comparison between results of the numerical models and those from the experiments is given in Section 6.6 in terms of force-deflection response, crack pattern, strain of reinforcements, and the ultimate failing of the tested beams.

6.5.1 Model 2D based on CSC approach

6.5.1.1 *Geometry, meshes, and boundary conditions*

Plain Stress FE with 4 nodes and 3 by 2 Gauss-Legendre integration points are used for simulation of HPFRC material. Additionally, 2D cable elements by using a 2 Gauss-Legendre integration scheme (one degree-of freedom per node), are employed for simulating the reinforcing bars (*i.e.* GFRP bars and steel strand). Finally, interface FE are utilized to simulate the bond conditions between the reinforcements (*i.e.* GFRP bar and the steel strand) and surrounding HPFRC. The geometric details, as well as the FE mesh characteristics of the 2D model implemented in FEMIX is shown in Figure 6-15. More details about the interface FE element can be found elsewhere (Sena Cruz 2004).

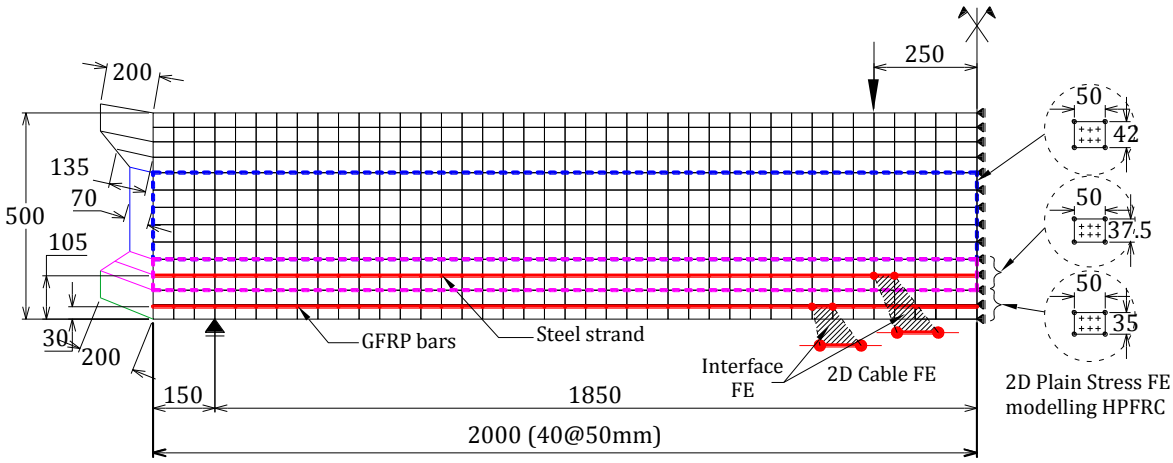

Figure 6-15: Geometrical details of numerical 2D model of the experimental hybrid GFRP/strand HPFRC I beams (dimensions in mm)

As shown in Figure 6-15, only half of the I-beam is simulated due to its symmetry

conditions. The thickness of Plane Stress FE located at the bottom and top flange varied according to the real shape of the I-beam specimens presented in Chapter 5. This thickness variation is implemented to the nodes at the same horizontal level in respect to its height. For example, 135 mm thickness is assigned to the nodes located at 105 mm height, which is the midway between the web and bottom flange of the beam.

6.5.1.2 Constitutive models and parameters

***HPFRC material**:* Assumed with a linear-elastic behavior in compression. The tensile behavior of HPFRC is defined by the four-linear constitutive law shown in Figure 6-2a, and it is based on the average curve between the two average post-cracking diagrams obtained in Section 6.4.5, as shown in Figure 6-16. In addition, the respective values that define these average diagrams are written in Table 6-3. The diagrams are presented in terms of the crack tensile stress *versus* crack width, which is converted to the crack tensile stress-strain constitutive law during the analysis by means of constant "crack band width" (*i.e.* l_b). The value of crack band width is taken the square root of the area assigned by each integration point.

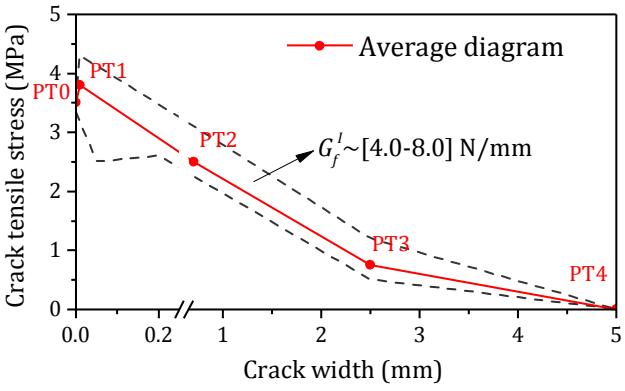

Figure 6-16: Average post-cracking tensile behavior of HPFRC adopted in 2D FE models

Table 6-3: The values define the post-cracking tensile behavior of HPFRC

Point		stress (MPa)	Crack width (mm)
Average	PT0	3.5	0.0
	PT1	3.8	0.01
	PT2	2.5	0.70
	PT3	0.75	2.50
	PT4	0.0	5.0
	G_f	6.07	N/mm

The sliding behavior of the crack surface is defined by the two approaches explained earlier in Section 6.2.3, that is, shear retention factor and shear softening diagram. The definition of the parameters in crack shear behavior is not straightforward, since the mode II behavior of a crack surface is always dependent of the mode I behavior. Therefore, the

parameters that define the shear retention factor (*i.e.* β_{cr} , p_1 and ε_{ctu}^{cr}), or define the shear softening law (*i.e.* β_{cr} , τ_m^{cr} and G_f^{II}) may be obtained by using a proper material test that includes the mixed fracture mechanism of flexural and shear behavior of the material. However, in the lack of available data from such material test, the shear parameters are defined by using a back analysis technique taking into consideration the results of the non-prestressed beams in terms of the force-deflection response. The calibrated shear behavior will be used for the further simulation of the prestressed I-beams. It should be noticed that the mode II fracture energy G_f^{II} utilized in shear softening diagram cannot be calibrated using a direct shear test, because, a pure shear behavior is only a particular case of a fracture mechanism in which the normal stress is almost null. For each intermediately mixed modes behavior (ratio of the crack normal stress to the crack shear stress), the mode I and II fracture energies need to be dependently updated in order to reflect the correct behavior of the fracture surface.

Longitudinal reinforcements: For GFRP bar, a linear elastic tensile behavior is assumed up to its failure, while an elasto-plastic behavior is employed for steel strand. These two behaviors are plotted in Figure 6-17. The values that define the elasto-plastic stress-strain relationship are provided in Table 6-4. The experimental tensile stress-strain response of steel strand, which was reported by the manufacturer, is also plotted in Figure 6-17.

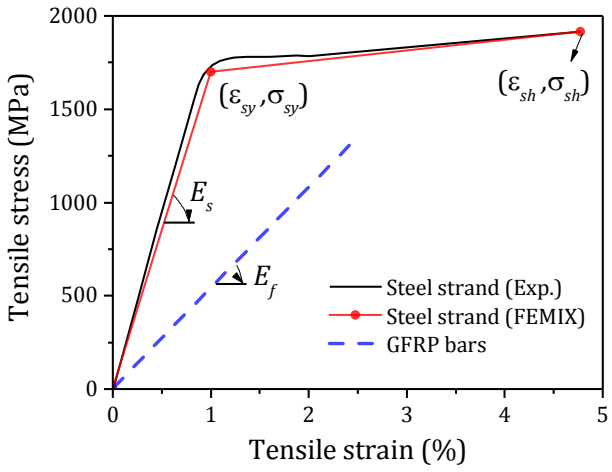

Figure 6-17: Tensile behavior of reinforcing bars

Table 6-4: The values define the tensile behavior of reinforcing bars

Parameter	value	unit
σ_{sy}	1600	MPa
σ_{sh}	1917	MPa
ε_{sy}	0.8	%
ε_{sh}	4.8	%
E_s	187.5	GPa
E_f	60.0	GPa

Simulation of bond between reinforcement and HPFRC: the interface FE is employed to simulate the bond shear stress-slip behavior between the reinforcing bars and HPFRC. Figure 6-18 shows the bond shear stress *versus* slip diagram to define the constitutive law of this interface element. In addition, the values that define this constitutive law are indicated in Table 6-5. These values are defined using Figure 5-8. More details about this constitutive model and interface FE can be found elsewhere in the study concluded by Sena Cruz in 2004.

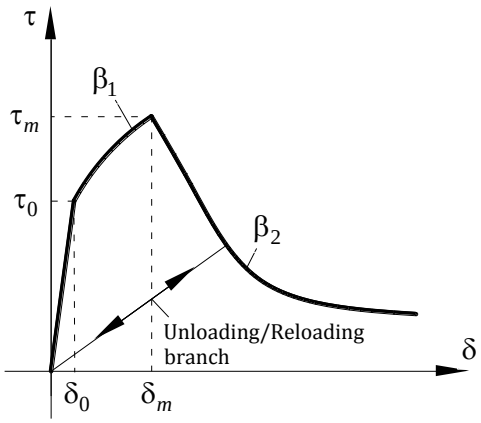

Figure 6-18: Bond shear stress-slip behavior of interface FEs

Table 6-5: The values define the bond-slip behavior of GFRP bar and steel strand

Parameter	Value for GFRP bars	Values for Steel strand
τ_0 (MPa)	11.1	7.8
τ_m (MPa)	21.5	18.1
δ_0 (mm)	0.12	0.09
δ_m (mm)	0.62	0.72
β_1 (-)	0.40	0.40
β_2 (-)	0.40	0.40
K_n (N/mm)*	10^6	10^6

* Normal stiffness in interface FE

6.5.1.3 Modeling of prestress in reinforcements

The prestress effect of reinforcements is included by giving the equivalent pre-strain magnitude to the 2D Cable FE using a thermal loading condition. In respect with the value of "thermal expansion coefficient" (*i.e.* α_T) defined for the reinforcement, the required temperature variation to exhibit a desired amount of pre-strain in the reinforcement can be simply obtained by the following equation:

$$\Delta T = \varepsilon_r^{pre} / \alpha_T \qquad (6\text{-}21)$$

where ΔT is the temperature variation, and ε_r^{pre} is the value of pre-strain in the reinforcement due to the prestressing, which should be taken as the value of pre-strain after calculating of the possible loss (refer to Table 5-7). In order to simulate releasing condition of the prestressing force, the temperature variation must be negative, meaning that the reinforcement is being contracted. Therefore, by giving $\alpha_T = -0.01$, the given temperature variation (ΔT) becomes equal to the pre-strain of reinforcement in percentage.

6.5.2 Model 3D based on CDP approach

The details of 3D numerical simulation in terms of geometry, mesh, constitutive models and values of the model parameters are provided in this section.

6.5.2.1 Geometry, meshes, and boundary conditions

The geometrical details of the 3D models are shown in Figure 6-19. Only one fourth of the I-beam is modelled due to two symmetrical planes, at mid span and through the beam longitudinal axis. This will be beneficial in terms of computational time efficiency. Standard Solid Hex FE with 8-nodes and 2×2×2 integration points are employed to simulate the behavior of HPFRC materials. In addition, the reinforcing bars are simulated employing truss FE embedded to the surrounding solid elements at the location of the reinforcements. This can be seen in Figure 6-19 for both steel strand and GFRP bar. By using this embedment technique, the strain in the embedded truss FE follows the strain of its host element (*i.e.* the surrounded solid element) during the analysis, which represents a perfect bond condition between bar and HPFRC. Later in this chapter, an attempt will be made to simulate the effect of slipping of reinforcing bars (truss element) inside the host element.

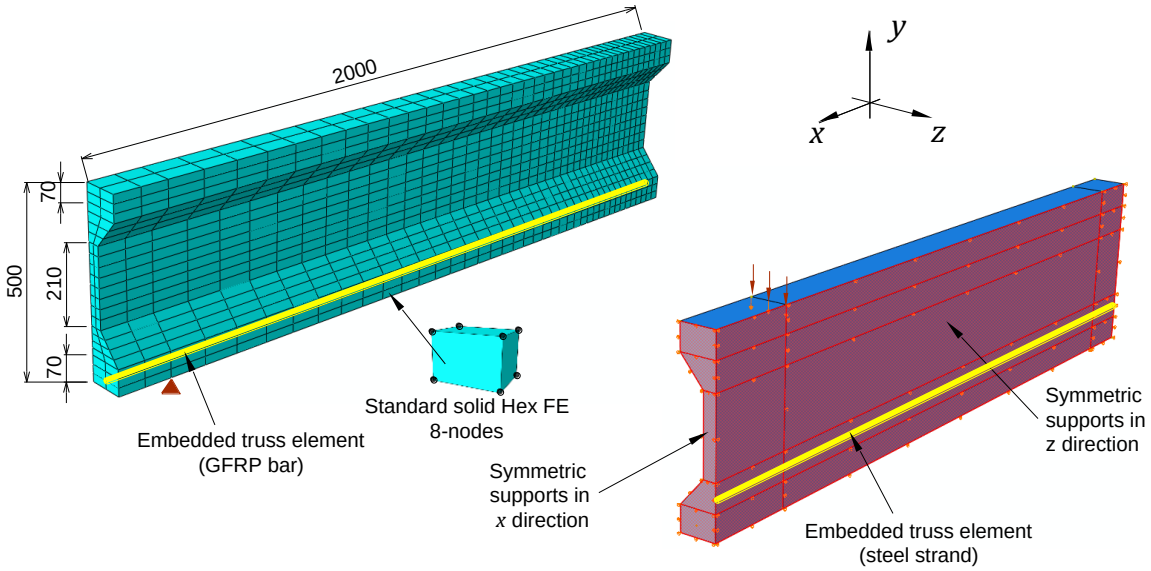

Figure 6-19: Geometrical details of numerical 3D model of the experimental hybrid GFRP/steel strand HPFRC I beams (dimensions in mm)

6.5.2.2 Constitutive models and parameters

HPFRC material: The CDP modelling behavior approach is assigned to the HPFRC

solid Hex FE, which is based on the damage-plasticity model described in Section 6.3. The uniaxial compressive behavior of HPFRC is defined according to the average experimental data obtained from the uniaxial compressive tests on the HPFRC cylinders described in Section 5.2.1.2. The average curve from these results are shown in Figure 6-20. The data points that define this average curve in the 3D models are included Table 6-6. The uniaxial tensile stress-strain of HPFRC is defined by computing the average value of mode I fracture energy, G_f^I, between the two average values that was obtained from the back analysis of the two series of notched beam bending tests in Section 6.4.5. The "*failure stress*" (the crack initiation of HPFRC) is considered to be equal to the average tensile strength (*i.e.* f_{ct}). The tension softening law is taken as a linear diagram defined according to the calcualted value of G_f^I. The adopted range of tensile softening in 3D models are shown in Figure 6-21.

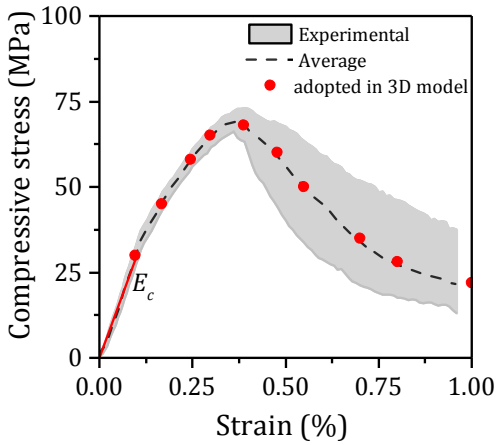

Figure 6-20: The average compressive stress-strain of HPFRC adopted in 3D FE models

Table 6-6: The values define the compressive stress-strain of HPFRC

stress (MPa)	Strain (%)
30	0.09
45	0.17
58	0.24
65	0.30
68	0.39
60	0.48
50	0.55
35	0.71
28	0.80
22	1.00
E_c	35 GPa

The other required parameters to define the CDP model for HPFRC material are reported in Table 6-7. The parameters K_c, e, and α are taken as the values normally recommended for plain concrete (see Table 6-7). However, the dilation angle (*i.e.* ψ), which is the most effective parameter to simulate the fracture mechanism of HPFRC in this type of model, is calibrated considering the results of the non-prestressed beam.

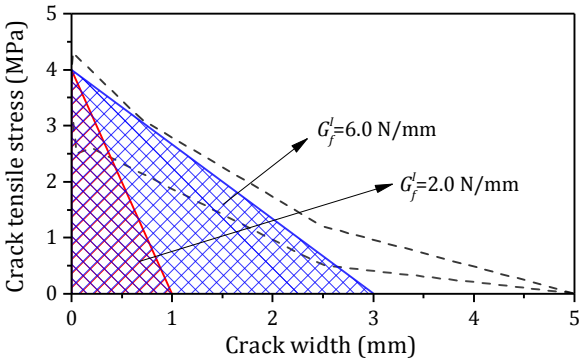

Figure 6-21: The post-cracking behavior adopted in 3D models based on the CDP modeling approach

Table 6-7: The values define the CDP model for HPFRC material in numerical 3D models

Parameter	f_{ct} (MPa)	E_c (GPa)	α * (-)	K_c (-)	e (-)	ψ (degree)
Values	4.0	35	1.16	0.67	0.1	[15-45]

* from Eq. (6-14)

Longitudinal reinforcement: the same tensile behaviors considered for the 2D Cable FEs is also given to the truss FE in 3D model. In addition, the thermal loading condition adopted in 2D model to simulate the prestressing effect of the reinforcements, is also used in the 3D models.

Slipping of the longitudinal reinforcements: When the truss elements (as "slave" elements) are embedded into the solid elements (as "master" elements or "host" element), a perfect bond condition is being considered between the reinforcement and HPFRC. This is due to the fact that the strain of reinforcement follows the equivalent tensile strain of the master element in the direction of the truss FE during the analysis. Hence, no slipping between these two elements is simulated. In order to include the effect of slipping in the truss elements while it is embedded into the solid elements, a degradation method is applied to the modulus of elasticity of the reinforcing materials in which by increasing the strain of the master element, the tensile stress (or axial stiffness) given to the system of the analysis by truss FE decreases, therefore, the slipping effect is indirectly modelled between these two elements.

An incremental deformation of the master element in the axial direction of the embedded

truss FE is shown in Figure 6-22a for two cases: 1) "Perfect bond" condition (no slipping); 2) "Slipping allowed". When the slipping is allowed, the deformation of the truss FE is lower than the master element, leading to obtain a lower value for its tensile stress. The relation between the deformation of the master element, δ^m, and slipping in relation to the slave element, δ^s, can be defined by angle α_r measured from the *perfect bond* condition line plotted in Figure 6-22b. This relation is mathematically expressed by

$$\delta^s = \delta^m \cdot \left(\tan\alpha_r - 1\right) \tag{6-22}$$

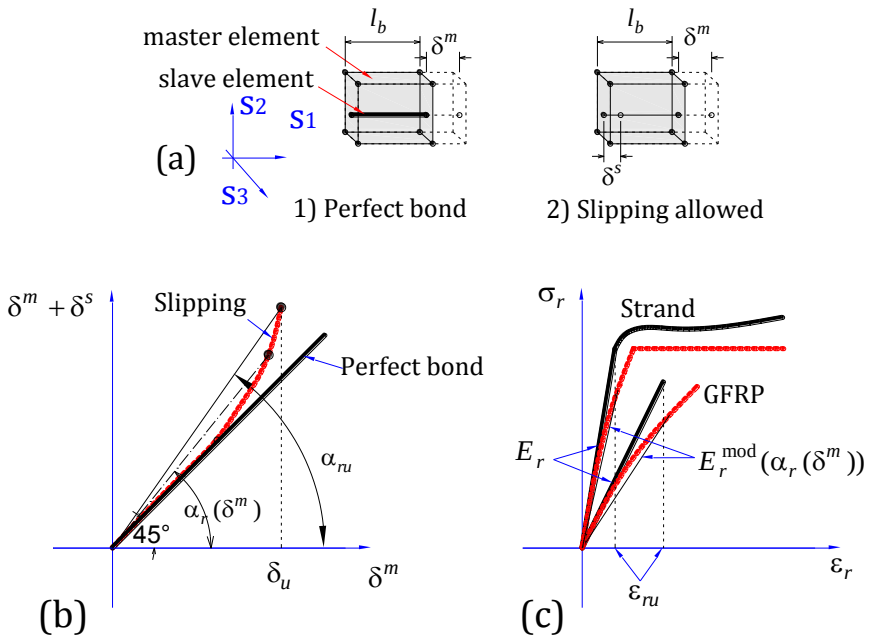

Figure 6-22: (a) concept of the perfect bond and slipping allowed in embedded truss elements, (b) definition of slipping rule, and (c) the degradation rule of the Young's modulus of the reinforcement

The value of δ^s increases with the δ^m, and it ends up to a deformation of the master element in which the slave element fails (δ^u). If a linear relation is assumed between α_r and δ^m, the Eq. (6-22) is known for a given value of δ_u and α_{ru} as defined in Figure 6-22b. Therefore, the updated value of the tensile stress in the truss element (*i.e.* σ_r^{mod}) due to the slipping effect can be obtained by

$$\sigma_r^{\mathrm{mod}} = \sigma_r - \Delta\sigma = \sigma_r - E_r\left(\delta^s / l_b\right) \tag{6-23}$$

where l_b is the length of the master element in the direction of the slave element, and σ_r is

the tensile stress of the slave element at each step of the analysis. Hence, by substituting Eq. (6-22) to Eq. (6-23), and taking the tensile strain of reinforcements equal to $\varepsilon_r = \left(\delta^m / l_b\right)$ at each step of the analysis, the updated value of Young's modulus of the reinforcing bars to include the slipping effect is derived as

$$E_r^{\text{mod}} = E_r \cdot \left(2 - \tan\alpha_r\right) \tag{6-24}$$

where E_r is the original elastic Young's modulus of the reinforcing bars measured from a direct tensile test (see Figure 6-17), and E_r^{mod} is the modified Young's modulus of the reinforcing bars that is updated at each step of the analysis. The definition of these two Young's modulus are illustrated in Figure 6-22c. Further, the angle α_r is given in degree by

$$\alpha_r = 45 + \left(\alpha_{ru} / \varepsilon_{ru}\right)\varepsilon_r \tag{6-25}$$

where ε_r is the value of reinforcing bar's strain at each step of the analysis, which is equal to the tensile strain of the master element (host element). In addition, the value of ε_{ru} is the strain of reinforcement at failing in case of GFRP bars, and it is the yielding strain in case of steel strand. Note that after yielding, the yield stress is assumed constant for whatever value of plastic strain (shown in Figure 6-22c). The value of α_r can be theoretically between 45 and 90 degree, however, for internal reinforcing bars utilized in concrete structures, it may be ranged between 45 to 55 degree depending on bond quality of reinforcement to concrete. Therefore, the given value of $\alpha_{ru} = 5$ for both steel strand and GFRP bars showed good agreement with the experiment as it will be shown in the next section. The calibration of α_{ru} by a pullout test is someway difficult, because, α_{ru} value is based on the absolute difference between concrete's deformation and bar's deformation at their interface at failure stage (if concrete does not fail earlier). This value may be calibrated by using a pullout test in which several strain gauges are installed on the bar.

The updated Young's modulus from Eq. (6-24) is implemented in 3D models in Abaqus by using an "user field variable" which is defined through a simple subroutine given in Annex 6A. The main value passed in the subroutine is the tensile strain of the truss element

(*i.e.* ε_r) at each iteration of the analysis. The Young's modulus assigned to this truss elements is set to be dependent on the defined "user field variable", while α_r is given to this "user field variable" inside the subroutine. Note that for case of the prestressed beams, the value of ε_r is replaced by $\left(\varepsilon_r - \varepsilon_r^{pre}\right)$ in Eq. (6-25).

6.6 Results and discussion

In this section, the results of the numerical simulations from both 2D and 3D models are discussed and compared with those obtained from the experiments. In Section 6.6.1, the adopted parameters in CSC and CDP models will be firstly validated by using the experimental results of the non-prestressed beam (*i.e.* IB5). Later, in the subsequent sections, the validated models will be employed to simulate the behavior of the prestressed beams (IB6, IB8 and IB10) in terms of force-deflection response, strain of the reinforcements, crack pattern and failure mode, respectively, in Sections 6.6.2, 6.6.3, and 6.6.4.

6.6.1 Model validation

The results of the 2D and 3D models is validated by comparing to the respective results of the non-prestressed beam in terms of the force-deflection response at mid span section.

6.6.1.1 2D/CSC model

In case of 2D/CSC model, the parameters in regard to the shear behavior of HPFRC are defined by using two available methods: 1) the shear retention factor, 2) the shear softening law. For case of the traditional shear retention factor, the force-deflection response is plotted in Figure 6-23a for $p_1 = 1, 2, \text{and } 3$ (the parametric study 'a' in Table 6-8). As shown, for a deflection higher than of about 15 mm at mid span, which is close to the serviceability deflection, the behavior of tested beam is overestimated by the 2D model. Further, no significant change is observed by adopting different values for p_1. In fact, due to the very high value of crack opening defined for HPFRC in normal direction when it compares to plain concrete, the progressive degradation of crack shear modulus based on Eq. (6-3) is very small. Therefore, crack shear stiffness degradation is not simulated as intensive as occurred

in the experimental tests, and these numerical simulations predict a flexural failure mode, which is similar to the response obtained from Def-DOCROS software in Chapter 5. The force-deflection response from Def-DOCORS is also included in the figure.

Table 6-8: Adopted parameters in the parametric studies in 2D/CSC model

Parameter / Study	Shear softening			Shear retention factor
	β_{cr}	G_f^{II}	τ_m^{cr}	p_1
	(-)	(N/mm)	(MPa)	(-)
Study a	-	-	-	1, 2 , and 3
Study b	0.05, 0.1, 0.5	2.5	0.75	-
Study c	0.1	1.0, 1.5, 2.5	0.75	-
Study d	0.1	2.5	0.75, 1.0, 1.5	-
Final 2D model	0.1	2.5	0.75	-

On the other hand, based on the shear softening law presented in Figure 6-3, three parameters must be defined: 1) constant shear retention factor, β_{cr}, that defines the first slope of diagram, 2) the crack shear strength, τ_m^{cr}, that defines where the ascending branch ends, and 3) the mode II fracture energy that defines the softening stage by allocating the amount of area under the bi-linear diagram of the shear softening. A parametric study is carried out in order to investigate the influence of these parameters on the force-deflection response of the beam. The respective results are plotted in Figure 6-23b, c, and d. Further, the range of adopted values for these parameters are included in Table 6-8. It should be noticed that in these models, the number of cracks allowed at each integration points is 2, and the threshold angle (*i.e.* α_{th}) is set to 30 degree. For study "b", which the results plotted in Figure 6-23b, no significant influence was observed by changing the value of β_{cr}. In study "c", by decreasing the mode II fracture energy, G_f^{II}, the stiffness and load carrying capacity of the beam decrease in the last stage of its response, as shown in Figure 6-23c. Finally, in study "d", the influence of the crack shear strength, τ_m^{cr}, is plotted in Figure 6-23d. As shown in this figure, the force deflection response of the beam is efficiently influenced by the variation of τ_m^{cr}. When the higher value is taken for the crack shear strength, the force-deflection response approaches to the curve obtained by means of the traditional shear retention factor.

Unlike, by using the smaller value for τ_m^{cr}, 0.75 MPa, the experimental response is fitted accurately.

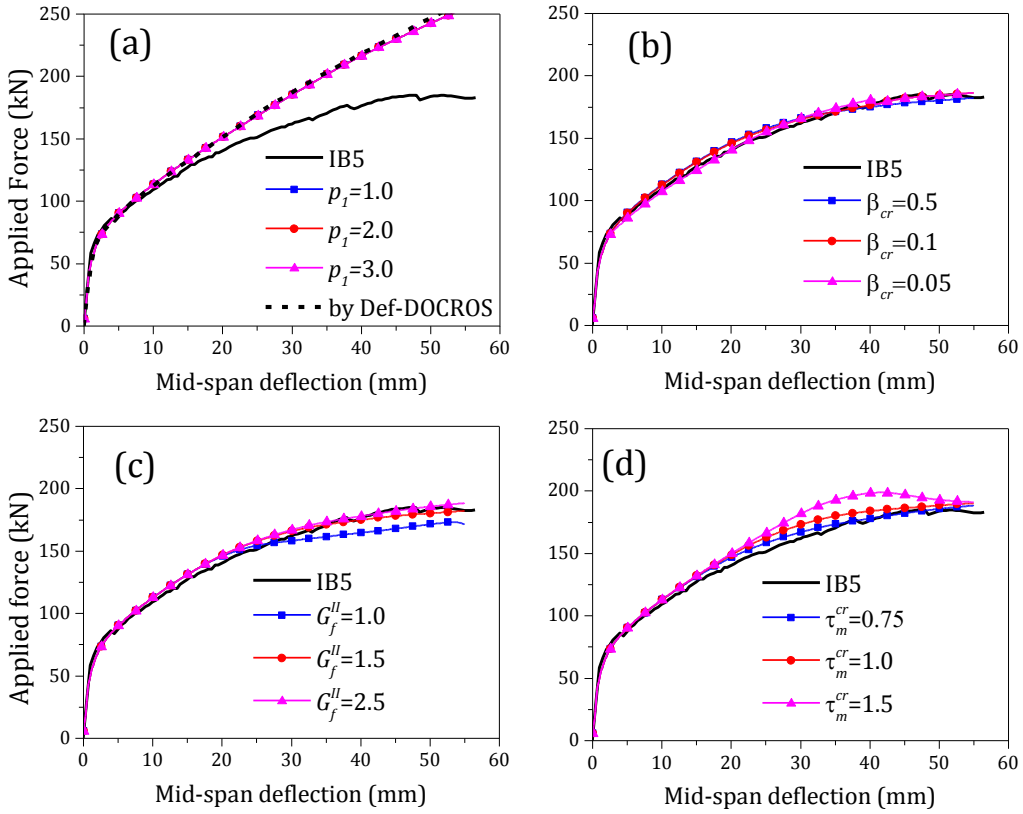

Figure 6-23: Validation of the shear parameters in CSC model: (a) power law in shear retention factor, (b) parameter β, (c) Mode II fracture energy, and (d) crack shear strength in shear softening law.

According to the parametric study, by adopting a set of values for the shear softening parameters (β_{cr}, τ_m^{cr} and G_f^{II}), the numerical force-deflection response predicts appropriately the respective results from the experimental tests. However, in order to assess the reliability of this result, the obtained crack pattern from the 2D model (whose the shear softening parameters are included in Table 6-8, the last row, the final model) is compared with the one obtained from the experimental test in Figure 6-24. As can be seen in this figure, the mode of failure in the model is different of what was obtained in the test. In 2D model, the junction between the bottom flange and the web plate is the weakest section in transferring shear stress due to its smaller thickness as well as the higher shear stress concentration provided by the reinforcements. The crack shear strength is reached at the junction prior to other section in the beam, and it forms a failure crack along this shear transition zone. Therefore,

a very high value of G_f^{II} (about 2.5 N/mm) is required in order to slow down the progressive failure of the beam at this section (see the change in the slope of the force-deflection response in Figure 6-23d). Besides, the failure mode obtained in the experimental test is different. The crack failure started from the bottom flange (at the location of the reinforcement) and progressed towards the point load. In fact, no sign of failure occurred in the junction of the tested beam (*i.e.* IB5) as it was observed in the model. Due to the lack of flexure-shear crack localization at the bottom flange in the 2D model, the concentration of the shear stress at the junction between the web and flange increased. As it was discussed in Section 5.3.3.2 in Chapter 5, the mode II fracture energy, G_f^{II}, is not independent from the mode I fracture energy, G_f^{I}. After a certain crack opening, the flexure-shear behavior of HPFRC material is predominantly influenced by the mixed modes fracture mechanism in which these two energies must be dependently updated during a flexure-shear analysis (such as the flexure-shear analysis of the tested beams in the shear span). However, in the shear softening approach, G_f^{II} was defined 2.5N/mm for all the plane stress FEs in shear span, while the mode I fracture energy was given the same value as defined in the bending zone (the zone that was mainly governed the flexural deformation). That means, the mode I fracture behavior of HPFRC was not influenced by the existence of shear stresses.

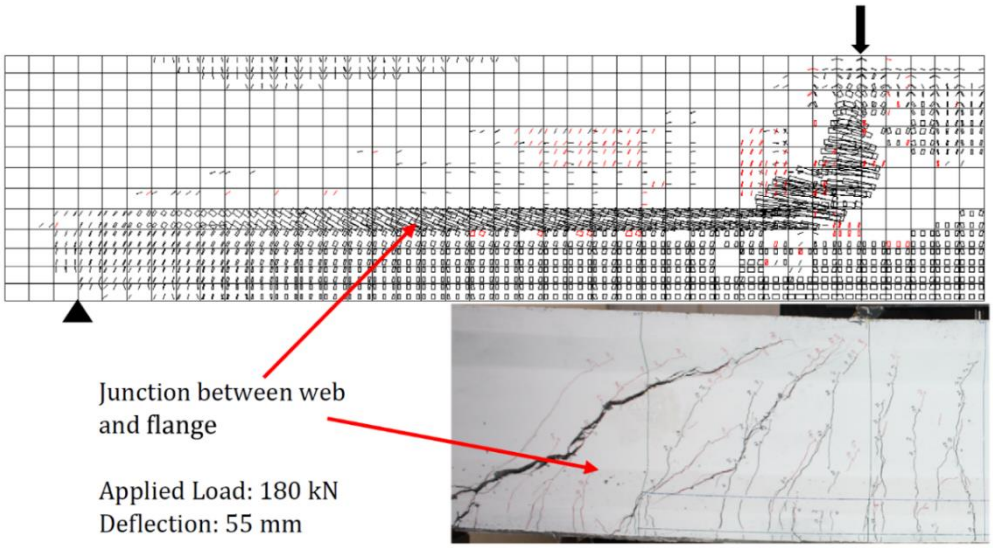

Figure 6-24: Comparison between crack pattern obtained from the test and from the 2D model

Although this shear softening law is unfortunate to capture the exact flexure-shear failure obtained in the tested beams, this approach is still relevant to predict the force-deflection response of the beam. In addition, as it will be seen later, the results in terms of tensile strain of the reinforcements will be well predicted by the model.

6.6.1.2 3D model

The results of 3D numerical model of the non-prestressed beam (IB5) is plotted in Figure 6-25 in terms of the total applied load *versus* mid span deflection. As reported in Table 6-7, a range of values between 15 and 45 degrees is considered for the dilation angle (*i.e.* ψ) in the model, due to the lack of data from material tests to obtain this value. As shown in Figure 6-25, by decreasing the value of dilation angle, the load carrying capacity of the beam decreases, and the numerical force-deflection curve approaches to the curve obtained experimentally. Note that in these simulations the dilation angle is the unique model's parameter that has varied. Furthermore, the slipping effect explained in Section 6.5.2.2 was not activated in these simulations. In order to understand better the influence of the dilation angle on the behavior of beam, in Figure 6-25a and b the field of the principal plastic strains for case of $\psi = 15$ is compared with the corresponding field obtained when a $\psi = 45$ is adopted. In addition, the crack pattern registered in the experimental test before failing, at mid span deflection about 55 mm, is shown in Figure 6-26c. When the value of dilation angle is lower, the rate of the softening flow potential is higher in the model (higher difference between ψ and β). Therefore, the damage introduced in shear zone of the beam is much higher than the case with higher value of the dilation angle. This can be observed by looking at Figure 6-26a and b. The total load carrying capacity of the beam in the model with $\psi = 15$ is lower than the model with that $\psi = 45$ was adopted. The maximum principal plastic strain field shown in case of $\psi = 15$ shows a good agreement with the experimental crack pattern in Figure 6-26c. The failure crack shown in the experimental crack pattern was opened about 5 mm in a rough measurements from the captured image. However, in case of model shown in Figure 6-26b

($\psi = 45$), the maximum principal plastic strain is less than 0.02. Hence, if the average length of the HPFRC element assumed about 25 mm, the maximum equivalent crack width in this figure is about 0.5 mm. But, this value in the case of model with $\psi = 15$, it can be approximately calculated around 3.0 mm (maximum principle plastic strain of about 0.13).

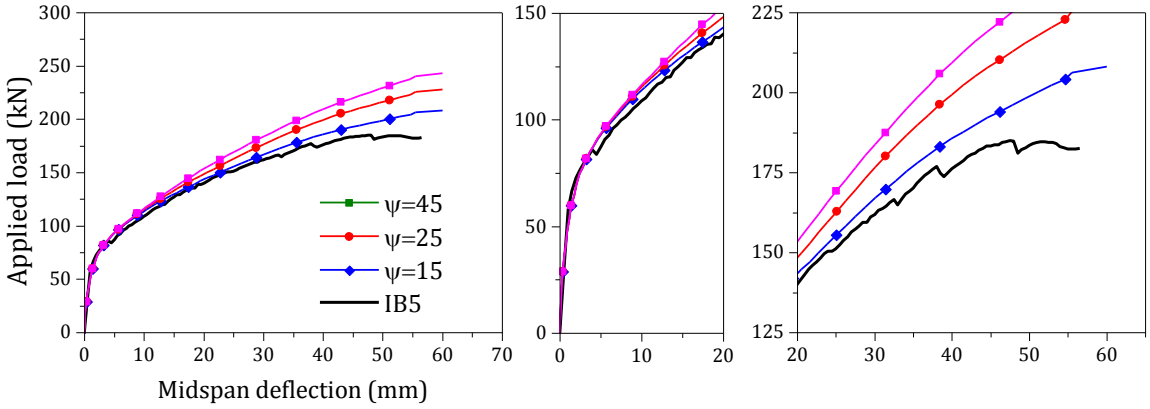

Figure 6-25: Validation of 3D model by using experimental result of the non-prestressed beam: influence of the dilation angle on the force-deflection response at mid span

For the numerical results plotted in Figure 6-25, a mode I fracture energy of $G_f^{II} = 4.0$N/mm was adopted, which was taken as the average value between the two average values were obtained from the results of the back analysis in Section 6.4. In order to see this dependency of the 3D model on G_f^{II}, two models were implemented by taking higher (*i.e.* 6.0 N/mm) and lower (2.0 N/mm) values of G_f^{I} in relation to the one obtained from the back analysis. The variation of G_f^{I} is mainly due to the fiber orientation (in respect to the fracture surface), fiber distribution, and the number of fibers bridging the crack plane in the matrix. The "*failure stress*" (or tensile strength) was taken as 4 MPa for both the model following a linear softening branch. The results of these two models in terms of the total force *versus* mid span deflection are plotted and compared with the experimental results in Figure 6-27. Note that in these models, the dilation angle was kept constant as 15 degree. Based on the results, the intermediate value of 4 N/mm seems assure that the numerical simulation fits better the experimental curve.

In order to include the slipping effect of the reinforcement in the 3D model, the proposed parameter α_r described in Section 6.5.2.2 is considered for $\psi = 15$ and $G_f = 4.0$N/mm. The

results of this model and the model without slipping effect were compared with the experimental response in Figure 6-28. As can be seen, taking value of 49 degree for α_r can assure a best fit of the experimental response. This effect is predominant for case of prestressed beams as it will be shown later in the next section.

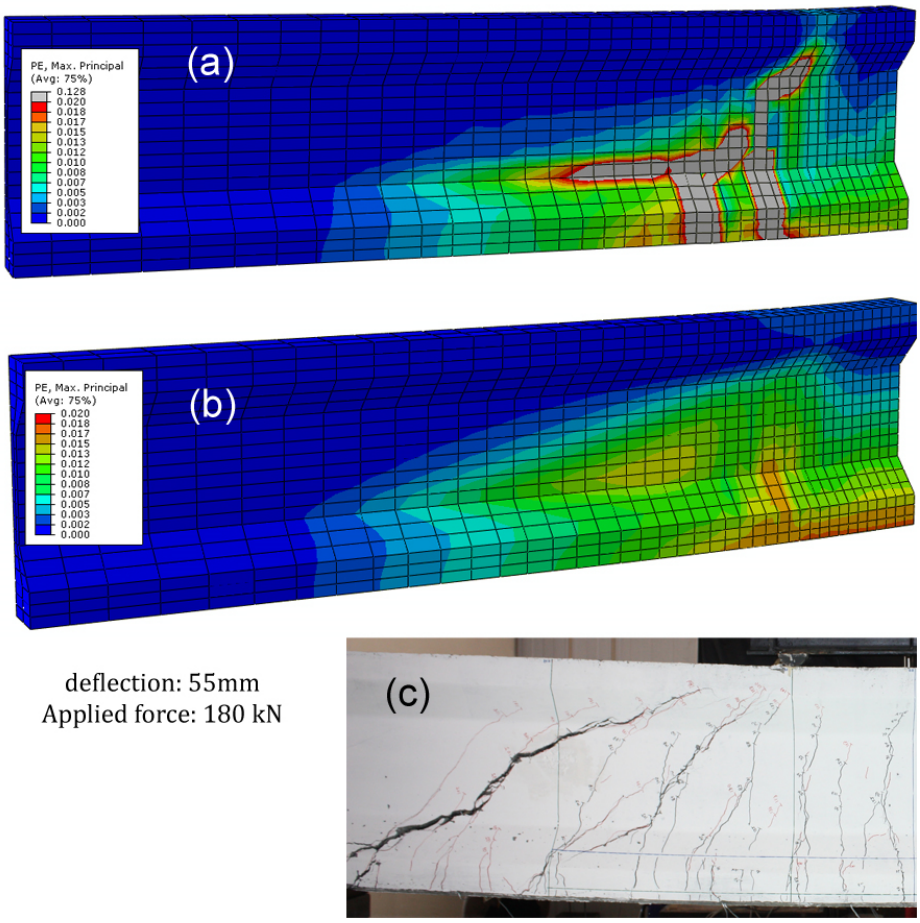

Figure 6-26: Comparison between the maximum principal plastic strain field for 3D model with: (a) dilation angle 15, (b) dilation angle 45, and (c) experimental crack pattern

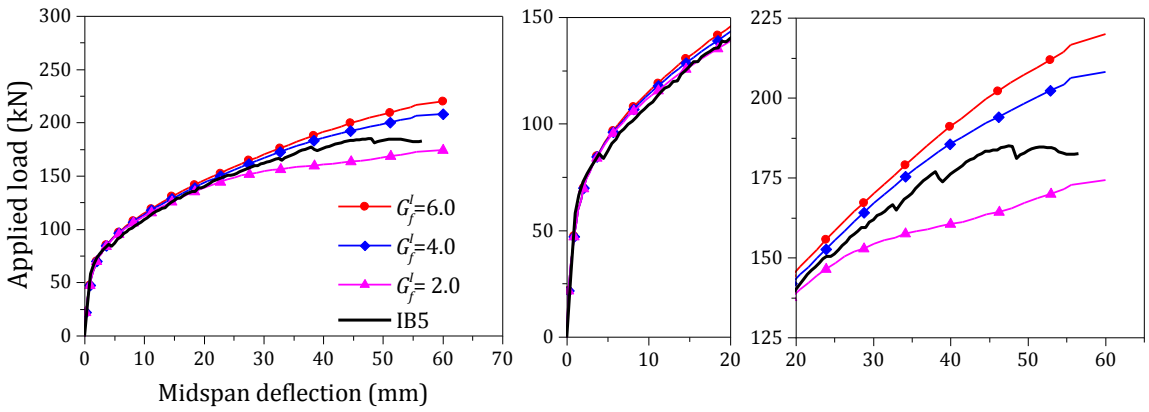

Figure 6-27: Validation of 3D model by using experimental result of the non-prestressed beam: influence of the mode I fracture energy on the force-deflection response at mid span

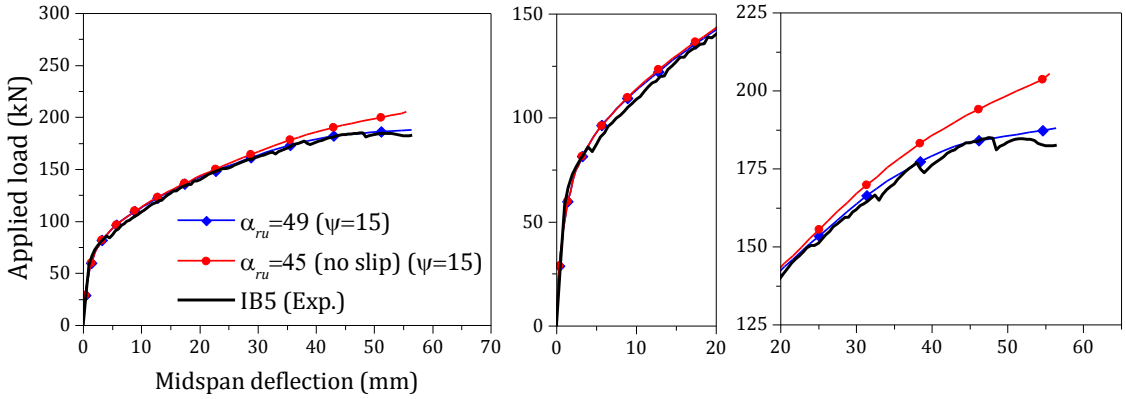

Figure 6-28: Validation of 3D model by using experimental result of the non-prestressed beam: influence of the slipping parameter, α_r , on the force-deflection response at mid span

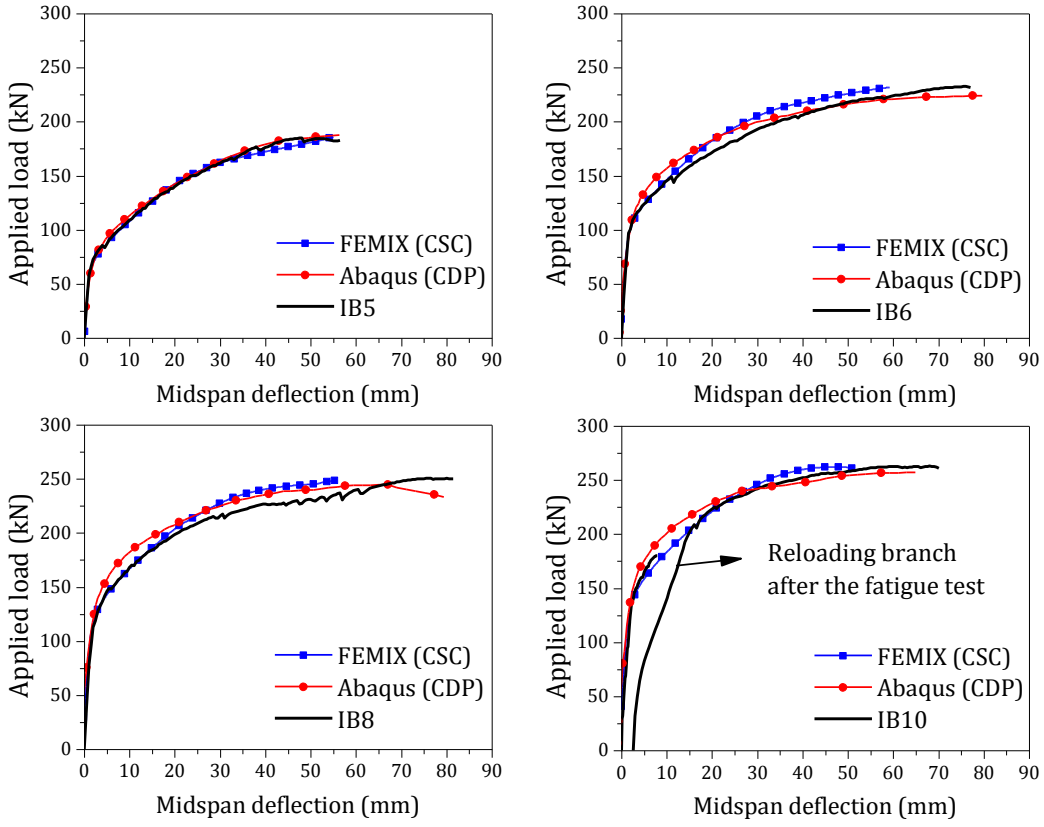

Figure 6-29: The applied force *versus* mid span deflection obtained by CSC and CDP models, and from the tests

6.6.2 Force-deflection response

The model calibrated in the previous section is now employed to simulate the structural behavior of the prestressed beams. In Figure 6-29, the results of the 2D models (by FEMIX) and 3D models (by Abaqus) are compared with the obtained results from the tests in terms of the total applied force *versus* mid span deflection. In addition to the mid span deflection, the total force *versus* deflection in shear span at distance 500 mm from the loading point

(results of LVDT1 in Section 1 shown in Figure 5-6) is also plotted in Figure 6-30. The results from both models show a good agreement with the experimental results. In fact by means of both CSC and CDP model, the flexural stiffness of the beam under monotonic loading condition was effectively predicted.

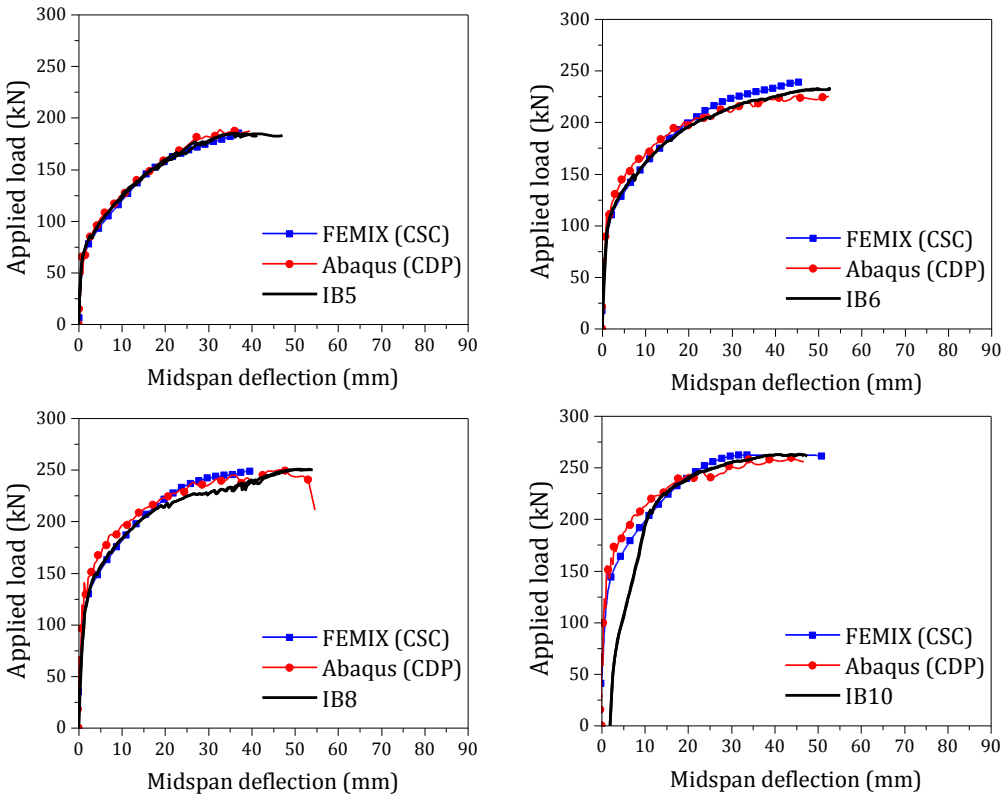

Figure 6-30: The total applied force *versus* deflection at shear span (Section 1 measured by LVDT1 and 5) obtained by CSC and CDP models, and from the tests

6.6.3 Strain of the longitudinal reinforcements

The tensile strain of GFRP bar was measured during the test by means of the installed strain gauges in both bending and shear zones. The installation of these strain gauges was previously shown in Figure 5-6 from Chapter 5. The strain gauges named by SG1 and 5 were installed in shear span, SG2 and 4 at the section under the loading point, and SG3 at mid span deflection. A comparison is given between the results of tensile strain obtained from the numerical models and those measured from the tests in Figure 6-31, Figure 6-32, Figure 6-33, and Figure 6-34, respectively, for IB5, IB6, IB8 and IB10. The tensile strain of GFRP bar in 3D model was calculated using the results of tensile stress, giving by

$$\varepsilon_f = \sigma_f / E_f \qquad (6\text{-}26)$$

where σ_f is the tensile stress of GFRP bar at each step of the analysis, E_f is the Young's modulus of GFRP bars obtained from a direct tensile test, and ε_f is the calculated tensile strain for GFRP bar. The results of tensile stress is used because the Young's modulus of GFRP bar was updating at each step of the analysis to include the slipping effect according to the technique described in 6.5.2.2 by using Eq. (6-24). However, in 2D model by FEMIX, the strain was directly obtained from the output results of the analysis since the interface FE was implemented to simulate the slipping of the reinforcements.

A very good agreement is achieved between the numerical and experimental results of the tensile strain of GFRP bar for all the tested beams at both bending and shear zones. This proofs the reliability of these models to predict the tensile behavior of the internal reinforcements. The comparison for results of the strain in steel strand is plotted in Figure 6-35. Unfortunately, the respective results for IB5 and IB10 are not presented since the strain gauges installed on steel strand failed at the beginning of the test. Based on the results plotted for IB6 and IB8, a good agreement was also achieved in terms experimental and numerical tensile strain in steel strand. It was very unlikely to have the strain gauge installed on steel strand working after yielding of steel. As shown in Figure 6-35, the tensile strain of strand was failed before 1% of strain, which is approximately the yielding strain of steel strand.

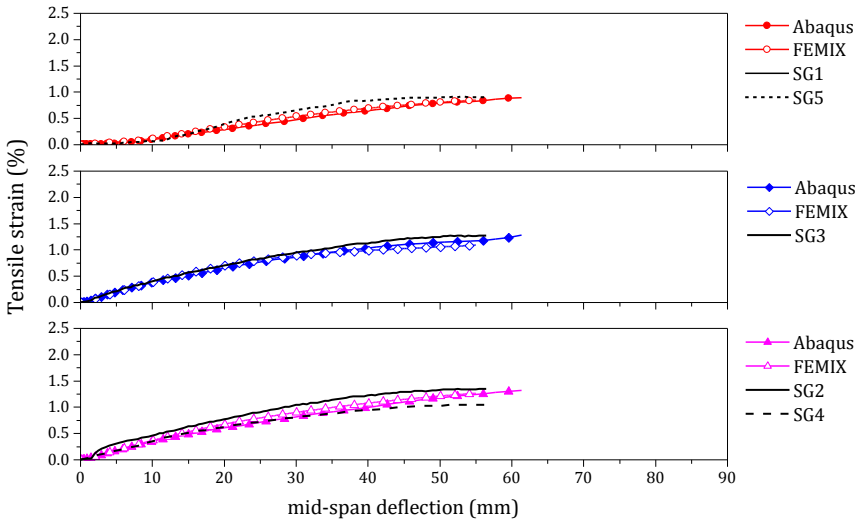

Figure 6-31: Comparison between the values of tensile strain obtained by the numerical models and the test for IB5

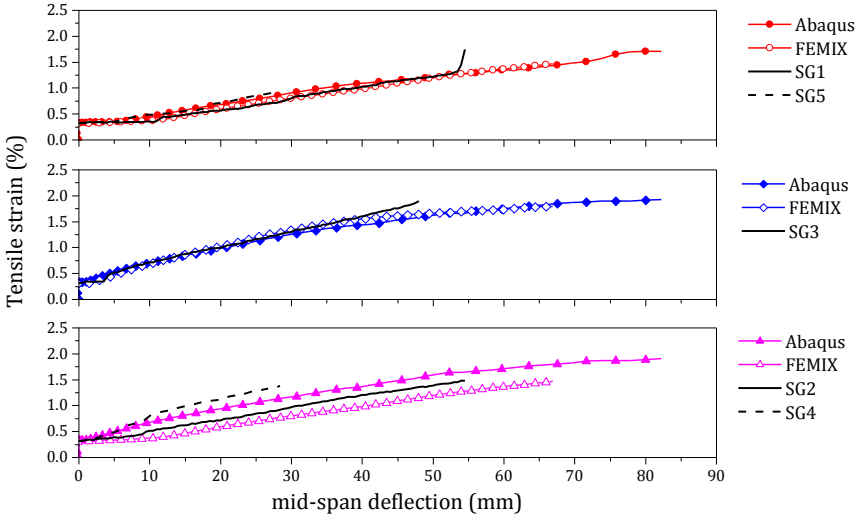

Figure 6-32: Comparison between the values of tensile strain obtained by the numerical models and the test for IB6

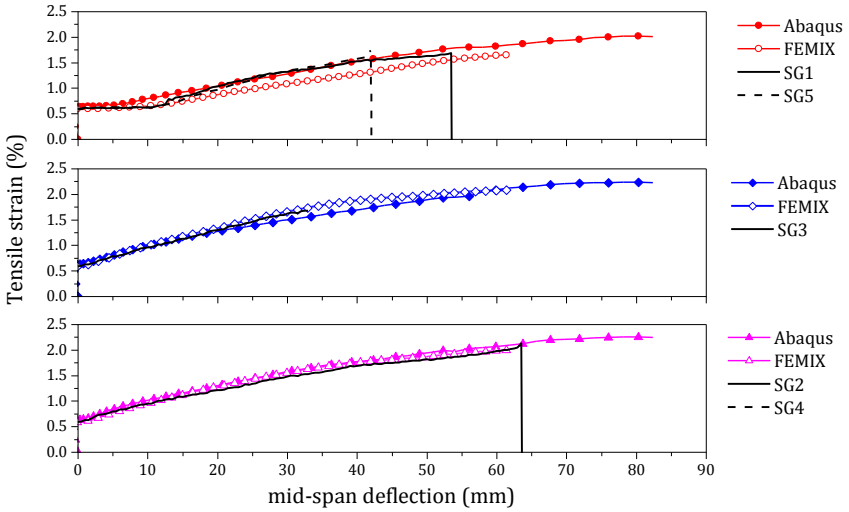

Figure 6-33: Comparison between the values of tensile strain obtained by the numerical models and the test for IB8

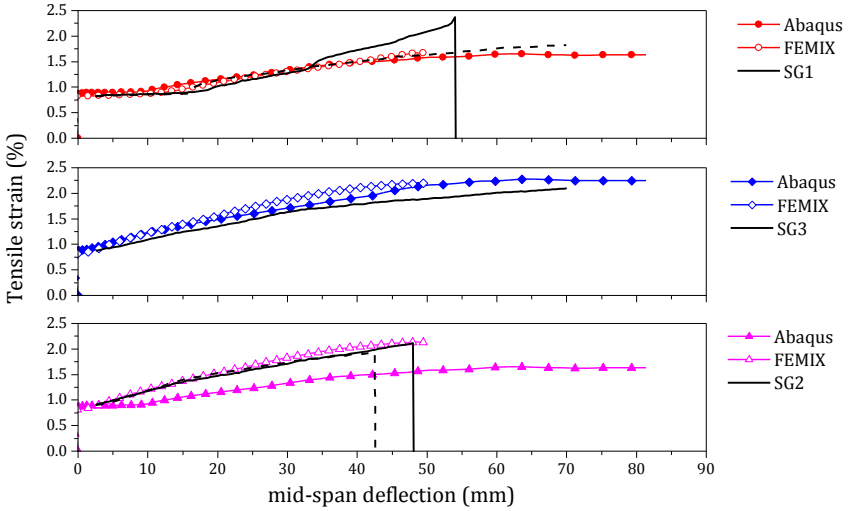

Figure 6-34: Comparison between the values of tensile strain obtained by the numerical models and the test for IB10

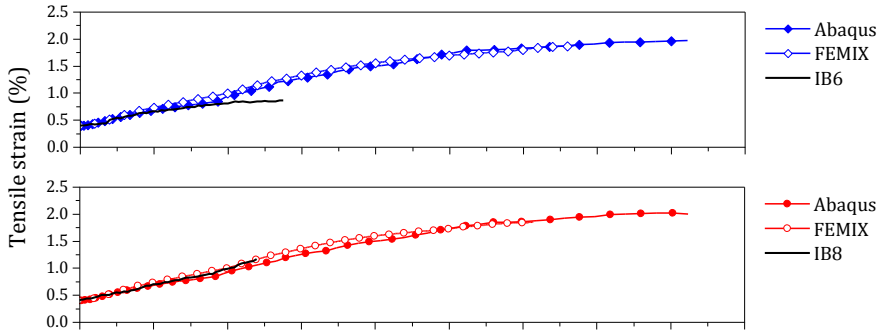

Figure 6-35: Comparison between the values of tensile strain in steel strand obtained by the numerical models and the experimental tests (by SGst) in IB6 and IB8 at mid span

6.6.4 Crack pattern and Failure

To verify the failure mode obtained from the models and the failure mode occurred in the experimental tests, the experimental crack pattern is compared with the maximum principal plastic strain field obtained in Abaqus, as well as with the crack pattern obtained from FEMIX. These comparisons are made in Figure 6-36, Figure 6-37, and Figure 6-38 for, respectively, IB6, IB8 and IB10.

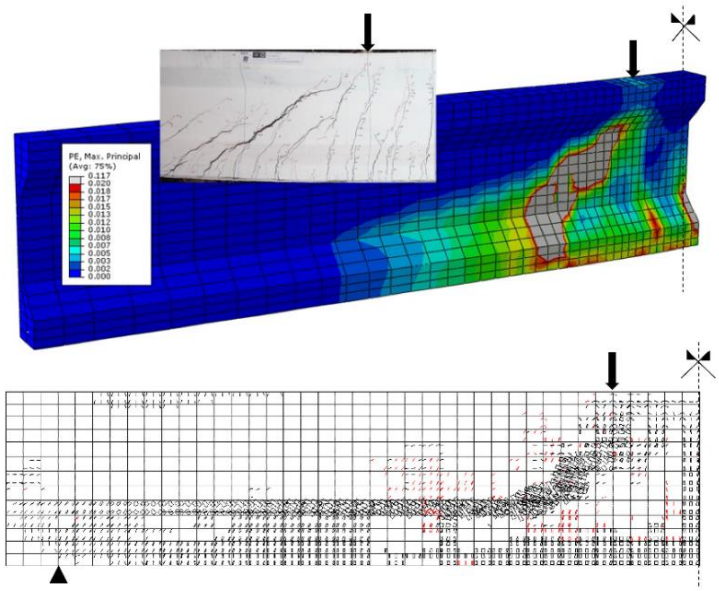

Figure 6-36: The ultimate failure obtained from the 2D Model, 3D Model and from the test for IB6

As shown, by using the calibrated numerical models using the results of the non-prestressed beams, the failure mode of the prestressed beams are well predicted by using the 3D models. For case of 2D model in FEMIX, the final failure crack was formed connecting the shear failure of the junction between the web and flange of beam, leading to the pointing

load (the same as the results of 2D model of non-prestressed beam discussed earlier). However, in the test, no sign of failure was seen in the junction, and the failure crack starts from the bottom flange of beam. In case of 3D modeling, by adopting a proper value for the dilation angle and also the technique to include the slipping effect of the reinforcement, the localization of shear cracks at bottom flange of the beam is somehow captured by the model. This, at the end, led to a failure mode fairly similar to what obtained from the tests.

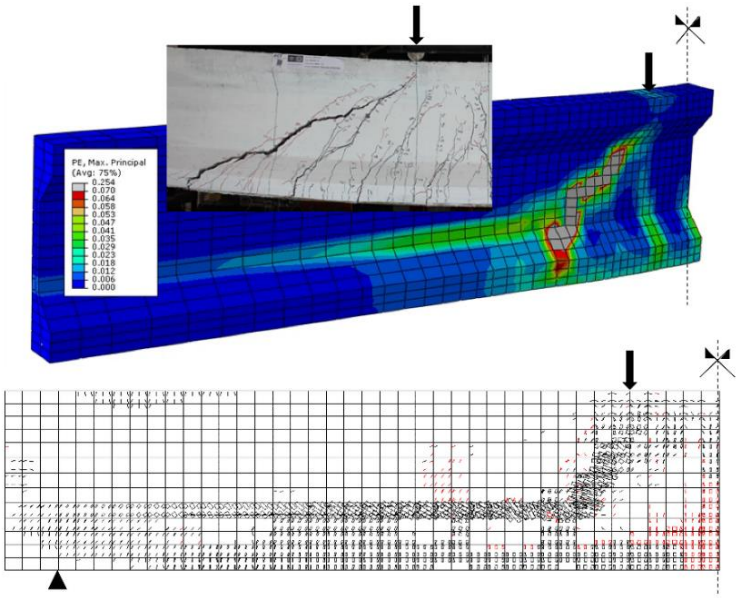

Figure 6-37: The ultimate failure obtained from the 2D Model, 3D Model and from the test for IB8

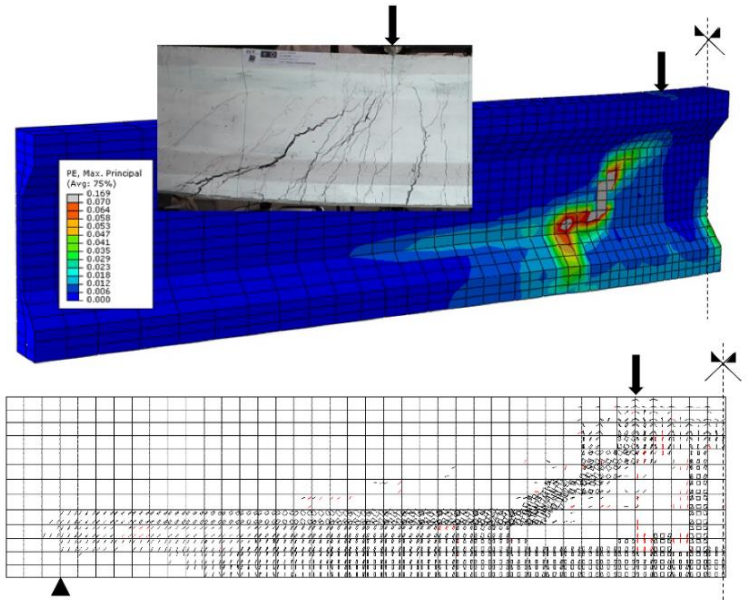

Figure 6-38: The ultimate failure obtained from the 2D Model, 3D Model and from the test for IB10

6.7 Summary and conclusion

In this chapter, 2D and 3D numerical models were employed to simulate the structural behavior of the hybrid reinforced HPFRC prestressed beams. These two models were basically based on two different approaches. The 2D model was based on a multi-directional fixed concrete smeared cracking (CSC) approach while the 3D model was based on the concrete damage-plasticity (CDP) model. The main parameters that define these two models were validated in this chapter in order to be used for case of HPFRC modeling.

For the CSC approach, two modeling methods were considered for shear behavior of cracked concrete: 1) shear retention factor, 2) shear softening law. The traditional shear retention factor showed deficiency to predict the shear behavior of cracked HPFRC. This was due to the fact that the basic assumption behind this method is not in agreement with the behavior of cracked fiber reinforced concrete (FRC) in shear. FRC material normally exhibits a large non-linear deformation in the normal direction to the fracture surface due to the efficient performance of fibers at this direction. But, the shear modulus of crack is significantly diminished while the crack is opening. However, the relation between the shear modulus and crack opening introduced by the adopted equation in the shear retention factor (*i.e.* Eq. (6-3)) is unable to model the rate and form of this degradation. On the other side, the developed crack shear softening law (Ventura-Gouveia 2011) available in FEMIX computer software gives the possibility of defining the degradation of crack shear modulus using a bi-linear softening law independently from the behavior of crack in the normal direction. This strategy gives better prediction to the behavior of FRC material in shear. Also, the method provides computational efficiency in numerical analysis since the global stiffness matrix of the system of the analysis will be kept symmetry. However, this shear modelling approach always relies on the empirical evidence and verification because the dependency of the mixed modes behavior of FRC is ignored. Additionally, the calibration of the mode II fracture energy cannot be obtained by direct shear test.

In case of CDP modelling approach, the model is more sophisticated to account for the modeling of mixed modes behavior. In this modeling approach, the combined

multidirectional nonlinear behavior is analyzed by means of "*yield surface*" and its flow potential rule. The flow rule of this yield surface is non-associated flow meaning that the increment of the equivalent plastic strain tensor (for case of hardening or softening) is not necessarily in the same direction with the defined material friction angle. This friction angle is basically defined in accordance with the traditional Mohr-Coloumb theory that was initially developed for soils, and then developed to be sued for concrete and rock. Therefore, this will be given the flexibility to the model for controlling inelastic behavior of the adopted brittle material in a mixed modes behavior (shear stress being dependent on normal stress). In this study, a constant value of 15 degree for the dilation angle (*i.e.* ψ) gave a good fit to the results from the experiments. However, more studies are required in this field to obtain a proper constitutive law between the dilation angle and the change in the plastic components of strain or stress tensors.

Notations

d	the stiffness reduction variable in CDP model	p_1	the decrease rate of β_{cr} in shear retention model
d_c	damage parameters to define the degradation of the elastic stiffness in compression	p_2	parameter defined in Eq. (6-4) for shear retention model
d_t	damage parameters to define the degradation of the elastic stiffness in tension	$\bar{q}$	the Von Mises equivalent deviatoric stress
D_{II}^{cr}	shear modulus of cracked concrete	w	crack width
$D_{II,1}^{cr}$	the stiffness of the first linear branch in shear softening diagram	α	parameter to define yield surface in CDP modeling approach
$D_{II,2}^{cr}$	the stiffness of the second linear branch in shear softening diagram	α_i	residual tensile stress factors define the post-cracking behavior of FRC ($i=1,2,3$)
e	CDP model's parameter defines the rate G approaches the asymptote	α_r	angle measured the slipping of embedded truss FE in respect with the host FE (Eq. (6-22)
E_c	Young's modulus of concrete material	α_{ru}	the ultimate value of α_r where truss FE failed
E_f	Young's modulus of GFRP bar	α_{th}	threshold angle in radian (Eq. (6-1)
E_r	Young's modulus of reinforcements obtained from standard direct tensile test	α_T	thermal expansion coefficient
E_r^{mod}	modified Young's modulus of reinforcements during the numerical analysis	β	parameter to define yield surface in CDP modeling approach
f_{ct}	concrete tensile strength	β_{cr}	shear retention factor
$f_{ct,L}$	limit of proportionality calculated for CMOD =0.05 mm in standard notched beam test	β_1	factor defines the post-peak behavior of bond-slip relation used in numerical model
$f_{R,j}$	the residual flexural stresses of HPFRC defined by Model Code 2010 ($j=1,2,3,4$)	β_2	factor defines the post-peak behavior of bond-slip relation used in numerical model
F_j	the applied force in notched beam test corresponding to $f_{R,j}$	γ	parameter to define yield surface in CDP modeling approach
G	Drucker-Prager hyperbolic function	γ^{cr}	crack shear strain
G_c	shear modulus of un-cracked concrete	γ_m^{cr}	crack shear strain corresponding to the peak crack shear stress in shear softening diagram
G_f^I	the mode I fracture energy of HPFRC	γ_u^{cr}	the ultimate crack shear in shear softening diagram
$G_{f,avg}^I$	the average mode I fracture energy of HPFRC	δ	crack sliding
G_f^{II}	the mode II fracture energy of HPFRC	δ_0	slip corresponding to bond shear stress τ_0
$G_{f,a}$	the fracture energy available for the new formed crack	δ^m	equivalent deformation of mother element in direction of the embedded element
G_f^{new}	the fracture energy of new formed crack at material point	δ^s	slip of embedded truss FE in respect with its host element
I	identity matrix	ΔT	temperature variation to include the prestress effect in numerical analysis
K_c	ratio between the tensile meridian and compressive meridian in CDP model	ε	strain tensor in numerical analysis
l_b	crack band width (or length of HPFRC FE element)	ε_c^{pl}	compressive plastic strain
$\bar{p}$	the equivalent pressure stress	ε_{ctu}^{cr}	the ultimate crack tensile strain

Notations

ε_{ct}^{pl}	tensile plastic strain	σ_c	concrete compressive stress
ε_{ct}^{cr}	crack tensile strain	σ_{ct}	concrete tensile stress
ε_f	GFRP tensile strain	σ_{ct}^{cr}	crack tensile stress
ε^{pl}	plastic strain tensor in 3D numerical analysis	σ_{c0}	concrete compressive stress at onset its plastic behavior
ε_r^{pre}	pre-strain of reinforcement	$\hat{\sigma}_{\max}$	the maximum principal effective stress
ε_{sh}	strain of mild steel at the initiation of the hardening phase in its direct tensile behavior	σ_{t0}	concrete tensile stress at crack initiation
ε_{sy}	Yielding strain of steel bar	σ_r	tensile stress of truss element in 3D model during the analysis
ξ_i	crack opening factors define the post-cracking behavior of FRC ($i=1,2,3$)	σ_r^{mod}	modified tensile stress of embedded truss element due to slipping effect
σ	concrete stress tensor	σ_s	steel bar's tensile stress
$\bar{\sigma}$	equivalent concrete stress tensor	σ_{sy}	yield stress of steel bar
σ_1	principal stress in plane stress FE	τ^{cr}	crack shear stress
σ_2	principal stress in plane stress FE	τ_m^{cr}	the peak crack shear stress in shear softening diagram
σ_{b0}	initial biaxial compressive yield stress	ψ	the dilation angle in CDP modeling approach

Chapter 7

7. SUMMARY AND CONCLUSION

7.1 Main conclusion remarks

The main aim of the present study (detailed from Chapters 3 to 6) is to introduce a durable and sustainable pre-fabricated concrete beam elements for our future building and construction, which is made of HPFRC material reinforced with hybrid steel and GFRP reinforcing bars. Under scope of this main objective, and based on the study carried out in the present work, the following conclusion remarks can be drawn:

7.1.1 Bond performance of GFRP bars

The first part of the present study was focused on the evaluation of bond behavior between GFRP bars and FRC material. It was found that the same parameters that normally influence the bond behavior of embedded steel reinforcing bars in concrete (such as bar diameter, concrete cover thickness, and surface characterization) also effect the bond behavior of GFRP bars and FRC. Due to the presence of discrete fibers at interface between GFRP bar and concrete matrix, a higher confinement was achieved at this interface resulting in high residual bond shear stress for GFRP bar in debonding process. Moreover, for the two adopted FRC concrete cover thicknesses, no sign of splitting was obtained (not even for the highest bond length adopted in the experiments, i.e. 20 times of bar diameter). This provides possibility of installing GFRP bars as near as possible to the outer surface of the concrete

element, which is beneficial in terms of structural performance of the reinforcing bar. Based on the bond test results, the appropriate FRC cover thickness, as well as the better type of GFRP bar in terms of bond quality was selected to be considered in the further steps of the research. Additionally, an analytical bond model was developed (second part of Chapter 3), and validated with the results obtained from the bond tests in order to be used for the further analysis in the subsequent research steps.

7.1.2 Structural performance of hybrid reinforced FRC in tension

The structural behavior of a RC element in tension is the most important aspect of the behavior for designing purpose. The second part of the present research was focused on the evaluation of cracking behavior of a FRC tensile member reinforced by hybrid GFRP and steel bars. This evaluation was carried out by considering the relevant boundary conditions that governed the bond problem of the reinforcing bars at distance between cracks. The governed bond formulations were solved by using the analytical bond model developed in the first step of the research, which was named as FBL model and detailed in Annex 4A.

By using the developed FBL model and a crack analysis procedure described in Chapter 4, the tension-stiffening effect of hybrid steel/GFRP reinforced FRC element was introduced as a modified crack stress-strain diagram for FRC. The modified crack tensile stress-strain diagram can be used in the sectional or finite elemental analysis of hybrid FRP/steel reinforced FRC elements where no attempt is made to simulate the effect of bond-slip behavior of the reinforcing bars.

7.1.3 Structural performance of hybrid steel/GFRP reinforced HPFRC prestressed beams

At the third step, the structural performance of beam made by HPFRC material and reinforced by GFRP bars and steel strand were experimentally and theoretically evaluated. I shaped cross section was adopted for the beams in order to optimize their flexural performance. This geometry of the cross section is beneficial in an economical point of view

when it compares to the rectangular cross section beam with equal volume of concrete material per unit length. The flexural stiffness of I shaped cross section is about 3 to 4 times higher than the equivalent rectangular cross section (For the same volume of concrete and HPFRC materials per 1 meter length of beam).

In addition, conventional shear reinforcements (e.g. steel stirrups) were totally replaced by HPFRC material in the proposed reinforcing system. Based on the results from the experiments, all tested beams failed in the shear zone through propagation of a critical diagonal crack at shear span. Despite of the obtained failure mode, a very ductile behavior, was observed, particularly, for second group of the tested beams (under-reinforced beams). For this group of beam, it was evidenced that the steel strand was yielded before the shear failure in shear span. The shear failure process in case of beams in the present study was not as brittle as what is typically known for concrete beams failing in shear, since the proposed system could carry the load up to a very high deflection at mid-span section.

Based on the developed analytical formulation in Chapter 5, a new concept was defined for the balanced reinforcement ratio in hybrid reinforcing system. To calculation of this balanced ratio, the mode I fracture energy of HPFRC (due to the contribution of steel fibers) and the steel reinforcement ratio were taken into account. This new balanced reinforcement ratio can be introduced as a new design criterion for the proposed hybrid system, in which the type of failure and the other structural behavior may be dependent on. Based on the results obtained from the experiments, it can be concluded that the prestressed GFRP reinforcement ratio in the proposed reinforcing system should be considered lower that the proposed balanced reinforcement ratio in order to optimize the flexural performance of the beam at ultimate limit state. This is in contrast with design procedure of FRP-RC beams that are commonly recommended to be over-reinforced in order to be failed in crushing of concrete.

Up to service load (i.e. mid span deflection of about $L/250$, being L the beam span), the force-deflection response of the tested prestressed beams was effectively predicted by the theoretical results obtained from DOCROS software (sectional analysis software), and by

the direct method presented in Chapter 5. By increasing in the amount of prestressed level in the longitudinal GFRP bars and steel strand, the service load carrying capacity increased. For the tested beam with the highest prestressing level, the strain of GFRP bars at mid-span section reached about 94% of its nominal ultimate tensile strain at rupture.

For the applied load higher than service load, the tested beams were efficiently influenced by the propagation of the flexure-shear cracks in the shear span. Although all tested beam failed in the shear zone through propagation of a critical diagonal crack at shear span, a very ductile behavior, particularly for second group of the beams (under-reinforced beams) was observed. This ductility was measured by multiplying the strength effect by the deformation effect, which were firstly defined by Jaejer *et al.* in 1997. The calculated ductility index from the experimental force-deflection was compared to the ductility index calculated by means of the "*reference response*", which was based on the force-deflection response that was governed by flexural deformation only (obtained from Def-DOCROS software). This comparison showed that the ductility of the under-reinforced prestressed beam was significantly increased in respect to the corresponding values by the "*reference response*". In fact, the propagation of shear cracks reduced the effective moment of inertia of the beam, and imposed higher curvature to the beam. This shear cracks propagation on one side, and the yielding of steel strand on the other side, gave a high ductility to the force-deflection response of the under-reinforced prestressed beams after service load. This can be a great achievement in terms of ductility for the beams reinforced by prestressed FRP bars, where are categorized as RC beams with brittle failure mode

7.1.4 Numerical simulation of hybrid reinforced HPFRC prestressed beams

In Chapter 6, 2D and 3D numerical models were employed to simulate the structural behavior of the hybrid reinforced HPFRC prestressed beams. The 2D model was based on a multi-directional fixed concrete smeared cracking (CSC) approach while the 3D model was based on the concrete damage-plasticity (CDP) model. The main challenge in these two models was simulation of the shear behavior of HPFRC (or in general steel FRC) in a mixed

modes fracture mechanism.

In case of the CSC model, it was found that the shear retention factor presented basically for shear modeling in case of plain concrete, it was not capable of simulating the shear behavior of HPFRC material in mixed modes fracture behavior (i.e. flexure-shear behavior). The obtained results of the 2D models by using this shear modeling approach overestimated the results obtained from the tested beam, and it was similar to the obtained results from Def-DOCROS (the results that was governed by flexural deformation of beam only). On the other hand, the 2D model with the shear softening model was capable of predicting with an acceptable accuracy the force-deflection response, as well as the tensile strain of the longitudinal reinforcements for all level of applied load. However, adopting the parameters that define this shear softening law in not straightforward. These parameters may be calibrated by using a series of material test that represents the behavior of HPFRC under different ratio between the crack shear and normal stresses. In the lack of data from such material test, the shear softening diagram was validated using the experimental results of the reference HPFRC beam (non-prestressed beam, IB5), and the obtained values were adopted for simulation of the prestressed beams. With this strategy in the numerical analysis, a good predictive performance was achieved from the 2D models in terms of the prestressed beams.

In case of 3D model, the concrete damage-plasticity (CDP) approach (available in Abaqus software) was employed to simulate the inelastic behavior of HPFRC. The CDP model does not deal with cracks at each material point as the CSC model does, but, the deformation at each material point is decomposed to elastic and plastic components. In this model, once the material point reaches the failure surface in tension, it enters to the plastic stage. The failure surface is defined as the yield function proposed by Lubliner et al. (1989) and incorporates the modifications proposed by Lee and Fenves (1998) to account for different evolution of strength under tension and compression. After failure, the plastic deformation of material point is obtained based on a Drucker-Prager hyperbolic function that defines the hardening or softening flow potential rule of the failure surface. The obtained results from the 3D model was succeed in predicting the structural response of the tested

beam. The main parameters to define the flow potential rule in CDP modeling approach was the dilation angle (as defined in Chapter 6). This parameter was the main parameter to distinguish between fracture mechanisms of different brittle materials under mixed modes fracture mechanism (shear and normal stress). A constant value of 15 degree for the dilation angle gave a good fit to the results from the experiments. However, more studies are required in this field to obtain a proper constitutive law between the dilation angle and the change in the plastic components of strain or stress tensors.

7.2 Recommendation for future research

In this section, a list of relevant research topics are recommended for doing further research and developments in the field of the present study.

- Deflection and cracking behavior of the proposed hybrid HPFRC prestressed beams under sustained loading conditions.
- Evaluation of the structural performance of the proposed hybrid HPFRC prestressed beam under corrosive environmental conditions.
- Evaluation of the structural performance of the proposed hybrid HPFRC prestressed beam exposing to high temperature conditions.
- A study should be carried out to evaluate the influence of different HPFRC strength class on the post-cracking behavior of HPFRC, as well as on the structural behavior of prestressed HPFRC beams reinforced with hybrid FRP-steel bars.
- Evaluation of the fracture behavior of steel fiber reinforced concrete (FRC) under flexure-shear loading conditions in order to develop macro modeling approach to address accurately the cracking behavior of this material under mixed modes fracture mechanism.

Appendix

Annex 4A

Definition:

Governing equation: $\frac{d^2\delta(x)}{dx^2} = J_r \cdot \tau(\delta(x))$ where $J_r = \frac{P_r}{E_r A_r}(1 + n_r \rho_r)$, $n_r = \frac{E_r}{E_c}$ and $\rho_r = \frac{A_r}{A_c}$; $\sigma_r(x) = E_r \frac{d\delta(x)}{dx}$; $\tau(x) = \frac{1}{J_r}\frac{d^2\delta(x)}{dx^2}$

(subscript "*r*" is for reinforcing bars, either FRP or steel bar)

Some constant parameters during the analysis:

$C_e = \frac{\tau_1 J_r}{\lambda_1^2}$; $\lambda_1 = \sqrt{\frac{(\tau_1 - \tau_0)}{\delta_1} J_r}$; $C_h = \frac{\tau_m J_r}{\lambda_2^2}$; $\lambda_2 = \sqrt{\frac{(\tau_m - \tau_1)}{(\delta_2 - \delta_1)} J_r}$; $C_p = \frac{\tau_m J_r}{2}$; $C_{so} = \frac{\tau_m J_r}{\gamma^2}$; $\gamma = \sqrt{\frac{(\tau_m - \tau_R)}{(\delta_4 - \delta_3)} J_r}$; $C_f = \frac{\tau_R J_r}{2}$

Stage 1:

Stage	Slip functions $\delta(x)$ $\Rightarrow$	Boundary conditions $\Rightarrow$	Slip solutions $\Rightarrow$	Compatibility conditions $\Rightarrow$	Equations derived by considering compatibility conditions
1	$C_1 e^{\lambda_1 x_e} + C_2 e^{-\lambda_1 x_e} - C_e$	$\delta(x_e = 0) = 0$ $\delta(x_e = L_{tr}^e) = \delta_i$	**Eq. (B1):** $C_1 = \frac{(\delta_i + C_e) - C_e e^{-\lambda_1 L_{tr}^e}}{2\sinh(\lambda_1 L_{tr}^e)}$ $C_2 = C_e - C_1$	-	**Eq. (A1):** $\lambda_1(C_1 - C_2) = 0 \Rightarrow C_1 = C_2$ **Eq. (A2):** $L_{tr} = L_{tr}^e = \left(\frac{1}{\lambda_1}\right)\left[\arccos\left(\frac{\delta_i + C_e}{C_e}\right)\right]$ **Eq. (A3):** $\varepsilon_r^{cr} = C_1(e^{\lambda_1 L_{tr}^e} + e^{-\lambda_1 L_{tr}^e} - 2)$

Annex 4A

Stage 2:

Stage	Slip functions $\delta(x)$ $\Rightarrow$	Boundary conditions $\Rightarrow$	Slip solutions $\Rightarrow$	Compatibility conditions $\Rightarrow$	Equations derived by considering compatibility conditions
2	$C_1 e^{\lambda_1 x_e} + C_2 e^{-\lambda_1 x_e} - C_e$	$\delta(x_e = 0) = 0$ $\delta(x_e = L_{tr}^e) = \delta_1$	**Eq. (B2):** $C_1 = \frac{(\delta_1 + C_e) - C_e e^{-\lambda_1 L_{tr}^e}}{2\sinh(\lambda_1 L_{tr}^e)}$ $C_2 = C_e - C_1$	$\frac{d\delta}{dx_e}(x_e = 0) = 0$ $\frac{d\delta}{dx_e}(x_e = L_{tr}^e) = \frac{d\delta}{dx_h}(x_h = 0)$	**Eq. (A4):** $L_{tr}^e = \left(\frac{1}{\lambda_1}\right)\left[\arccos\left(\frac{\delta_1 + C_e}{C_e}\right)\right]$ **Eq. (A5):** $\delta_i = A\sinh(\lambda_2 L_{tr}^h) + C_h\cosh(\lambda_2 L_{tr}^h) + \delta_1 - C_h$ where $A = \frac{\lambda_1}{\lambda_2}(C_1 e^{\lambda_1 L_{tr}^e} - C_2 e^{-\lambda_1 L_{tr}^e})$ **Eq. (A6):** $L_{tr} = L_{tr}^e + L_{tr}^h$ **Eq. (A7):** $\varepsilon_r^{cr} = C_3 e^{\lambda_2 L_{tr}^h} + C_4 e^{-\lambda_2 L_{tr}^h} - C_h + \delta_1$
	$C_3 e^{\lambda_2 x_h} + C_4 e^{-\lambda_2 x_h} - C_h + \delta_1$	$\delta(x_h = 0) = \delta_1$ $\delta(x_h = L_{tr}^h) = \delta_i$	**Eq. (B3):** $C_3 = \frac{(\delta_i - \delta_1) + C_h(1 - e^{-\lambda_2 L_{tr}^h})}{2\sinh(\lambda_2 L_{tr}^h)}$ $C_4 = C_h - C_3$		

Stage 3:

3	$C_1 e^{\lambda_1 x_e} + C_2 e^{-\lambda_1 x_e} - C_e$	$\delta(x_e = 0) = 0$ $\delta(x_e = L_{tr}^e) = \delta_1$	**Eq. (B2):** $C_1 = \frac{(\delta_1 + C_e) - C_e e^{-\lambda_1 L_{tr}^e}}{2\sinh(\lambda_1 L_{tr}^e)}$ $C_2 = C_e - C_1$	$\frac{d\delta}{dx_e}(x_e = 0) = 0$ $\frac{d\delta}{dx_e}(x_e = L_{tr}^e) = \frac{d\delta}{dx_h}(x_h = 0)$ $\frac{d\delta}{dx_h}(x_h = L_{tr}^h) = \frac{d\delta}{dx_p}(x_p = 0)$	**Eq. (A8):** $A\sinh(\lambda_2 L_{tr}^h) + C_h\cosh(\lambda_2 L_{tr}^h) = (\delta_2 - \delta_1) + C_h$ where $A = \frac{\lambda_1}{\lambda_2}(C_1 e^{\lambda_1 L_{tr}^e} - C_2 e^{-\lambda_1 L_{tr}^e})$ **Eq. (A9):** $\delta_i = C_p(L_{tr}^p)^2 + B \cdot L_{tr}^p + \delta_2$ where $B = \lambda_2(C_3 e^{\lambda_2 L_{tr}^h} - C_4 e^{-\lambda_2 L_{tr}^h})$ **Eq. (A10):** $L_{tr} = L_{tr}^e + L_{tr}^h + L_{tr}^p$ **Eq. (A11):** $\varepsilon_r^{cr} = C_p(L_{tr}^p)^2 + C_5 L_{tr}^p + C_6$
	$C_3 e^{\lambda_2 x_h} + C_4 e^{-\lambda_2 x_h} - C_h + \delta_1$	$\delta(x_h = 0) = \delta_1$ $\delta(x_h = L_{tr}^h) = \delta_2$	**Eq. (B4):** $C_3 = \frac{(\delta_2 - \delta_1) + C_h(1 - e^{-\lambda_2 L_{tr}^h})}{2\sinh(\lambda_2 L_{tr}^h)}$ $C_4 = C_h - C_3$		
	$C_p x_p^2 + C_5 x_p + C_6$	$\delta(x_p = 0) = \delta_2$ $\delta(x_p = L_{tr}^p) = \delta_i$	**Eq. (B5):** $C_5 = \frac{(\delta_i - \delta_2)}{L_{tr}^p} - C_p L_{tr}^p$ $C_6 = \delta_2$		

Annex 4A

Stage 4:

Stage	Slip functions $\delta(x)$ $\Rightarrow$	Boundary conditions $\Rightarrow$	Slip solutions $\Rightarrow$	Compatibility conditions $\Rightarrow$	Equations derived by considering compatibility conditions
4	$C_1 e^{\lambda_1 x_e} + C_2 e^{-\lambda_1 x_e} - C_e$	$\delta(x_e = 0) = 0$ $\delta(x_e = L_{tr}^e) = \delta_1$	**Eq. (B2):** $C_1 = \frac{(\delta_1 + C_e) - C_e e^{-\lambda_1 L_{tr}^e}}{2\sinh(\lambda_1 L_{tr}^e)}$ $C_2 = C_e - C_1$	$\frac{d\delta}{dx_e}(x_e = 0) = 0$ $\frac{d\delta}{dx_e}(x_e = L_{tr}^e) = \frac{d\delta}{dx_h}(x_h = 0)$ $\frac{d\delta}{dx_h}(x_h = L_{tr}^h) = \frac{d\delta}{dx_p}(x_p = 0)$ $\frac{d\delta}{dx_p}(x_p = L_{tr}^p) = \frac{d\delta}{dx_{so}}(x_{so} = 0)$	**Eq. (A12):** $C_p (L_{tr}^p)^2 + B \cdot L_{tr}^p = (\delta_3 - \delta_2)$ where $B = \lambda_2 (C_3 e^{\lambda_2 L_{tr}^h} - C_4 e^{-\lambda_2 L_{tr}^h})$ **Eq. (A13):** $\delta_i = C \cdot \sin(\gamma L_{tr}^s) - C_{so} \cos(\gamma L_{tr}^s) + \delta_3 - C_{so}$ where $C = \frac{1}{\gamma}(C_5 + 2C_p L_{tr}^p)$ **Eq. (A14):** $L_{tr} = L_{tr}^e + L_{tr}^h + L_{tr}^p + L_{tr}^{so}$ **Eq. (A15):** $\varepsilon_r^{cr} = C_7 \sin(\gamma L_{tr}^{so}) + C_8 \cos(\gamma L_{tr}^{so}) + C_{so} + \delta_3$
	$C_3 e^{\lambda_2 x_h} + C_4 e^{-\lambda_2 x_h} - C_h + \delta_1$	$\delta(x_h = 0) = \delta_1$ $\delta(x_h = L_{tr}^h) = \delta_2$	**Eq. (B4):** $C_3 = \frac{(\delta_2 - \delta_1) + C_h (1 - e^{-\lambda_2 L_{tr}^h})}{2\sinh(\lambda_2 L_{tr}^h)}$ $C_4 = C_h - C_3$		
	$C_p x_p^{\,2} + C_5 x_p + C_6$	$\delta(x_p = 0) = \delta_2$ $\delta(x_p = L_{tr}^p) = \delta_3$	**Eq. (B6):** $C_5 = \frac{(\delta_3 - \delta_2)}{L_{tr}^p} - C_p L_{tr}^p$ $C_6 = \delta_2$		
	$C_7 \sin(\gamma x_{so}) + C_8 \cos(\gamma x_{so}) + C_{so} + \delta_3$	$\delta(x_{so} = 0) = \delta_3$ $\delta(x_{so} = L_{tr}^s) = \delta_i$	**Eq. (B7):** $C_7 = \frac{(\delta_i - \delta_3) - C_{so}(\cos(\gamma L_{tr}^s) - 1)}{\sin(\gamma L_{tr}^s)}$ $C_8 = -C_{so}$		

Annex 4A

Stage 5:

Stage	Slip functions $\delta(x)$ $\Rightarrow$	Boundary conditions $\Rightarrow$	Slip solutions $\Rightarrow$	Compatibility conditions $\Rightarrow$	Equations derived by considering compatibility conditions
5	$C_1 e^{\lambda_1 x_e} + C_2 e^{-\lambda_1 x_e} - C_e$	$\delta(x_e = 0) = 0$ $\delta(x_e = L_{tr}^e) = \delta_1$	**Eq. (B2):** $C_1 = \frac{(\delta_1 + C_e) - C_e e^{-\lambda_1 L_{tr}^e}}{2\sinh(\lambda_1 L_{tr}^e)}$ $C_2 = C_e - C_1$	$\frac{d\delta}{dx_e}(x_e = 0) = 0$ $\frac{d\delta}{dx_e}(x_e = L_{tr}^e) = \frac{d\delta}{dx_h}(x_h = 0)$ $\frac{d\delta}{dx_h}(x_h = L_{tr}^h) = \frac{d\delta}{dx_p}(x_p = 0)$ $\frac{d\delta}{dx_p}(x_p = L_{tr}^p) = \frac{d\delta}{dx_{so}}(x_{so} = 0)$ $\frac{d\delta}{dx_{so}}(x_{so} = L_{tr}^{so}) = \frac{d\delta}{dx_f}(x_f = 0)$	**Eq. (A16):** $C \cdot \sin(\gamma L_{tr}^{so}) - C_{so}\cos(\gamma L_{tr}^{so}) = (\delta_4 - \delta_3) + C_{so}$ where $C = \frac{1}{\gamma}(C_5 + 2C_p L_{tr}^p)$ **Eq. (A17):** $\delta_i = C_f (L_{tr}^f)^2 + D \cdot L_{tr}^f + \delta_4$ where $D = \gamma(C_7 \cos(\gamma L_{tr}^{so}) - C_8 \sin(\gamma L_{tr}^{so}))$ **Eq. (A18):** $L_{tr} = L_{tr}^e + L_{tr}^h + L_{tr}^p + L_{tr}^{so} + L_{tr}^f$ **Eq. (A19):** $\varepsilon_r^{cr} = C_f (L_{tr}^f)^2 + C_9 L_{tr}^f + C_{10}$
	$C_p x_p^2 + C_5 x_p + C_6$	$\delta(x_p = 0) = \delta_2$ $\delta(x_p = L_{tr}^p) = \delta_3$	**Eq. (B6):** $C_5 = \frac{(\delta_3 - \delta_2)}{L_{tr}^p} - C_p L_{tr}^p$ $C_6 = \delta_2$		
	$C_7 \sin(\gamma x_{so}) + C_8 \cos(\gamma x_{so}) + C_{so} + \delta_3$	$\delta(x_{so} = 0) = \delta_3$ $\delta(x_{so} = L_{tr}^{so}) = \delta_4$	**Eq. (B8):** $C_7 = \frac{(\delta_4 - \delta_3) - C_{so}(\cos(\gamma L_{tr}^{so}) - 1)}{\sin(\gamma L_{tr}^{so})}$ $C_8 = -C_{so}$		
	$C_f x_f^2 + C_9 x_f + C_{10}$	$\delta(x_f = 0) = \delta_4$ $\delta(x_f = L_{tr}^f) = \delta_i$	**Eq. (B9):** $C_9 = \frac{(\delta_i - \delta_4)}{L_{tr}^f} - C_p L_{tr}^f$ $C_{10} = \delta_4$		

Notice: δ_i is the value of imposed slip at loaded end of the bond length, L_{tr}

Annex 4A

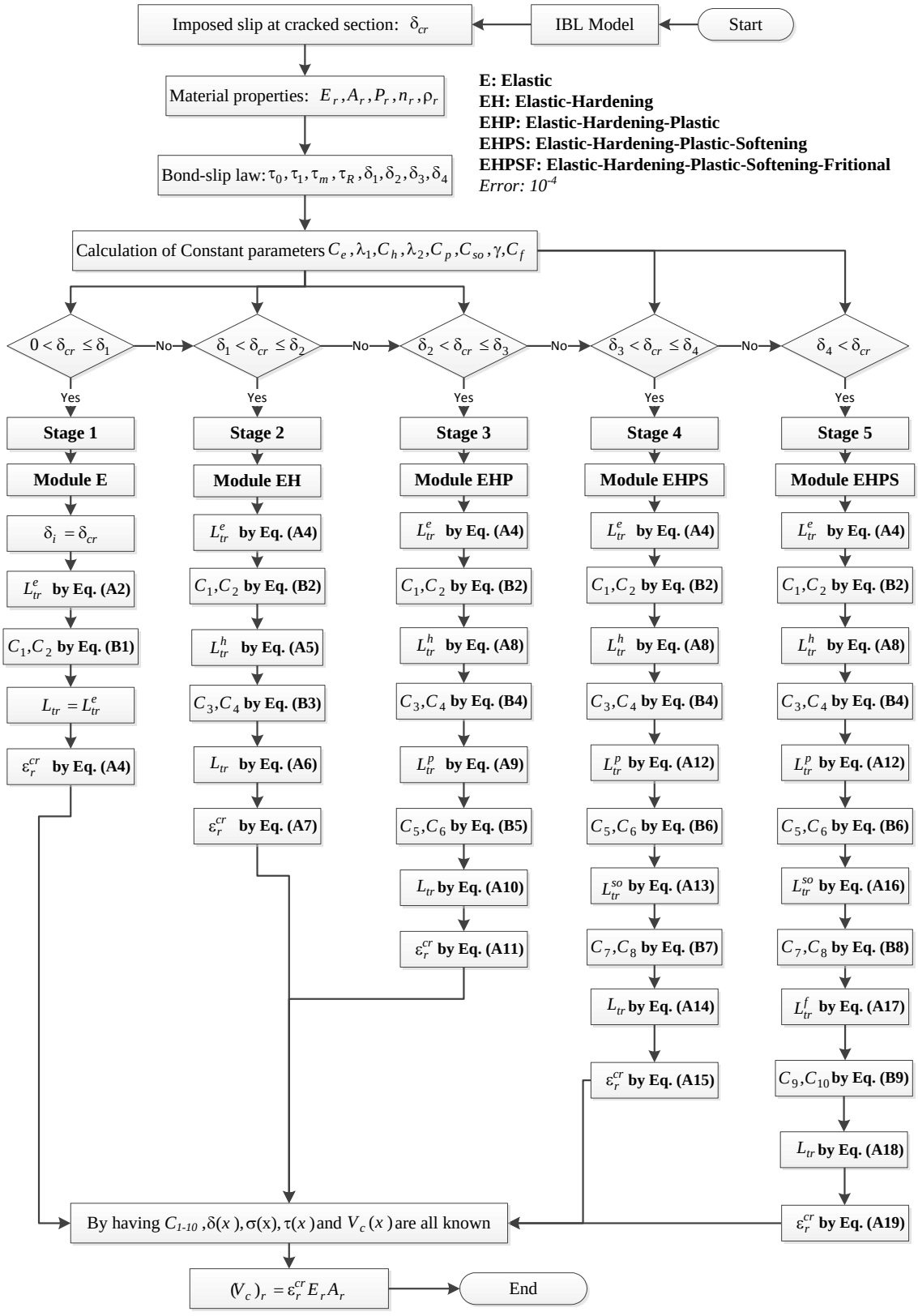

Figure 4A. 1: Algorithm of IBL model

Annex 4B

Definition:

Governing equation: $\frac{d^2\delta(x)}{dx^2} = J_r \cdot \tau(\delta(x))$ where $J_r = \frac{P_r}{E_r A_r}(1 + n_r \rho_r)$, $n_r = \frac{E_r}{E_c}$ and $\rho_r = \frac{A_r}{A_c}$; $\sigma_r(x) = E_r \frac{d\delta(x)}{dx}$; $\tau(x) = \frac{1}{J_r}\frac{d^2\delta(x)}{dx^2}$

(subscript "*r*" is for reinforcing bars, either FRP or steel bar)

Some constant parameters during the analysis:

$C_e = \frac{\tau_1 J_r}{\lambda_1^2}$; $\lambda_1 = \sqrt{\frac{(\tau_1 - \tau_0)}{\delta_1} J_r}$; $C_h = \frac{\tau_m J_r}{\lambda_2^2}$; $\lambda_2 = \sqrt{\frac{(\tau_m - \tau_1)}{(\delta_2 - \delta_1)} J_r}$; $C_p = \frac{\tau_m J_r}{2}$; $C_{so} = \frac{\tau_m J_r}{\gamma^2}$; $\gamma = \sqrt{\frac{(\tau_m - \tau_R)}{(\delta_4 - \delta_3)} J_r}$; $C_f = \frac{\tau_R J_r}{2}$

Stage 1:

Stage	Slip functions $\delta(x)$ $\Rightarrow$	Boundary conditions $\Rightarrow$	Slip solutions $\Rightarrow$	Compatibility conditions $\Rightarrow$	Equations derived by considering compatibility conditions
1	$C_1 e^{\lambda_1 x_e} + C_2 e^{-\lambda_1 x_e} - C_e$	$\delta(x_e = 0) = 0$ $\delta(x_e = L_{tr}^e) = \delta_i$	**Eq. (B1):** $C_1 = \frac{(\delta_i + C_e) - C_e e^{-\lambda_1 L_{tr}^e}}{2\sinh(\lambda_1 L_{tr}^e)}$ $C_2 = C_e - C_1$	-	**Eq. (A1):** $L_{tr}^e = L_b$ **Eq. (A2):** $\varepsilon_r^m = \lambda_1 (C_1 - C_2)$ **Eq. (A3):** $\varepsilon_r^{cr} = C_1 e^{\lambda_1 L_{tr}^e} + C_2 e^{-\lambda_1 L_{tr}^e} - C_e$

Annex 4B

Stage 2:

Stage	Slip functions $\delta(x)$ $\Rightarrow$	Boundary conditions $\Rightarrow$	Slip solutions $\Rightarrow$	Compatibility conditions $\Rightarrow$	Equations derived by considering compatibility conditions
2	$C_1 e^{\lambda_1 x_e} + C_2 e^{-\lambda_1 x_e} - C_e$	$\delta(x_e = 0) = 0$ $\delta(x_e = L_{tr}^e) = \delta_1$	**Eq. (B2):** $C_1 = \frac{(\delta_1 + C_e) - C_e e^{-\lambda_1 L_{tr}^e}}{2\sinh(\lambda_1 L_{tr}^e)}$ $C_2 = C_e - C_1$	$\frac{d\delta}{dx_e}(x_e = L_{tr}^e) = \frac{d\delta}{dx_h}(x_h = 0)$	**Eq. (A2):** $\varepsilon_r^m = \lambda_1 (C_1 - C_2)$ **Eq. (A4):** $L_{tr}^h = L_b - L_{tr}^e$ **Eq. (A5):** $\delta_i = A \sinh(\lambda_2 L_{tr}^h) + C_h \cosh(\lambda_2 L_{tr}^h) + \delta_1 - C_h$ where $A = \frac{\lambda_1}{\lambda_2}(C_1 e^{\lambda_1 L_{tr}^e} - C_2 e^{-\lambda_1 L_{tr}^e})$ **Eq. (A6):** $\varepsilon_r^{cr} = C_3 e^{\lambda_2 L_{tr}^h} + C_4 e^{-\lambda_2 L_{tr}^h} - C_h + \delta_1$
	$C_3 e^{\lambda_2 x_h} + C_4 e^{-\lambda_2 x_h} - C_h + \delta_1$	$\delta(x_h = 0) = \delta_1$ $\delta(x_h = L_{tr}^h) = \delta_i$	**Eq. (B3):** $C_3 = \frac{(\delta_i - \delta_1) + C_h (1 - e^{-\lambda_2 L_{tr}^h})}{2\sinh(\lambda_2 L_{tr}^h)}$ $C_4 = C_h - C_3$		

Stage 3:

3	$C_1 e^{\lambda_1 x_e} + C_2 e^{-\lambda_1 x_e} - C_e$	$\delta(x_e = 0) = 0$ $\delta(x_e = L_{tr}^e) = \delta_1$	**Eq. (B2):** $C_1 = \frac{(\delta_1 + C_e) - C_e e^{-\lambda_1 L_{tr}^e}}{2\sinh(\lambda_1 L_{tr}^e)}$ $C_2 = C_e - C_1$	$\frac{d\delta}{dx_e}(x_e = L_{tr}^e) = \frac{d\delta}{dx_h}(x_h = 0)$ $\frac{d\delta}{dx_h}(x_h = L_{tr}^h) = \frac{d\delta}{dx_p}(x_p = 0)$	**Eq. (A2):** $\varepsilon_r^m = \lambda_1 (C_1 - C_2)$ **Eq. (A7):** $A \sinh(\lambda_2 L_{tr}^h) + C_h \cosh(\lambda_2 L_{tr}^h) = (\delta_2 - \delta_1) + C_h$ where $A = \frac{\lambda_1}{\lambda_2}(C_1 e^{\lambda_1 L_{tr}^e} - C_2 e^{-\lambda_1 L_{tr}^e})$ **Eq. (A8):** $L_{tr}^p = L_b - L_{tr}^e - L_{tr}^h$ **Eq. (A9):** $\delta_i = C_p (L_{tr}^p)^2 + B \cdot L_{tr}^p + \delta_2$ where $B = \lambda_2 (C_3 e^{\lambda_2 L_{tr}^h} - C_4 e^{-\lambda_2 L_{tr}^h})$ **Eq. (A10):** $\varepsilon_r^{cr} = C_p (L_{tr}^p)^2 + C_5 L_{tr}^p + C_6$
	$C_3 e^{\lambda_2 x_h} + C_4 e^{-\lambda_2 x_h} - C_h + \delta_1$	$\delta(x_h = 0) = \delta_1$ $\delta(x_h = L_{tr}^h) = \delta_2$	**Eq. (B4):** $C_3 = \frac{(\delta_2 - \delta_1) + C_h (1 - e^{-\lambda_2 L_{tr}^h})}{2\sinh(\lambda_2 L_{tr}^h)}$ $C_4 = C_h - C_3$		
	$C_p x_p^2 + C_5 x_p + C_6$	$\delta(x_p = 0) = \delta_2$ $\delta(x_p = L_{tr}^p) = \delta_i$	**Eq. (B5):** $C_5 = \frac{(\delta_i - \delta_2)}{L_{tr}^p} - C_p L_{tr}^p$ $C_6 = \delta_2$		

Annex 4B

Stage 4:

Stage	Slip functions $\delta(x)$ $\Rightarrow$	Boundary conditions $\Rightarrow$	Slip solutions $\Rightarrow$	Compatibility conditions $\Rightarrow$	Equations derived by considering compatibility conditions
4	$C_1 e^{\lambda_1 x_e} + C_2 e^{-\lambda_1 x_e} - C_e$	$\delta(x_e = 0) = 0$ $\delta(x_e = L_{tr}^e) = \delta_1$	**Eq. (B2):** $C_1 = \frac{(\delta_1 + C_e) - C_e e^{-\lambda_1 L_{tr}^e}}{2\sinh(\lambda_1 L_{tr}^e)}$ $C_2 = C_e - C_1$	$\frac{d\delta}{dx_e}(x_e = L_{tr}^e) = \frac{d\delta}{dx_h}(x_h = 0)$ $\frac{d\delta}{dx_h}(x_h = L_{tr}^h) = \frac{d\delta}{dx_p}(x_p = 0)$ $\frac{d\delta}{dx_p}(x_p = L_{tr}^p) = \frac{d\delta}{dx_{so}}(x_{so} = 0)$	**Eq. (A2):** $\varepsilon_r^m = \lambda_1 (C_1 - C_2)$ **Eq. (A7):** $A \sinh(\lambda_2 L_{tr}^h) + C_h \cosh(\lambda_2 L_{tr}^h) = (\delta_2 - \delta_1) + C_h$ where $A = \frac{\lambda_1}{\lambda_2}(C_1 e^{\lambda_1 L_{tr}^e} - C_2 e^{-\lambda_1 L_{tr}^e})$ **Eq. (A11):** $C_p (L_{tr}^p)^2 + B \cdot L_{tr}^p = (\delta_3 - \delta_2)$ where $B = \lambda_2 (C_3 e^{\lambda_2 L_{tr}^h} - C_4 e^{-\lambda_2 L_{tr}^h})$ **Eq. (A12):** $L_{tr}^{so} = L_b - L_{tr}^e - L_{tr}^h - L_{tr}^p$ **Eq. (A13):** $\delta_i = C \cdot \sin(\gamma L_{tr}^s) - C_{so} \cos(\gamma L_{tr}^s) + \delta_3 - C_{so}$ where $C = \frac{1}{\gamma}(C_5 + 2C_p L_{tr}^p)$ **Eq. (A14):** $\varepsilon_r^{cr} = C_7 \sin(\gamma L_{tr}^{so}) + C_8 \cos(\gamma L_{tr}^{so}) + C_{so} + \delta_3$
	$C_3 e^{\lambda_2 x_h} + C_4 e^{-\lambda_2 x_h} - C_h + \delta_1$	$\delta(x_h = 0) = \delta_1$ $\delta(x_h = L_{tr}^h) = \delta_2$	**Eq. (B4):** $C_3 = \frac{(\delta_2 - \delta_1) + C_h (1 - e^{-\lambda_2 L_{tr}^h})}{2\sinh(\lambda_2 L_{tr}^h)}$ $C_4 = C_h - C_3$		
	$C_p x_p^{\,2} + C_5 x_p + C_6$	$\delta(x_p = 0) = \delta_2$ $\delta(x_p = L_{tr}^p) = \delta_3$	**Eq. (B6):** $C_5 = \frac{(\delta_3 - \delta_2)}{L_{tr}^p} - C_p L_{tr}^p$ $C_6 = \delta_2$		
	$C_7 \sin(\gamma x_{so}) + C_8 \cos(\gamma x_{so}) + C_{so} + \delta_3$	$\delta(x_{so} = 0) = \delta_3$ $\delta(x_{so} = L_{tr}^s) = \delta_i$	**Eq. (B7):** $C_7 = \frac{(\delta_i - \delta_3) - C_{so}(\cos(\gamma L_{tr}^s) - 1)}{\sin(\gamma L_{tr}^s)}$ $C_8 = -C_{so}$		

Annex 4B

Stage 5:

Stage	Slip functions $\delta(x)$ $\Rightarrow$	Boundary conditions $\Rightarrow$	Slip solutions $\Rightarrow$	Compatibility conditions $\Rightarrow$	Equations derived by considering compatibility conditions
5	$C_1 e^{\lambda_1 x_e} + C_2 e^{-\lambda_1 x_e} - C_e$	$\delta(x_e = 0) = 0$ $\delta(x_e = L_{tr}^e) = \delta_1$	**Eq. (B2):** $C_1 = \frac{(\delta_1 + C_e) - C_e e^{-\lambda_1 L_{tr}^e}}{2\sinh(\lambda_1 L_{tr}^e)}$ $C_2 = C_e - C_1$	$\frac{d\delta}{dx_e}(x_e = L_{tr}^e) = \frac{d\delta}{dx_h}(x_h = 0)$ $\frac{d\delta}{dx_h}(x_h = L_{tr}^h) = \frac{d\delta}{dx_p}(x_p = 0)$ $\frac{d\delta}{dx_p}(x_p = L_{tr}^p) = \frac{d\delta}{dx_{so}}(x_{so} = 0)$ $\frac{d\delta}{dx_{so}}(x_{so} = L_{tr}^{so}) = \frac{d\delta}{dx_f}(x_f = 0)$	**Eq. (A2):** $\varepsilon_r^m = \lambda_1 (C_1 - C_2)$ **Eq. (A7):** $A\sinh(\lambda_2 L_{tr}^h) + C_h \cosh(\lambda_2 L_{tr}^h) = (\delta_2 - \delta_1) + C_h$ where $A = \frac{\lambda_1}{\lambda_2}(C_1 e^{\lambda_1 L_{tr}^e} - C_2 e^{-\lambda_1 L_{tr}^e})$ **Eq. (A11):** $C_p (L_{tr}^p)^2 + B \cdot L_{tr}^p = (\delta_3 - \delta_2)$ where $B = \lambda_2 (C_3 e^{\lambda_2 L_{tr}^h} - C_4 e^{-\lambda_2 L_{tr}^h})$ **Eq. (A15):** $C \cdot \sin(\gamma L_{tr}^{so}) - C_{so}\cos(\gamma L_{tr}^{so}) = (\delta_4 - \delta_3) + C_{so}$ where $C = \frac{1}{\gamma}(C_5 + 2C_p L_{tr}^p)$ **Eq. (A16):** $L_{tr}^f = L_b - L_{tr}^e - L_{tr}^h - L_{tr}^p - L_{tr}^{so}$ **Eq. (A17):** $\delta_i = C_f (L_{tr}^f)^2 + D \cdot L_{tr}^f + \delta_4$ where $D = \gamma(C_7 \cos(\gamma L_{tr}^{so}) - C_8 \sin(\gamma L_{tr}^{so}))$ **Eq. (A18):** $\varepsilon_r^{cr} = C_f (L_{tr}^f)^2 + C_9 L_{tr}^f + C_{10}$
	$C_7 \sin(\gamma x_{so}) + C_8 \cos(\gamma x_{so}) + C_{so} + \delta_3$	$\delta(x_{so} = 0) = \delta_3$ $\delta(x_{so} = L_{tr}^{so}) = \delta_4$	**Eq. (B8):** $C_7 = \frac{(\delta_4 - \delta_3) - C_{so}(\cos(\gamma L_{tr}^{so}) - 1)}{\sin(\gamma L_{tr}^{so})}$ $C_8 = -C_{so}$		
	$C_f x_f^{\,2} + C_9 x_f + C_{10}$	$\delta(x_f = 0) = \delta_4$ $\delta(x_f = L_{tr}^f) = \delta_i$	**Eq. (B9):** $C_9 = \frac{(\delta_i - \delta_4)}{L_{tr}^f} - C_p L_{tr}^f$ $C_{10} = \delta_4$		

Notice: δ_i is the value of imposed slip at loaded end of the bond length, L_{tr}

Annex 4B

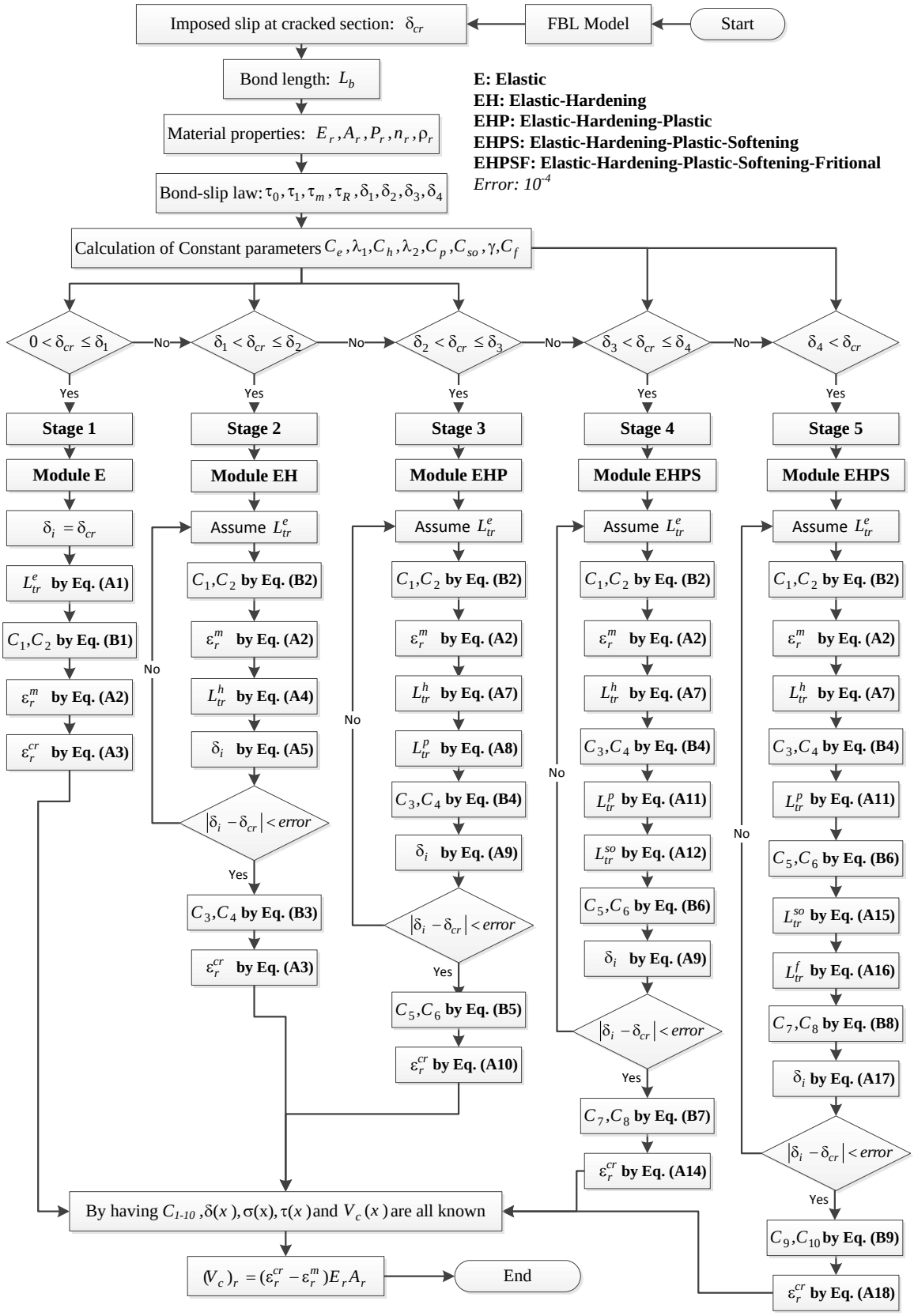

Figure 4B. 1: Algorithm of FBL model

Annex 4B

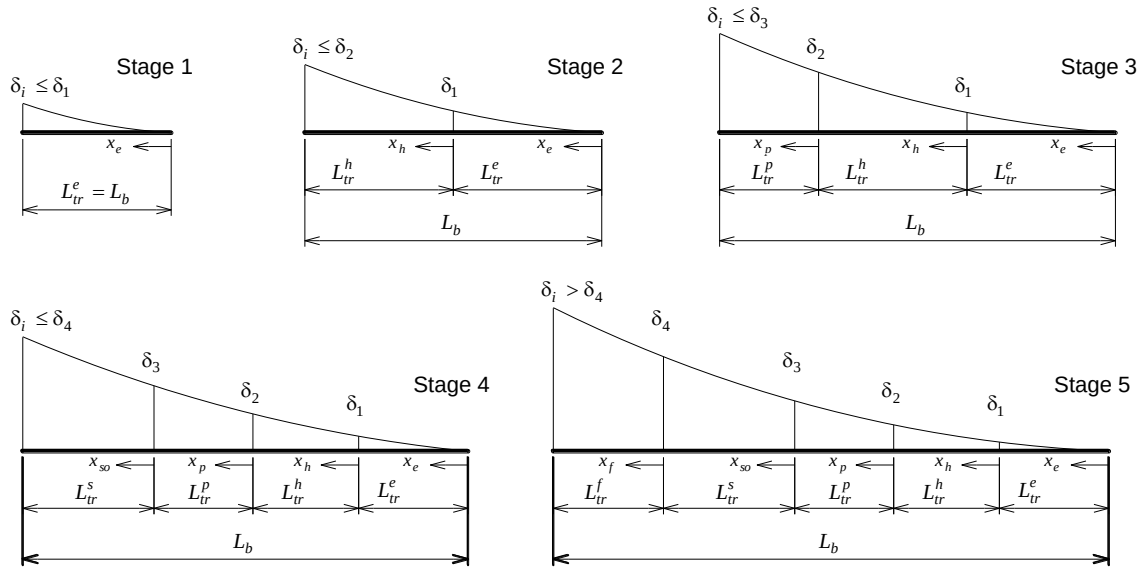

Figure 4B. 2: Schematic illustration of the reference coordinate system, as well as the transferred bond length of each bond phases

Annex 5A

Calculation of d_{fr}

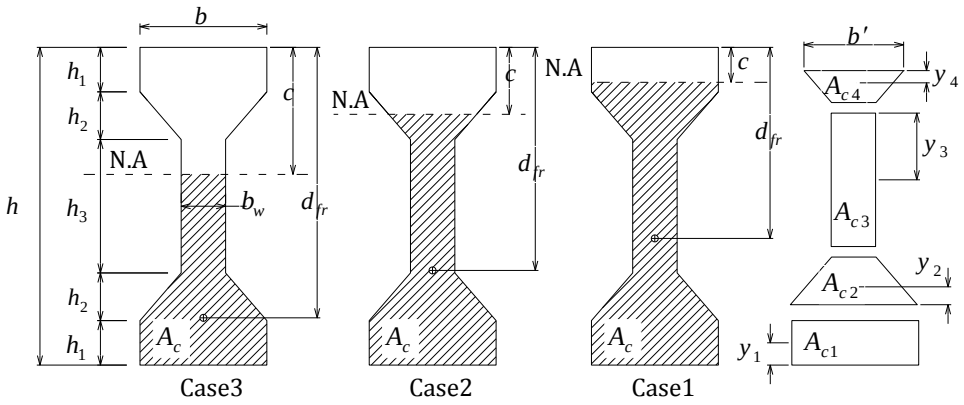

Case 1:

$$y_1 = \frac{h_1}{2}, y_2 = \frac{h_2}{2}\left(\frac{2b_w + b}{b_w + b}\right), y_3 = \frac{h_3}{2}, y_4 = \frac{h_2}{3}\left(\frac{2b_w + b'}{b_w + b'}\right) \tag{A-1}$$

$$A_{c1} = bh_1, A_{c2} = \frac{h_2}{2}(b + b_w), A_{c3} = b_w h_3, A_{c4} = \frac{h_2}{2}(b' + b_w), A_{c5} = b(h - c) \tag{A-2}$$

$$d_{fr} = \frac{A_{c1}y_1 + A_{c2}h + A_{c3}(h_1 + h_2 + y_3) + A_{c5}\left(h - \frac{1}{2}(h_1 - c)\right)}{A_{c1} + 2A_{c2} + A_{c3} + A_{c5}} \tag{A-3}$$

Case 2:

$$b' = \frac{(b - b_w)(h_1 + h_2 - c)}{h_2} + b_w \tag{A-4}$$

$$d_{fr} = \frac{A_{c1}y_1 + A_{c2}(h_1 + y_2) + A_{c3}(h_1 + h_2 + y_3) + A_{c4}(h - c - y_4)}{A_{c1} + A_{c2} + A_{c3} + A_{c4}} \tag{A-5}$$

Case 3:

$$A_{c3} = (h_1 + h_2 + h_3 - c)b_w \tag{A-6}$$

$$y_3 = \frac{1}{2}(h_1 + h_2 + h_3 - c) \tag{A-7}$$

$$d_{fr} = \frac{A_{c1}y_1 + A_{c2}(h_1 + y_2) + A_{c3}(h_1 + h_2 + y_3)}{A_{c1} + A_{c2} + A_{c3}} \tag{A-8}$$

Annex 5B

Algorithm to calculate the nominal shear strength (V_n)

Start

Material properties

$$\left\{\left(E_f,\varepsilon_{fu},\varepsilon_f^{pre},A_f\right),\left(E_s,\varepsilon_{sy},\varepsilon_s^{pre},A_s\right),\left(\sigma_{ct}^{cr}-w_{cr},f_{ct},E_c,w_a,\tau_{cr}^{\max}\right)\right\}$$

Geometry

$$\{b,b_w,h_1,h_2,h_3,h,S,a,d_s,d_f\}$$

Definition of some parameters

$$\{\beta_1,S_{cr},\alpha,\varphi,\beta,w_0,w_u\}$$

Loop 1: $c_v:\left(h_1+h_2\right)$ to $0.05\left(h_1+h_2\right)$

Loop 2: $w_{cr}:w_0$ to w_u

$$l_{cr,w}=\left(h_1+h_2+h_3-c\right)\csc\alpha,\quad l_{cr,fl}=\left(h_1+h_2\right)\csc\alpha,\quad l_{cr}=l_{cr,w}+l_{cr,fl}$$

$$l_v=\left(w_a/w_{cr}\right)l_{cr,w}$$

$$\omega(\varphi)=\left(1+\tan\varphi\right)^{-1}$$

Loop 3: $x:0$ to l_{cr}

$$w(x)=\begin{cases}\dfrac{w_{cr}}{l_{cr,w}}\cdot x & 0\le x\le l_{cr,w}\\ w_{cr}-\dfrac{(1-\beta_3)w_{cr}}{l_{cr,fl}}\left(x-l_{cr,w}\right) & l_{cr,w}<x\le l_{cr}\end{cases}$$

$$\sigma_{ct}^{cr}(w(x))=\begin{cases}\omega\cdot\sigma_{ct}^{cr}(w(x)) & w(x)\le w_a\\ \sigma_{ct}^{cr}(w(x)) & w(x)>w_a\end{cases}$$

$$d_{fr}=c_v+\frac{\int_0^{l_{cr}}\omega\sigma_{ct}^{cr}(w(x))x\,dx}{\int_0^{l_{cr}}\omega\sigma_{ct}^{cr}(w(x))\,dx}\sin\alpha$$

End loop 3

$$F_{fr,n}=b_w\int_0^{l_{cr}}\omega\sigma_{ct}^{cr}(w(x))\,dx,\quad F_{fr,v}=\begin{cases}\tau_{cr}^{\max}b_w\,l_v & w(x)\le w_a\\ F_{fr,n}\tan\varphi & w(x)>w_a\end{cases}$$

$$\delta_s=\frac{1}{2}w\left(x_s=\left(d_s-c_v\right)\csc\alpha\right),\quad \delta_f=\frac{1}{2}w\left(x_f=\left(d_f-c_v\right)\csc\alpha\right)$$

$$\varepsilon_s=\frac{\delta_s}{S_{cr}},\ \varepsilon_f=\frac{\delta_f}{S_{cr}}$$ (assuming linear distribution of slip between two consecutive crack)

$$F_f=\left(\varepsilon_f+\varepsilon_f^{pre}\right)E_f\rho_f bd_f=\left(\varepsilon_f+\varepsilon_f^{pre}\right)E_fA_f$$

$$F_s=\begin{cases}\left(\varepsilon_s+\varepsilon_s^{pre}\right)E_s\rho_s bd_s=\left(\varepsilon_s+\varepsilon_s^{pre}\right)E_sA_s & \varepsilon_s\le\varepsilon_{sy}-\varepsilon_s^{pre}\\ f_{sy}\rho_s bd_s=f_{sy}A_s & \varepsilon_s>\varepsilon_{sy}-\varepsilon_s^{pre}\end{cases}$$

$$V_n=F_{fr,n}\cos\alpha+F_{fr,v}\sin\alpha$$

$$M_1=F_f\left(d_f-\frac{\beta_1c_v}{2}\right)+F_s\left(d_s-\frac{\beta_1c_v}{2}\right)+F_{fr,n}\left(d_{fr}-\frac{\beta_1c_v}{2}\right)$$

$$M_2=V_n\left(a-c_v\cot\alpha\right)$$

$$\Delta M=\left|M_1-M_2\right|$$ (If variation less than 0.1kN.m then break)

End loop 2

$$F_1=F_{fr}\sin(\alpha-\varphi)+F_f+F_s$$

$$F_2=(\beta_1c_v)(\beta_2b)f_c'$$

$$\Delta F=\left|F_1-F_2\right|$$ (If variation is less than 0.1kN then break)

End loop 1

Annex 5C

Calculation of primary crack spacing (S_{cr})

Start

Material properties

$$\left\{\left(E_f,\varepsilon_{fu},\varepsilon_f^{pre},A_f\right),\left(E_s,\varepsilon_{sy},\varepsilon_s^{pre},A_s\right),\left(\sigma_{fr}-w_{cr},\varepsilon_{cr},E_c\right)\right\}$$

Geometry

$$\left\{b,b_w,h_1,h_2,h_3,h,d_s,d_f,d_f',\phi_f,A_g,I_g\right\}$$

Bond-slip parameters

$$\left\{\left(\tau_0,\tau_1,\tau_m,\delta_1,\delta_2\right)_{FRP},\left(\tau_0,\tau_1,\tau_m,\delta_1,\delta_2\right)_{steel}\right\}$$

Defined some paramters

$$\left\{M_n,\beta_4\right\}$$

Calculation of the cracking moment

$$N_{ps}=\varepsilon_s^{pre}E_sA_s,\quad N_{pf}=\varepsilon_f^{pre}E_fA_f$$

$$M_{ps}=N_{ps}(d_s-h/2),\quad M_{pf}=N_{pf}(d_f-h/2)$$

$$\sigma_c^{pre}=\frac{N_{ps}+N_{pf}}{A_g}+\frac{M_{ps}h}{2I_g}+\frac{M_{pf}h}{2I_g}$$

$$M_{cr}=\frac{2(f_{ct}+\sigma_c^{pre})I_g}{h}\quad c\cong\left(\frac{M_n}{\beta_4M_{cr}}\right)c_n\geq\tfrac{1}{2}h$$

Loop 2: w_f : 0.01 to 0.2

$$\delta_f=\tfrac{1}{2}w_f,\ \delta_s=\left(\frac{d_s-c}{d_f-c}\right)\delta_f$$

V_f, $L_{b,f}$ is calculated calling IBL Model for FRP bars

V_s, $L_{b,s}$ is calculated calling IBL Model for FRP bars

$$A_{p1}=2.5\left(h-d_{eff}\right)$$

$$\varepsilon_{ct1}=\frac{V_s+V_f}{E_cA_{p1}}+\frac{\bar{\sigma}_{fr}(\delta_s+\delta_f)}{E_c}$$ (If the strain reaches its cracking strain then break)

End loop 2

$$S_{cr,1}=\max(L_{b,s},L_{b,f})$$

Loop 2: w_f : 0.01 to 0.2

$$\delta_f=\tfrac{1}{2}w_f$$

V_f, L_b is calculated calling IBL Model

$$A_{p2}=\min\left\{2.5\left(d_f'+\phi_f/2\right),2.5\left(h-d_f\right)\right\}$$

$$\varepsilon_{ct2}=\frac{V_f}{E_cA_{p2}}+\frac{\bar{\sigma}_{fr}(w_f)}{E_c}$$ (If the strain reaches its cracking strain then break)

End loop 2

$$S_{cr,1}=L_{b,f}$$

$$S_{cr}=\min\left\{S_{cr,1},S_{cr,2}\right\}$$

Annex 5D

Calculation of applied moment versus crack width ($M_a - w_f$)

Start

Material properties

$\{(E_f, \varepsilon_{fu}, \varepsilon_f^{pre}, A_f), (E_s, \varepsilon_{sy}, \varepsilon_s^{pre}, A_s), (\sigma_{ct}^{cr} - w_{cr}, f_{ct}, E_c, f_c')\}$

Geometry

$\{b, b_w, h_1, h_2, h_3, h, d_s, d_f\}$

Bond-slip parameters

$\{(\tau_0, \tau_1, \tau_m, \delta_1, \delta_2)_{FRP}, (\tau_0, \tau_1, \tau_m, \delta_1, \delta_2)_{steel}\}$

Definition of some parameters

$\{S_{cr}, w_0, w_u\}$

Loop 1: $w_{cr} : w_0$ to w_u

Loop 2: $c : 0.1$ to $\frac{1}{2}h$

$w_f = [(d_f - c)/(h - c)]w_{cr}$, $\delta_f = \frac{1}{2}w_f$ %% Calculation of tensile force in FRP bars

ε_f *is calculated by calling FBL Model for FRP bars*

$F_f = (\varepsilon_f + \varepsilon_f^{pre})E_f \rho_f b d_f = (\varepsilon_f + \varepsilon_f^{pre})E_f A_f$

$w_s = [(d_s - c)/(d_f - c)]w_f$, $\delta_s = \frac{1}{2}w_s$ %% Calculation of tensile force in steel strand

ε_s *is calculated by calling FBL Model for steel strand*

$$F_s = \begin{cases} (\varepsilon_s + \varepsilon_s^{pre})E_s \rho_s b d_s = (\varepsilon_s + \varepsilon_s^{pre})E_s A_s & \varepsilon_s \le \varepsilon_{sy} - \varepsilon_s^{pre} \\ f_{sy} \rho_s b d_s = f_{sy} A_s & \varepsilon_s > \varepsilon_{sy} - \varepsilon_s^{pre} \end{cases}$$

$D_c = [c/(h - c)]w_{cr}$, $\varepsilon_c = D_c / S_{cr}$ %% Calculation of tensile and compressive force of HPFRC

$D_{cp} \cong \varepsilon_{cp} S_{cr}$, $D_{cr} = (f_{ct}/E_c)S_{cr}$

$$b(y) = \begin{cases} b & y \le h_1 \\ b - (b - b_w)y/h_2 & h_1 < y \le h_2 \\ b_w & h_2 < y < h \end{cases}$$

Loop 3: $y : 0$ to $(h - c)$

$w(y) = w_{cr} - w_{cr}/(h - c)y$

$$\sigma_{ct}(w(y)) = \begin{cases} E_c \cdot w(y)/S_{cr} & w(y) \le D_{cr} \\ \sigma_{ct}^{cr}(w(y)) & w(y) > D_{cr} \end{cases}$$

$F_{fr} = \int_0^{(h-c)} b(y)\sigma_{ct}(w(y))dy$

$d_{fr} = h - \left(\int_0^{(h-c)} \sigma_{ct}(w(y_t))y_t dy_t\right) / \left(\int_0^{(h-c)} \sigma_{ct}(w(y_t))dy_t\right)$

End loop 3

Loop 4: $y : 0$ to c

$D_c(y) = D_c - (D_c/c)y$

$$\sigma_c(D_c(y)) = \begin{cases} f_c' & D_c(y) > D_{cp} \\ E_c D_c(y) & D_c(y) \le D_{cp} \end{cases}$$

$F_c = \int_0^c b(y)\sigma_c(y)dy$

$d_c = \left(\int_0^c \sigma_c(y_c)y_c dy_c\right) / \left(\int_0^c \sigma_c(y_c)dy_c\right)$

End loop 3

$\Delta F = |F_c - (F_s + F_f + F_{fr})|$ (If variation is less than 0.1kN then break)

End loop 2

$M_a = (d_s - c)F_s + (d_f - c)F_f + (d_{fr} - c)F_{fr} + (c - d_c)F_c$

End loop 1

Annex 5E

Photos from the failure of the tested beams in Chapter 5

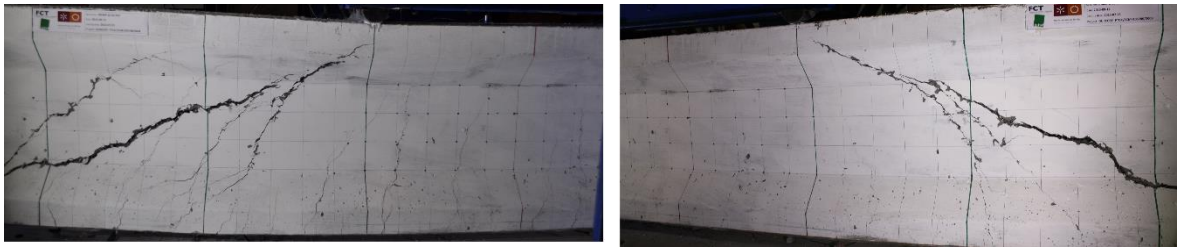

IB1

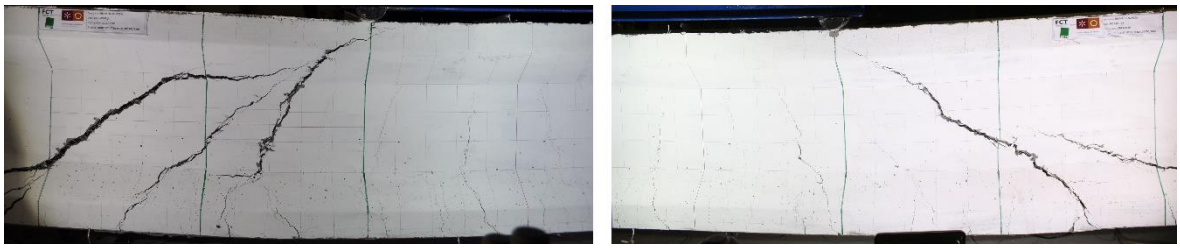

IB2

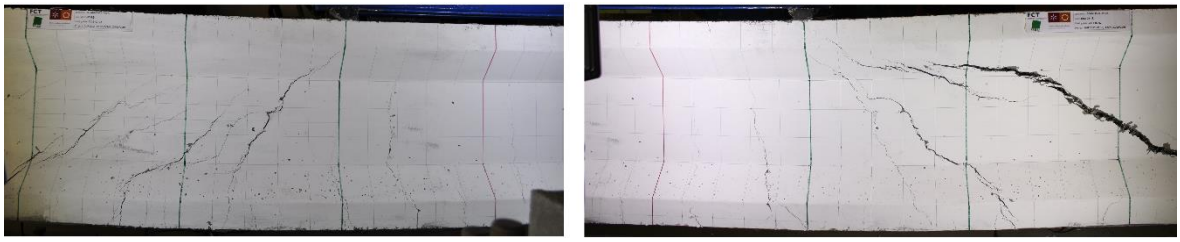

IB3

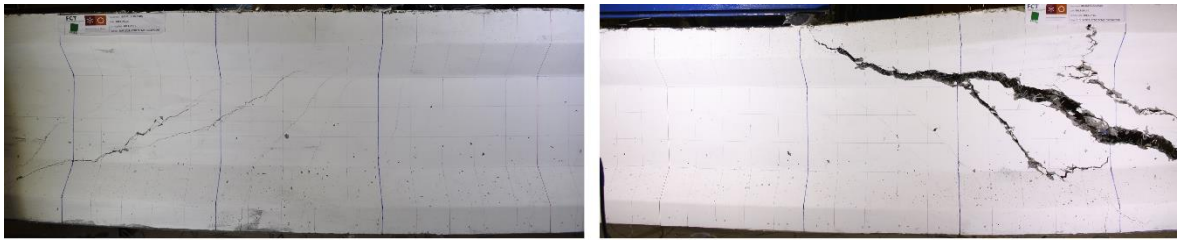

IB4

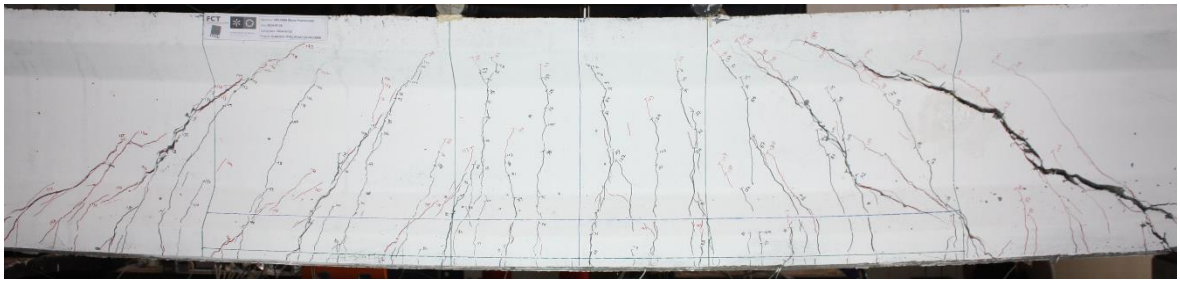

IB5

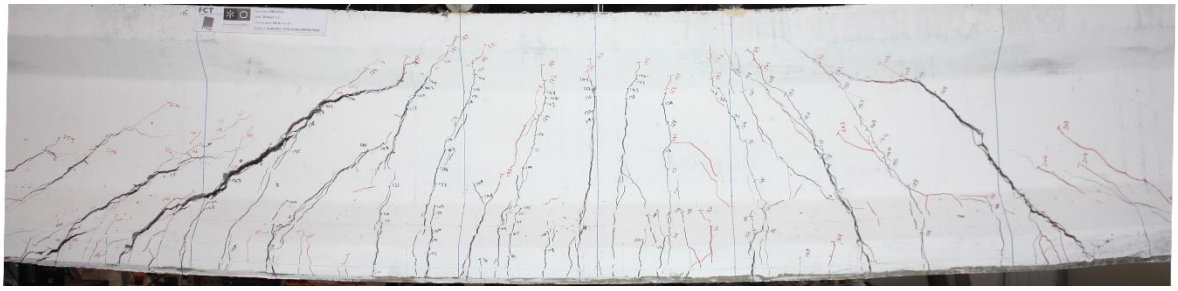

IB6

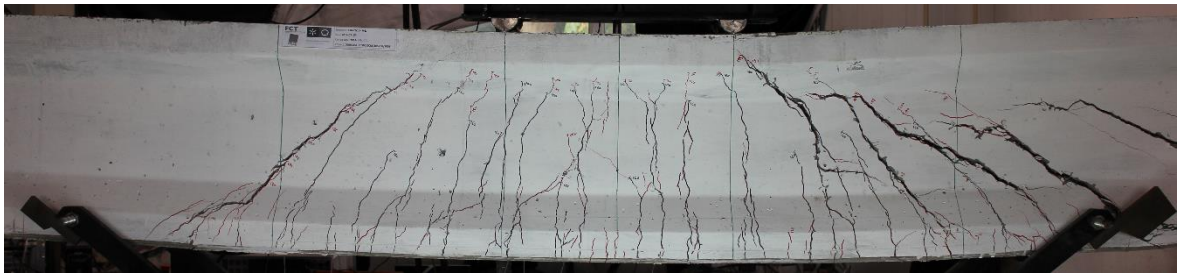

IB7

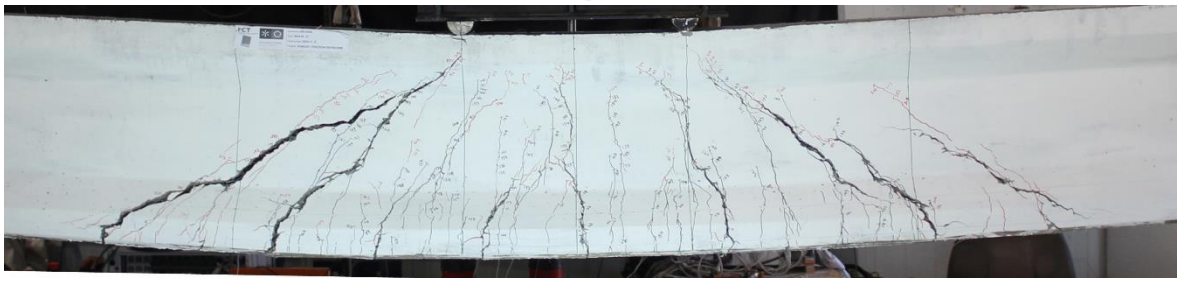

IB8

IB10

Annex 6A

User subroutine implemented in Abaqus (VUSDFLD)

```
      subroutine vusdfld(
c Read only -
     *   nblock, nstatev, nfieldv, nprops, ndir, nshr,
     *   jElem, kIntPt, kLayer, kSecPt,
     *   stepTime, totalTime, dt, cmname,
     *   coordMp, direct, T, charLength, props,
     *   stateOld,
c Write only -
     *   stateNew, field )
c
      include 'vaba_param.inc'
c
      dimension jElem(nblock), coordMp(nblock,*),
     *          direct(nblock,3,3), T(nblock,3,3),
     *          charLength(nblock), props(nprops),
     *          stateOld(nblock,nstatev),
     *          stateNew(nblock,nstatev),
     *          field(nblock,nfieldv)
      character*80 cmname
c
c     Local arrays from vgetvrm are dimensioned to
c     maximum block size (maxblk)
c
      parameter( nrData=6 )
      character*3 cData(maxblk*nrData)
      dimension rData(maxblk*nrData),jData(maxblk*nrData)
c
            jStatus = 1
            call vgetvrm( 'LE', rData, jData, cData, jStatus )
c
            if( jStatus .ne. 0 ) then
                  call xplb_abqerr(-2,'Utility routine VGETVRM '//
     *            'failed to get variable.',0,zero,' ')
                  call xplb_exit
            end if
c
            call setField( nblock, nstatev, nfieldv, nrData,
     *       rData, stateNew, field, coordMp, stateOld,
     *       cmname, jElem )
c
      return
      end
c
      subroutine setField( nblock, nstatev, nfieldv, nrData,
     *   strain, stateNew, field, coordMp, stateOld, cmname, jElem)
c
```

```
      include 'vaba_param.inc'
C
      dimension stateNew(nblock,nstatev), stateOld(nblock, nstatev),
     *   field(nblock,nfieldv), strain(nblock,nrData), coordMp(nblock,*)
     *   , jElem(nblock)
C
      do k = 1, nblock
C
C        strain of truss elements at each step of the analysis
           er = strain(k,1)
           stateNew(k,1) = er
C
C        modifying the Young's modulus for GFRP bars
      if (cmname .eq. 'GFRP') then
C        given value for alpha_ru, e_ru and E
                 e_ru = 0.025
                 alpha_ru = 49.0 * 4 * ATAN(1) / 180.0
                 Er = 60000.0
C        calculation of alpha_r
                 alpha_r = 45 + (alpha_ru / e_ru) * er
C                calculation of modified E
                 E_mod = Er * (2 - TAN(alpha_r))
                 field(k,1) =  1.0 - E_mod / Er
      endif
C
C        modifying the Young's modulus for steel strand
      if (cmname .eq. 'Strand') then
C        given value for alpha_ru, e_ru and E
                 e_ru = 0.01
                 alpha_ru = 49.0 * 4 * ATAN(1) / 180.0
                 Er = 187500.0
C        calculation of alpha_r
                 alpha_r = 45 + (alpha_ru / e_ru) * er
C                calculation of modified E
                 E_mod = Er * (2 - TAN(alpha_r))
                 field(k,1) =  1.0 - E_mod / Er
      endif
C
      end do
C
      return
      end
```

References

Achillides, Zenon, *Bond behaviour of FRP bars in concrete*, 1998. University of Sheffield.

ACI Committee 224, *Cracking of Concrete Members in Direct Tension (ACI 224.2R-92)*, 1997. American Concrete Institute, Farmington Hills, MI, USA.

ACI Committee 318, *Building Code Requirments for Reinforced Concrete (ACI 318-08)*, 2008. American Concrete Institute, Farmington Hills, MI, USA. p. 353.

ACI Committee 440, *Guide for the design and construction of concrete reinforced with FRP bars (ACI 440.1R-06)*, 2001. American Concrete Institute, Farmington Hills, MI, USA.

ACI Committee 440, *Prestressing Concrete Structures with FRP Tendons (ACI 440.4R-04)*, 2004. American Concrete Institute, Farmington Hills, MI, USA.

ACI Committee 440, *Guide for the design and construction of structural concrete reinforced with FRP bars (ACI 440.1R-06)*, 2006. American Concrete Institute, Farmington Hills, MI, USA.

Canadian Standard Association (CSA), *Design and construction of building component with fiber-reinforced polymers*, 2002. CSA Standard S806-02, Toronto, Cananda.

Canadian Standards Association, *Canadian highway bridge design code*, 2006. Ontario, Canada.

CEB-FIB, *Model Code 2010 – Final draft*, 2010. Thomas Thelford, Lausanne, Switzerland.

CEB-FIB, fib Task Group 9.3, *FRP reinforcement in RC structures*, 2007. Lausanne, Switzerland.

Japan Society of Civil Engineers (JSCE), *Recommandation for design and construction of concrete structure using continous fiber reinforcing materials*, 1997. N23, Concrete engineering series, Japan.

RILEM TC162-TDF, *Test and design methods for steel fibre reinforced concrete: Bending test*, 2000. p. 3-5.

RILEM, TC9-RC, *RC 5 Bond test for reinforcement steel. 1. Beam test, 1982*, 1994. p. 213-217.

Abdalla, H., "*Evaluation of deflection in concrete members reinforced with fibre reinforced polymer (FRP) bars*". Composite Structures, 2002. **56**(1): p. 63-71.

Abdelrahman, A. A. and S. H. Rizkalla, "*Serviceability of concrete beams prestressed by carbon-fiber-reinforced-plastic bars*". ACI Structural Journal, 1997. **94**(4).

Abrishambaf, A., J. A. O. Barros, and V. M. C. F. Cunha, "*Relation between fibre distribution and post-cracking behaviour in steel fibre reinforced self-compacting concrete panels*". Cement and Concrete Research, 2013. **51**: p. 57-66.

Abrishami, H. H. and D. Mitchell, "*Influence of Steel Fibers on Tension Stiffening*". ACI Structural Journal, 1997. **94**(6): p. 769-776.

Achillides, Z. and K. Pilakoutas, "*Bond behavior of fiber reinforced polymer bars under direct pullout conditions*". Journal of Composites for Construction, 2004. **8**(2): p. 173-181.

Achillides, Z. and K. Pilakoutas, "*FE modelling of bond interaction of FRP bars to*

concrete". Structural Concrete, 2006. **7**(1): p. 7-16.

Aiello, M. and L. Ombres, "*Cracking analysis of FRP-reinforced concrete flexural members"*. Mechanics of composite materials, 2000. **36**(5): p. 389-394.

Aiello, M. A., M. Leone, and M. Pecce, "*Bond performances of FRP rebars-reinforced concrete"*. Journal of materials in civil engineering, 2007. **19**(3): p. 205-213.

Aiello, M. A. and L. Ombres, "*Structural performances of concrete beams with hybrid (fiber-reinforced polymer-steel) reinforcements"*. Journal of Composites for Construction, 2002. **6**(2): p. 133-140.

Al-Salloum, Y. A. and T. H. Almusallam, "*Creep effect on the behavior of concrete beams reinforced with GFRP bars subjected to different environments"*. Construction and Building Materials, 2007. **21**(7): p. 1510-1519.

Al-Zahrani, M. M., S. U. Al-Dulaijan, A. Nanni, C. E. Bakis, and T. E. Boothby, "*Evaluation of bond using FRP rods with axisymmetric deformations"*. Construction and building materials, 1999. **13**(6): p. 299-309.

Almusallam, T. H., "*Analytical prediction of flexural behavior of concrete beams reinforced by FRP bars"*. Journal of composite materials, 1997. **31**(7): p. 640-657.

Alsayed, S., Y. Al-Salloum, and T. Almusallam, "*Performance of glass fiber reinforced plastic bars as a reinforcing material for concrete structures"*. Composites Part B: Engineering, 2000. **31**(6): p. 555-567.

Alsayed, S. H., "*Flexural behaviour of concrete beams reinforced with GFRP bars"*. Cement and Concrete Composites, 1998. **20**(1): p. 1-11.

Alsayed, S. H. and A. M. Alhozaimy, "*Ductility of concrete beams reinforced with FRP bars and steel fibers"*. Journal of composite materials, 1999. **33**(19): p. 1792-1806.

Baena, M., L. Torres, A. Turon, and C. Barris, "*Experimental study of bond behaviour between concrete and FRP bars using a pull-out test"*. Composites Part B: Engineering, 2009. **40**(8): p. 784-797.

Baena, M., L. Torres, A. Turon, and C. Miàs, "*Analysis of cracking behaviour and tension stiffening in FRP reinforced concrete tensile elements"*. Composites Part B: engineering, 2013. **45**(1): p. 1360-1367.

Baena, M., A. Turon, L. Torres, and C. Miàs, "*Experimental study and code predictions of fibre reinforced polymer reinforced concrete (FRP RC) tensile members"*. Composite Structures, 2011. **93**(10): p. 2511-2520.

Baghi, H., "*Shear strengthening of reinforced concrete beams with SHCCFRP panels"*. 2015. PhD Thesis, Universidade do Minho: Guimaraes, Portugal.

Baghi, H., J. A. Barros, M. Rezazadeh, and J. Laranjeira, "*Shear Strengthening of Damaged RC Beams with Hybrid Composite Plates"*. Journal of Composites for Construction (ASCE), 2015: p. 04015041.

Barris, C., L. Torres, A. Turon, M. Baena, and A. Catalan, "*An experimental study of the flexural behaviour of GFRP RC beams and comparison with prediction models"*. Composite Structures, 2009. **91**(3): p. 286-295.

Barros, J., "*Behaviour of fibre reinforced concrete–experimental analysis and numerical*

simulation". Unpublished PhD thesis). Dep. Civil Eng., Faculty of Eng., Porto University, 1995: p. 502.

Barros, J. and J. Sena Cruz, "*Fracture energy of steel fiber-reinforced concrete"*. Mechanics of Composite Materials and Structures, 2001. **8**(1): p. 29-45.

Barros, J. A., H. Baghi, S. J. Dias, and A. Ventura-Gouveia, "*A FEM-based model to predict the behaviour of RC beams shear strengthened according to the NSM technique"*. Engineering Structures, 2013. **56**: p. 1192-1206.

Barros, J. A. and J. A. Figueiras, "*Experimental behaviour of fiber concrete slabs on soil"*. 1998. **3**: p. 277-290.

Barros, J. A. and A. Fortes, "*Flexural strengthening of concrete beams with CFRP laminates bonded into slits"*. Cement and Concrete Composites, 2005. **27**(4): p. 471-480.

Barros, J. A., J. T. Oliveira, E. Bonaldo, and P. B. Lourenco, "*Flexural behavior of reinforced masonry panels"*. American Concrete Institute (ACI), 2006. **103**(3): p. 418-26.

Barros, J. A., R. K. Varma, J. M. Sena-Cruz, and A. F. Azevedo, "*Near surface mounted CFRP strips for the flexural strengthening of RC columns: Experimental and numerical research"*. Engineering Structures, 2008. **30**(12): p. 3412-3425.

Bažant, Z. P. and B. H. Oh, "*Crack band theory for fracture of concrete"*. Matériaux et construction, 1983. **16**(3): p. 155-177.

Benmokrane, B., O. Chaallal, and R. Masmoudi, "*Flexural response of concrete beams reinforced with FRP reinforcing bars"*. ACI Structural Journal, 1996. **93**(1).

Bianco, V., J. A. Barros, and G. Monti, "*Bond model of NSM-FRP strips in the context of the shear strengthening of RC beams"*. Journal of Structural Engineering, 2009. **135**(6): p. 619-631.

Bischoff, P. H., "*Tension Stiffening and Cracking of Steel Fiber-Reinforced Concrete"*. Journal of Materials in Civil Engineering, ASCE, 2003. **15**(2): p. 174-182.

Bischoff, P. H. and R. Paixao, "*Tension stiffening and cracking of concrete reinforced with glass fiber reinforced polymer (GFRP) bars"*. Canadian Journal of Civil Engineering, 2004. **31**(4): p. 579-588.

Breveglieri, M., A. Aprile, and J. Barros, "*Embedded Through-Section shear strengthening technique using steel and CFRP bars in RC beams of different percentage of existing stirrups"*. Composite Structures, 2015. **126**: p. 101-113.

Fiber Reinforced Polymers – Strengths, Weaknesses, Opportunities and Threats, 2009. Sydney, Australia.

Castel, A., R. François, and C. Tourneur, "*Effect of surface pre-conditioning on bond of carbon fibre reinforced polymer rods to concrete"*. Cement and Concrete Composites, 2007. **29**(9): p. 677-689.

Chang, X., G. Yue, H. Lin, and C. Tang, "*Modeling the pullout behavior of fiber reinforced polymer bars from concrete"*. Construction and Building Materials, 2010. **24**(4): p. 431-437.

Choi, C.-K. and S.-H. Cheung, "*Tension stiffening model for planar reinforced concrete*

members". Computers & Structures. **59**(1): p. 179-190.

Choi, D.-U., S.-C. Chun, and S.-S. Ha, "*Bond strength of glass fibre-reinforced polymer bars in unconfined concrete"*. Engineering Structures, 2012. **34**: p. 303-313.

Cosenza, E., G. Manfredi, and R. Realfonzo, "*Behavior and modeling of bond of FRP rebars to concrete"*. Journal of composites for construction, 1997. **1**(2): p. 40-51.

Cosenza, E., G. Manfredi, and R. Realfonzo, "*Development length of FRP straight rebars"*. Composites Part B: Engineering, 2002. **33**(7): p. 493-504.

Cosenza, E., G. Manfredi, and R. Realfonzo. "*Analytical modelling of bond between FRP reinforcing bars and concrete*". in *RILEM PROCEEDINGS*. 1995. CHAPMAN & HALL.

Cuenca, E. and P. Serna, "*Failure modes and shear design of prestressed hollow core slabs made of fiber-reinforced concrete"*. Composites Part B: Engineering, 2013. **45**(1): p. 952-964.

Cunha, V. M., J. A. Barros, and J. Sena-Cruz, "*An integrated approach for modelling the tensile behaviour of steel fibre reinforced self-compacting concrete"*. Cement and Concrete Research, 2011. **41**(1): p. 64-76.

Cunha, V. M. C. F., "*Steel Fibre Reinforced Self-Compacting Concrete (from Micro-Mechanics to Composite Behaviour)*." 2010. 2010, Guimaraes, Portugal: University of Minho.

Cunha, V. M. C. F., J. A. O. Barros, and J. M. Sena-Cruz, "*Pullout behaviour of steel fibres in self-compacting concrete"*. Journal of Materials in Civil Engineering (ASCE), 2010. **22**(1): p. 1-9.

Davalos, J. F., Y. Chen, and I. Ray, "*Effect of FRP bar degradation on interface bond with high strength concrete"*. Cement and Concrete Composites, 2008. **30**(8): p. 722-730.

Dias, S. J. and J. A. Barros, "*Shear strengthening of RC beams with NSM CFRP laminates: Experimental research and analytical formulation"*. Composite Structures, 2013. **99**: p. 477-490.

Ehsani, M., H. Saadatmanesh, and S. Tao, "*Design recommendations for bond of GFRP rebars to concrete"*. Journal of Structural Engineering, 1996. **122**(3): p. 247-254.

Eligehausen, R., E. P. Popov, and V. V. Bertero, "*Local bond stress-slip relationships of deformed bars under generalized excitations"*. 1982.

Focacci, F., A. Nanni, and C. E. Bakis, "*Local bond-slip relationship for FRP reinforcement in concrete"*. Journal of composites for construction, 2000. **4**(1): p. 24-31.

Gribniak, V., H. A. Mang, R. Kupliauskas, and G. Kaklauskas, "*Stochastic Tension-Stiffening Approach for the Solution of Serviceability Problems in Reinforced Concrete: Constitutive Modeling"*. Computer-Aided Civil and Infrastructure Engineering, 2015 (DOI: 10.1111/mice.12133).

Hao, Q.-d., Y.-l. Wang, Z.-c. Zhang, and J.-p. Ou, "*Bond strength improvement of GFRP rebars with different rib geometries"*. Journal of Zhejiang University SCIENCE A, 2007. **8**(9): p. 1356-1365.

Hao, Q., Y. Wang, Z. He, and J. Ou, "*Bond strength of glass fiber reinforced polymer ribbed*

rebars in normal strength concrete". Construction and Building materials, 2009. **23**(2): p. 865-871.

Hao, Q., Y. Wang, and J. Ou, "*Design recommendations for bond between GFRP/steel wire composite rebars and concrete"*. Engineering Structures, 2008. **30**(11): p. 3239-3246.

Harajli, M. and M. Abouniaj, "*Bond performance of GFRP bars in tension: Experimental evaluation and assessment of ACI 440 guidelines"*. Journal of Composites for Construction, 2010. **14**(6): p. 659-668.

Harajli, M., B. Hamad, and K. Karam, "*Bond-slip response of reinforcing bars embedded in plain and fiber concrete"*. Journal of Materials in Civil Engineering, 2002. **14**(6): p. 503-511.

Harris, H. G., W. Somboonsong, and F. K. Ko, "*New ductile hybrid FRP reinforcing bar for concrete structures"*. Journal of Composites for Construction, 1998. **2**(1): p. 28-37.

He, Z. and G.-w. Tian, "*Reliability-based bond design for GFRP-reinforced concrete"*. Materials and structures, 2011. **44**(8): p. 1477-1489.

Hegemier, G. A., H. Murakami, and L. J. Hageman, "*On tension stiffening in reinforced concrete"*. Mechanics of Materials, 1985. **4**(2): p. 161-179.

Hibbitt, Karlsson, and Sorensen, "*ABAQUS/standard user's Manual*." 2001. Vol. 1. 2001: Hibbitt, Karlsson & Sorensen.

Issa, M. S., I. M. Metwally, and S. M. Elzeiny, "*Influence of fibers on flexural behavior and ductility of concrete beams reinforced with GFRP rebars"*. Engineering Structures, 2011. **33**(5): p. 1754-1763.

Jaejer, L., A. Mufti, and G. Tadros. "*The concept of the overall performance factor in rectangular-section reinforced concrete beams*". in *Proceedings of the 3rd International Symposium on Non-Metallic (FRP) Reinforcement for Concrete Structures*. 1997.

Jones, R. M., "*Deformation theory of plasticity*." 2009. 2009: Bull Ridge Corporation.

Kashwani, G. A. and A. K. Al-Tamimi, "*Evaluation of FRP Bars Performance under High Temperature"*. Physics Procedia, 2014. **55**: p. 296-300.

Katz, A., "*Bond mechanism of FRP rebars to concrete"*. Materials and structures, 1999. **32**(10): p. 761-768.

Katz, A., "*Bond to concrete of FRP rebars after cyclic loading"*. Journal of composites for construction, 2000. **4**(3): p. 137-144.

Katz, A. and N. Berman, "*Modeling the effect of high temperature on the bond of FRP reinforcing bars to concrete"*. Cement and Concrete Composites, 2000. **22**(6): p. 433-443.

Katz, A., N. Berman, and L. C. Bank, "*Effect of high temperature on bond strength of FRP rebars"*. Journal of Composites for Construction, 1999. **3**(2): p. 73-81.

Kreyszig, E., "*Advanced Engineering Mathematics*." 1993. 1993, Berlin: John Wiley & Sons.

Lau, D. and H. J. Pam, "*Experimental study of hybrid FRP reinforced concrete beams"*.

Engineering Structures, 2010. **32**(12): p. 3857-3865.

Lee, J.-Y., T.-Y. Kim, T.-J. Kim, C.-K. Yi, J.-S. Park, Y.-C. You, and Y.-H. Park, "*Interfacial bond strength of glass fiber reinforced polymer bars in high-strength concrete"*. Composites Part B: Engineering, 2008. **39**(2): p. 258-270.

Lee, J. and G. L. Fenves, "*Plastic-damage model for cyclic loading of concrete structures"*. Journal of engineering mechanics, 1998. **124**(8): p. 892-900.

Lee, S.-C., J.-Y. Cho, and F. J. Vecchio, "*Diverse Embedment Model for Steel Fiber-Reinforced Concrete in Tension: Model Development"*. ACI Materials Journal, 2011. **108**(5): p. 516-525.

Lee, S., J. Cho, and F. Vecchio, "*Tension-stiffening model for steel fiber-reinforced concrete containing conventional reinforcement"*. ACI Structural Journal, 2013. **110**(4): p. 639-648.

Leung, H. and R. Balendran, "*Flexural behaviour of concrete beams internally reinforced with GFRP rods and steel rebars"*. Structural Survey, 2003. **21**(4): p. 146-157.

Li, F., Q. L. Zhao, H. S. Chen, J. Q. Wang, and J. H. Duan, "*Prediction of tensile capacity based on cohesive zone model of bond anchorage for fiber-reinforce dpolymer tendon"*. Composite Structures, 2010. **92**(10): p. 2400-2405.

Lubliner, J., J. Oliver, S. Oller, and E. Onate, "*A plastic-damage model for concrete"*. International Journal of solids and structures, 1989. **25**(3): p. 299-326.

Malvar, L. J., "*Tensile and bond properties of GFRP reinforcing bars"*. ACI Materials Journal, 1995. **92**(3).

Masmoudi, R., A. Masmoudi, M. B. Ouezdou, and A. Daoud, "*Long-term bond performance of GFRP bars in concrete under temperature ranging from 20 C to 80 C"*. Construction and Building Materials, 2011. **25**(2): p. 486-493.

Masmoudi, R., M. Theriault, and B. Benmokrane, "*Flexural behavior of concrete beams reinforced with deformed fiber reinforced plastic reinforcing rods"*. ACI Structural Journal, 1998. **95**(6).

Mazaheripour, H., J. A. Barros, F. Soltanzadeh, and D. Gonçalves. "*Interfacial bond behaviour of GFRP bar in self-compacting fiber reinforced concrete*". 2012. 8th RILEM International Symposium on Fibre Reinforced Concrete: challenges and opportunities.

Mazaheripour, H., J. A. O. Barros, J. Sena-Cruz, and F. Soltanzadeh, "*Analytical Bond Model for GFRP Bars to Steel Fiber Reinforced Self-Compacting Concrete"*. Journal of Composites for Construction, 2013. **17**(6): p. 04013009.

Mazaheripour, H., J. A. O. Barros, J. M. Sena Cruz, M. Pepe, and E. Martinelli, "*Experimental study on bond performance of GFRP bars in self-compacting steel fiber reinforced concrete"*. Composite Structures, 2013. **95**: p. 202-212.

Moreno, D. M., W. Trono, G. Jen, C. Ostertag, and S. L. Billington, "*Tension stiffening in reinforced high performance fiber reinforced cement-based composites"*. Cement & Concrete Composites, 2014. **50**: p. 36-46.

Moreno, D. M., W. Trono, G. Jen, C. Ostertag, and S. L. Billington, "*Tension-Stiffening in Reinforced High Performance Fiber-Reinforced Cement-Based Composites under*

Direct Tension". in *High performance fiber reinforced cement composites 6*, 2012, R.H. Parra-montesinos GJ, Naaman AE, Editor., Springer. p. 263–70.

Nanni, A., M. Al-Zaharani, S. Al-Dulaijan, C. Bakis, and I. Boothby. "*17 BOND OF FRP REINFORCEMENT TO CONCRETE-EXPERIMENTAL RESULTS*". in *Non-Metallic (FRP) Reinforcement for Concrete Structures: Proceedings of the Second International RILEM Symposium*. 1995. CRC Press.

Nayal, R. and H. A. Rasheed, "*Tension Stiffening Model for Concrete Beams Reinforced with Steel and FRP Bars"*. Journal of Materials in Civil Engineering, ASCE, 2006. **18**(6): p. 831-841.

Norris, T., H. Saadatmanesh, and M. R. Ehsani, "*Shear and flexural strengthening of R/C beams with carbon fiber sheets"*. Journal of structural engineering, 1997. **123**(7): p. 903-911.

Oehlers, D. J., M. Mohamed Ali, M. Haskett, W. Lucas, R. Muhamad, and P. Visintin, "*FRP-Reinforced concrete beams: unified approach based on IC theory"*. Journal of Composites for Construction, 2010. **15**(3): p. 293-303.

Okelo, R. and R. L. Yuan, "*Bond strength of fiber reinforced polymer rebars in normal strength concrete"*. Journal of composites for construction, 2005. **9**(3): p. 203-213.

Pecce, M., G. Manfredi, and E. Cosenza, "*Experimental Response and Code Modelsof GFRP RC Beams in Bending"*. Journal of Composites for Construction, 2000. **4**(4): p. 182-190.

Pecce, M., G. Manfredi, R. Realfonzo, and E. Cosenza, "*Experimental and analytical evaluation of bond properties of GFRP bars"*. Journal of Materials in Civil Engineering, 2001. **13**(4): p. 282-290.

Pepe, M., H. Mazaheripour, J. Barros, J. Sena-Cruz, and E. Martinelli, "*Numerical calibration of bond law for GFRP bars embedded in steel fibre-reinforced self-compacting concrete"*. Composites Part B: engineering, 2013. **50**: p. 403-412.

Pereira, E. B., G. Fischer, and J. A. Barros, "*Direct assessment of tensile stress-crack opening behavior of Strain Hardening Cementitious Composites (SHCC)"*. Cement and Concrete Research, 2012. **42**(6): p. 834-846.

Pisani, M. A., "*A numerical survey on the behaviour of beams pre-stressed with FRP cables"*. Construction and building materials, 1998. **12**(4): p. 221-232.

Qu, W., X. Zhang, and H. Huang, "*Flexural Behavior of Concrete Beams Reinforced with Hybrid (GFRP and Steel) Bars"*. Journal of Composites for Construction, 2009. **13**(5): p. 350-359.

Rasheed, H. A., R. Nayal, and H. Melhem, "*Response prediction of concrete beams reinforced with FRP bars"*. Composite Structures, 2004. **65**(2): p. 193-204.

Ren, W., L. H. Sneed, Y. Yang, and R. He, "*Numerical Simulation of Prestressed Precast Concrete Bridge Deck Panels Using Damage Plasticity Model"*. International Journal of Concrete Structures and Materials, 2014. **9**(1): p. 45-54.

Rezazadeh, M., I. Costa, and J. Barros, "*Influence of prestress level on NSM CFRP laminates for the flexural strengthening of RC beams"*. Composite Structures, 2014. **116**: p. 489-500.

Robert, M. and B. Benmokrane, "*Effect of aging on bond of GFRP bars embedded in concrete"*. Cement and Concrete Composites, 2010. **32**(6): p. 461-467.

Rosenboom, O., T. K. Hassan, and S. Rizkalla, "*Flexural behavior of aged prestressed concrete girders strengthened with various FRP systems"*. Construction and building materials, 2007. **21**(4): p. 764-776.

Rossetti, V. A., D. Galeota, and M. M. Giammatteo, "*Local bond stress-slip relationships of glass fibre reinforced plastic bars embedded in concrete"*. Materials and Structures, 1995. **28**(6): p. 340-344.

Ruiz, M. F., A. Muttoni, and P. Gambarova, "*Analytical modeling of the pre-and postyield behavior of bond in reinforced concrete"*. Journal of Structural Engineering, 2007. **133**(10): p. 1364-1372.

Ryu, D., J. Ko, and T. Noguchi, "*Effects of simulated environmental conditions on the internal relative humidity and relative moisture content distribution of exposed concrete"*. Cement & Concrete Composites, 2001. **33**(1): p. 142-53.

Saadatmanesh, H. and M. Ehsani, "*Fiber composite bar for reinforced concrete construction"*. Journal of Composite Materials, 1991. **25**(2): p. 188-203.

Sena-Cruz, J., J. A. Barros, Á. F. Azevedo, and A. V. Gouveia. "*Numerical simulation of the nonlinear behavior of RC beams strengthened with NSM CFRP strips*". in *CMNE 2007 – Congress on Numerical Methods in Engineering and XXVIII CILAMCE – Iberian Latin American Congress on Computational Methods in Engineering,*. 2007. FEUP, Porto, Portugal.

Sena Cruz, J., "*Strengthening of concrete structures with near-surface mounted CFRP laminate strips"*. 2004. PhD Thesis, Universidade do Minho: Guimaraes, Portugal.

Soltanzadeh, F., J. A. O. Barros, and R. F. C. Santos, "*High performance fiber reinforced concrete for the shear reinforcement: Experimental and numerical research"*. Construction and Building Materials, 2015. **77**: p. 94-109.

Soltanzadeh, F., H. Mazaheripour, J. Barros, and J. Sena-Cruz. "*Shear capacity of HPFRC beams flexurally reinforced with steel and prestressed GFRP bars*". in *11th International Symposium on Fiber Reinforced Polymers for Reinforced Concrete Structures (FRPRCs-11)*. 2013. Guimaraes, Portugal.

Soltanzadeh, F., H. Mazaheripour, J. A. Barros, M. Taheri, and J. Sena-Cruz. "*Experimental study on shear behavior of HPFRC beams reinforced by hybrid pre-stressed GFRP and steel bars*". in *The 7th International Conference on FRP Composites in Civil Engineering (CICE 2014)*. 2014. Vancouver, Canada.

Sooriyaarachchi, H., K. Pilakoutas, and E. Byars. "*Tension Stiffening Behavior of GFRP-Reinforced Concrete*". in *7th International Symposium on Fiber Reinforced Polymer Reinforcement for Reinforced Concrete Structures (FRPRCS-7)*. 2005. New Orleans, Louisiana, USA.

Steffens, A., D. Dinkler, and H. Ahrens, "*Modeling carbonation for corrosion risk prediction of concrete structures"*. Cement and Concrete Research, 2002. **32**(6): p. 935-41.

Stoll, F., J. E. Saliba, and L. E. Casper, "*Experimental study of CFRP-prestressed high-strength concrete bridge beams"*. Composite structures, 2000. **49**(2): p. 191-200.

Taheri, M., J. A. O. Barros, and H. Salehian, "*A design model for strain-softening and strain-hardening fiber reinforced elements reinforced longitudinally with steel and FRP bars"*. Composites Part B: engineering, 2011. **42**(6): p. 1630-1640.

Taheri, M., J. A. O. Barros, and H. Salehian, "*A parametric study on the use of strain softening/hardening FRC for RC elements failing in bending"*. Journal of Materials in Civil Engineering (ASCE), 2012. **24**(3): p. 259-274.

Tang, W., T. Lo, and R. V. Balendran, "*Bond performance of polystyrene aggregate concrete (PAC) reinforced with glass-fibre-reinforced polymer (GFRP) bars"*. Building and environment, 2008. **43**(1): p. 98-107.

Tastani, S. and S. Pantazopoulou, "*Bond of GFRP bars in concrete: experimental study and analytical interpretation"*. Journal of Composites for Construction, 2006. **10**(5): p. 381-391.

Tastani, S. P., S. J. Pantazopoulou, and P. Karvounis, "*Local Bond-Slip Characteristics of G-FRP Bars"*. ACI Special Publication, 2005. **230**.

Tavares, D. H., J. S. Giongo, and P. Paultre, "*Behavior of reinforced concrete beams reinforced with GFRP bars"*. RIEM-Revista IBRACON de Estruturas e Materiais, 2008. **1**(3).

Tepfers, R. and L. De Lorenzis, "*Bond of FRP reinforcement in concrete-a challenge"*. Mechanics of composite materials, 2003. **39**(4): p. 315-328.

Theriault, M. and B. Benmokrane, "*Effects of FRP reinforcement ratio and concrete strength on flexural behavior of concrete beams"*. Journal of composites for construction, 1998. **2**(1): p. 7-16.

Tighiouart, B., B. Benmokrane, and D. Gao, "*Investigation of bond in concrete member with fibre reinforced polymer (FRP) bars"*. Construction and Building Materials, 1998. **12**(8): p. 453-462.

Tighiouart, B., B. Benmokrane, and P. Mukhopadhyaya, "*Bond strength of glass FRP rebar splices in beams under static loading"*. Construction and Building Materials, 1999. **13**(7): p. 383-392.

Toutanji, H. and Y. Deng, "*Deflection and crack-width prediction of concrete beams reinforced with glass FRP rods"*. Construction and Building Materials, 2003. **17**(1): p. 69-74.

Toutanji, H. A. and M. Saafi, "*Flexural behavior of concrete beams reinforced with glass fiber-reinforced polymer (GFRP) bars"*. ACI structural journal, 2000. **97**(5).

Valcuende, M. and C. Parra, "*Bond behaviour of reinforcement in self-compacting concretes"*. Construction and Building Materials, 2009. **23**(1): p. 162-170.

Vandewalle, L., "*RILEM TECHNICAL COMMITTEES-Recommendations of RILEM TC 162-TDF: Test and design methods for steel fibre reinforced concrete"*. Materials and structures, 2000. **33**(225): p. 3-5.

Varma, R. K., "*Numerical models for the simulation of the cyclic behaviour of RC structures incorporating new advanced materials"*. 2013. PhD thesis, University of Minho: Guimaraes, Portugal.

Ventura-Gouveia, A., "*Constitutive models for the material nonlinear analysis of concrete*

structures including time dependent effects". Guimaraes, Portugal: University of Minho, 2011.

Vilanova, I., L. Torres, M. Baena, G. Kaklauskas, and V. Gribniak, "*Experimental study of tension stiffening in GFRP RC tensile members under sustained load"*. Engineering Structures, 2014. **79**(15): p. 390-400.

Visintin, P., "*A generic segmental analysis of all types of RC members"*. University of Adelaide, Adelaide, Australia, 2012.

Visintin, P., D. Oehlers, C. Wu, and M. Haskett, "*A mechanics solution for hinges in RC beams with multiple cracks"*. Engineering Structures, 2012. **36**: p. 61-69.

Vogel, H. and D. Svecova, "*Thermal compatibility and bond strength of FRP reinforcement in prestressed concrete applications"*. Journal of Composites for Construction, 2007. **11**(5): p. 459-468.

Wambua, P., J. Ivens, and I. Verpoest, "*Natural fibres: can they replace glass in fibre reinforced plastics?"*. composites science and technology, 2003. **63**(9): p. 1259-1264.

Wang, H. and A. Belarbi, "*Ductility characteristics of fiber-reinforced-concrete beams reinforced with FRP rebars"*. Construction and Building Materials, 2011. **25**(5): p. 2391-2401.

Wang, Y., "*Mechanics of fiber reinforced cementitious composites"*. 1989. PhD Thesis, Massachusetts Institute of Technology (MIT), USA.

Won, J.-P., C.-G. Park, H.-H. Kim, S.-W. Lee, and C.-I. Jang, "*Effect of fibers on the bonds between FRP reinforcing bars and high-strength concrete"*. Composites Part B: Engineering, 2008. **39**(5): p. 747-755.

Yang, J.-M., K.-H. Min, H.-O. Shin, and Y.-S. Yoon, "*Effect of steel and synthetic fibers on flexural behavior of high-strength concrete beams reinforced with FRP bars"*. Composites Part B: Engineering, 2012. **43**(3): p. 1077-1086.

Youakim, S. A. and V. M. Karbhari, "*An approach to determine long-term behavior of concrete members prestressed with FRP tendons"*. Construction and Building Materials, 2007. **21**(5): p. 1052-1060.

Zhang, B. and B. Benmokrane, "*Pullout bond properties of fiber-reinforced polymer tendons to grout"*. Journal of materials in civil engineering, 2002. **14**(5): p. 399-408.

Zhang, B., B. Benmokrane, and A. Chennouf, "*Prediction of tensile capacity of bond anchorages for FRP tendons"*. Journal of Composites for Construction, 2000. **4**(2): p. 39-47.

Zhao, X. and M. Cai, "*A mobilized dilation angle model for rocks"*. International Journal of Rock Mechanics and Mining Sciences, 2010. **47**(3): p. 368-384.

Zou, P. X., "*Flexural behavior and deformability of fiber reinforced polymer prestressed concrete beams"*. Journal of composites for Construction, 2003. **7**(4): p. 275-284.

Zou, P. X., "*Theoretical study on short-term and long-term deflections of fiber reinforced polymer prestressed concrete beams"*. Journal of composites for construction, 2003. **7**(4): p. 285-291.